EXPERIMENTAL AND NUMERICAL ANALYSIS OF ISOTHERMAL TURBULENT FLOWS IN INTERACTING LOW NOx BURNERS IN COAL-FIRED FURNACES

by

Valentina Cvoro

Doctor of Philosophy
The University of Edinburgh
2007

Abstract

Coal firing power stations represent the second largest source of global NOx emissions. The current practice of predicting likely exit NOx levels from multi-burner furnaces on the basis of single burner test rig data has been proven inadequate. Therefore, to further improve current NOx reduction technologies and assist in the assessment of NOx levels in new and retrofit plant cases, an improved understanding of the impact of burner interactions is required.

The aim of this research is two-fold: firstly, to experimentally investigate isothermal flow interactions in multi-burner arrays for different swirl directions and burner pitches in order to gain a better understanding of burner interaction effects within multi-burner furnaces. Secondly, to carry out numerical modelling in order to determine turbulence models which give the best agreement to experimental data. Experimental investigations were carried out using flow visualisation for qualitative and 3D laser Doppler anemometry for quantitative measurements. Numerical modelling was performed using the computational fluid dynamics software, Fluent, to compare performance between k-ε, k- ω and RSM turbulence models.

Experimental investigation showed that the recirculation zone of the chequerboard configuration is more sensitive to the change in pitch than that of the columnar configuration. Further, it was found that the smaller pitch is more sensitive to change in configuration than the wider pitch. The analysis of fluctuating components, u′, v′ and w′ showed that the burner flow is highly anisotropic at burner exit.

Numerical investigation showed that the k-ω turbulence model consistently performed below the other two models. The statistical comparison between k-ε and RSM turbulence models revealed that, for prediction of the swirl velocity profiles, the RSM model overall performed better than the k-ε turbulence model. The visual and statistical analyses of turbulent kinetic energy profiles also showed that the RSM

turbulence model provides a closer match to the experimental data than the k-ε turbulence model.

Declaration

I declare that this thesis has been composed by myself and is all my own work except where otherwise stated.

Signed

Valentina Cvoro
Edinburgh, December 2006

Acknowledgements

I dedicate this thesis to my parents, Vukosava and Cedomir, whose unconditional love and words of wisdom gave me strength and motivation to persevere through the most difficult moments.

My thanks go to my husband, Gavin, for his encouragement, his ability to bring clarity to my thoughts, his patience, love and support.

I would like to express my deepest gratitude to my supervisor and friend, Professor William J. Easson. His enthusiastic guidance was essential to build up this thesis. Bill, I truly hope that our next project will take many years and involve the repeated 'analysis of golf ball trajectories' on sunny golf courses in France.

Many thanks to Mitsui Babcock Energy Limited for their support in realisation of the DTI and BCURA projects, and for kindly allowing me to use their computational model of a coal fired furnace.

Table of contents

Chapter 1

Chapter 2

Chapter 3

Chapter 4

Chapter 5

Chapter 6

Chapter 7

Chapter 8

Chapter 9

Table of figures

Table of tables

Nomenclature

Acronyms

ASTM Algebraic Stress Models
BSA Burst Spectrum Analyser
CFD Computational Fluid Dynamics
CCT Clean Coal Technologies
FGD flue gas desulphurisation
LDA Laser Doppler Anemometry
LES Large Eddy Simulation
NKEM Nonlinear k-ε Model
PIV Particle Image Velocimetry
RANS Reynolds Averaged Navier-Stokes
RSM Reynolds Stress Model
RSTM Reynolds Stress Transport Model
SCR Selective Catalytic Reduction
SNCR Selective Non-Catalytic Reduction

Symbols

d	nozzle diameter
dh	hub diameter
Gφ	axial flux of angular momentum
Gx	axial flux of linear momentum
I	intensity of turbulence
K	kinetic energy
S	swirl number
$\overline{u}$	mean axial velocity
$\overline{v}$	mean radial velocity
$\overline{w}$	mean swirl velocity
u'	fluctuating components of axial velocity
v'	fluctuating components of radial velocity

w'	fluctuating components of swirl velocity
$-\overline{\rho u_i'^2}$	normal Reynolds stress component
$-\overline{\rho u_i' u_j'}$	Reynolds shearing stress components
ρ	density of fluid
ε	dissipation rate
μ_t	turbulent viscosity

Chapter 1

Introduction

Coal is forecast to maintain the dominant role in world electricity generation over the next couple of decades. The resource availability and economic viability are the two key factors that underpin the future of coal as one of the key components in the world's energy mix. Therefore, improving the efficiency of coal-fired power plants and the minimisation of their environmental impacts is paramount, for both economic and environmental reasons. To this end, a range of Clean Coal Technologies (CCTs) have been developed to minimise the emission of a variety of undesirable substances emitted from coal-fired power plants.

1.1 Coal – an important energy resource

Coal has been used as an energy source for hundreds of years – it has fuelled the Industrial Revolution of the 19^{th} Century, and continued to be the main fuel for the speedy development of electricity generation in the 20th century.

With the world electricity demand projected to grow at an annual rate of 2.5%, nearly doubling from 16.1 trillion kilowatt-hour in 2002 to 31.7 trillion kilowatt-hour in 2030 (IEA, 2005), there is little doubt that coal will retain a very important position in fuelling this electricity generation capacity.

Currently, two-thirds of the coal consumed worldwide is used for electricity generation (IEA, 2005). While coal use in some of the more developed countries remains static or is in decline, significant increases in coal-fired generation capacity are taking place in many of the developing nations, such as China and India, and large capacity increases are planned. In almost every region world-wide, power generation accounts for most of the projected growth in coal consumption of some 1.5% per annum. Coal-fired power plants provided 39% of global electricity needs in 2002. This share is expected to fall only slightly, to 38% in 2030 (IEA, 2005).

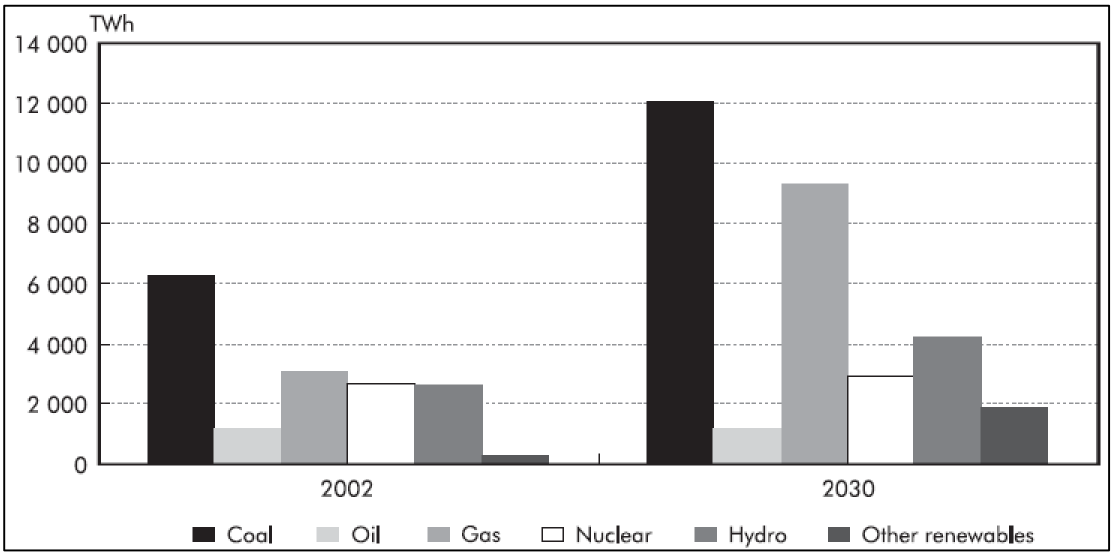

Figure 1.1 World electricity generation by energy sources, Source: IEA World Energy Outlook 2004 (IEA, 2005)

Figure 1.1 illustrates the major role coal is forecast to play in world electricity generation over the next couple of decades. According to IEA's 2004 World Energy Outlook, despite the forecast of gas-based electricity production tripling by 2030, coal will remain the dominant fuel worldwide (IEA, 2005).

The two factors that underpin the future of coal as one of the key components in the world's energy mix are the resource availability and economic viability. Coal resources are far more abundant than other fossil fuel resources, and coal is the least capital-intensive of the fuels - supply of one unit of energy from coal is only about one-sixth as capital-intensive as producing and transporting the same unit from gas (IEA, 2003).

1.2 Clean-coal technologies

Despite its strong demand, growth projection and importance it plays in the power generation energy mix, coal has been under strong attack. Coal is the least clean fossil fuel with respect to both local and global environment issues. The UN Framework Convention on Climate Change, and most recently the Kyoto Protocol, poses threats to fossil fuel use by placing limitations on carbon dioxide emissions (IEA, 1999).

Coal's on-going role underlines the importance of improving the efficiency of coal-fired power plants and the minimisation of their environmental impacts, for both economic and environmental reasons. Therefore, a range of technologies has been developed to minimise the emission of a variety of undesirable substances emitted from coal-fired power plants. Collectively, these systems are often referred to as Clean Coal Technologies (CCTs). A CCT is a technology which, in an economically viable manner, reduces plant emissions to enable the facility to meet or exceed any emissions standards in force. CCTs are becoming increasingly important, as they provide a means for coal-fired plant to meet the requirements of the increasingly stringent environmental legislation applied in many countries (IEA*, 2003).

CCTs used throughout the world to control emissions of particulate matter, SO_2 and NOx from pulverized coal combustion include:

- particulate emissions control technologies
- flue gas desulphurisation (FGD) for SO_2 control and
- NOx emissions abatement and control by:
    - primary measures (burner optimisation, air staging, flue gas recirculation, fuel staging, low NOx burners), or
    - flue gas treatment (selective catalytic reduction (SCR), selective non-catalytic reduction (SNCR), combined SO_2/NOx control systems).

My PhD research was focused towards development of CCTs, where reduction in NOx emissions could be achieved by implementation of primary measures.

1.3 Coal-fired power plants

Pulverised fuel (PF)-fired stations have been in use for more than 60 years and they remain the main form of coal-fired power generation. PF-based plant is found throughout the world and is in widespread use in both developed and developing nations (IEA*, 2003).

1.3.1 Process overview

Figure 1.2 presents a simplified schematic of a coal-fired electric utility boiler operated at a conventional electric utility power plant. Coal is typically delivered to a power plant by railcars, trucks, or barges. The coal is then crushed or pulverized before being fed to the boiler.

The coal is ignited and burned in the section of the boiler called the ‘furnace chamber’. Blowing ambient air into the furnace chamber provides the oxygen required for combustion. The carbon and hydrogen comprising the coal are oxidized at the high temperatures produced by combustion to form the primary combustion products of carbon dioxide (CO_2) and water (H_2O). Sulphur in the coal is oxidized to form SO_2. Molecular nitrogen in the combustion air and nitrogen bound in the coal react with oxygen in certain sections of the combustion zone in the furnace chamber to form NOx.

The walls of the furnace chamber are lined with vertical tubes containing water. Heat transfer from the hot combustion gases in the furnace boils the water in the tubes to produce high-temperature, high-pressure steam. This steam flows from the boiler to a steam turbine. In the turbine, the thermal energy in the steam is converted to mechanical energy to drive a shaft that spins a generator, which produces electricity (USEPA, 2002).

After the steam exits the turbine, it is condensed and the water is pumped back to the boiler. To improve overall energy conversion efficiency, modern coal-fired electric utility boilers contain a series of heat recovery sections. These heat recovery sections are located downstream of the furnace chamber and are used to extract additional heat from the flue gas. The first heat recovery section contains a 'superheater', which is used to increase the steam temperature. The second heat recovery section contains a 'reheater', which reheats the steam exhausted from the first stage of the turbine. This steam is then returned for another pass thorough a second stage of the turbine. The reheater is followed by an 'economizer', which preheats feed water to the boiler tubes in the furnace. The final heat recovery section is the 'air heater', which preheats ambient air used for combustion of the coal (USEPA, 2002).

A portion of all coals is composed of mineral matter that is non-combustible. This matter forms the ash that continuously must be removed from the operating utility boiler. The finer, lighter ash particles are entrained in the combustion gases and vented from the furnace section with the flue gas. This portion of the coal ash is referred to as "fly ash". The coarser, heavier ash particles fall to the bottom of the furnace section in the boiler unit. This portion of the coal ash is referred to as "bottom ash" .The flue gas exhausted from the boiler passes through air pollution control equipment and is vented to the atmosphere through a tall stack (USEPA, 2002).

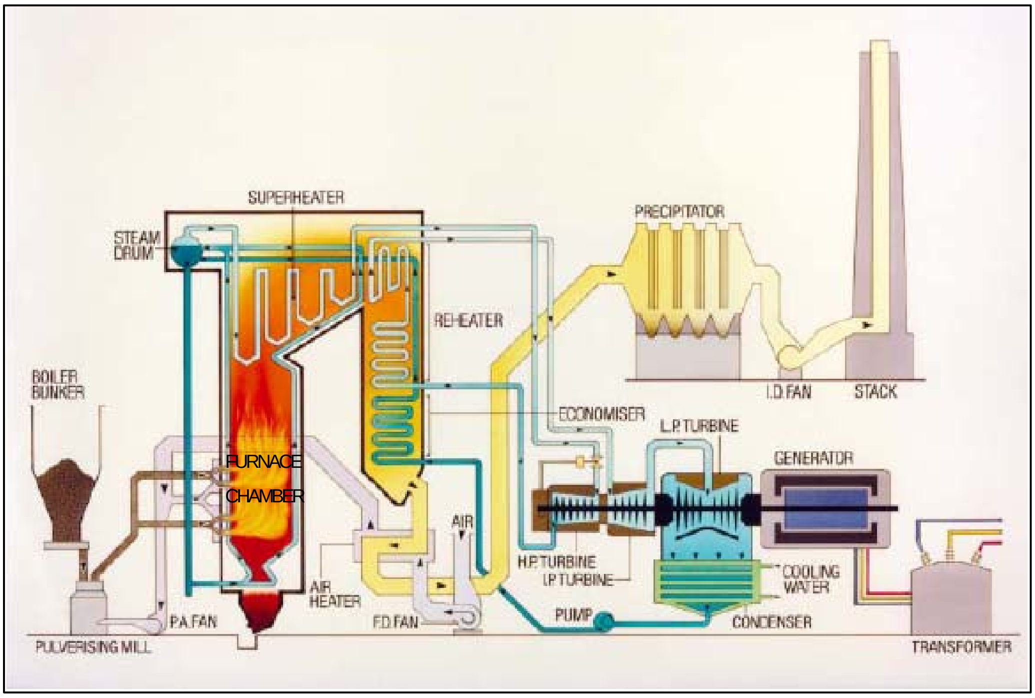

Figure 1.2 Layout of a PF power plant (IEA, 2003)*

1.4 Furnace and burner design – impact on reduction of NOx emissions

Power stations firing coal represent the second largest source of global NOx emissions. The ever more stringent legislation and emission standards are putting increasing pressure on power plant operators to develop new technologies which would enable them to achieve the required emission targets. In order to achieve both environmental improvements and attain economic benefits, power plant operators require more effective furnace utilisation with fully optimised pulverised coal (PF) burners. This would lead to lower cost NOx control and therefore a reduced capital expenditure for operators of such plant (Duncan et al., 2002).

Both burner manufacturers and utility plant operators have recognised that the interaction of burner flames within multi-burner furnaces can potentially represent a significant contribution to NOx levels. The current practice of predicting the likely exit NOx levels from a multi-burner furnace on the basis of single burner test rig data has been proven inadequate (Lockwood and Parodi, 1998). Therefore, to further improve current NOx reduction technologies and assist in the assessment of NOx levels in new and retrofit plant cases, an improved understanding of the impact of burner interactions is required (Cvoro and Easson, 2003; Tarr and Allen, 1997).

In order to achieve improved understanding of burner jet interactions, a mixture of scaled isothermal modelling and computational fluid dynamics (CFD) has been performed as part of this PhD work, in an attempt to gain better knowledge of the key parameters that are proved to influence NOx emissions, such as burner spacing and swirl orientation.

1.5 Thesis outline

A comprehensive review of the literature relating to the experimental and numerical modelling of multiple swirling burner flows is presented in chapter 2. Chapter 3 follows on with the theoretical background, describing the fundamental properties of turbulence together with the governing equations of turbulent flows. The underlying physical principles of turbulent jets are also described.

Chapter 4 gives an overview of the experimental apparatus, describing a design procedure implemented in construction of a physical model of a front wall fired furnace and a swirled burner. Flow measurement techniques, flow visualisation and 3-D LDA, which were used to investigate the effect of swirl jet interaction, are presented in chapter 5.

Numerical modelling, featuring the fundamentals of closure modelling with a detailed overview of the turbulence models applied in numerical simulations, as well as description of the Computational Fluid Dynamics (CFD) model used, is described in chapter 6.

Experimental and numerical results are presented in chapters 7 and 8 respectively. In chapter 7, the experimental results, obtained using flow visualisation and 3-D Laser Doppler Anemometry, are discussed and compared to the previously published work. Numerical modelling results, obtained using three different turbulence models: k-ε, k-ω and Reynolds Stress Model (RSM), were analysed and compared with the experimental data in order to identify the numerical model that provides the best match to the experimental data. The numerical results are also discussed with respect to the previously published work.

Conclusions of my PhD research are presented in Chapter 9, together with recommendations for future work.

Chapter 2

Review of the literature

A comprehensive review of the literature relating to the experimental and numerical modelling of multiple swirling burner flows has been carried out. The survey showed that limited research work has been done in this area. There are only a handful of authors whose work and findings can be directly compared to the results of my PhD research. The literature review also included other relevant topics such as isothermal and combusting swirl flows, single burner flows and jet mixing (a topical area of research in the aerospace industry). These topics have been investigated either experimentally or numerically, or both.

2.1 Turbulent swirling flows

There have been numerous experimental and theoretical studies on turbulent swirling flows that have taken place over the past fifty years. Although studies conducted by Becker and Brown (1969), Gunther and Simon (1969), Vranos et al. (1969) and Williams et al. (1969) using tracer techniques and pressure probes brought some significant contributions in understanding of turbulent mass transport as well as measurement of velocity fluctuations in turbulent flows, they have failed to address the important case of swirling flow.

2.1.1 Characterisation and importance of degree of swirl

In the early 1960s, Chigier and Beér (1964) carried out a comprehensive experimental study on swirling air jets at the International Flame Research Institution, Holland. They obtained mean-velocity and static pressure measurements in a series of swirling air jets issuing from annular and divergent nozzles into stagnant air surroundings. The differential pressures were measured using a Beaudouin pressure transducer.

Chigier and Beér (1964) varied the amount of swirl by varying proportions of the mass-flow rates of air introduced tangentially and axially into the swirl generator. They concluded that the degree of swirl can be characterised by the non-dimensional group $G_{\phi}/G_{x}r_{2}$[*] obtained from the integration of the radial distributions of mean velocity and static pressure.

A comparison of non-dimensionalised velocity and static pressure distributions showed that the basic non-dimensional characteristics of swirling jets, i.e. pressures in swirl generator, exit profiles, minimum pressure, maximum reverse flow velocity, and length of the internal vortex, were largely determined by the ratio of the momenta.

---

[*] *G_{φ}= axial flux of angular momentum, kg m sec^{-2}*
G_{x}= axial flux of linear momentum, kg m sec^{-2}
r = radial distance from axis, m

However, it also became clear that the shape of the nozzle as well as the method of introduction of the tangential air can also influence the behaviour of the jets. Therefore, whilst it could not be claimed that the ratio $G_\phi/G_x r_2$ is the sole universal criterion for swirling, it represents the significant criterion of similarity for all swirling jets with similar swirl generators.

As part of an experimental study carried out at the Department of Aeronautical Engineering (Israel Institute of Technology) in the late 1960s, Chigier and Chervinsky (1967) performed an investigation of swirling vortex motion in jets. They carried out experiments in a series of axisymmetric free turbulent jets with degrees of swirl covering weak, moderate, and strong ranges, from 0.066 to 0.64, including the case of the onset of reversed flow in the central region of the jet.

The measurements were taken using a five-hole spherical impact probe. Velocity magnitudes were determined from the five pressure measurements made at each measuring point.

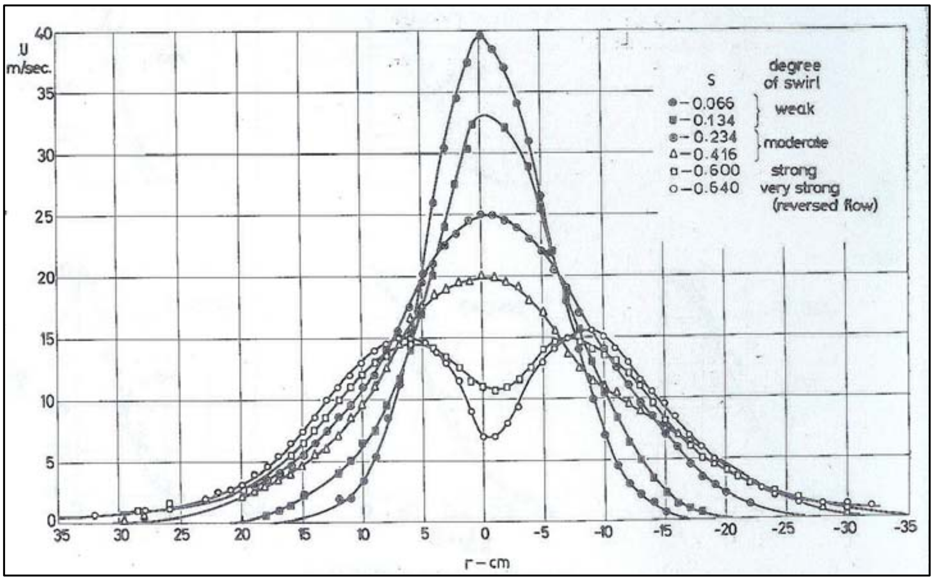

Figure 2.1 Radial distributions of velocity vector (x/d = 4.1) (Chigier and Chervinsky, 1967)

They showed that the decay of velocity along the axis and spread of the jets are both functions of the degree of swirl. The radial distributions of axial velocity, *U*, showed that the form of the profiles is Gaussian for weak degrees of swirl (Figure 2.1). For strong swirl (0.6), the velocity maximum is displaced from the jet axis, whilst for very strong swirl (0.64), reversed flow was measured up to three diameters from the orifice. Theoretical background and calculation of the swirl strength, S, is presented in chapter 3.

2.1.2 Recirculation zones

Flames in combustion chambers are generally stabilised by means of recirculation zones. The recirculation zone acts as a continuous heat source by transporting hot combustion products upstream toward the burner and therefore supplying energy required for ignition. Since the strength of the recirculation eddy is directly proportional to the main stream velocity, flame stabilisation is possible over a large range of velocities. In addition to the stability of the flame, the size and shape of the recirculation zone have been shown to affect the volumetric heat release rate and the combustion efficiency (Chigier and Gilbert, 1968).

In his earlier studies, conducted at the Flame Research Foundation in Ijmuiden, Holland, in 1964, and at the Department of Aeronautical Engineering in Haifa, Israel, in 1967, Chigier had already found that, for strong swirl, velocity went into reversed flow. Chigier and Gilbert (1968) carried out an experimental study made of recirculation eddies set up in the wake of flame holders. They concluded that the size and shape of reverse flow zones are determined by the following:

- the shape and diameter of the swirler
- the degree of swirl imparted to the flow
- the angle of the divergent quarl and
- flameholder - quarl blockage ratio.

They found that the length of the recirculation zone increases up to swirl number of 1.5, beyond which it start to decrease. The authors also showed that an increase in the blockage ratio can lead to a substantial reduction in the length of the recirculation zone.

Syred et al. (1971) carried out an experimental study of recirculation zones set up in the central region of a large diameter swirl burner with air introduced into the burner through tangential slots. They obtained measurements of spatial distributions of mean temperature and mean velocity under both combustion and isothermal conditions using a hot-wire anemometer.

Measurements taken in both cold and flame conditions showed that the recirculation zone occupies a large proportion of the main flow field. Figure 2.2 gives spatial distributions of stream function in the cold conditions. It shows the eye of the vortex to be just outside the burner exit (x/D = 0.35). Deflection of streamlines occurs well inside the burner and rapid expansion of the jet is seen soon after emergence from the burner exit.

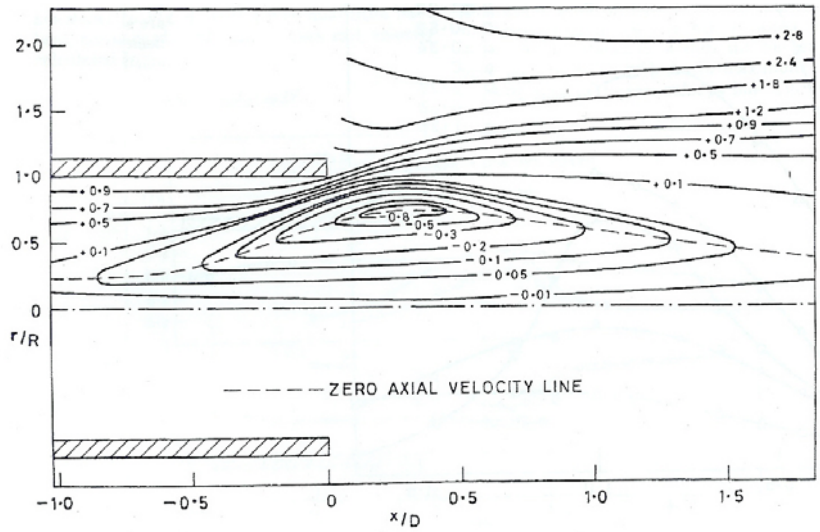

Figure 2.2 Spatial distribution of normalised stream function, Ψ/Ψ₀ (Syred et al., 1971)

Syred et al. (1971) compared boundaries of the reverse flow region under hot and cold conditions (Figure 2.3). This figure shows that under combustion conditions, the size of the reverse flow zone is slightly reduced but the shape is essentially the same. The authors also compared the reverse flow rates for the two conditions and found very little difference between the two states.

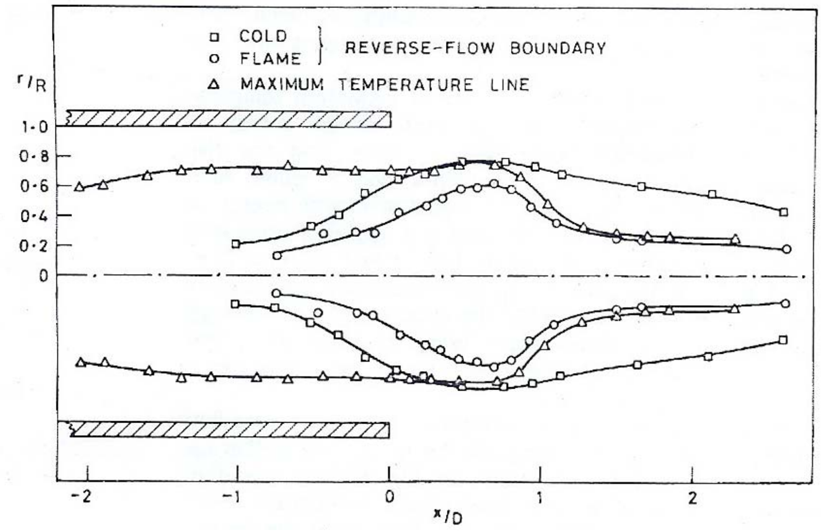

Figure 2.3 Boundaries of reverse-flow region and maximum temperature line (Syred et al., 1971)

Syred et al. (1971) concluded that the similarity in the size and shape of the recirculation zones in the 'hot' and 'cold' states suggests that aerodynamic forces dominate and measurements in a 'cold' model of such a burner will often be sufficient to predict the size of the recirculation zone under 'hot' conditions.

2.1.3 Turbulent stress distribution

Building on the previous work by Chigier and Chervinsky (1967), and using their predictions made from experimental mean data, Lilley and Chigier (1970) carried out calculations which proved that the turbulent stress distribution is anisotropic (not the same in all directions, i.e. opposite of isotropic).

Lilley and Chigier recognised that in systems with high levels of turbulence, there is difficulty in obtaining accurate turbulence measurements in comparison to the relative ease of measuring mean velocities. The method they employed in their research utilised only axial and swirl velocity measurements, which allowed information of shear stress distribution to be determined.

Their results showed that, as the degree of swirl increased in a jet, shear stress, turbulence intensity and rate of entrainment increased in the initial region of the jet. They also showed that the assumption of an isotropic uniform mixing length parameter distribution is quite feasible for weak swirl but is progressively less valid as the degree of swirl increases.

2.1.4 New measurement techniques – better understanding of swirling flows

Emergence of modern, and much more accurate measuring techniques in the 1970s, such as Laser Doppler Anemometry, marked a new era in understanding of turbulent swirling flows.

Baker* et al. (1973) carried out a research programme at Imperial College, London in order to develop and test instrumentation which can be used in industrial furnaces for diagnostic purposes, and to assist the design of burners. They measured values of three components of mean velocity and turbulence intensity on a single combusting burner, with a swirl number of 0.5, using laser anemometry. They showed that this technique allows taking of measurements in the highly turbulent recirculation zone of the flame.

Baker et al. (1973), in addition to demonstrating suitability of anemometers for measurements in diffusion flames, had also found that the turbulence measurements in flame conditions showed little difference from isothermal air jet measurements. This apparent lack of the influence of the combustion on the turbulence properties was supported by measurements such as those of Becker and Brown (1969).

In a further study, Baker et al (1974) used laser anemometer to obtain measurements of three components of velocity and the corresponding correlations in non-swirling and swirling flow on a single burner, with and without combustion. Their results demonstrated that the isothermal swirling flow has a substantial region of recirculation on the axis in contrast to the non-swirling flow, which on the other hand, has a larger recirculation region in the corner of the enclosure. Similar behaviour was also observed in combusting flows, noting the difference in the length of recirculation zones. Longer recirculation with combustion was consistent with larger values of axial velocities which were observed, and which stem from the combustion and the associated reductions in density. They also found that isothermal swirling flows were non-isotropic.

Chigier and Dvorak (1975) investigated flow fields in turbulent swirling jets under isothermal and combustion conditions, using a laser Doppler anemometer with frequency shift. Their findings detected substantial changes in flow patterns between ‘hot’ and ‘cold’ velocity profiles, whilst the kinetic energy of turbulence under combustion was higher than in the corresponding cold conditions, in almost all regions of the flame. They found that there was a large-scale increase in root mean square (rms) values of axial velocity fluctuations, with a maximum value increasing from 2.3 m/s under cold conditions to 3.7 m/s under flame conditions. Maximum values of circumferential rms fluctuations on the axis increased from 2.5 to 3.5 m/s, while the changes in radial velocity fluctuations were relatively small. These results were in contrast to the results obtained by Baker et al. (1973), who found that there was little difference between the turbulence measurements taken under flame and isothermal conditions.

At the Indian Institute of Technology, Madras, Sampath and Ganesan (1986) carried out experimental measurements on a single swirl burner using a hot-wire anemometer and compared them to the predicted values obtained mathematically, using a finite difference scheme adapted for recirculating flows. They found that, whilst the overall agreement between the predictions and measurements was satisfactory, the region close to the burner exit showed relatively poor agreement, which was put down to the lack of accurate knowledge of the exact inlet conditions of velocities, swirl intensity etc.

2.1.5 Turbulent swirling flows – still causing a stir

During the 1990s and 2000s, research into turbulent swirling flows has continued to be of considerable interest to both engineers and scientists, thus emphasising the complexity and the importance of this research topic. The resurgence of interest in experimental modelling has also been driven by the increase in computational studies of swirling flows, which needed to be validated using the experimental results.

Kihm et al. (1990) carried out research of swirling flowfields using a laser Doppler anemometer operating in the dual beam, single component, forward scatter mode. Measurements of three components of mean velocity, turbulent intensities, and Reynolds stresses were taken on an air swirler, with varying swirl angles. The objective of the research was to provide benchmark data for comparison with numerical predictions based on models for turbulent swirling flows. Conclusions of the study indicated that there is close similarity between the profiles of normalised mean velocity components, u′, v′ and w′, and that the distributions of the turbulence shear stress components, u′v′ and u′w′, are strongly anisotropic.

Durão et al. (1991), working at the Technical University of Lisbon, Portugal, obtained laser Doppler measurements of mean and turbulent velocity characteristics in the developing region of the isothermal flow on a model of an industrial oxy-fuel burner. The burner configuration was similar to that of coaxial jets, where the annulus had been replaced by sixteen peripheral jets. The results showed existence of zones characterised by large turbulence anisotropy and large values of Reynolds shear stresses. The authors concluded that the results provided evidence that the calculation of aerodynamic field in multi-jet burner assemblies requires consideration of the individual stresses.

The same authors, Durão et al. (1993), building upon the previous findings, carried out research where they showed that swirl attenuates the three-dimensional structure typical of multi-jet flows in such a way that turbulence production and transport in the near burner zone are dominated by swirl-induced processes. They used the same experimental technique and model set-up as in the previous study.

Further contribution towards better understanding of multi-jet swirling flows came from Heitor and Moreira (1992), also from Technical University of Lisbon. They used the same experimental set-up and the measurement technique as Durão et al. (1991) to carry out experiments on isothermal burner flows and quantify the effect of swirl between zero and 0.9 on the mixing efficiency of the burner assembly. Heitor and

Moreira (1992) found that the flows are characterised by large values of the Reynolds stresses and by zones of large turbulence anisotropy, which extend throughout the length of the measurements. The development of the swirling flow is strongly influenced by turbulent production in the near burner zone, upstream of x/d=3, where the normal stresses are associated with large mean velocity gradients.

Similar research has been done by Ahmed (1997), who performed measurements of flowfield characteristics of a confined, isothermal strongly swirling flow in a combustor model using a two-component fibre optic laser Doppler anemometer. Again, the objective was to gain better understanding of such complex flow-fields and to provide complete benchmark data for comparisons with numerical models. He concluded that the axial, radial and swirl mean velocity components are all of the same order of magnitude up to x/D = 0.167. The radial component decays most rapidly due to the swirl jet impinging on the combustor wall. Ahmed's measurements also confirmed that the turbulence is highly anisotropic.

Research into swirling flows continued into the 21st century, with calculation of swirling flames still representing a challenge, despite the widespread use of swirl burners in industrial applications. Al-Abdeli and Masri (2003) point out that this challenge is due to many issues that characterise swirling flows and which include:

- complex recirculation flow patterns induced by vortex breakdown
- asymmetries either in the generation of swirl or as a consequence of the type of fuel nozzle used
- unsteady, or time dependent phenomena, and
- vaguely defined, intricate or non-homogeneous boundary conditions, such as those associated with a quarl type burner mouth.

Al-Abdeli and Masri (2003) used the latest advancements in laser diagnostics to carry out an experimental study on a single combusting burner. They measured mean velocities, turbulent kinetic energy and obtained comprehensive maps of flame shapes for swirling flames with varying fuel mixtures. Results of the investigation of flames indicated the presence of unsteady behaviour at some axial locations. Al-Abdeli and

Masri (2004) experimental work involving laser sheet visualisation of non-reacting swirling flows had already shown that the centre jets can be susceptible to precession.

Schneider et al. (2005) carried out an experimental study at the Institute for Energy and Powerplant Technology in Darmstadt, Germany, where they analysed isothermal and combusting swirling flows discharging from a single burner. The measurements were taken using the 2-D LDA technique and were intended to be used for validation of a numerical model.

Schneider et al. (2005) found that, as it exits the nozzle, the flow is characterised by an inner and an outer shear layer. They also concluded that downstream axial velocity is maintained while tangential momentum is passed over to radial momentum, and that turbulence is non-isotropic.

2.2 Multiple burner flows

Whilst numerous research studies on single swirling flows have been undertaken, they have not answered many of the fundamental questions concerning multiple burner flows.

2.2.1 Initial research into multiple burner flows

Research carried out at the International Flame Research Foundation, IJmuiden, Holland in the late 1960s and early 1970s gave significant contributions to better understanding of multiple burner flows.

Fricker et al. (1971) studied groups of two, three, four and five burner systems, with linear triangular and square arrays, under both swirling and non-swirling flame conditions. They found that the major parameters considered to affect flame stability, flame length, flow and combustion patterns and flame temperature are:

- burner spacing
- burner array

- degree of swirl and
- direction of swirl.

A comprehensive research programme into behaviour and characteristics of multiple burners was performed at the Department of Fuel Technology and Chemical Engineering at the University of Sheffield, which can be credited for much of the 1970s research into turbulent swirling flows.

As part of his PhD work at this department, Allen (1970) studied the principal factors which affect the interactions of multiple jets under isothermal conditions. He investigated the effect of rotation and the number and spacing of the jets on the turbulence and mixing characteristics, with a view to optimum design of the system.

Allen's experimental set-up consisted of three swirling (or non-swirling) jets placed horizontally. Pitch between the burners was varied from 1.25 to 2 diameters. Pitch (P) is defined as a distance between central axes of two adjacent burners. The jets issued from a flat wall, into an enclosure at the opposite end. The box and end walls were fabricated from Perspex to facilitate easy probe positioning. The measurements were taken using a hot-wire anemometer in both isothermal and combusting conditions.

Allen investigated both the 'out of mesh' (columnar) and 'in mesh' (chequerboard) configurations. The difference between the two systems was clearly demonstrated in the tangential velocity distributions, where the jets in the 'in mesh' system attempted to combine whereas the jet in the 'out of mesh' system tended to push each other apart. As a result of this, the maximum $\bar{u}$ values appeared to be higher for the 'in mesh' jets than for the 'out of mesh jets'. Allen also found that the shear stress in the 'out of mesh' system is typically higher than that of the 'in mesh' system.

Reflecting on the effect of pitching (distance between adjacent burners) and proximity to the burner exit, Allen found that the differences between the 'in mesh' and 'out of mesh' systems are most marked when pitching, P=1 and in the region close to the nozzle ($x/D < 3$). Beyond $x/D = 3$ there is little effect of variation of pitch and meshing sense. In terms of the intensities of turbulence, he found that in swirling jets the turbulence intensity is so high in the regions close to the nozzle exit that variations in pitch and meshing sense have little effect on its values.

Allen concluded that the direction sense of the swirl velocity to each jet has an effect upon the degree of interaction, and he found that adjacent jets each having the same direction sense for the swirl velocity (termed 'out of mesh') display less interaction affects, greater stability and uniformity, and give conditions which are more suitable to multiple jet flame systems.

Building on Allen's findings, Chigier and Apak (1975) conducted an experimental study of multiple turbulent diffusion flames with swirl. They found that there was no significant interaction between flames separated by more than two burner exit diameters. However, as flames were brought closer to each other, interaction increased, and it reached its maximum when burners were positioned adjacent to one another. They concluded that burner crowding reduced large scale mixing and entrainment of air from the surroundings, thus delaying combustion. Further, in predicting flame length for multiple burners, account must be taken of the increase in flame length as a consequence of separation distance from other flames.

2.2.2 Recent achievements

Since 1990, there have been only a few published experimental studies on multi-burner swirling flows. Most of them were carried out in conjunction with computer modelling studies, and were used to validate the numerical models. The numerical studies are reviewed and presented separately, in the Section 2.4 of this chapter.

In 1997, as part of the European Commission's Clean Coal Technology Programme, Tarr and Allen prepared a study on flame interactions in multi-burner furnaces (Tarr & Allen, 1997).

The study was carried out on a 1/13 scale model furnace with burners arranged on a 3x3 array. The furnace model was manufactured out of Perspex, and both qualitative and quantitative measurements were taken. Isothermal measurements, performed using 2-D laser Doppler anemometry, were taken in planes parallel to the burner exit plane at several axial distances downstream of the burners in order to determine flow patterns on single and multiple-burner arrangements, with varying swirl orientations and burner pitches. This technique was applied to investigate the burner–burner interaction on groups of two, four and six burners of either clockwise or anti-clockwise orientation. The burner–burner interaction on a 3×3 burner array was investigated using only flow visualisation.

Tarr and Allen (1997) concluded that, whilst the isothermal burner interactions affected burner entrainments, the central cores of the jets were not significantly influenced by the interactions occurred. The results suggested that the central recirculations downstream of the burners maintained their size and strength, and the individual flows maintained their jet-like structure. In the case where the closest pitch (1.3d) was examined, impingement between flames also occurred, and an external recirculation between burners could be seen as a result.

Aroussi et al. (2000) carried out a similar study, using the same experimental set-up as Tarr and Allen (1997). Aroussi et al. investigated burner interactions on a 3×3 burner array using 2-D laser Doppler anemometry, and used the experimental results to validate a numerical model.

Kucukgokoglan and Aroussi (2001) carried out an experimental study of multi-burner interactions on a bank of four burners arranged on a 2x2 array. They used the Particle Image Velocimetry (PIV) technique to obtain the velocity measurements. They found that the decay of the swirl is not symmetrical and invariably one burner dominates and sustains swirl for longer. The results obtained for the four burners arranged on the 2x2 array showed that the bottom two burners and the upper right burner decayed faster, whilst the upper left burner persisted for at least three diameters for co-rotating configuration and four diameters counter-rotating configuration further along the burner axis. Kucukgokoglan and Aroussi give no explanation for this behaviour.

2.2.3 Multi-jet interactions

Multi-jet interactions, apart from being of great importance in gas- and coal-fired furnaces, also have numerous other technological applications, for example, in aerospace and automobile industries.

Research carried out by Nasr and Lai (1997) at the School of Aerospace and Mechanical Engineering (Australian Defence Force Academy) at Canberra, Australia, gave some important insights into main characteristics of flow discharging from two unventilated parallel plane jets. The authors used 2D laser Doppler anemometry to obtain measurements for mean velocity distributions, velocity decay, recirculation, and Reynolds shear stresses distribution. They also used the experimental results to validate the numerical model, details of which can be found in Section 2.4 of this chapter.

2.4 Numerical studies

Development of computer technology represents a significant milestone in the evolution of understanding of turbulent swirling flows. It created a new, world-wide challenge where scientists and engineers, using the power of computers, endeavoured to simulate this complex physical phenomenon by solving systems of equations with application of appropriate turbulence models.

2.4.1 Simulation and prediction of turbulent swirling flows

Studies on predictability of swirling flows span over more than two decades, with the emphasis on examining applicability of various turbulence models (Truelove et al., 1982).

Sloan et al (1986) found that the assumptions leading to the formulation of the k-ε turbulence model are inadequate for the modelling of turbulence in highly swirling flows.

Research carried out by Riahi et al (1990) at the University of British Colombia, Canada, focused on computer simulation of turbulent swirling flows. The authors used the finite volume analysis to carry out numerical calculations, whilst the turbulence effects were represented by two-equation turbulence models. It was found that the k-ε model (with curvature accounted for by Launder modification) successfully represented the decay of swirling velocity and turbulence intensity in a short cylinder.

Duggins (1993), working at the Australian Defence Force Academy, Canberra, Australia, used the basic k-ε turbulence model, modified for the Reynolds stresses and for anisotropy, for the numerical modelling of swirling flows in a round pipe. Comparison of tangential velocities obtained experimentally and numerically showed that the modified turbulence model gave a much closer match than the basic k-ε turbulence model.

Hwang et al. (1993) used the finite volume analysis to model two combustor geometries: a) the flow in a round pipe entering an expansion into another coaxial round pipe, and b) the flow in two confined co-axial swirling jets. Both geometries were modelled using a standard and a nonlinear k-ε turbulence model. The results showed that there were no significant differences in the performance of the two models, thus suggesting that the differences were possibly masked by the weaknesses in the performance of the modelled equations for k and ε.

At the University of Alabama, USA, Sharif et al. (1995) spent a few years researching and evaluating the performance of three turbulence models in the prediction of confined swirling flows. The following turbulence models were employed:

- a nonlinear k-ε turbulence model (NKEM),
- the Reynolds stress transport model (RSTM), and
- the algebraic stress models (ASTM).

Sharif et al. (1995) found that the mean flow fields are reasonably well predicted by the RSTM and ASTM. The NKEM predictions for the mean flow field were less satisfactory. For rotating shear flows, the NKEM was not able to alleviate the deficiencies of the standard k-ε model. The standard k-ε model was oblivious to the presence of rotational strains i.e. it failed to distinguish between the physically distinct cases of plane shear, plane strain, and rotating plane shear.

Lockwood and Shen (1994) performed modelling of flames in swirl-stabilised burners using the Reynolds stress model, and the conventional k-ε turbulence model. They found that the Reynolds stress model did not demonstrate any consistent advantage over the simple k-ε model. In fact, the Reynolds stress model suffered severe numerical instability limitations when applied to practical flames.

Research on predicting the near-burner zone flow field of low-NOx flames using the RNG-k-ε (an alternative for standard k-ε model for high Reynolds number flows), RSM and k-ε turbulence models was carried out at the International Flame Research Institute in Holland by Breussin et al. (1996).

Contrary to Lockwood and Shen's findings, Breussin et al. (1996) found that, whereas RSM predictions were in good agreement with the measurements, both RNG-k-ε and k-ε turbulence models predicted too short and too intensive flames, ultimately resulting in excessive NO_x levels. These findings were supported by the results of the research carried out by Ahlstedt (1997) at Tampere University of Technology, Finland.

Hart et al. (1999) applied the same turbulence models (RNG-k-ε, RSM and k-ε) on three different geometries. They found that the k-ε turbulence model gave a very good match with experimental data in the case where a burner jet was discharging perpendicularly into the furnace. However, for more complicated geometries, with the burner jets discharging into the furnace at a 60° angle, it was the RNG-k-ε model that gave excellent predictions, whilst the RSM failed to produce a solution.

Gutmark and Grinstein (2002) compared experimental and computational data obtained for isothermal swirling flows. The numerical results, obtained using the k-ε turbulence model, showed a reasonable agreement with the velocity profiles obtained experimentally, thus suggesting that this simulation approach can be effective design tool in flow field simulation of swirling flows.

Even though most of the studies discussed above showed that turbulent swirling flows are more accurately predicted by the Reynolds stress model as opposed to the k-ε turbulence model, the fact that some of the studies showed indifference between the two models makes the k-ε turbulence model still a focus of current research. The popularity of this method is also attributed to its low computational overhead.

Some of the most recent research in prediction of turbulent swirling flows deals, yet again, with comparison between the Reynolds stress and the k-ε turbulence models applied to swirl burner flows was performed by German and Mahmud (2004). They concluded that the overall agreement between the experimental data and the predictions obtained using the two turbulence models was reasonably good. However, the k-ε turbulence model failed to reproduce the sub-critical nature of the isothermal flow.

2.4.2 Multiple burner flows

The numerical modelling of multiple swirling flows still remains a relatively unexplored area of research.

Lockwood and Parodi (1998), working in conjunction with Tarr and Allen (1998) who provided the experimental data, carried out numerical modelling of single and multi-burner arrays (co-rotating and counter-rotating) under both isothermal and combusting conditions. They used the k-ε turbulence model to account for the turbulent stresses and turbulent flux transport terms.

The research of Lockwood and Parodi (1998) highlighted the importance of using multi-burner experimental and numerical set-ups in the design and optimisation of coal-fired furnaces. They found that, when the number of burners in the array is more than two, there is a significant interaction between the flows of the bottom burners (a row of burners adjacent to the hopper) and the hopper flow. Also, there is a strong interaction between the side of the walls of the combustor and the burner flows. Since these interactions will distort the performance of a burner developed in a single burner test rig, the authors concluded that the overall optimisation of boiler performance demands that the burner-burner and burner-wall interactions are recognised and accounted for.

Aroussi et al. (2000) used the standard k-ε turbulence model to predict flow behaviour of two burners discharging into the furnace. They found that application of this turbulence model, with a high mesh resolution and second-order differencing scheme, provided good agreement between the measured and predicted results.

Using the results of their PIV study on multiple burner interactions, Kucukgokoglan et al. (2001) performed numerical modelling using the same geometry. They found that the mixing of swirling flows issuing from typical isothermal scale models of burner geometries can be accurately predicted using the standard k-ε, RNG k-ε, and realisable turbulence models, together with a fine computational mesh.

2.4.2.1 Modelling of interacting swirl flows in the aerospace industry

Lai and Nasr (1998) used the results obtained from an experimental study (Nasr and Lai, 1997) of two parallel plane jets to validate the numerical model. They examined the performance of three turbulence models, k-ε, RNG k-ε and Reynolds stress, in predicting this flow field. Lai and Nasr (1998) found that, while the features of two parallel plane jets have been qualitatively predicted by all three turbulence models, quantitative agreement between predictions and experimental data varies from 10 percent for the merging length to 50 percent for turbulence quantities. They concluded that, the standard k-ε model give as good a prediction of complex shear flows as RNG k-ε and Reynolds stress models.

Contrary to the Lai and Nasr’s conclusions, Yang et al. (2003) found that the Reynolds stress model outperformed the standard k-ε turbulence model, and was recommended as a favourable method for providing predictions of turbulent swirling flow within a combustor.

Yang et al. (2003) carried out numerical modelling on a lean direct injection (LDI) combustor, which included inlets at nine inflow locations. Both counter-rotating and co-rotating configurations, with a varying swirl angle (45° and 60°) were examined. The results showed the superiority of the RSM over the k-ε turbulence model, when compared to the experimental results. The RSM model gave much better prediction of the recirculation zones. The results also showed that the RSM velocity levels varied over a greater range, which was in line with the experimental results.

Chapter 3

Fundamentals of turbulent jets

Theoretical background describing the fundamental properties of turbulence is presented together with the governing equations of turbulent flows. The underlying physical principles of turbulent jets are described. The case of swirling turbulent jets is considered in the context of theory.

3.1 Basic characteristics of turbulent flows

In the absence of a short and complete definition, turbulence is probably best summarised as 'a state of continuous instability'. The nature of turbulent motion is essentially irregular motion on a small scale. The movements of individual particles have no definite frequency, nor any ordered pattern, which can be observed in large-scale eddies. The reason that a deterministic treatment of turbulent flows is not in practice possible is that important features of the motion (large-scale eddies) develop from entirely insignificant perturbations (Massey, 1968; Tritton, 1977).

3.1.1 Velocity, turbulence intensity and kinetic energy of turbulence

Components of velocity at any point in turbulent flow can be decomposed into a time-averaged, mean velocity component relative to the main flow, $\bar{u}$, plus a component representing the random difference between the instantaneous vector velocity at a point, and the mean velocity at that point, u' (Birkhoff and Zarantonello, 1957)

$$u = \bar{u} + u' \tag{3.1}$$

$\bar{u}$ indicates the mean motion of the fluid. Information about the structure of the velocity fluctuations is given by other average quantities, the first being the mean square fluctuation, $\overline{u'^2}$. $\sqrt{\overline{u'^2}}$ is known as the intensity of turbulence component, and

$$(\overline{I'^2})^{1/2} = (\overline{u'^2} + \overline{v'^2} + \overline{w'^2})^{1/2} \tag{3.2}$$

as the intensity of the turbulence. It is directly related to the kinetic energy per unit volume (k) associated with velocity fluctuations (Tritton, 1977).

$$k = 0.5\rho\overline{I'^2} = 0.5\rho(\overline{u'^2} + \overline{v'^2} + \overline{w'^2}) \tag{3.3}$$

3.1.2 Turbulence equations and Reynolds stresses

Elementary statistical notions were first introduced into the consideration of the turbulent flow by Osborne Reynolds. The motion of a fluid, as usually considered in hydrodynamics, is obtained by considering the means of the molecular motions, and according to the kinetic theory of gases. For example, the velocity components, pressure, stress tensor, density, temperature etc. of a gas may be defined, to approximately satisfy the Navier-Stokes equations (Pai, 1954).

As Pai (1954) explains, assuming that the fluid is incompressible and that a variation of density of the fluid is negligible, substitution of (3.1) into the Navier-Stokes equations of motion of an incompressible fluid (Appendix A.1), will yield a new set of equations, called Reynolds equations. Reynolds equations differ from Navier-Stokes equations only on the presence of additional terms added to the mean value of the stresses due to viscosity (Appendix A.2). These additional terms are called the Reynolds stresses or eddy stresses. They form a tensor with components $-\overline{\rho u_i' u_i'}$, the normal Reynolds stress components being $-\overline{\rho u_i'^2}$, and the Reynolds shearing stress components being $-\overline{\rho u_i' u_j'}$ $(i \neq j)$, where ρ is the density of fluid.

The Reynolds stresses can be written as:

$$\begin{aligned} &-\overline{\rho u'^2}, -\overline{\rho u'v'}, -\overline{\rho u'w'} \\ &-\overline{\rho u'v'}, -\overline{\rho v'^2}, -\overline{\rho v'w'} \\ &-\overline{\rho u'w'}, -\overline{\rho v'w'} - \overline{\rho w'^2}, \end{aligned} \tag{3.4}$$

As Tritton (1977) clarifies, the Reynolds stress arises from the correlation of two components of the velocity fluctuation at the same point. A non-zero value of this correlation implies that the two components are not independent of one another. For example, if $u'v'$ is negative, then at moments at which u' is positive, v' is more likely to be negative then positive, and conversely when u' is negative.

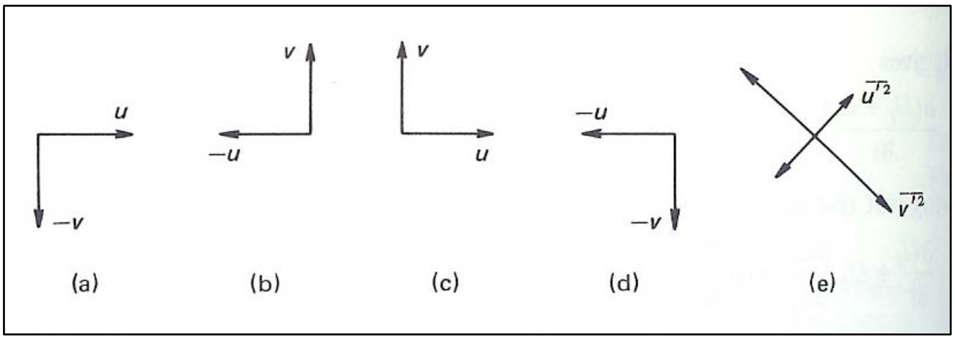

Figure 3.1 Geometrical interpretation of Reynolds stresses (Tritton, 1977)

In his geometrical interpretation of Reynolds stresses shown in figure 3.1, Tritton (1977) explains that, if patterns of velocity fluctuations shown in (a) and (b) occur more frequently than those in (c) and (d), giving negative $u'v'$, then $\overline{v'^2}$ is larger than $\overline{u'^2}$, as indicated by (e).

3.2 Turbulent jets

3.2.1 General overview

A *jet* is defined as a stream of material which travels for many diameters in a nearly constant direction. To produce such a jet would simply require making a hole or inserting a tube into a reservoir, whose local pressure is higher than the surrounding pressure.

Jets have been used since the earliest times. The discharge rate from the orifices supplying public water in ancient Rome was governed by the Roman law. Jets from fountains, faucets, and fire hose nozzles are familiar examples whose behaviour has been studied by scientists since the Renaissance times, at least (Birkhoff and Zarantonello, 1957).

Over the past century, both liquid and gas jets have been carefully studied and analysed in relation with a number of applications in various industries, ranging from automotive and aerospace to water industry.

3.2.2 Fundamental concepts of turbulent jets

Most jets encountered in engineering practice are turbulent. The flows of turbulent jets involve many small, rapidly fluctuating eddies, distributed in space-time. Real jets tend to be turbulent if the Reynolds number ($R = Ud/\nu$) is greater than 1000 (Birkhoff and Zarantonello, 1957).

As Pai (1954) describes, in the study of turbulent jet flows, turbulent fluctuations which are random in nature, must be taken into account. To accommodate this requirement, various statistical theories by scientists such as Taylor, von Karman, Heisenberg and Kolmongoroff were developed, which were applicable to continuous movements and satisfied the equation of motion. Unfortunately, most of these theories deal only with the simplest type of turbulence – isotropic turbulence, whilst little has been done to develop sound theories relating to anisotropic turbulence. To assist studies of anisotropic turbulent flows, some semi-empirical theories have been developed and successfully applied to some engineering problems.

Pai (1954) also highlights the effect of compressibility on turbulence. In the study of turbulent flow of compressible fluid, besides the correlation of velocity components, the correlations of velocity and density and of pressure and velocity must also be taken into account. This hugely complicates the analysis of turbulent jet flows. However, assuming that the heat transfer is not large and the mean velocity is low, then the heat transfer problem in turbulent flow may be considered as a problem of an incompressible fluid to a first approximation.

Theoretical principles of turbulent jets presented in this chapter are largely related to turbulent jets of incompressible fluid.

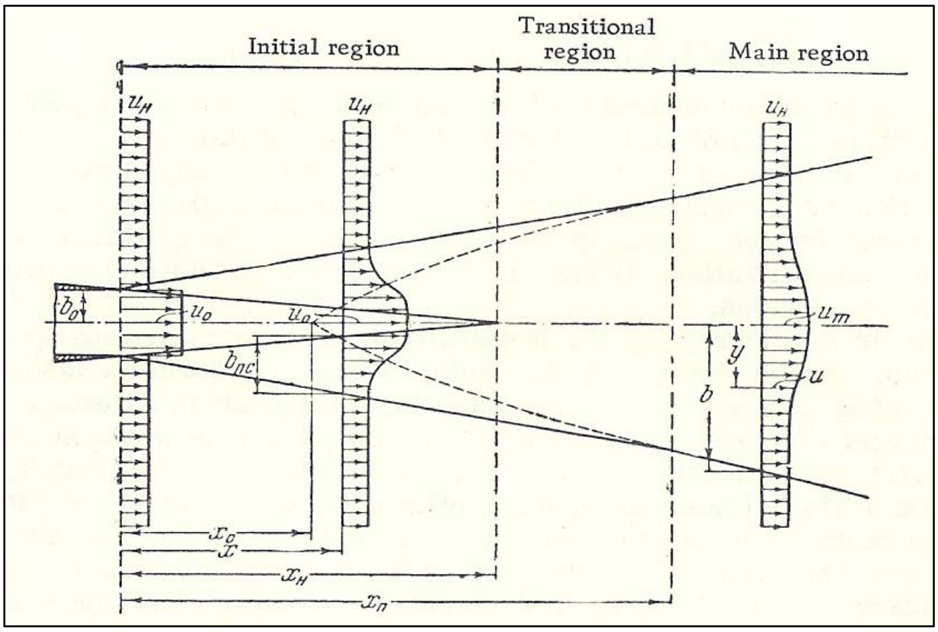

Figure 3.2 Diagram of jet discharging fluid with a uniform initial velocity field (u_0 = const) into a medium moving at a constant velocity (u_H = const) (Abramovich, 1963)

The fundamental concepts of the theory of turbulent jets were studied to a great detail by Abramovich (1963). A jet represents a flow of fluid on either side of the tangential separation surface, which arises in many cases of motion of a liquid or gas. Tangential separation affects parameters, such as flow velocity, temperature, and species concentration, though the distribution of static pressure remains continuous.

Prandtl (1934) proved that the instability of the tangential separation causes eddies on it, which move in disorderly fashion both along and across the stream. This causes an exchange of matter between neighbouring jets, i.e. there is a transverse transfer of momentum, heat and constituents. As a result, a region of finite thickness with a continuous distribution of velocity, temperature and species concentration is formed on the boundary between the two jets. This region is called the turbulent jet boundary layer.

As Abramovich (1963) showed in figure 3.2, the turbulent jet boundary layer thickens as it moves away from the initial section, leading to an increase in cross-section of the jet, and to a gradual 'eating up' of its non-viscous core (the region between the inside boundaries of the turbulent jet boundary layers).

3.2.3 Submerged jet

The type of turbulent jets most studied is one spreading through a medium at rest. This type of jet is called a submerged jet (figure 3.3). Assuming that the velocity field at the initial cross section of the submerged jet is uniform, the boundary of the mixing layers form diverging surfaces, which intersect at the edge of the nozzle.

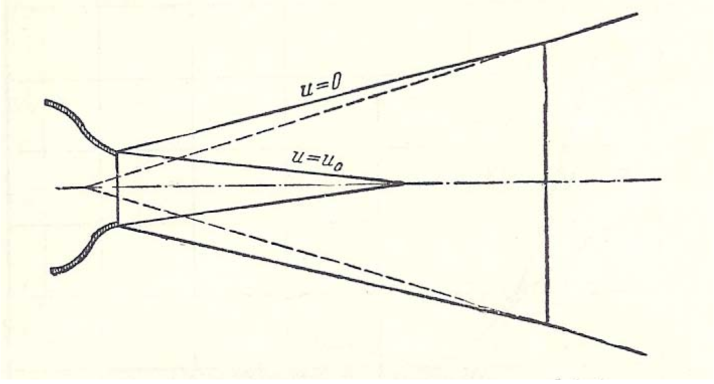

Figure 3.3 Diagram of submerged jet (Abramovich, 1963)

On the outside, the boundary layer comes into contact with the stationary liquid, where u=0, whilst on the inside, the boundary layer changes to a constant velocity core, where the flow velocity is equal to the discharge velocity, $u=u_0$ (Abramovich, 1963).

3.2.4 The turbulent spreading of jets

As described in section 3.1.1, for two-dimensional motion of a turbulent jet, components of velocity at any point can be decomposed into a time-averaged, mean velocity component relative to the main flow, plus a component representing the random difference between the instantaneous vector velocity t at point, and the mean velocity at that point, $u = \bar{u} + u'$ and $v = \bar{v} + v'$ (Birkhoff and Zarantonello, 1957; Rouse, 1959; Abramovich, 1963; Goldstein, 1965).

The fluctuation components are equal to zero, when the flow is averaged over some finite time interval:

$$\overline{u'} = \overline{v'} = 0 \tag{3.5}$$

If the mean free path of a fluid particle (mixing length) in a turbulent stream is equal to *l*, when moved in a transverse direction, the particle reaches a layer in which the mean velocity differs from what it was in the layer from which the particle separated by the following value:

$$\Delta\bar{u} = l\frac{\partial\bar{u}}{\partial y} \tag{3.6}$$

The loss in individuality of the fluid particle and its merging with the mass of the new layer should be accompanied by a discontinuous variation (perturbation) in velocity of

$$u' = \Delta\bar{u} \tag{3.7}$$

Therefore, perturbations of the streamwise velocity component are of the order

$$u' \sim l\frac{\partial\bar{u}}{\partial y} \tag{3.8}$$

The transverse perturbations in velocity v′ are usually assumed to be proportional to the streamwise perturbations u′, but with the opposite sign

$$-v' \sim u'\text{, i.e., } -v' \sim l\frac{\partial\bar{u}}{\partial y} \tag{3.9}$$

Based on the above characteristics of the turbulent jet, and Prandtl's assumption that the growth of the jet (i.e. the rate at which the thickness of the jet boundary layer increases) is controlled by the transverse perturbation velocity

$$\frac{db}{dt} \sim v' \sim -l\frac{\partial\bar{u}}{\partial y} \tag{3.10}$$

the law, governing the increase in thickness of the submerged jet and the mixing length in the direction of flow, can be written as:

$$\frac{db}{dx} = const, \quad b = x \cdot const, \quad l = cx \tag{3.11}$$

where, b represents the breadth of the jet.

3.3 Turbulent jets with swirling flows

3.3.1 Swirl flow characterisation

Gupta et al. (1984) define swirling flows as flows which are caused by a spiralling motion, where a swirl velocity component (also known as a tangential or azimuthal velocity component) is being imparted to the flow by the use of swirl vanes, axial-and-tangential swirl generators, or by direct tangential entry into the chamber. Characterisation of swirling flows and swirling jets presented in section 3.3 is largely based on Gupta's work and work of his co-authors included in publications by Gupta et al. (1984), Gupta and Lilley (1985) and Beer and Chigier (1972).

Experimental studies show that swirl has large-scale effects on flowfields. Jet growth, entrainment and jet decay (for inert jets), and flame size, shape, stability and combustion intensity (for reacting jets) are affected by the degree of swirl imparted to the flow. This degree of swirl is characterised by the swirl number, S.

The swirl number is a non-dimensional number, which can be expressed as:

$$S = \frac{G_\theta}{G_x d / 2} \tag{3.12}$$

where,

$$G_\theta = \int_0^\infty (\rho u w + \rho \overline{u' w'}) r^2 dr \tag{3.13}$$

is the axial flux of swirl momentum, including the x-θ direction turbulent shear stress term;

$$G_x = \int_0^\infty (\rho u^2 + \rho \overline{u'^2} + (p - p_\infty)) r dr \tag{3.14}$$

is the axial flux of axial momentum, including the x direction turbulent normal stress term and a pressure term (axial thrust);
d/2 = nozzle radius;
u, v, w = velocity components in (x, r, θ) cylindrical polar coordinate directions
p = static pressure
p_∞ = static pressure of surroundigs.

Sometimes it is inconvenient to deduce the swirl number S from its definition, leading to application of more practically useful ideas. In order to simplify calculation of the swirl number, the turbulent stress terms and the pressure terms are sometimes omitted from the formulae.

If the flow is produced from an axial-plus-tangential entry swirl generator, the exit flow through the nozzle is likely to be plug flow with solid body rotation at low and medium swirl strengths. This does not apply at very high swirl strengths, since much of the axial flow leaves near to the outer edge of the domain. If solid body rotation plug flow is assumed, the following deduction applies:

$$\begin{aligned} u &= u_{m0} \\ w &= w_{m0} \frac{r}{d/2} \end{aligned} \tag{3.15}$$

That is, axial velocity u is a constant flat profile, swirl velocity w increases from 0 (at r=0) to w_{m0} (at r=d/2, the outer wall of the nozzle). If the pressure contribution to G_x is retained in the form of a $w^2/2$ term, but the turbulent stress terms are omitted, the analysis leads to:

$$G_\theta = \frac{\pi}{2} \rho u_{m0} w_{m0} (d/2)^3 \tag{3.16}$$

$$Gx = \frac{\pi}{2} \rho u_{m0} (d/2)^2 (1-(G/2)^2) \tag{3.17}$$

where, G=w_{m0}/u_{m0} represents the ratio of maximum velocities measured at the exit plane. Therefore, the swirl number S can be calculated from

$$S = \frac{G/2}{1-(G/2)^2} \tag{3.18}$$

In figure 3.4, Gupta et al (1984) illustrate the relationship between S and G, and also show experimental values of S and G, measured independently. The theoretical S ~ G relation for solid body rotation plug flow describes realistically the actual case for flow from a swirl generator for values of G less than 0.4 (S ≅ 0.2). For higher degrees of swirl, however, the axial velocity distribution deviates considerably from plug flow, and the major portion of the flow leaves the orifice near the outer edge. In the case of the high degree of swirl, the theoretical S ~ G relationship (3.18) underestimates the swirl strength S for a given G. This leads to a more physically realistic S ~ G relationship

$$S = \frac{G/2}{1-(G/2)} \tag{3.19}$$

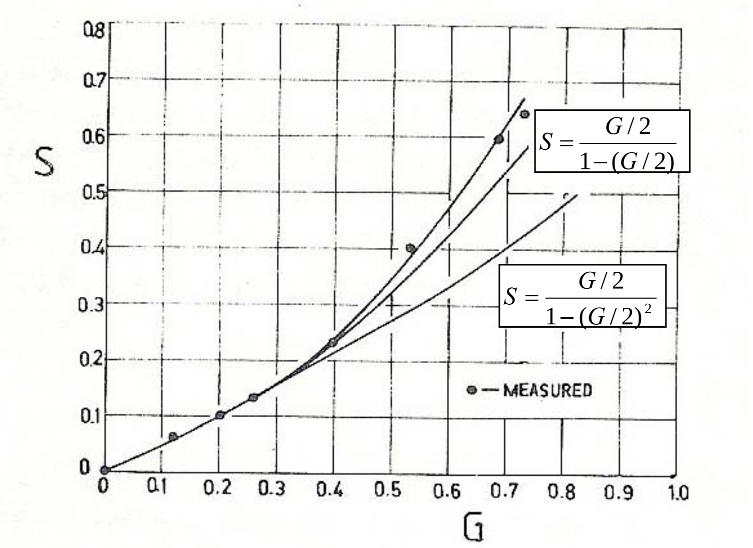

Figure 3.4 Relationship between swirl parameters S and G (Gupta et al., 1984)

Flows may also be characterised directly, in terms of the vane angle and nozzle geometry. When swirl is produced via a vane swirler with flat vanes at angle *ϕ* to the mainstream direction, *S* and *ϕ* are approximately related by

$$S = \frac{2}{3}\left[\frac{1-(d_h/d)^3}{1-(d_h/d)^2}\right]\tan\phi \tag{3.20}$$

where d and d_h are nozzle and vane pack hub diameters, respectively. When $d_h \ll d$, this reduces to

$$S \approx \frac{2}{3}\tan\phi \tag{3.21}$$

so that vane angles of 15, 30, 45, 60, 70 and 80 degrees, correspond to S values of approximately 0.2, 0.4, 0.7, 1.2, 2.0 and 4.0, respectively. This relationship assumes 100 percent efficiency for the swirl vanes. The efficiency, in fact deteriorates, as the vane angle increases.

3.3.2 Recirculation zones

One of the most significant and useful phenomena of swirling jet flows is the recirculation bubble generated centrally for super-critical swirl numbers. A super-critical swirl number is a number beyond which reversed flow is shown on the axis (Gupta et al., 1984). The recirculation flows are generally associated with high rates of shear and values of turbulence intensity, so that instantaneously large-scale spatial fluctuations of boundaries and stagnation points occur.

Recirculation zones play an important role in combustion process, since their dimensions are crucial for flame stabilisation in stationary burners and NOx reduction due to flue gas recirculation (Syred et al., 1971).

Previous work and experimental findings relating to recirculation zones have been comprehensively overviewed and are presented in chapter 2. Detailed discussion on recirculation zones, including the finding from my research are presented in chapter 7.

3.3.3 Interaction of multiple swirling jets

A comprehensive overview of experimental and numerical studies on interaction of multiple swirling jets was presented in chapter 2. Further discussion, including results of my research is presented in chapter 7.

Chapter 4

Experimental apparatus

A physical model of a front wall fired furnace with nine burners was designed using a geometrical scale of 1:10. The velocities were scaled using the constant residence time scaling criteria.

Burner models, based on a simplified representation of a low NOx burner, featured unswirled primary and swirled secondary air registers. Burner swirls were designed both in clockwise and anti-clockwise direction, to accommodate testing of chequerboard and columnar configurations.

4.1 Review of furnace design

The furnace model design was based on the results of the comprehensive design review of wall-fired furnaces, which was completed by Duncan et al (2002), as part of the DTI-sponsored, Cleaner Coal R&D project.

A general overview of coal-fired furnaces used by electric utilities for power generation is given in introduction, section 1.3.

4.1.1 Review of wall fired furnaces

Duncan et al. (2002) carried out a design review of existing plant adopted by MBEL and its main industry competitors. The review examined burner versus furnace size and burner pitching features of the plant design. The results of this review provided the information required to define suitable baseline cases and practical variations for the physical and mathematical modelling activities.

Duncan et al. (2002) reviewed both the front and opposed wall furnace designs. They found that for furnace sizes of 300 and 500 MWe, the typical thermal ratings of the burners employed are between 40 and 60 MWth. A non-dimensionalised horizontal, vertical and wall clearance pitch value of around 2.75d (2.75 x throat diameter) was representative of the units examined, with a number of units featuring burners having considerably tighter pitches (around 2d). Tarr and Allen (1998) obtained similar results from their furnace and burner design survey, which revealed that typical horizontal, vertical and wall-clearance pitches are 2.7d, 2.9d and 2.8d respectively.

Duncan et al (2002) review also defined the dimensions of generic front and opposed wall fired furnaces. The review was limited to wall fired plant.

The industry survey conducted by Tarr and Allen (1998), showed that, out of the 20 furnace configurations included in the sample, 75% were front wall, 20% opposed wall and 5% downshot fired furnaces. The sample was generated from the responses received from leading industry players, including MBEL, RWE, Endesa and ENEL.

Wall-fired furnaces account for more than 80% of all US coal-fired plants (USEPA, 2002).

4.1.2 Review of furnace parameters

Furnace design criteria used to construct a physical furnace model was outlined by MBEL as part of DTI project 78567/D001 (Duncan et al., 2002).

Duncan et al. (2002) found that the sizing of a large multi-burner utility furnace must be such as to give good combustion performance whilst recognising constructional constraints and the slagging/fouling characteristics of the design coal to be fired, as well as assisting in the economic design of the entire plant. In the case of modern boilers, pollutant formation is also an increasingly important consideration at the initial design phase.

The principal furnace dimensions, width (W), depth (D), the burner horizontal and vertical pitches (Ph and Pv), and the burner side wall clearance (Pwc) are shown in figure 4.1.

Furnace parameters, including number of burners employed, furnace depth, side-wall clearance and horizontal and vertical pitch, have been reviewed.

4.1.2.1 Burner numbers

According to Duncan et al. (2002), the number of burners and the heat input per burner, in conjunction with the furnace sizing, are selected to minimise flame impingement on the furnace walls. Multiple burners at moderate heat inputs, in an opposed wall fired arrangement, are favoured to provide uniform heat distribution across the furnace. This reduces thermal gradients and helps prevent localised slagging, while improving NOx emissions control and combustion efficiency. There are cost advantages if burner numbers are reduced (i.e. fewer burners, boiler penetrations, quarls, etc.), and fewer burners are generally more easily fitted into the space available on the boiler walls.

4.1.2.2 Furnace depth

As explained by Duncan et al. (2002), furnace depth, D, is correlated against burner heat input, which means that a deeper furnace is required for a higher burner heat input. It is also correlated against the furnace plan area rating (MW/m^2), the value of this parameter usually being higher for opposed wall firing. It is worth noting that although an opposed wall fired furnace must accommodate two flames, the depth of the furnace is seldom double that of the corresponding front wall fired design.

4.1.2.3 Side wall clearance

Side wall clearance, Pwc, is defined as burner centreline to side or division wall. Similar to the furnace depth parameter, D, side wall clearance is also typically correlated against burner heat input (i.e. for a higher burner heat input there will be a greater wall clearance). Adequate wall clearance is required to avoid flame impingement, which leads to water wall wastage. This clearance will be greater for opposed wall units where there is greater volume utilisation by the flames (Duncan et al., 2002).

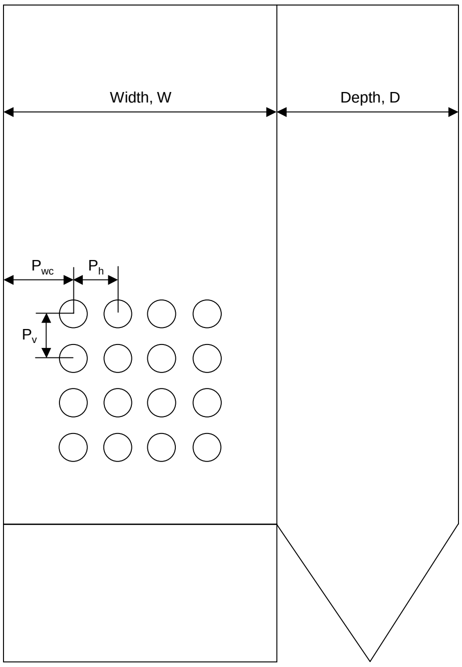

Figure 4.1 Principal furnace dimensions (Duncan et al., 2002)

4.1.2.4 Horizontal and vertical pitch

In its assessment of horizontal and vertical pitch parameters, Duncan et al. (2002) found that the minimum possible horizontal pitch, Ph, is determined through structural considerations (i.e. the furnace wall tube setting required). A minimum number of straight tubes are required to support the weight of the furnace

According to the Duncan et al. (2002) assessment, the major considerations for vertical pitching, Pv, are sufficient clearance for services and personnel at burner front and buckstay pitchings. It is the minimum buckstay pitch that is the limiting factor when defining vertical pitching. This minimum increases with burner throat diameter.

It was also found that, in practice, the burner pitches used in utility plant are often greater than the limiting value derived from purely mechanical considerations. This arises from concerns about the possible interactions between flames, and the minimum pitch used by most boiler manufacturers is therefore based on process considerations – i.e. a minimum pitch will be specified to ensure operation in a "safe" regime having negligible risk of the negative effects of flame interaction (Duncan et al, 2002).

4.2 Review of burner design

The burner design was based on a simplified representation of a low NOx burner.

4.2.1 Low NOx burners

Low NOx burners, together with burner optimisation and air staging, represent the primary measures for control of NOx emissions. These measures are now considered integral parts of a newly built power plant and existing units retrofit them whenever they are required to reduce their NOx emissions.

Low NOx burners are designed to control fuel and air mixing at each burner in order to create larger and more branched flames. This causes reduction in the peak flame temperature, and results in lower NOx emissions. The improved flame structure also reduces the amount of oxygen available in the hottest part of the flame thus improving burner efficiency. Combustion, reduction and burnout are achieved in three stages within a conventional low NOx burner. In the initial stage, combustion occurs in a fuel rich, oxygen deficient zone where the NOx are formed. A reducing atmosphere follows where hydrocarbons are formed which react with the already formed NOx. In the third stage internal air staging completes the combustion but may result in additional NOx formation. This however can be minimised by completing the combustion in an air lean environment.

Low NOx burners can be combined with other primary measures such as overfire air, reburning or flue gas recirculation. Plant experience shows that the combination of low NOx burners with other primary measures is achieving up to 74% NOx removal efficiency (IEA-Clean Coal, http://www.iea-coal.org.uk/content/default.asp?PageId=97).

4.2.2 Low NOx burner generic design

A typical generic low NOx burner, used for large scale coal combustion experiments is shown in figure 4.2. This is a triple concentric annular register, air staged, low NOx burner design, which has a central tube containing start-up gas burner lances and an air swirler.

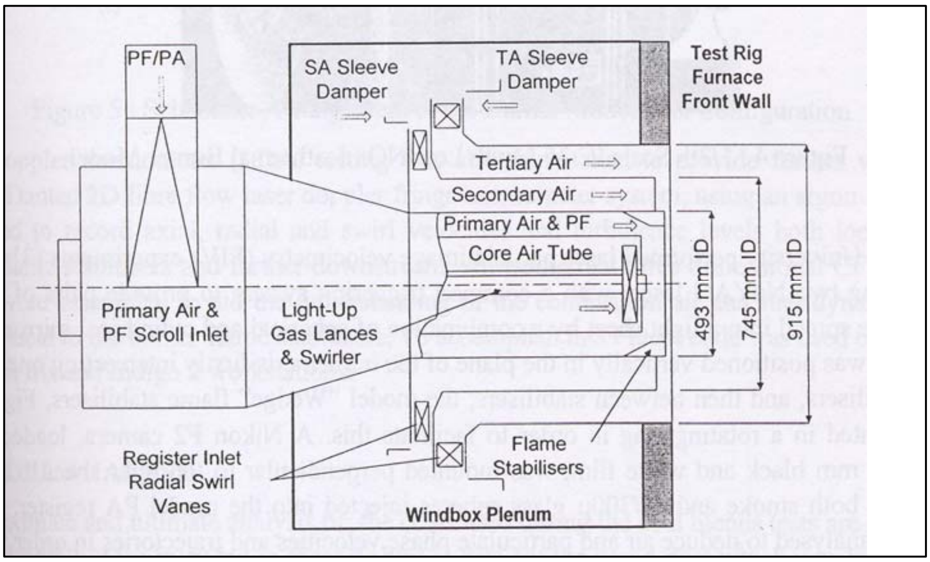

Figure 4.2 Generic burner used for large scale coal combustion experiments (courtesy of MBEL)

The pulverised fuel (PF) is administered via a scroll inlet primary air (PA) register, and the final air is to complete combustion is delivered via the windbox plenum into the secondary and tertiary (SA and TA) registers.

The burner model design is a simplified representation of a generic low NOx burner. Its design consists of an unswirled primary and swirled secondary air registers, and a core ignition tube, which is blocked to give zero flow. Detailed overview of the burner model design and manufacture is given in section 4.4.2.

4.3 Scaling criteria

Application of scaling criteria on small-scale experiments has been previously reviewed and considered by various authors (Smart, 1992; Weber and Breussin, 1998; Orsino and Weber, 2000).

According to Boullettini et al. (2000), when considering scaling of a combustion system, the two elements which must be considered simultaneously are the burner and the furnace. Therefore, the total system should be scaled according to the following criteria:

- Geometric similarity
- Kinematics, or aerodynamic and mixing similarity between the fuel and air streams and
- Thermal similarity.

Furthermore, in order to preserve the overall flow pattern, Reynolds and Froude numbers should be sufficiently high - a condition usually satisfied in industrial practice.

Since my PhD research dealt exclusively with isothermal flow, thermal similarity criterion did not apply, and the scaling criteria for the physical model were chosen to ensure geometric and kinematic similarity to the full-scale model.

The furnace and burner models were designed to a 1/10 scale. The full-scale furnace and burner dimensions are given in tables 4.2 and 4.3 respectively.

Two scaling criteria were considered for the velocity scaling in the burner design: Constant Velocity Scaling (CVS) and Constant Residence Time Scaling (CRTS). These are the most frequently used scaling criteria in industry.

4.3.1 Constant Velocity Scaling (CVS)

The CVS method, based on the principle where combustion air velocity is maintained constant for the different scaled burners, U_0=const., and the scaled characteristic diameter is evaluated through the relation:

$$D_{0,scaled}=(Q_{0,scaled}/Q_0)^{1/2}xD_0 \quad (4.1)$$

where, D_0 is characteristic burner diameter [m], Q_0 is burner throughput [kg/s] and U_0 is characteristic burner velocity [m/s].

The CVS criterion is the most widely used approach for burner scaling (Weber et al., 1998, Boullettini et al., 2000).

This approach had also been considered as a criterion for furnace and burner scaling in my PhD work. However, it was found unsuitable, since it required using velocities of up to 40 m/s. Application of such high velocities in a small-scale model would not be representative of the real state. Furthermore, it raised issues concerned with operating safety within the laboratory environment.

4.3.2 Constant Residence Time Scaling (CRTS)

Consequently, CRTS method was applied to the burner air flows to ensure practical operating velocities and fully turbulent flow (Smart, 1998). The velocities were calculated using the following CRTS formulae:

$$\frac{Qo,baseline}{Qo,scaled} = \left(\frac{Do,baseline}{Do,scaled}\right)^3 = \left(\frac{Uo,baseline}{Uo,scaled}\right)^3 \quad \Rightarrow \quad Uo\,,scaled = \sqrt[3]{\frac{Qo\,,scaled}{Qo\,,baseline}}\,.Uo\,,baseline \tag{4.2}$$

It was found that the velocities that need to be applied under this method are much smaller and easier to achieve. The Reynolds numbers of 2718 for the primary register and 9225 for the secondary register indicated that the flow is in transition in the primary register and fully turbulent in the secondary register (table 4.1).

	Q base (MWth)	**D base (m)**	**U base (m/s)**	**Re base**	**1/10 D scale (m)**	**U scale (m/s)**	**Re scale**
SA+TA	36.6	0.362	38.65	922503	0.036	3.87	9225
CA+PA	36.6	0.19	21.7	271846	0.019	2.17	2718

Table 4.1 *Constant residence time scaling (CRTS) parameters*

Calculations of Reynolds numbers for the primary and secondary registers, which were based on the preliminary velocity measurements taken by the Pitot tube meter, showed that the flow is fully turbulent in both registers of the scaled burner model. Differences between the inner and outer diameters for the primary and secondary registers were used in calculations (table 4.2).

	1/10 D model (m)	**U model exp (m/s)**	**Re model**
SA+TA	0.036	6.90	16469
CA+PA	0.019	3.80	4760

Table 4.2 *Physical model parameters*

4.4 Manufacture of physical model

4.4.1 Design and manufacture of small-scale furnace model

4.4.1.1 Furnace dimensions

Furnace dimensions were defined based on the findings of the review of furnace parameters given in section 4.1.2. The dimensions given in table 4.3 are typical and representative of wall fired furnace configurations.

Furnace Dimensions (m)	**Full Scale**
Total Height	23.7
Height of Hopper	5.2
Width (with Pitch=2.025m)	8.3
Depth	8.8

Table 4.3 *Furnace dimensions*

The typical furnace dimensions which transpired from the survey carried out by Tarr and Allen (1998) were 31.1, 10.2 and 8.5 metres for the total furnace height (including hpper), width and depth respectively. These are in line with the dimensions given in table 4.3.

4.4.1.2 Furnace model design

The physical model of the front wall-fired furnace was designed using 1:10 scale. All design drawings were created using a computer design and modelling package, Solid Edge. A 3D representation of the furnace, showing its principal dimensions in a case where the pitching arrangement between the burners is the largest, P=202.5 mm (P=2.5d) is presented in figure 4.3.

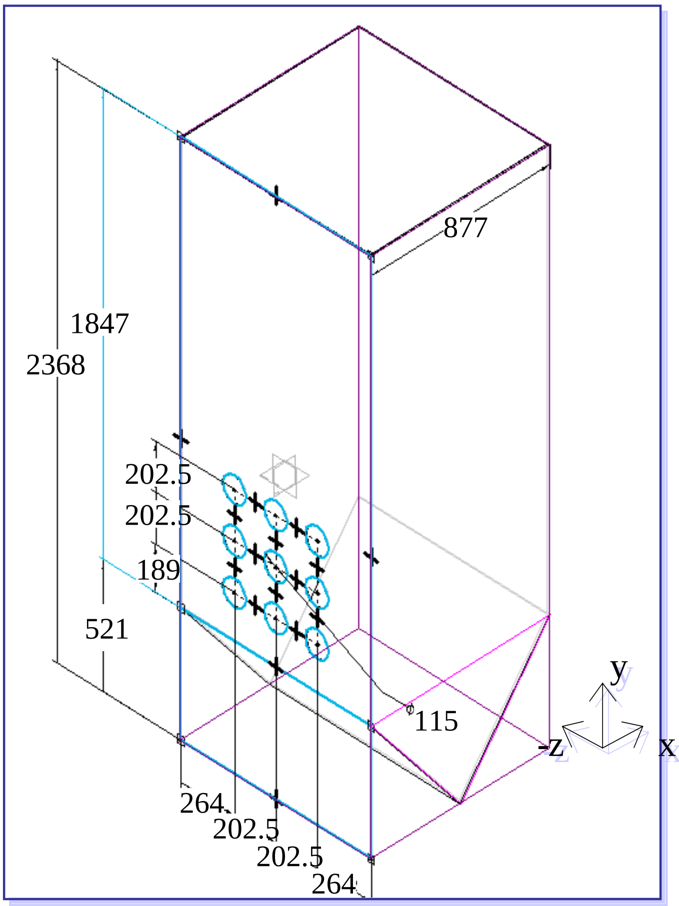

Figure 4.3 Furnace model

Appendix B, figure B.1 shows the front furnace wall featuring burner panels with varying pitches. A side wall is also shown. Each of the front panels was designed with nine holes of 114.6 mm diameter, arranged in a 3x3 array, on four different pitching arrangements of 202.5 mm, 180 mm, 157.5 mm and 144 mm.

The furnace model panels were attached to a solid structure constructed out of rigid tubular metal frames of 50 mm width. 100 mm was added to the width of the front and back furnace panels, so that the structural support could be fitted at the edges. The side walls of the furnace were designed so that they can be moved in/out in order to maintain the constant wall clearance at 214.2 mm.

Figure B.2 in Appendix B shows all parts and dimensions of the furnace assembly. Four front burner panels were also manufactured so that they can be easily changed to allow testing of different pitching arrangements. Table 4.4 gives the pitch and wall clearance details.

	Pitch (mm)	**Wall Clearance (mm)**
Panel 1	144.0	309.2
Panel 2	157.5	322.7
Panel 3	180.5	286.7
Panel 4	202.5	264.2

Table 4.4 *Pitch and wall clearance details*

The furnace model was made out of Perspex, 6 mm thickness, apart from one side panel which was made out of float glass. The float glass was used to avoid potential refractivity problems of Perspex due to uneven thickness, and hence, make sure that the LDA measurements are accurate. The model was positioned vertically in the lab, ensuring easy access for LDA measurements.

4.4.2 Design and manufacture of small-scale burner model

4.4.2.1 Burner design and dimensions

The burner model consists of two registers and a core bluff body. Its design is a simplified representation of a low NOx burner, featuring unswirled primary and swirled secondary air registers as well as a core ignition tube (blocked to give zero flow). Full scale dimensions of a simplified burner model are given in table 4.5. The burner was designed using 1:10 scale. Scaled burner dimensions are shown on a schematic drawing of primary and secondary burner registers and burner sleeve given in figure 4.4.

Burner Dimensions (mm)	**Full Scale**
Core OD	323
Primary Register ID	513
Primary Register OD	538
Secondary Register OD	900
Quarl OD	1146
Quarl length	264
Throat length	376

Table 4.5 *Burner dimensions*

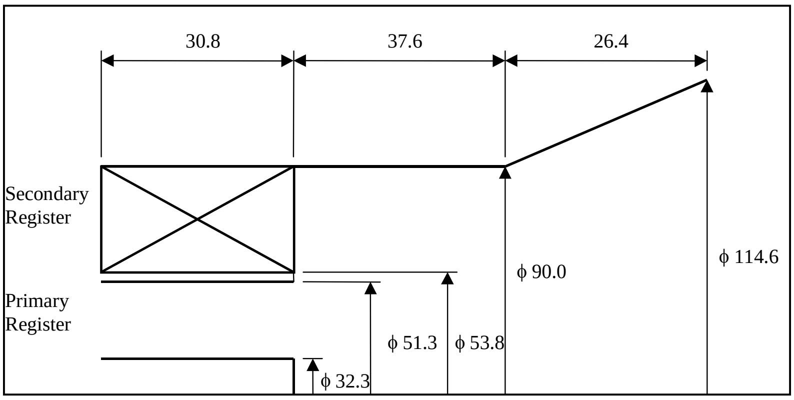

Figure 4.4 Burner and sleeve dimensions (mm), scale 1:10

The secondary register was designed with swirl vanes constructed at an angle of 35° with respect to the burner axis (figure 4.5).

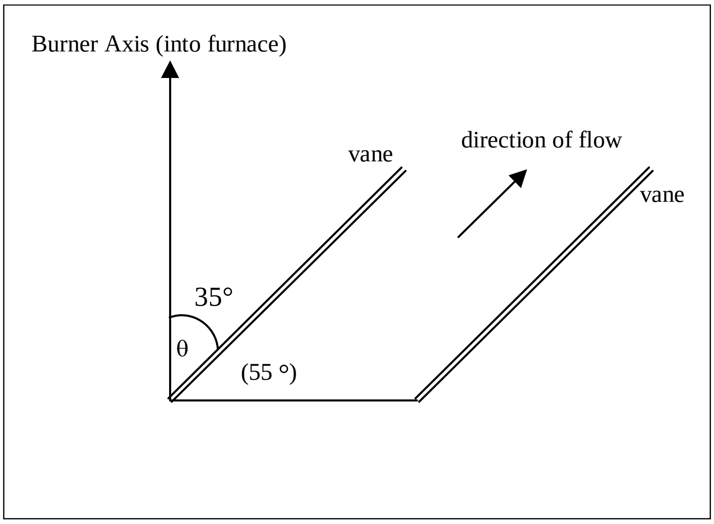

Figure 4.5 Plan view on swirl generator

The core bluff body is designed with four straight vanes along its length to enable the core body to be inserted inside the primary register. This design feature ensured that the flow in the primary register remained swirl-free.

Since primary and secondary register air-flow rates needed to be controlled separately, the burner was designed to accommodate this requirement. The primary register was extended by 50 mm beyond the swirl length, so that a separate hose supplying the air-flow rate for the primary register could be fitted.

The length of swirl vanes on the secondary register was calculated to ensure a sufficient overlap between adjacent vanes. Each swirl vane makes a 120° turn around the outside diameter of the primary register.

A computer generated image of the burner model is presented in figure 4.6.

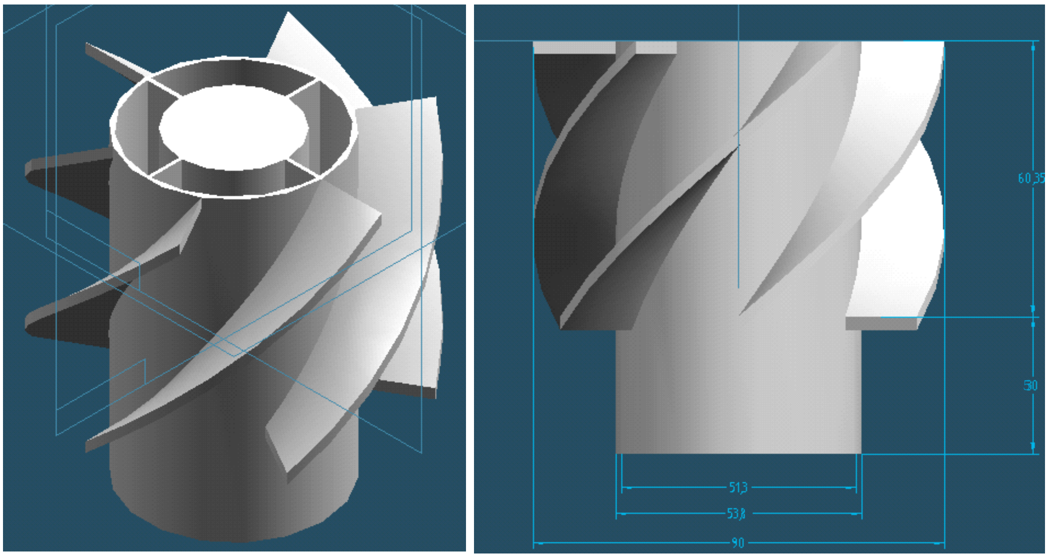

Figure 4.6 Burner model created using the SolidEdge design software

The burners were made out of DELRIN polymer material.

A total of 11 burners were manufactured, five with clockwise and six with anti-clockwise orientation of swirl. This was in order to enable testing of both chequerboard and columnar configurations (figure 4.7).

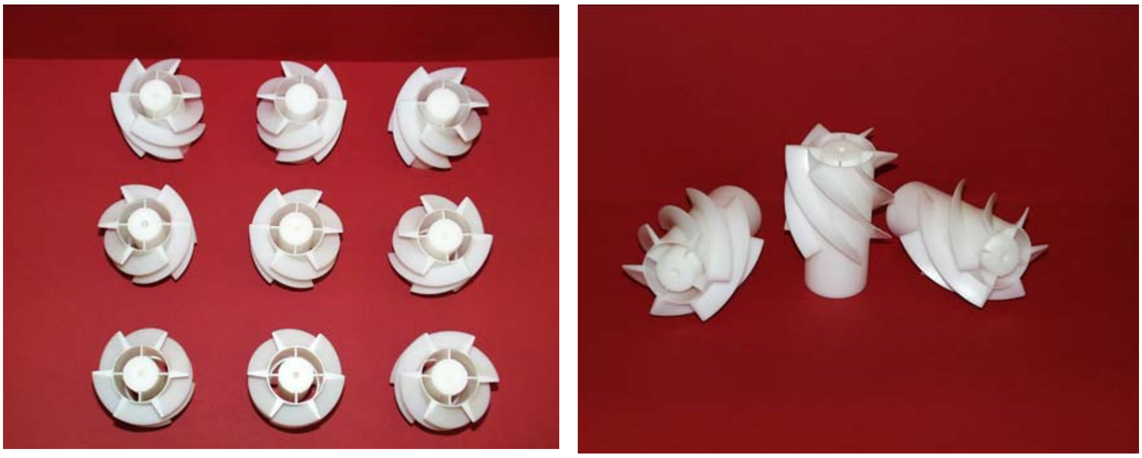

Figure 4.7 Burners with clockwise and anti-clockwise swirl orientation

4.4.2.2 Burner sleeve design and dimensions

Burner sleeves were designed so that they could be fitted around the burners. They consist of a 90 mm internal diameter thin-walled cylinder, with a quarl expanding to a wider diameter of 114.6 mm (figure 4.4).

The length of the burner sleeve was adjusted according to the extended length of the swirl vanes and the hose attachment extension on the primary register. The modified length of the burner sleeve is shown in figure 4.8.

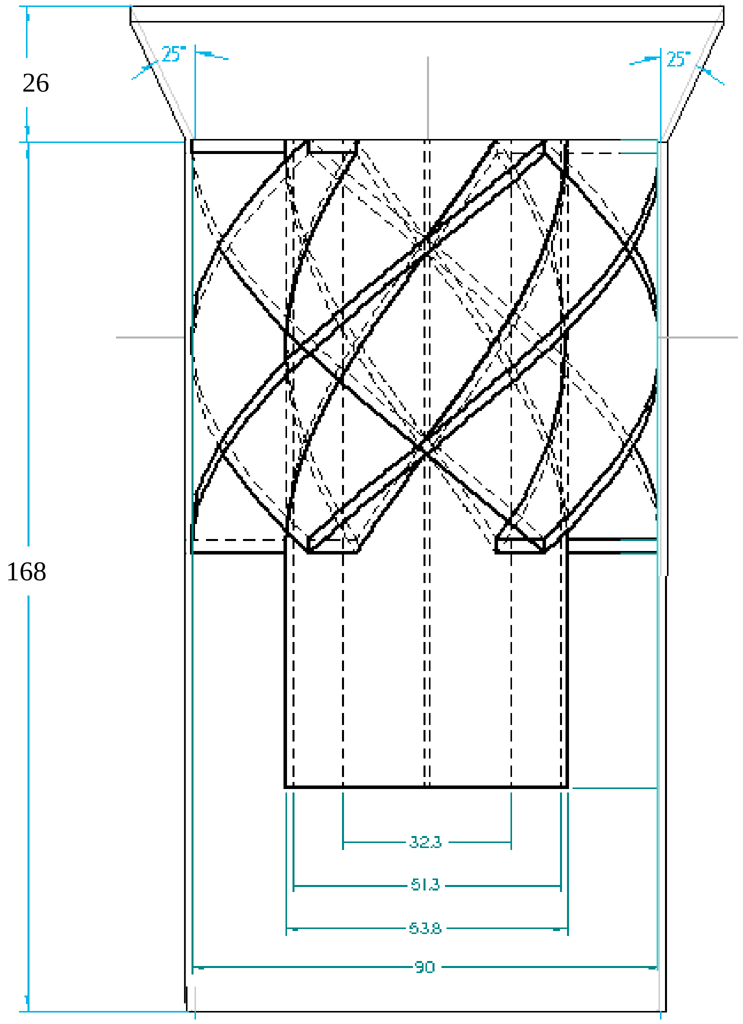

Figure 4.8 Burner and burner sleeve dimensions

4.4.2.3 Windbox design

Burner design accommodated an independent supply of air to the burner primary and secondary registers. A windbox was used to supply two separate airflows to the primary and secondary registers. Nine pairs of concentric flexible pipes were connected to the windbox at one end and to the burners at the other (figure 4.9).

Figure 4.9 Furnace and windbox assembly

The air supply to the windbox was provided by an air generator.

A commissioning programme to check the air supply, windbox balancing and the structural integrity of the model was undertaken prior to testing.

A pitot tube meter was used to measure velocities at six windbox exits. Measurements were taken every two seconds over one minute period, in order to establish the extent of fan fluctuations. Figure 4.10 shows velocity fluctuations at each of the windbox exits.

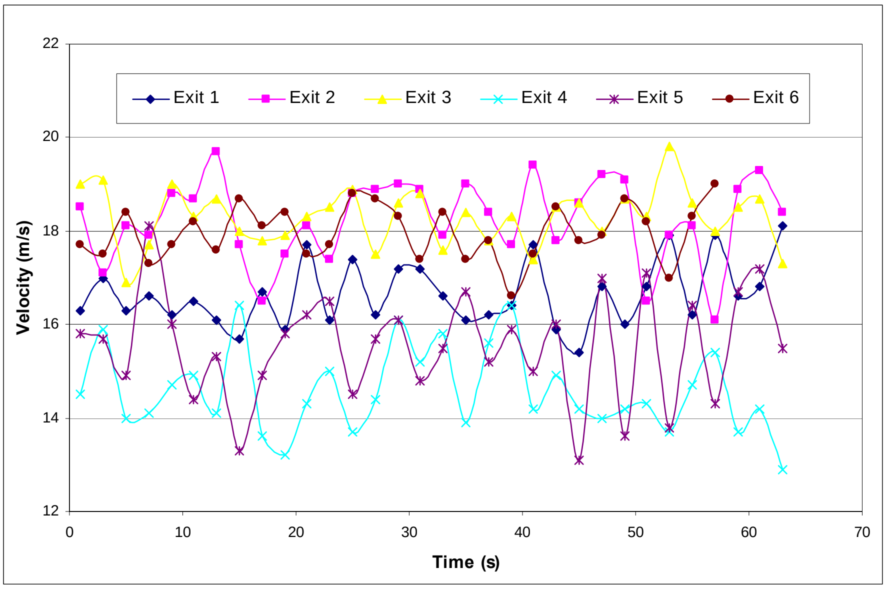

Figure 4.10 Velocity fluctuations at measured at six windbox exits

The pressure in the windbox was tested to ensure equal flow to all nine burners. In order to control the ratio of the air flow rate to primary and secondary registers, control valves have been placed at the inlet of the flexible pipes which take the air from the windbox to the primary stage of the burners. A Pitot tube meter was used to obtain pressure and velocity measurements for each burner. The valves were adjusted and set to maintain the correct ratio of flow rates.

The tests were carried out using three different pressures, and velocities from the primary and secondary registers were then measured. Table 4.6 gives pressures and corresponding values for primary and secondary register velocities.

Pressure (Pa)	**Velocity (Pitot) (m/s)**	
	Outer Register	**Inner Register**
130	6.9 (+/- 0.5)	3.8
100	5.5 (+/- 0.5)	2.9
70	4.5 (+/- 0.5)	2.4

Table 4.6 *Primary and secondary register velocities measure at three different pressures*

Chapter 5

Flow measurement techniques

Two techniques were used to investigate the effect of swirl jet interaction: flow visualisation and 3-D Laser Doppler Anemometer (LDA). The flow visualisation technique was used to qualitatively establish the extent of interaction between adjacent jets. Quantitative velocity data was gathered using a three-component LDA. The principles of these two techniques are described, together with details of the experimental set-up employed for each of the techniques.

5.1 Flow visualisation

5.1.1 Flow visualisation basic principles

Flow visualisation is one of many available tools in experimental fluid mechanics. It differs from other experimental methods in that it renders certain properties of a flow field directly accessible to visual perception. Visual inspection of a flow pattern always provides much better insight into a physical process. Observation of a flow pattern, which might be stationary or variable with time, reveals the whole development of the flow, which, in most cases (due to the transparent nature of fluids), remains invisible to the human eye (Merzkirch, 1974).

Merkzkirch (1974) classified flow visualisation methods into three groups. The first group, mainly associated with incompressible flows, comprises all techniques by which a foreign material is added to the flowing fluid. The foreign material must be visible, and if the particles of which the material is composed are small enough, it can be assumed that the motion of these particles is the same as that of the fluid, in direction and magnitude of velocity. This is an indirect visualisation method, since the motion of the foreign material is observed rather than the fluid itself.

The second group of visualisation methods is associated with compressible flows, which can be made visible by means of certain optical methods that are sensitive to changes of the index of refraction in the field under investigation. Compressible flow fields display a variation of the fluid density, which is a function of the refractive index of the flowing medium. The compressible flow field is, in optical terms, a phase object – a light beam transmitted through this object is affected with respect to its optical phase, but the intensity or amplitude of the light remains unchanged after passage through the object. An optical device behind the object provides in a recording plane a nonuniform illumination, according to the phase changes caused by the object. Pattern in the recording plane reveals density variations of the flow field. These optical methods are purely non disturbing test methods.

The third group of visualisation methods, identified by Merkzkirch (1974), includes a mixture of the methods from the first two groups.

The visualisation method used in my research belongs to the third group, since it combines addition of smoke to the flow field (first group) and the use of laser light for illumination (second group).

5.1.2 Flow visualisation experimental set-up

Flow visualisation was used to qualitatively establish the extent of interaction between adjacent jets in an isothermal, multi-burner furnace model. A smoke generator was used to provide a seeding medium for the air and a laser light sheet was used to illuminate burner flow fields. A Sony digital video camera (DCR-TRV900) was used to capture the flow visualisation images. A schematic diagram of the flow visualisation experimental set up is shown in figure 5.1.

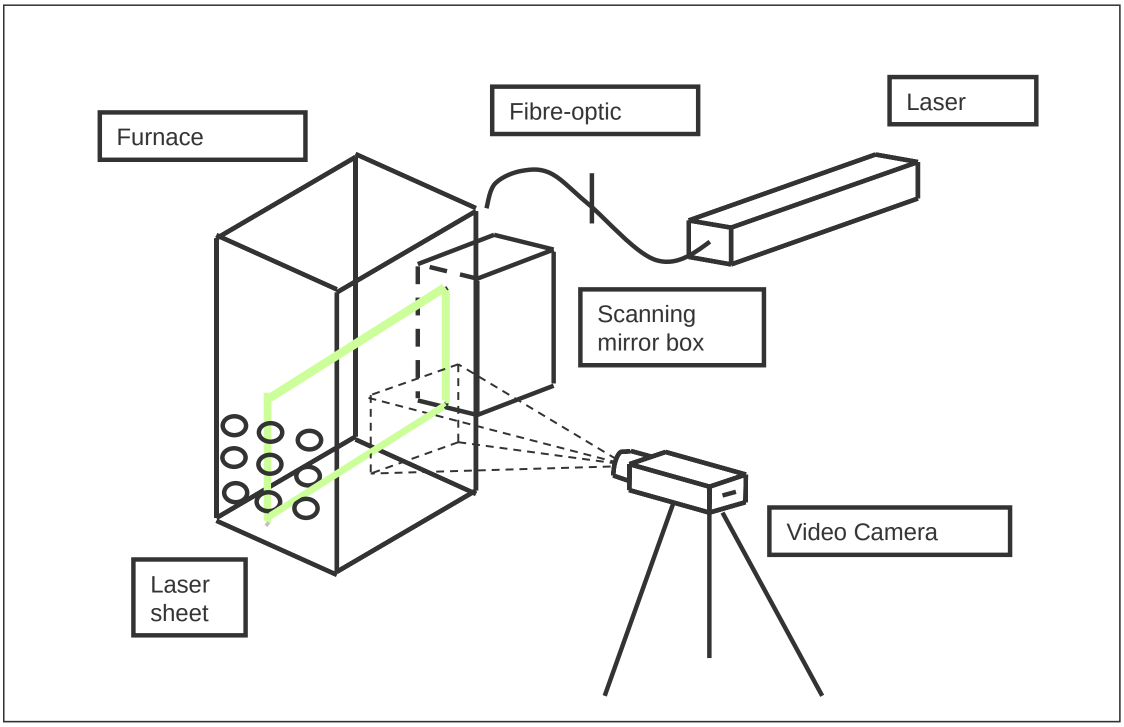

Figure 5.1 Flow visualisation experimental set-up

Smoke was added to the airflow at the windbox exit, where each of the burner air inlets was fitted with a valve designed to allow smoke being injected into each burner separately (figure 5.2). Flow seeding was provided by using the ROSCO 1700 smoke machine to manually pulse smoke into the classifier model. Smoke was injected into specific burner combinations detailed in section 7.1.

Figure 5.2 Points of smoke injection into the airflow

A 15W Spectra-Physics 171 Argon-Ion laser was used to illuminate the flow field. The laser produced a continuous wave (CW) of light beam. The laser beam was directed to the experimental set-up through a fibre optic.

In order to pulse the laser beam, a scanning beam illumination method was employed. As described by McCluskey (1992) and Losenno (2005), this method consists of scanning an unexpanded beam through the region of interest within the flow by using a polygon scanner. A laser beam is directed on to a rapidly rotating mirror, which has several facets. Successive mirrors reflect the beam through an arc of $4\pi/N_{facets}$, where N_{facets} is the number of facets on the mirror. The beam passes through the arc every $T=1/FN_{facets}$ seconds, where F is the rotational frequency of the mirror system. The polygon mirror deflects the laser beam onto a parabolic mirror and therefore the angular rotation of the beam is translated into a parallel scan (Gray et al., 1991).

The polygon scanner used for this study has 18 facets and rotates at frequencies up to 850 Hz. The polygon scanner was housed in a special case and produced a laser sheet 0.5 m wide. As shown in figure 5.1, the scanning mirror box was placed against the back furnace wall, directly opposite of the burner panel, and positioned in the centre, thus enabling illumination of the flow coming from the middle burner column.

Images of the particles were captured with a Sony digital camera (DCR-TRV900). This is a high-resolution camera, featuring three ¼” CCDs with 380,000 pixels each (gross pixels 3x380,000). Photo-editing software was used to manipulate the images and obtain measurements. Results of the flow visualisation study are presented in section 7.4.

5.2 Laser Doppler anemometry

5.2.1 Laser-Doppler anemometry (LDA) principles

Standard methods for measuring local mean velocity include pitot-static probes, hot-wire and hot-film probes and eddy-shedding devices. All require the insertion of an object into the flow, cause flow disturbances and are sensitive to the particulate content of the flow. In contrast, laser-Doppler anemometry (LDA) is an optical technique which allows the measurements of the local, instantaneous velocity of tracer particles suspended in the flow without disturbing the flow. The availability of a measuring technique which does not disturb the flow is particularly relevant to recirculating flows where mechanical probes cannot be used without disturbing the recirculation pattern (Durst et al., 1976). This was one of the factors that influenced selection of laser-Doppler anemometry as a preferred technique for quantitative measurements on multi-burner swirling flows in my research. The recirculating nature of multi-burner flows is described in section 7.3.

Laser-Doppler anemometry was first applied by Yeh and Cummins in 1964, who measured in a fully developed laminar pipe flow of water. Since then, LDA has been widely used in various research and development applications, and is nowadays a well-established technique for fluid dynamic investigations in gases and liquids (Durst et al., 1976; Durrani and Greated, 1977).

LDA is based on a simple optical principle, which comprises a light source (a laser), optical arrangement to transmit and collect light, a photocathode and a signal processing arrangement. A schematic diagram describing a typical laser-Doppler anemometer with its various components is presented in figure 5.3. The laser is a source of coherent light of appropriate intensity – its beam may be split into two parts which cross to provide an interference pattern in the local region of the flow where velocity measurements are required. Part of the volume of interference is observed by a light collecting system and imaged on a photodetector. The photodetector converts the optical signal to an electronic signal, which is processed by an appropriate signal-processing arrangement (Durst et al., 1976).

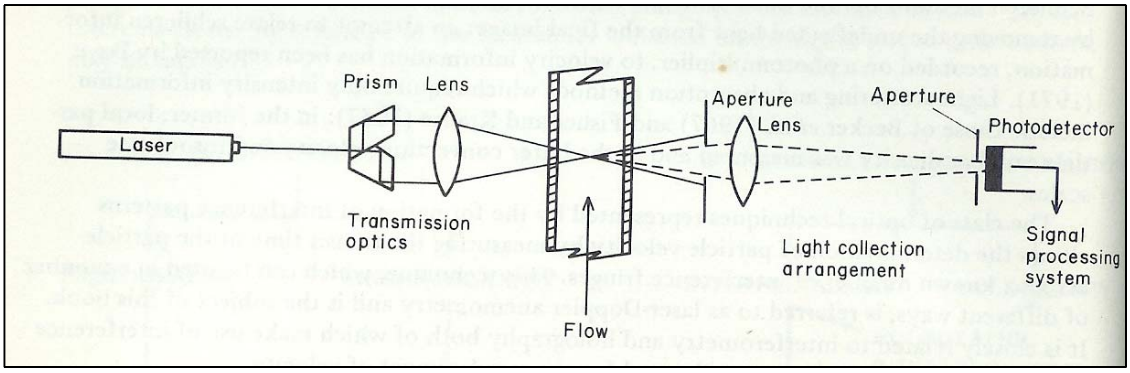

Figure 5.3 Laser-Doppler anemometer (Durst et al., 1976)

Since 1970s, there have been many technological improvements behind each one of the components constituting a laser-Doppler anemometer. However, the principles of operation have remained the same.

Dantec's schematic diagram of a laser-Doppler anemometer is presented in figure 5.4.

Figure 5.4, as described by Losenno (2005), shows LDA components, including a continuous wave laser, transmitting optics, receiving optics, a signal conditioner and a signal processor. The transmitting optics includes a beam splitter, usually a Bragg cell.

This a glass crystal with a vibrating piezo crystal attached. The vibration generates acoustical waves acting like an optical grid. The Bragg cell produces two beams of equal intensity with frequencies f_0 and f_{shift}. The two beams are focused into optical fibres, which transmit them to a probe. A lens focuses the parallel beams from the fibres. The focused beams intersect and form the measurement volume, referred to as probe volume.

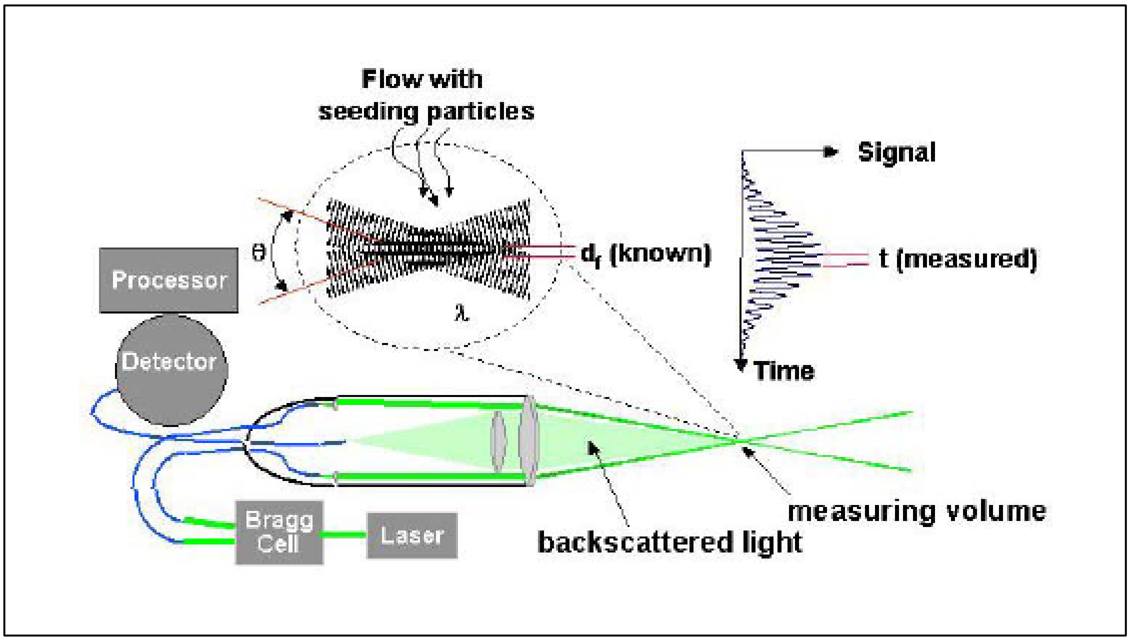

Figure 5.4 LDA system (Dantec Dynamics)

The probe volume is typically a few millimetres long. The light intensity is modulated due to interference between the laser beams. This produces parallel planes of high light intensity, so called fringes. The fringe distance d_f is defined by the wavelength of the laser light and the angle between the beams. Each particle scatters light proportional to the local light intensity as it moves through the probe volume.

The scattered light contains a Doppler shift, the Doppler frequency f_D, which is proportional to the velocity component perpendicular to the bisector of the two laser beams. The scattered light is collected by a receiver lens and focused on a photo-detector. An interference filter mounted before the photo-detector passes only the required wavelength to the photo-detector removing noise from ambient light and from other wavelengths. The photo-detector converts the fluctuating light intensity to an electrical signal, the Doppler burst, which is sinusoidal with a Gaussian envelope due to the intensity profile of the laser beams. The Doppler bursts are filtered and amplified in the signal processor, which determines f_D for each particle, often by frequency analysis using the robust Fast Fourier Transform (FFT) algorithm. The fringe spacing, d_f provides information about the distance travelled by the particle whilst the Doppler frequency f_D provides information about the time: $t = 1/f_D$. The velocity is thus given by the product of the fringe spacing d_f and the Doppler frequency f_D.

The addition of one or two more beam pairs of different wavelengths to the transmitting optics and one or two photodetectors and interference filters permits two or all three velocity components to be measured. Each velocity component also requires an extra signal processor channel.

Modern LDA optics employs optical fibres to guide the laser light from the often bulky laser to compact probes and to guide the scattered light to the photodetectors.

The advantages of this optical flow measurement technique over techniques such as Particle Image Velocimetry (PIV) are the high spatial and temporal resolution.

5.2.2 LDA apparatus

Three-dimensional velocity measurements were carried out using a DANTEC 3D Laser Anemometer mounted on a 3D Traverse.

A photograph of a Dantec's 3D LDA system, similar to the one used for my experiments, is shown in figure 5.5.

The LDA system consisted of one 2D probe, housing pairs of frequency shifted green (U1) and blue (U2) beams, and another 1D probe, housing a pair of violet (U3) beams. The beams were split from their source at a 5-Watt Coherent Innova 90C Argon-ion laser. A fibre-optic system was used for delivery and collection, in back-scatter mode, with a beam spacing of 80 mm and a focal length for 511, 508 and 501 mm for U1, U2 and U3 beams respectively.

To measure three velocity components required a careful alignment of 2D and 1D probes. The two probes were aligned so that their intersection volumes coincide. This was done by using a fine pinhole, with an opening just large enough that the focused beam can passed through. A fine adjustment was carried out using a power meter behind the pinhole maximising the power of light passing through the pinhole for each beam.

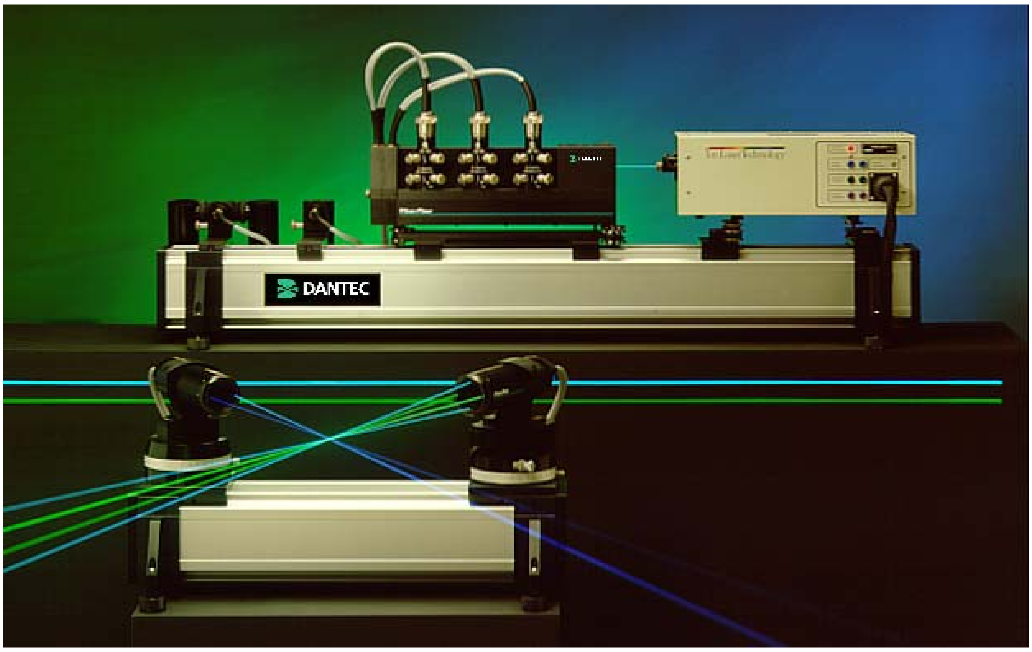

Figure 5.5 Three-dimensional LDA system (Dantec Dynamics)

A transformation matrix was used to convert the raw LDA signals to velocity data. Coordinate transformation is normally used, when limited optical access or other physical restraints have forced velocities to be measured along directions not coinciding with the coordinate directions otherwise used in the model and calculations. This was the case in my experimental set up, and new coordinates were calculated so that the axis orientation x, y and z of the traverse corresponded to the axial velocity u, the radial velocity v and the tangential velocity w, respectively.

Flow seeding was provided by using the ROSCO 1700 smoke machine to manually pulse smoke into the classifier model. The smoke particles were characterised by a mean diameter estimated to be 1μm, and a density relative to air of 800. The same principle for smoke injection was used as for the flow visualisation experiments, described in section 5.1.2.

The LDA heads were mounted on a Dantec three-axis traverse. The traverse has a positional accuracy of 0.05 mm in three orthogonal directions and was programmed to automatically execute the measurements at each axial position. A Burst Spectrum Analyser (BSA) automatically processes the recorded signal burst information.

A schematic diagram of the experimental set-up is shown in figure 5.6.

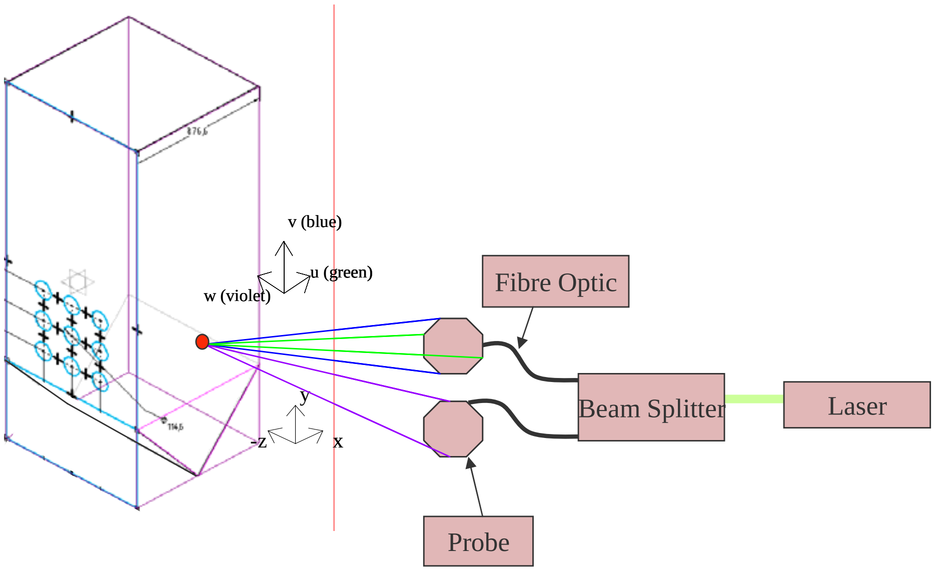

Figure 5.6 LDA experimental set-up

5.2.3 LDA experimental procedure

Measurements were taken in both vertical and horizontal directions. Vertical measurements, along the y-axis, were taken by programming the 3D traverse to acquire data at regular 5 mm intervals, starting at the centre of the bottom burner, and ending at the centre of the top burner. Horizontal measurements were taken along the central burner axis (x-direction) across a distance of 450 mm starting at the burner exit, with data points acquired at regular 5 mm intervals. Summary of selected experiments and parameters measured using the LDA is given is section 7.1.

The experimental procedure involved seeding the flow with smoke and initiating the LDA system and the traverse, resulting in an automatic data acquisition at pre-programmed positions.

Each measurement was taken over a period of 30 seconds, with the maximum number of samples set at 50,000. It was found that this number was more than sufficient to yield good quality measurements. Exceeding this number of acquired samples created problems with the computational memory space required to save the experimental runs. The number of samples acquired varied for each measurement locations, but was generally between the thousands and the tens of thousands (capped at 50,000).

Time-averaged measurements were performed in burst-and-coincidence mode to provide simultaneous three-component velocity measurements.

In order to maximise the number of velocity measurements at each data point, the LDA was operated at different laser powers. Generally measurements at each location were undertaken with a laser power of 2 Watt.

The data was processed by the BSA and acquired in a 300 MHz PC.

Interpretation of the experimental data is described in Experimental Results, presented in chapter 7.

Chapter 6

Numerical modelling

The fundamentals of closure modelling are presented, together with a detailed overview of the turbulence models applied in numerical simulations, which were performed as part of my PhD study. CFD model set-up was described, including the geometry, mesh size and boundary conditions. Refinement of the CFD model is also discussed.

6.1 Turbulence modelling

6.1.1 Closure modelling

For decades, comprehending and modelling turbulent fluid motion has stimulated the creativity of scientists, engineers and applied mathematicians. Analyses of turbulent flow inevitably invoke a statistical description, since, at the statistical level, turbulent phenomena become reproducible and subject to systematic study. Statistics provide a basis for theoretical descriptions and for a diversity of prediction methods. However, exact equations for the statistics do not exist. Therefore, the aim is to develop methods to predict the flow fields of practical devices.

The equations for statistics of turbulent flow are fewer in number than unknowns contained in them, and hence do not form a closed set of predictive equations. Closure modelling is applied to formulate further equations so that a soluble set of equations is obtained. In practical situations, closure relations are not exact or derivable. They invoke empiricism, and consequently, any closure model has a limited range of use, implicitly restricted by its empirical content. Over the past few decades, a number of very useful semi-empirical models have been developed to calculate engineering flows (Durbin and Pettersson Reif, 2001).

6.1.2 Turbulence models

There are many turbulence models which are used as computational procedures to close the system of mean flow equations allowing the calculation of the mean flow without first calculating the full time-dependent flow field. The most common turbulence models, based on Reynolds Averaged Navier-Stokes (RANS) equations (time averaged) are:

- Zero equation model: mixing length model
- One equation model: Spalart-Almaras
- Two equation models: k-ε style models (standard, RNG, realizable), k-ω model, and algebraic stress model (ASM)

- Seven equation model: Reynolds stress model (RSM).

The number of equations denotes the number of additional partial differential equations (PDEs) that are being solved.

Three of the above mentioned turbulence models were selected for the purpose of modelling interacting multi-burner swirl flows, as part of my PhD research: k-ε (standard), k-ω and RSM. A detailed overview of the selected turbulence models is given below.

6.1.2.1 The k-ε turbulence model

The k-ε model is a semi-empirical model based on model transport equations for the turbulence kinetic energy (k) and its dissipation rate (ε) (Bakker, 2005). By solving these equations, an eddy viscosity is created for the purpose of predicting the mean flow. A full set of equations for the k-ε turbulence model is given in Appendix C.1.

The derivation of the k-ε model assumes that the flow is fully turbulent and isotropic, and the effects of molecular viscosity are negligible.

The k-ε model is the most widely used turbulence transport model. Although an enormous number of variations of the k-ε model have been proposed, the standard k-ε model is still the basis for most calculations (Durbin and Pettersson Reif, 2001).

According to the FLUENT 6 User’s Guide, the advantages of using the k-ε turbulence model are that its is relatively simple to implement, leads to stable calculations that converge relatively easily, and that it gives a reasonable predictions for many flows.

The disadvantages of the k-ε turbulence model are that it gives poor predictions for: swirling and rotating flows, flows with strong separation, axisymmetric jets, certain unconfined flows, and fully developed flows in non-circular ducts; it is valid only for fully turbulent flows; and that it employs a simplistic equation for the dissipation rate, ε.

6.1.2.2 The k-ω turbulence model

The standard k-ω model in FLUENT is based on the Wilcox k- ω model (Wilcox, 1998), which incorporates modifications for low-Reynolds-number effects, compressibility, and shear flow spreading. The Wilcox model predicts free shear flow spreading rates that are in close agreement with measurements for far wakes, mixing layers, and plane, round, and radial jets, and is thus applicable to wall-bounded flows and free shear flows (FLUENT 6 User's Guide).

The standard k-ω turbulence model is another two equation model. In this model ω is an inverse time scale that is associated with the turbulence. This model solves two additional PDEs: a modified version of the k equation used in the k-ε model (where k equation is altered by changing ε to kω) and a transport equation for ω. The turbulent viscosity is then calculated as:

$$\mu_t = \rho \frac{k}{\omega} \tag{6.1}$$

The numerical behaviour of the k-ω turbulence model is similar to that of the k-ε models, and it suffers from some of the same drawbacks, such as the assumption that μt is isotropic (FLUENT 6 User's Guide).

6.1.2.3 The RSM turbulence model

The Reynolds stress model (RSM) is the most elaborate turbulence model that FLUENT provides. Abandoning the isotropic eddy-viscosity hypothesis, the RSM closes the Reynolds-averaged Navier-Stokes equations by solving transport equations for the Reynolds stresses, together with an equation for the dissipation rate. This means that four additional transport equations are required in 2D flows and seven additional transport equations must be solved in 3D flows.

Since the RSM accounts for the effects of streamline curvature, swirl, rotation, and rapid changes in strain rate in a more rigorous manner than one-equation and two-equation models, it has greater potential to give accurate predictions for complex flows. However, the reliability of RSM predictions is still limited by the closure assumptions employed to model various terms in the exact transport equations for the Reynolds stresses. A full set of Reynolds stress transport equations is given in Appendix C.2.

The RSM might not always yield results that are clearly superior to the simpler models in all classes of flows to warrant the additional computational expense. However, use of the RSM is recommended when the flow features of interest are the result of anisotropy in the Reynolds stresses. Among the examples are cyclone flows, highly swirling flows in combustors, rotating flow passages, and the stress-induced secondary flows in ducts (FLUENT 6 User's Guide).

6.2 Mathematical model of physical model

6.2.1 Model set-up

An existing MBEL numerical model created in FLUENT (Duncan et al., 2002), was used to simulate the flow in a multi-burner furnace and examine the effects of various turbulence models on flow velocity and turbulent quantities.

A generic front-wall fired furnace was used to study the effect of burner pitching and swirl orientation on burner interactions. Furnace sidewall and bottom row burner-to-hopper clearances were held constant between models and therefore furnace width increased with burner horizontal pitch. Hopper and total furnace height were maintained between cases. Geometry of the CFD model was based on a 1/10 scale physical model, shown in figures 4.1 and 4.2.

All models were constructed using hexahedral cells for the more accurate resolution of complex swirling flows. As the work is primarily concerned with the burner zone, the arch level was chosen as the furnace exit for all the models. The near burner mesh detail is shown in figure 6.1.

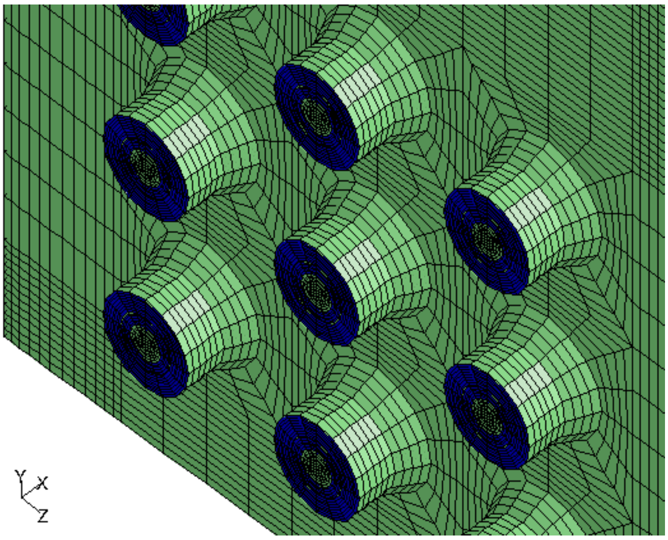

Figure 6.1 Burner panel mesh (Duncan et al. 2002)

The mesh extends back to the primary air inlet and the exit of the secondary air swirl generator. To reduce the complexity of the furnace models, and so reduce computational expense, burner inlet velocity profiles (clockwise and anticlockwise swirl) were derived from a separate, detailed, single burner model (figure 6.2).

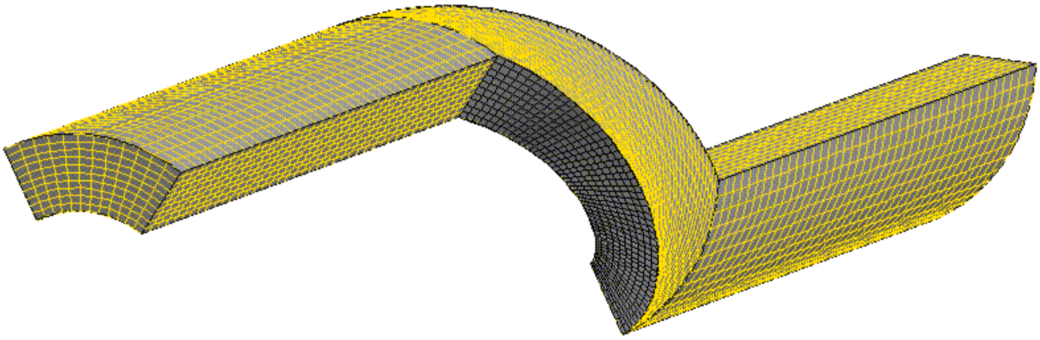

Figure 6.2 Physical model axial swirl generator – mesh detail (Duncan et al. 2002)

Originally, it had been intended to apply a measured inlet profile to the mathematical models. However, access restrictions on the LDA equipment meant that it was not feasible for this to be done. Instead, measurements were taken as near to the swirl generator exit as was practically possible (i.e. within the divergent quarl section of a wing burner) to provide an additional near burner traverse. These measurements confirmed that the predicted swirl generator outlet profile was acceptable, and are discussed more fully in chapter 8.

An equal distribution of airflows between burners was assumed, with the split of air between primary and secondary air annuli also assumed to be constant. This was verified during the physical model commissioning tests. An ambient, isothermal laboratory temperature of 20°C was applied. The flow rates for primary and secondary registers have been calculated from the experimental LDA measurements.

Whilst the presence of the transient phenomena was evident from the flow visualisation experiments (section 7.2), the complex geometry of the furnace model and limited computing power prohibited modelling of unsteady flows. Hence, the computational modelling was carried out using the steady flow assumptions.

6.2.2 CFD model refinement

Gradient refinement was carried out to test the sensitivity of velocity results to the increase in mesh size. The test was carried out on the 1.6 d pitch of the chequerboard configuration, simulated using the k-ε turbulence model.

The results showed that there was no improvement in prediction of the axial velocity profiles. Therefore, numerical simulations were reverted to the original mesh size. Details of the procedure in Fluent, undertaken to perform the gradient refinement are given in Appendix C.3.

6.2.3 Selection of numerical models, pitching and swirl orientation

CFD geometries were chosen to reflect the selection of experimental runs described in section 7.1.

The numerical simulations were performed for 1.6d and 2d pitches of chequerboard and columnar configurations. Each of these four cases has been modelled using three different turbulence models: k-ε, k-ω and RSM. Numerical results obtained using these three turbulence models are presented and discussed in chapter 8.

Chapter 7

Experimental results

The experimental results were obtained using flow visualisation, for the qualitative assessment of the multi-burner flow; and 3D Laser Doppler Anemometry, for the quantitative velocity and turbulence measurements. The experimental results are discussed and validated with respect to the previously published work.

7.1 Summary of experiments selected

In order to investigate the effect of pitch and burner panel configuration on jet interaction, the following experiments were conducted:

1. Flow visualisation tests on four pitching arrangements (1.6d, 1.75d, 2d, 2.25d[*]). Industrial literature shows that pitches of 2d-2.75d are currently used in front- and opposed-wall fired furnaces (Duncan et al., 2002). Tighter pitches of 1.6d and 1.75d were investigated in order to examine the effects of pitch reduction.

Tests were carried out with all nine burners active, with smoke injected in the following burner-register combinations:

- Central burner-inner register
- Central burner-outer register
- Central burner-inner and outer
- Central and upper burner-inner registers
- Central and lower burner-inner registers
- Central and upper burner-outer registers
- Central and lower burner-outer registers

A video camera was used to capture the flow visualisation images.

The subsequent analysis of these images led to a decision to carry out further quantitative measurements using 1.6d and 2d pitches. These two pitches were chosen because 2d pitch is the most representative of the current industrial standard pitching arrangement, whereas 1.6d pitch, the smallest of the initial four pitching arrangements, represents an extreme case of pitch reduction.

2. Two sets of 3D LDA experiments were carried out for 1.6d and 2d pitches of both chequerboard (five clockwise and four anticlockwise burners) and columnar (three clockwise swirl and six anticlockwise burners) swirl configurations (figure 7.1) Choice

---

[*] d is the burner diameter.

of configurations was based on industry recommendations; both are standard industry configurations. The following sets of experiments were carried out:

a) Velocity profiles and turbulent quantities in the vertical direction, across the central burner at 0, 0.5d, 1d, 2d and 5d distances from the burner exit plane.

This set of LDA experiments was carried out in order to establish the development of the vertical velocity profile measured at five stations along the horizontal (x) axis. The profiles were measured on the vertical central burner line, starting from the centre of the top middle burner and finishing at the centre of the bottom middle burner. These experiments clearly showed developing velocity patterns, areas of re-circulation and points of interaction between the central and top/bottom burners, where the jets start to merge.

b) Velocity profiles and turbulent quantities in the horizontal direction, along the burner axis of the central burner.

This set of LDA experiments was carried out to identify the behaviour of the centre-line velocity profile, as the flow moves away from the burner exit plane.

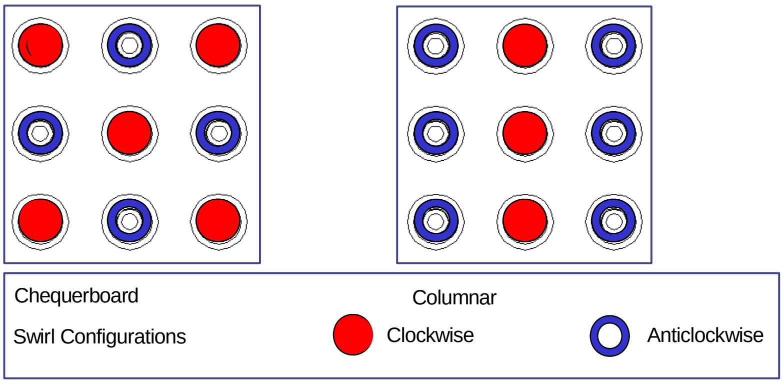

Figure 7.1 Chequerboard and columnar configurations (Duncan et al., 2002)

Figure 7.2 shows both the vertical and horizontal directions of the measured velocity profiles. The following parameters were measured:

- Axial, radial and swirl velocities (u, v and w);
- Root mean square (r.m.s.) of the fluctuating velocities (u′, v′ and w′) and
- Reynold’s shear stresses (u′v′, v′w′ and u′w′).

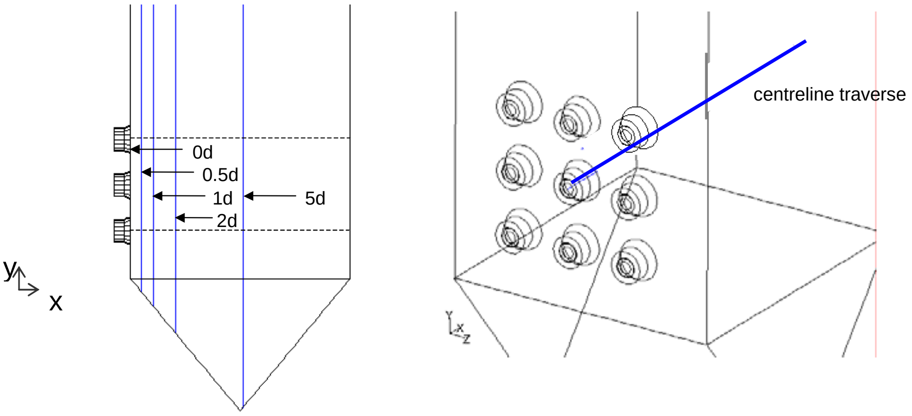

Vertical Traverses

Horizontal Traverses

Figure 7.2 Vertical and horizontal directions of measured velocity profiles (Duncan et al. 2000)

7.2 Flow visualisation results

Flow visualisation tests have been carried out in order to establish and qualitatively assess the interaction between burner flows in the 1/10 scale multi-burner furnace model. Four different pitches of chequerboard configuration (1.6d, 1.75d, 2d and 2.25d) were used in the tests, with the purpose of finding the correlation between the points of jet interaction and the pitch size. The images of the four pitches showing the jet interactions between the central and upper burners, given in figures 7.3a-d, were analysed. It was found that, as the pitch size decreased, the interaction between the burner flows became more evident. Figure 7.3a shows that, for the smallest pitch, the burner jets start interacting almost immediately at the burner exit.

The relationship between the pitch size and the point of intersection of the two adjacent jets (upper middle and central middle) after leaving the burner exit is shown in figure 7.4 for all four pitches. Points of intersection are points where two adjacent jets begin to merge. Photo-editing software was used to manipulate the images and measure the distances between the burner exit and the point of intersection between the two burners. The graph clearly shows that the burner jet interaction is a function of the pitch size.

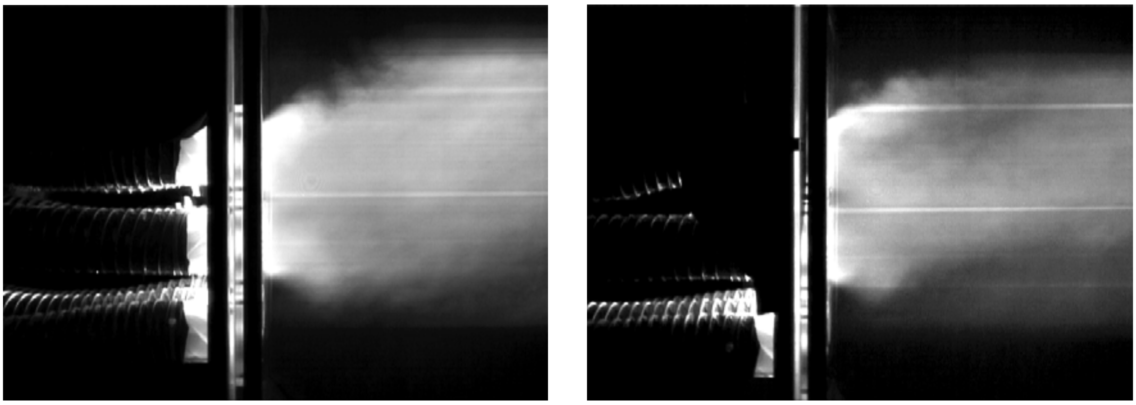

Figure 7.3a Pitch 1.6d, Central and Upper Burner-Outer Registers

Figure 7.3b Pitch 1.75d, Central and Upper Burner-Outer Registers

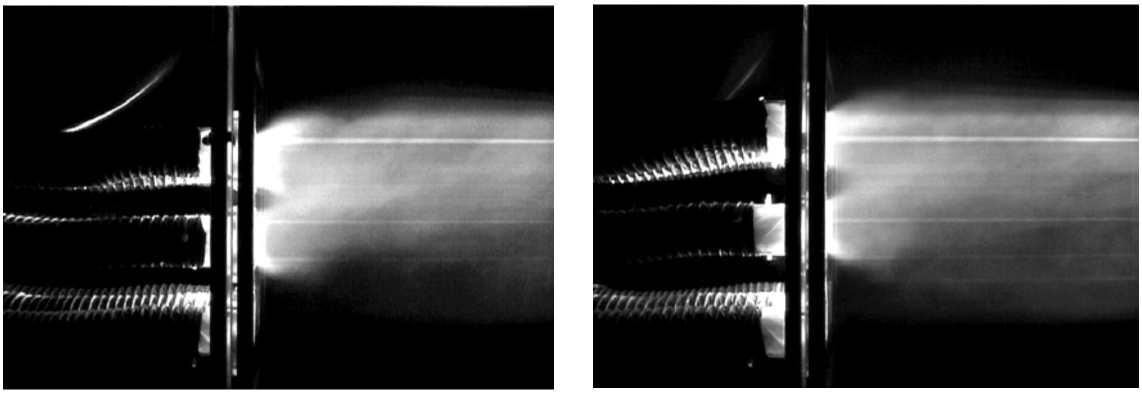

Figure 7.3c Pitch 2d, Central and Upper Burner-Outer Registers

Figure 7.3d Pitch 2.25d, Central and Upper Burner-Outer Registers

Figure 7.3 Jet interactions between the central and upper burners

These findings are consistent with those of Tarr and Allen (1998), who carried out a flow visualisation study on a 3x3 swirling burner array of a 1/13 scale furnace model. They found that, at a 3.2d burner pitch, the burner flows were not interacting. On the other hand, when they used 1.3d burner pitch, they found that the individual burner flows impinged on one another soon after leaving the burner exit, thus forming a cohesive single flow.

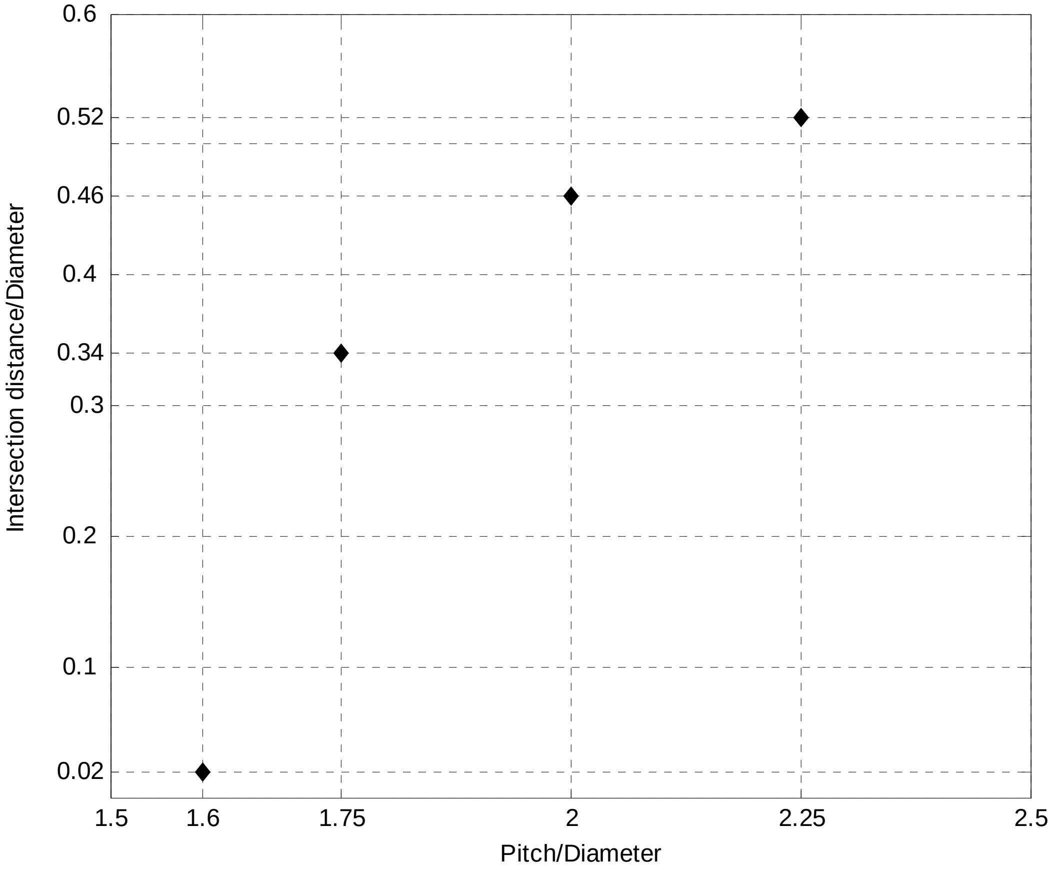

Figure 7.4 Relationship between the pitch size and the point of intersection after leaving the burner exit for all four pitches

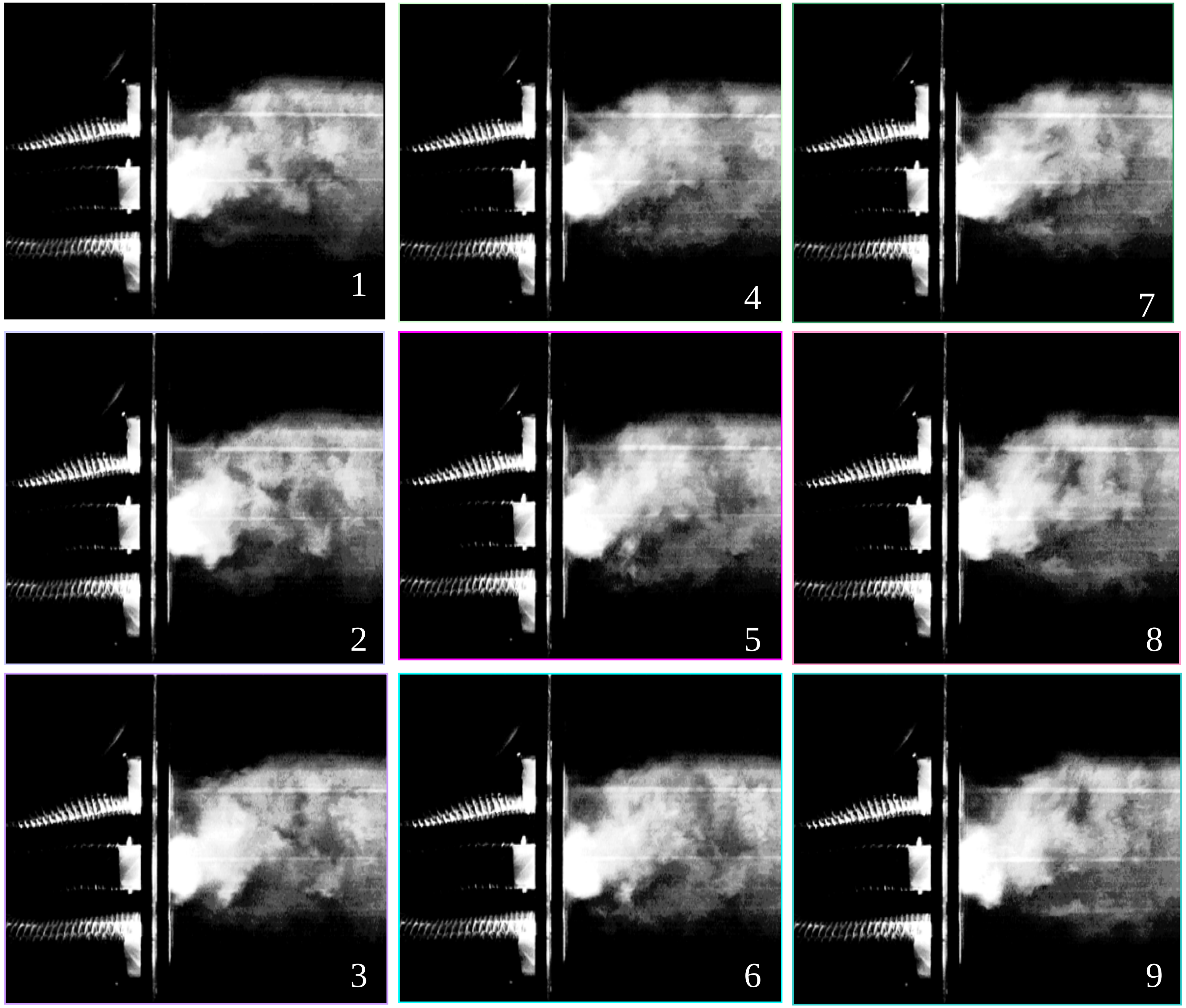

Figure 7.5 Burner jet fluctuations in central burner, 2d pitch, chequerboard configuration

Figure 7.5 shows nine consecutive images of a smoke-simulated flame, taken for the central burner of the 2d pitch of chequered board configuration. The sequence clearly shows the random fluctuation of the burner jet. This implies that the flow is time-dependant, and that transient phenomena are present. Al-Abdeli and Masri (2003) refer to the unsteady or time dependent phenomena as one of the key challenges in modelling of swirling flows.

7.3 Three-dimensional Laser Doppler Anemometry results

3D LDA experiments were carried out in order to analyse interactions between burner flows for 1.6d and 2d pitches of both chequerboard and columnar configurations by taking quantitative measurements of velocity components and turbulent quantities, and for comparison with the numerical model.

Velocity profiles of u, v and w velocity components were studied, as well as profiles of turbulent kinetic energy and Reynolds shear stresses. Formation of recirculation zones, their extents and widths were analysed and presented below. The results obtained in this research are compared to the previously conducted experimental studies.

7.3.1 Axial (*u*) velocity profiles

Figure 7.6 shows vertical profiles of axial velocity (u) taken at distances of x=0, 0.5d, d, 2d and 5d from the burner exit plane, along the burner centreline (z=0), for 1.6d pitch of both chequerboard and columnar configurations. The flat regions that can be seen in figure 7.6a (burner exit) represent the inter-burner spacing. Analysis of figures 7.6a–e highlights the differences between the vertical velocity profiles of chequerboard and columnar configurations obtained for 1.6d burner pitch.

The difference in the width of the recirculation zone, measured at 0.5d distance from the burner exit plane shows the columnar configuration to have a wider recirculation region and a flatter velocity profile than the chequerboard configuration (figure 7.6b). The extent (or length) of the recirculation zone for the 1.6d pitch, obtained from the horizontal velocity profiles (figure 7.7a), shows a deeper jet penetration into the furnace in the case of the columnar configuration. More detailed analysis of recirculation zones is given in section 7.3.1.1.

The analysis of figures 7.8a-e shows that the differences between the vertical velocity profiles of the chequerboard and columnar configurations obtained for 2d burner pitch are not as pronounced as those obtained for 1.6d pitch. The width of the recirculation zone, measured at 0.5d distance from the burner exit plane, was found to be only slightly greater in the case of the chequerboard configuration (figure 7.8b). The difference in the extent of the recirculation zone between the two configurations was found to be insignificant (figure 7.7b).

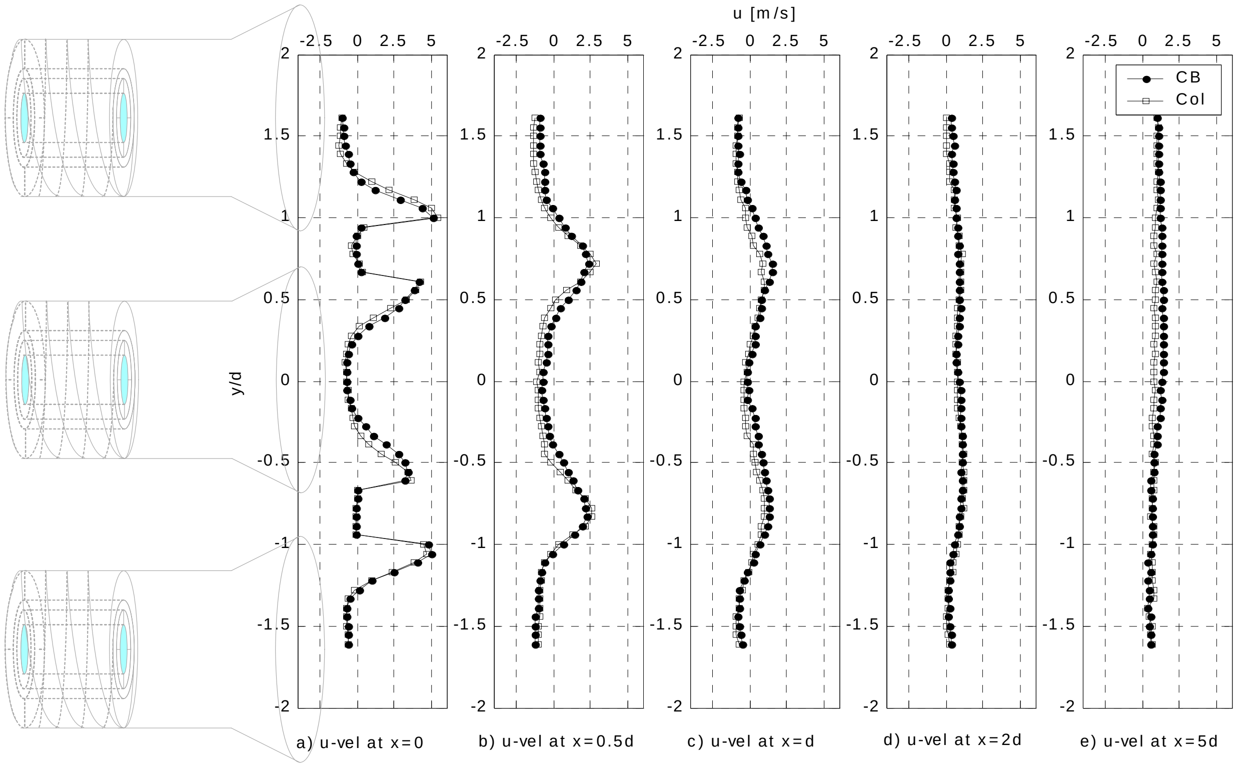

Figure 7.6 Vertical profiles of u velocity in the direction of flow, taken for 1.6d pitch of chequered board and columnar configurations at x=0d, 0.5d, d, 2d and 5d distances from the burner panel.

Allen's findings (Allen, 1970), given in figure 7.9, demonstrated that the maximum *u* values were higher for the 'in mesh' (chequerboard) configuration due to the fact that jets are likely to combine more readily than in the case of the 'out of mesh' (columnar) configuration, where they push each other apart. It needs to be noted that, while Allen's columnar set-up consisted of three horizontally placed jets with the same direction of swirl ('out of mesh'), my columnar set-up contained both 'in mesh' and 'out of mesh' features of flow (figure 7.1). Further details on Allen's work can be found in section 2.2.1.

Results of my PhD research only partly support Allen's observations: In the case of the 2d pitch, the chequerboard configuration gives higher maximum *u* velocities at each of the stations along the x-axis (figure 7.8). On the other hand, for 1.6d pitch, the difference in peak *u* velocities is only evident at x=d distance away from the burner exit (figure 7.6). The effect of configuration on maximum axial velocities stops being evident at x=2d, in the case of the 1.6d pitch, and x=5d in the case of the 2d pitch.

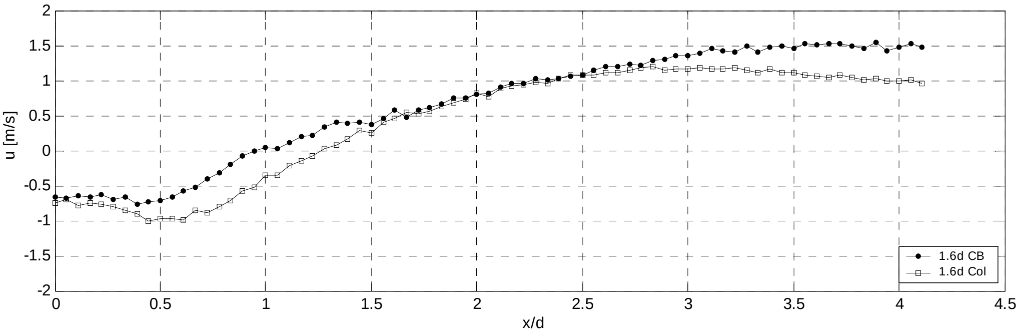

a) Horizontal traverse along the central burner axis, Pitch=1.6d

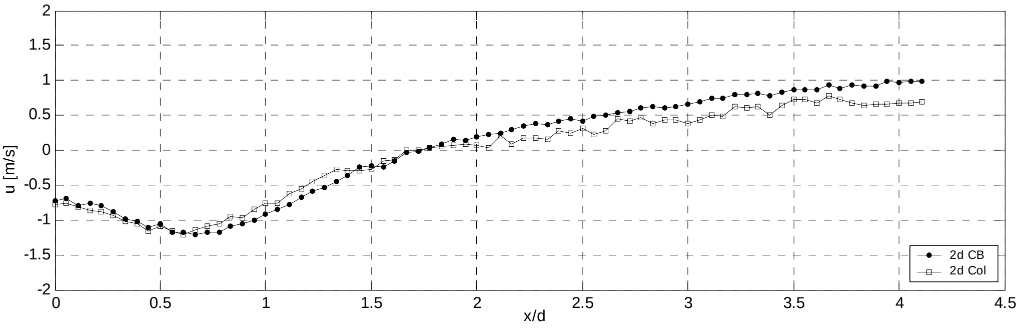

b) Horizontal traverse along the central burner axis, Pitch=2d

Figure 7.7 Horizontal profiles of u velocity in the direction of flow, taken for 1.6d and 2d pitches of chequered board and columnar configurations along the central burner line.

Allen also found that the axial velocity distributions for the 'in mesh' system have two peaks, whereas the 'out of mesh' system has three peaks. Whilst the 'in-mesh' observation is in line with my axial velocity results for the chequerboard configuration, Allen's 'out of mesh' velocity profile differs significantly from mine, which consistently showed two peaks in case of the columnar configuration. This difference is believed to be caused by the 'in mesh' systems acting within the columnar configuration used in my research.

The effect of the burner configuration on multiple burner jet interactions, based on the results of this PhD work, has also been described in a publication by Cvoro and Easson (2002).

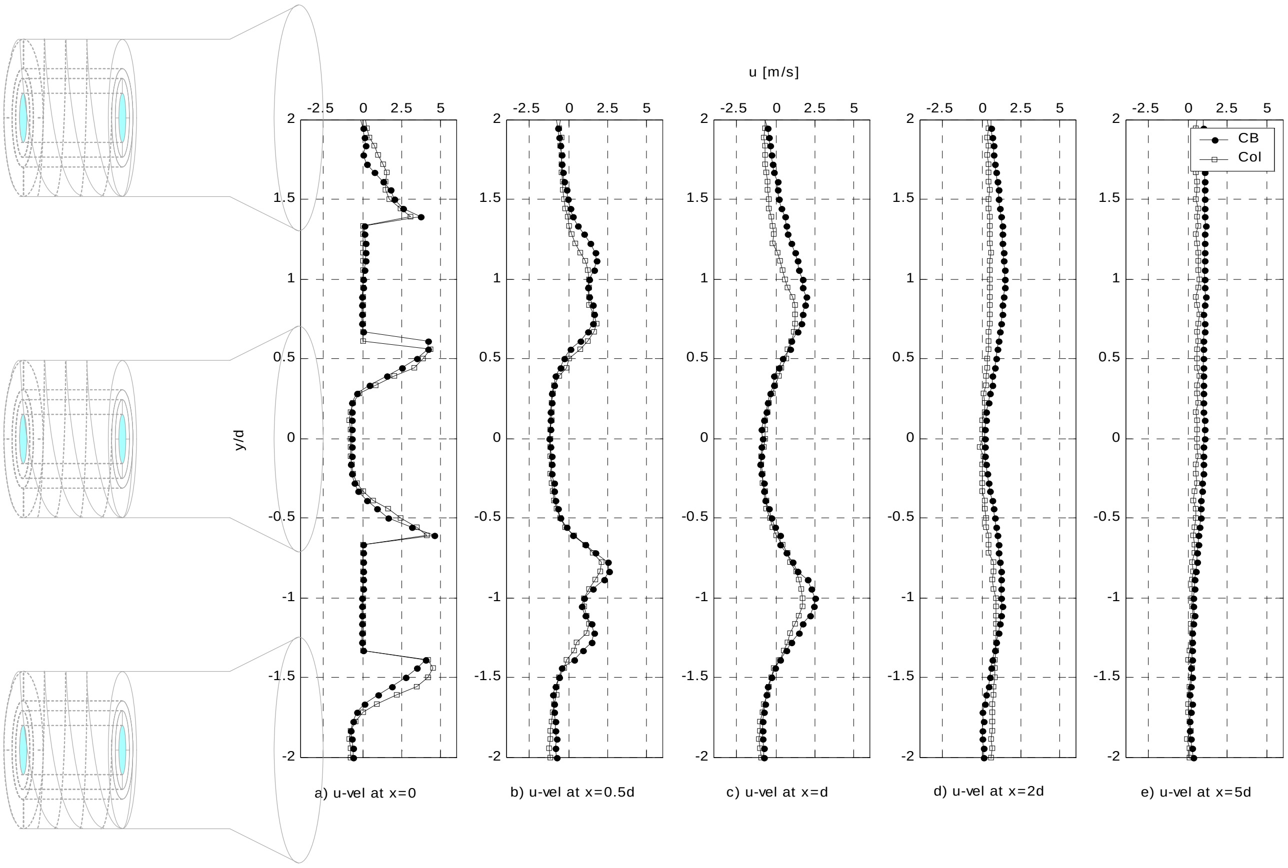

Figure 7.8 Vertical profiles of u velocity in the direction of flow, taken for 2d pitch of chequered board and columnar configurations at x=0d, 0.5d, d, 2d and 5d distances from the burner exit plane.

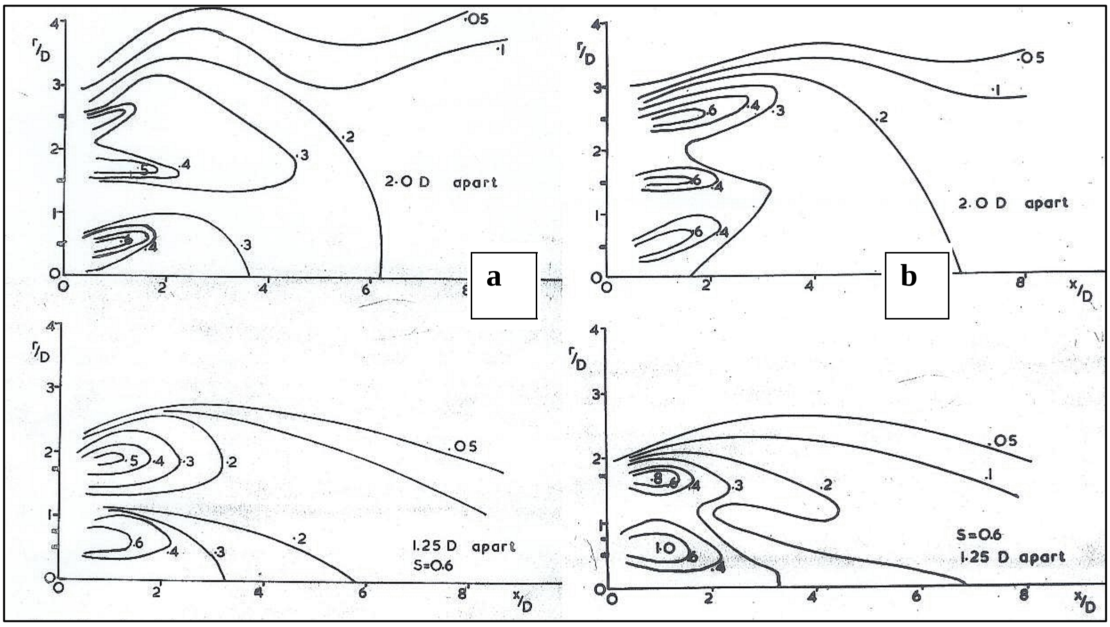

Figure 7.9 Spatial $\frac{\bar{u}}{u_0}$ *distribution for three swirling jets a)'out of mesh' and b)'in mesh' (Allen, 1970)*

Kihm et al. (1990) carried out measurements of three components of mean velocity on a single burner, using a laser Doppler velocimeter operating in the dual-beam, single component mode. Figure 7.10 shows axial velocity profiles at different stages along the central burner line, taken for the 40° swirler, which is closest to the swirl angle of 35° (with respect to the burner axis) used in this research. A 40° swirler approximately corresponds to the swirl number of 0.6 (Gupta et al, 1984). The shape of the profiles and locations of peak velocities are very similar to the findings presented in figures 7.6 and 7.8. Key differences are that, from Kihm's results, the recirculation continues past x/d=2 and profiles are still clearly defined at x/d=4, whilst my results show recirculation disappearing by x/d=2, for both 1.6 and 2 pitches (figure 7.7), with velocity profiles losing definition by x/d=5, as adjacent jets merge (figures 7.6 and 7.8). The extended appearance of the recirculation zone can be attributed to the findings by Chigier and Gilbert (1968), who concluded that the length of recirculation zone depends on the degree of swirl imparted to the flow, with higher swirl causing deeper recirculation.

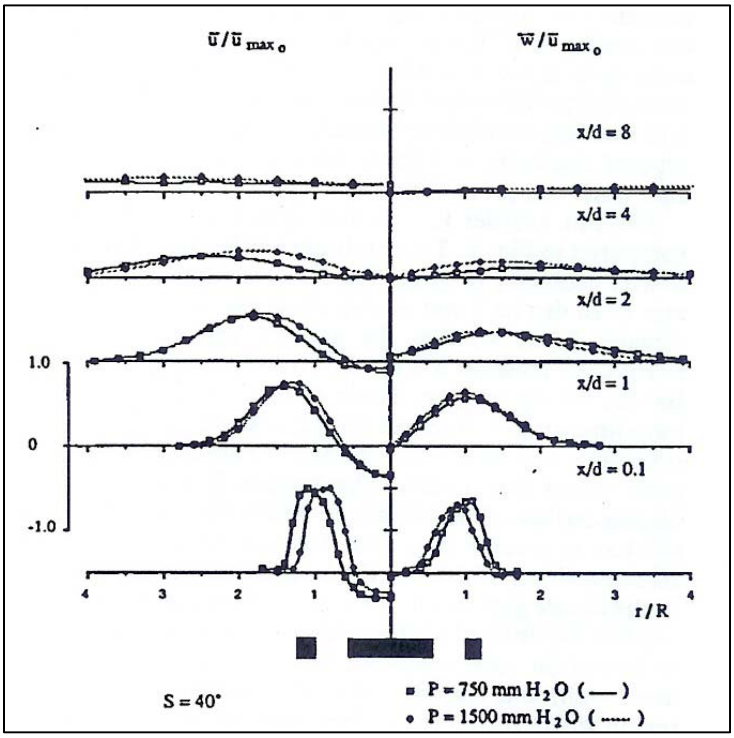

Figure 7.10 Axial and tangential mean velocity profiles normalised by the maximum axial velocity at the nozzle exit u_{max} *for the 40° swirler (Kihm et al, 1990)*

Tarr and Allen (1998) conducted their experiments on a scaled furnace model, using different pitching arrangements between burners and swirl orientations. The six-burner set up from which they obtained their LDA measurements is the most similar to the experimental set-up used in this research. Unfortunately, the results for this set-up have not been included in their publication. The next closest set-up involves interaction between four burners set on a 2d pitch, and these results are shown in figure 7.11.

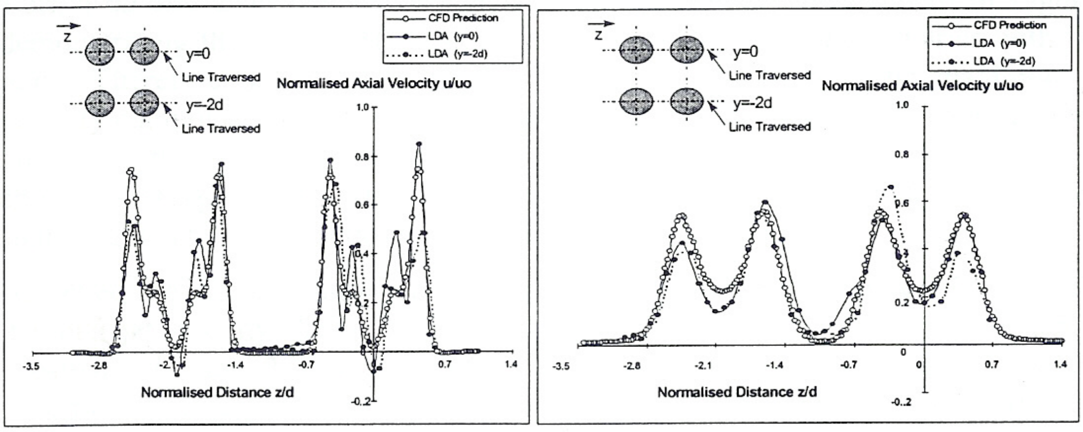

x/d=0.3 *x/d=1.2*

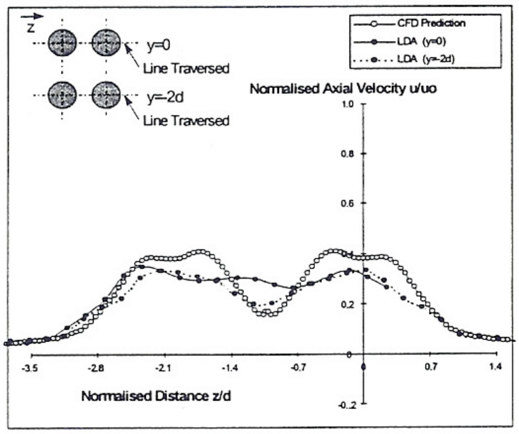

x/d=2.0

Figure 7.11 Axial velocity distribution for the four burner counter-rotating array (Tarr and Allen, 1998)

Figure 7.11 shows that velocity profiles taken at varying distances from the furnace burner wall are similar to those presented in figure 7.8. However, this comparison can only be qualitative and not direct, since the experimental set-up differed in terms of the number of burners used, burner design and the swirl number. The average swirl number measured by Tarr and Allen (1998) was approximately 0.6, compared to the swirl number of 0.5, used in this research.

Aroussi et al. (2000) carried out a similar study to Tarr and Allen (1998), where they used 2D laser Doppler anemometry measurements on a 3x3 burner array with a 2d pitch. The burners consisted of three registers, with the swirl number of 0.6. Figure 8.5

shows the experimental values (together with numerical results) obtained for axial velocities for two burners discharging into the furnace. Whilst the shapes of the velocity profiles were similar to those given in figures 7.6 and 7.8, the extents of the recirculation zones were shorter for Aroussi's results, and they disappeared past the distance of x/d=0.3. What is interesting is that Aroussi's measurements for a single burner, which were superimposed over the results for two burners, show the same behaviour. This contradicts the findings by Khim (1990) presented earlier, which showed much deeper extent of recirculation in the case of a single burner with a swirl number of 0.6. Comparison of my results with Aroussi's, as was the case with Tarr and Allen's (1998), can only be qualitative, considering the differences in the burner design used in their study compared to this research.

7.3.1.1 Recirculation zones

Syred et al. (1971) recognised the importance of recirculation zones in the combustion process occurring in industrial furnaces with swirling flames. Recirculation zones play an important role in combustion process, since their dimensions are crucial for flame stabilisation in stationary burners and NOx reduction due to flue gas recirculation. Further, they found that it is the aerodynamics of the 'cold' swirling flow that plays a dominant role, suggesting that the 'cold' burner model will often be sufficient to predict the size of the recirculation zone under 'hot' conditions.

Given the importance of this phenomenon, recirculation zones were analysed and compared for the two pitches of both configurations. The recirculation zones were analysed at a distance of 0.5d from the from the burner exit panel. This distance was chosen due to the following reasons:

Gupta et al. (1984) showed that turbulent kinetic energy levels are highest at the burner exit, with a rapid decay occurring after one exit diameter. The x=0.5d position was chosen over x=0 in order to capture the effect of multiple jet interactions, which is not evident at x=0.

Further, investigation of the jet flow development given in figures 7.6 and 7.8 showed that at x=0.5d, the difference between velocity profiles taken for 1.6d and 2d pitching arrangements is still noticeable in terms of the jet development and velocity magnitudes: jets arranged on a tighter pitch are already merged and showing a single peak, whilst jets that are arranged on a 2d pitch are showing weaker interaction, resulting in delayed merging and 'double-peak' appearance. At x=2d, however, the jet decay is apparent in both pitches and configurations.

	1.6d pitch		2d pitch	
Recirculation Zones [mm]	Chequerboard	Columnar	Chequerboard	Columnar
Width (at x= 0.5d from burner exit)	80	89	100	96
Extent (along central burner x-axis)	86	114	157	155

Table 7.1 *Extents and widths of recirculation zones for 1.6d and 2d pitches of chequerboard and columnar configurations*

The widths of the recirculation zones measured at 0.5d distance from the burner exit plane, and the extents, measured along the central burner line for both pitches and configurations are given in table 7.1.

A decrease in pitch from 2d to 1.6d causes the width of the recirculation, measured at 0.5d distance from the burner exit plane, to decrease by 20% for the chequerboard configuration and 7% for the columnar configuration. Further, decrease in pitch causes the extent of the recirculation, measured along the central burner line, to decrease by 45% for the chequerboard configuration and 26% for the columnar configuration. This clearly shows that the burner flow is sensitive to the change in pitch, for both configurations. This sensitivity is much more evident in the case of the chequerboard configuration, both in terms of the effect on the width and the extent of the recirculation zone.

It is interesting to observe the effect of configuration on the widths and extents of recirculation zones. From figures 7.6-7.8 and table 7.1, it can be seen that the effect of burner configuration is much more evident in the case of the 1.6d pitch than 2d pitch. For 1.6d pitch, both the width and the extent of recirculation are higher in the columnar configuration case by 10% and 25% respectively. The opposite trend is observed for 2d pitch, where both the width and the extent are lower for the columnar configuration, but only by 4% and 1% percent respectively.

Gupta et al. (1984) present the downstream development of centreline axial velocity as a function of swirl number (figure 7.12). They argue that for low degrees of swirl $S < 0.1$, the potential core (no velocity change) can be seen near the orifice. With increase in swirl number the length of the potential core decreases, and that beyond $S=0.6$, reversed flow is shown on the axis. This finding slightly disagrees with the findings of this research referring to the development of the downstream centreline velocity, given in figures 7.7a and 7.7b. It appears that axial velocity profiles presented in figures 7.7a and 7.7b exhibit the behaviour of a highly swirled flow by showing the recirculation region forming at the burner mouth. In fact, the recirculation zones are deeper than those obtained by Aroussi et al (2000), where a swirl number of 0.6 was used.

Gupta et al. (1984) also explain that even basic features of the recirculating flow are not known quantitatively with certainty. For example, in addition to the swirl strength, there are numerous other factors that affect the existence, size and shape of recirculation zones, such as:

- Swirl strength – swirl number S or vane angle ϕ
- Choice between swirl vanes and swirl generator
- Central hub or not (d/d_h ratio)
- Expansion to main chamber (D/d ratio)
- Quarl (divergent) exit or sudden expansion-effect of side-wall angle α and dome geometry
- Combustion or isothermal flow
- Swirl vane angle constant with radius or not
- Other factors.

Gupta et al. (1984) used a swirl generator for detailed experimental study, which could account for some of the differences in results corresponding to the swirl number of 0.5.

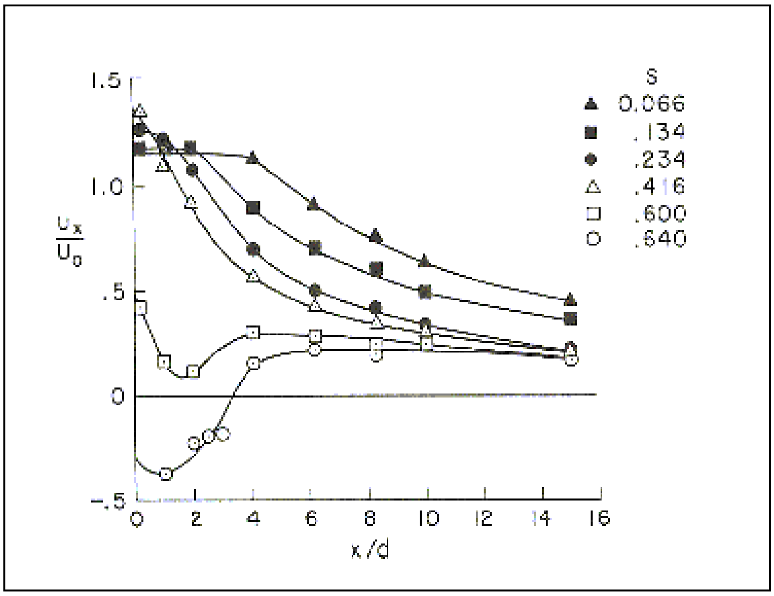

Figure 7.12 Downstream development of centreline velocity as a function of swirl number (Gupta et al, 1984)

Chigier and Dvorak (1975), who investigated flow fields in turbulent swirling jets under isothermal and combustion conditions, also produced a similar set of results relating to axial velocity profiles along the central burner line (figure 7.13). Their study was carried out on a single burner, with the swirl number of 0.3. They used a laser Doppler anemometer with frequency shift to obtain velocity measurements.

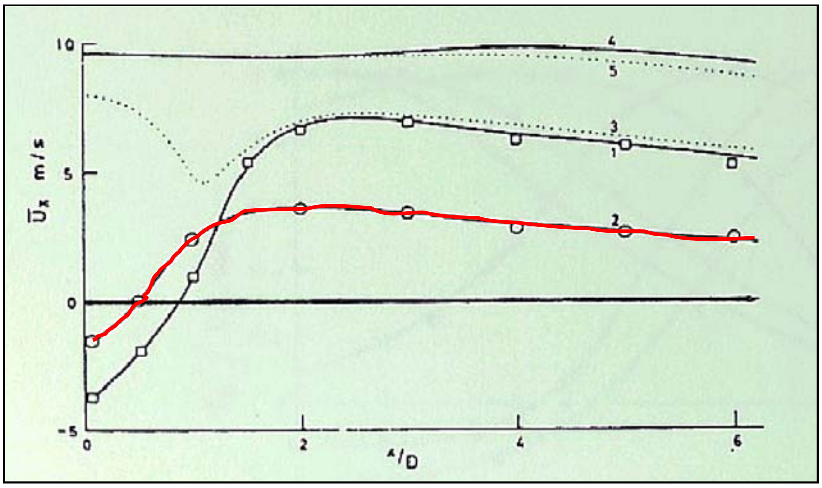

Figure 7.13 Axial component of mean velocity on the jet centreline (Chigier and Dvorak, 1975)

Line 2 in figure 7.13 represents the axial velocity profile of a cold jet. Their results show that the axial velocities are in the reverse flow at the burner exit. This contradicts Gupta's finding that only beyond S=0.6, reversed flow is shown on the axis. On the other hand, Chigier and Dvorak's results are in line with the results of this PhD work, with a shorter recirculation length due to the reduced swirl.

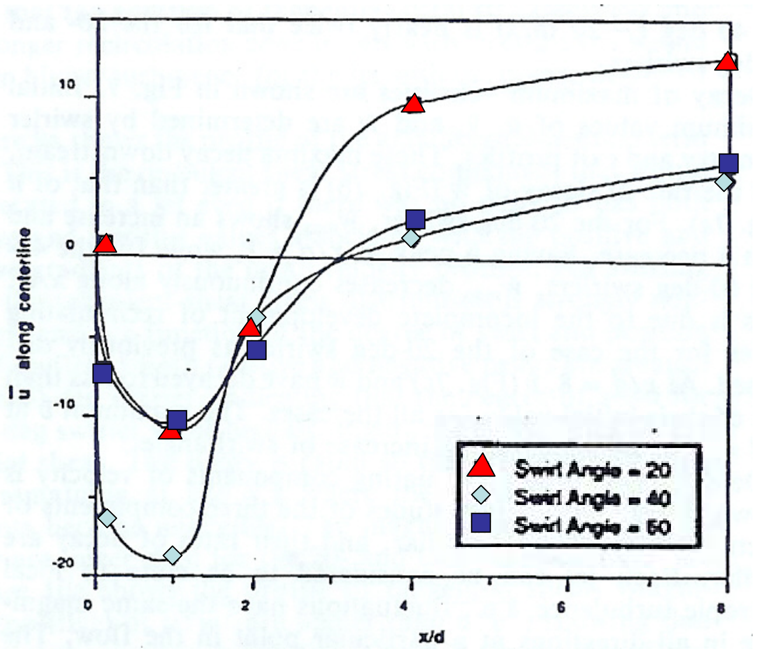

Figure 7.14 Axial component of mean velocity on the jet centreline (Kihm et al, 1990)

Kihm et al. (1990) also presented axial velocity on the jet centreline for different cases of swirl (figure 7.14). Here, it is interesting to observe that all three velocity profiles show recirculating flows at the burner exit, with the peak reverse velocity occurring at the swirl angle of 40°. Swirl angles of 20°, 40° and 60° approximately correspond to swirl numbers of 0.3, 0.6 and 1.5 respectively (Gupta et al, 1984).

Neither of the previously conducted studies presented above can be directly compared to the results of this research due to one or more differences between each one them and the study carried out in this research. However, qualitative comparisons with previous studies provide confidence that the magnitudes of recirculation zones in axial velocity profiles measured along the x-axis and in this research are as expected.

7.3.2 Radial (*v*) velocity profiles

Radial velocity profiles taken at the burner mouth, for 1.6d and 2d pitches of both configurations, show peaks at the edges of the burner quarl and flat regions across the face of the burner (figure 7.15). As the flow moves away from the burner-furnace wall, radial velocity components become insignificant, both in shape and magnitude.

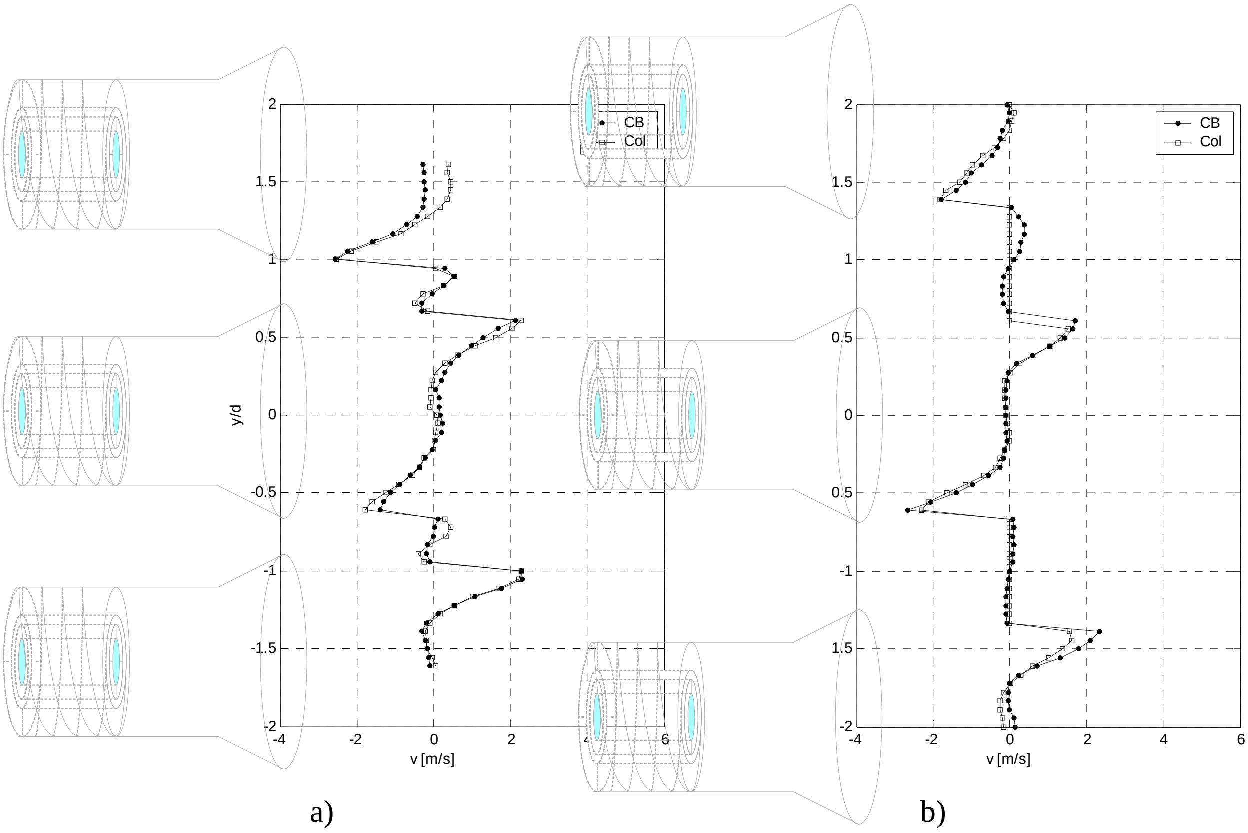

a) b)

Figure 7.15 Vertical profiles of v velocity, taken for a) 1.6d and b) 2d pitch of chequered board and columnar configurations at x=0d distance from the burner panel.

(Full sets of radial velocity profiles taken at distances from x=0-5d, for 1.6d and 2d pitches of both configurations are given in Appendix D.)

This finding is supported by Ahmed (1997), who found that the radial component decays most rapidly due to the swirl jet impinging on the combustor wall. Figure 7.16

shows Ahmed's findings for the evolution of the radial velocity profile, where x1 position refers to x/d=0.063 and x6 to x/d=0.5.

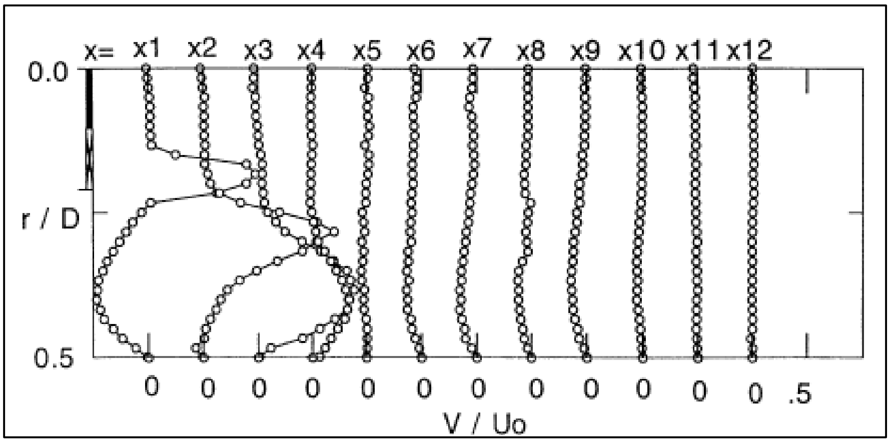

Figure 7.16 Evolution of non-dimensional mean radial velocity profiles (Ahmed, 1997)

7.3.3 Swirl (*w*) velocity profiles

Swirl velocity profiles show that peak swirl velocities occur at the burner exit. Figure 7.17 shows decay of swirl velocity profiles for 1.6d pitch, of both chequerboard and columnar configurations.

Swirl velocity profiles across the central burner are identical for both configurations at the burner exit. This is because the central burner is of clockwise orientation in both chequerboard and columnar configurations. However, figure 7.17a shows peak swirl velocities generated at the exit of the two side burners are slightly higher for the chequerboard configuration than for the columnar. This is expected, since the chequerboard configuration has burner columns with alternating burner swirl where jets tend to combine, whilst the columnar configuration has burner columns with the same direction of burner swirl (as shown in figure 7.1), resulting in jets pushing each other apart. As the flow moves into the furnace, swirl velocity profiles decay rapidly, while the swirl velocities become more radially distributed.

Allen (1970) observed the same phenomena when he investigated multiple burner flows for the chequerboard and columnar configurations. He found that the shear stresses in the 'out-of-mesh' (columnar) configuration are typically higher than in the 'in-mesh' (chequerboard) configuration, resulting in higher axial and swirl velocity components in the latter case.

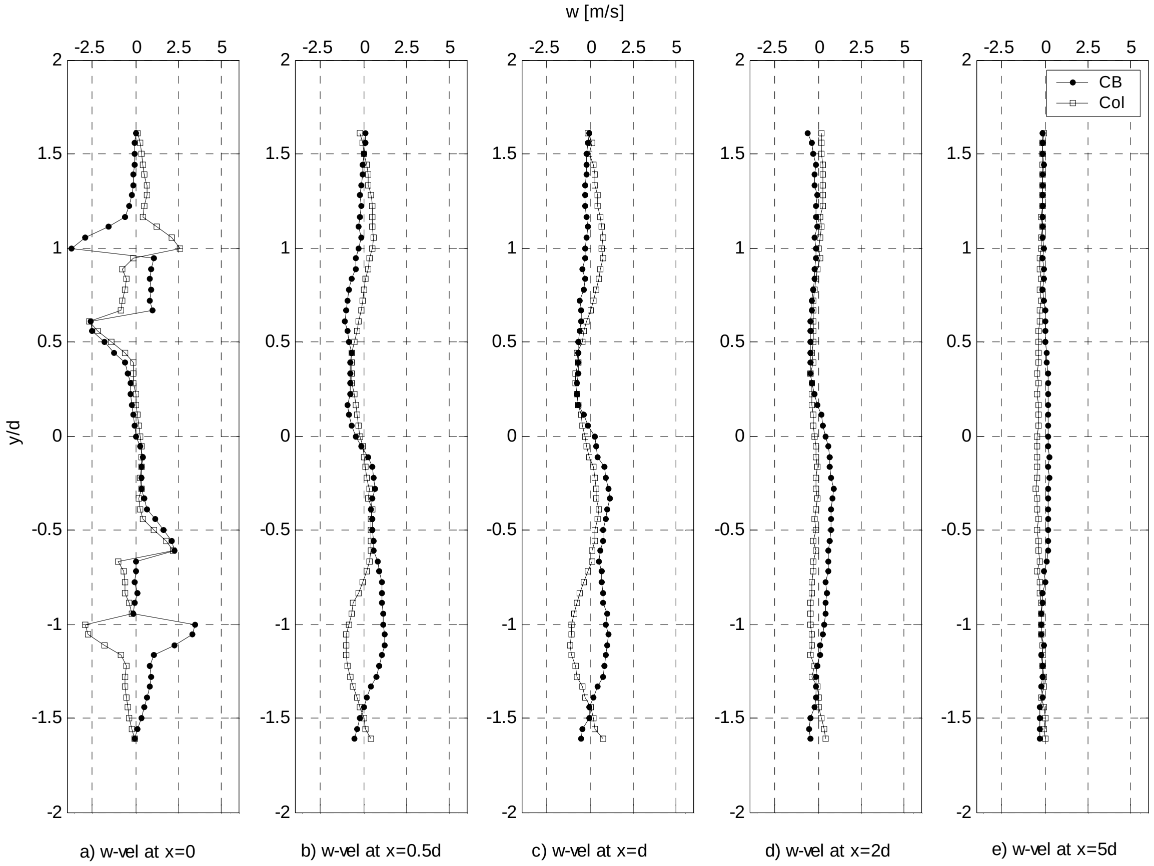

Figure 7.17 Vertical profiles of w velocity, taken for 1.6d pitch of chequered board and columnar configurations at x=0d, 0.5d, d, 2d and 5d distances from the burner panel.

Figure 7.18 shows swirl velocity profiles for 2d pitch of both configurations. Segment a) of this figure shows swirl velocities at the burner exit. They are very similar to those obtained for the 1.6d pitch. This is expected, since the measurements are taken at the burner wall, before any flow interaction between the adjacent burners takes place. As was the case for the 1.6d pitch, swirl velocities were higher for the chequerboard configuration than for the columnar. However, as the flow moves away from the burner wall, swirl velocity profiles decay even more rapidly than for the 1.6d pitch.

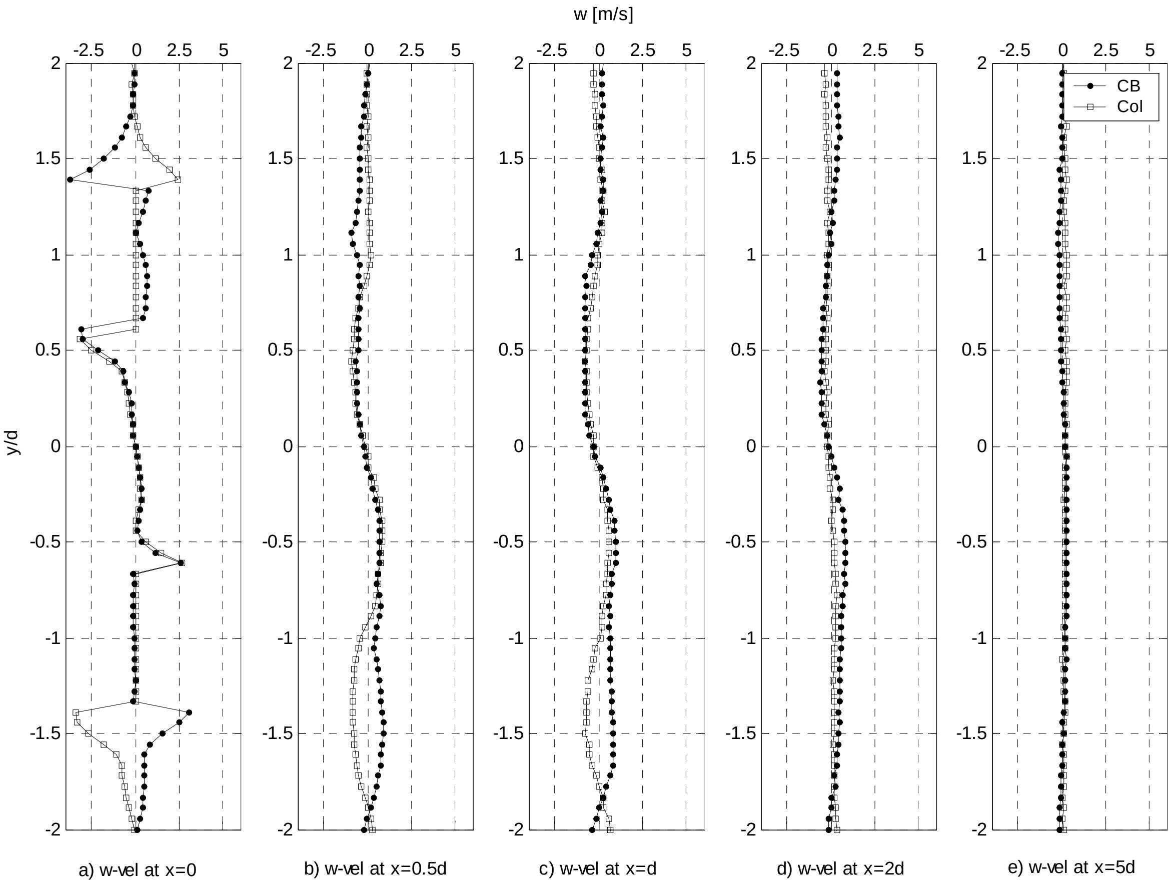

Figure 7.18 Vertical profiles of w velocity, taken for 2d pitch of chequered board and columnar configurations at x=0d, 0.5d, d, 2d and 5d distances from the burner panel.

Figure 7.10 shows results of the research carried out by Kihm et al. (1990). The right-hand side of the figure shows swirl velocity profiles for a single burner at the swirl angle of 40°. The development of the profile, as the flow moves away from the burner wall, is similar to the swirl velocity profiles found in this research and presented in figures 7.17 and 7.18.

Aroussi et al. (2000) also measured swirl velocity component at the burner exit (figure 7.19), showing a very similar velocity profile to those obtained in this research.

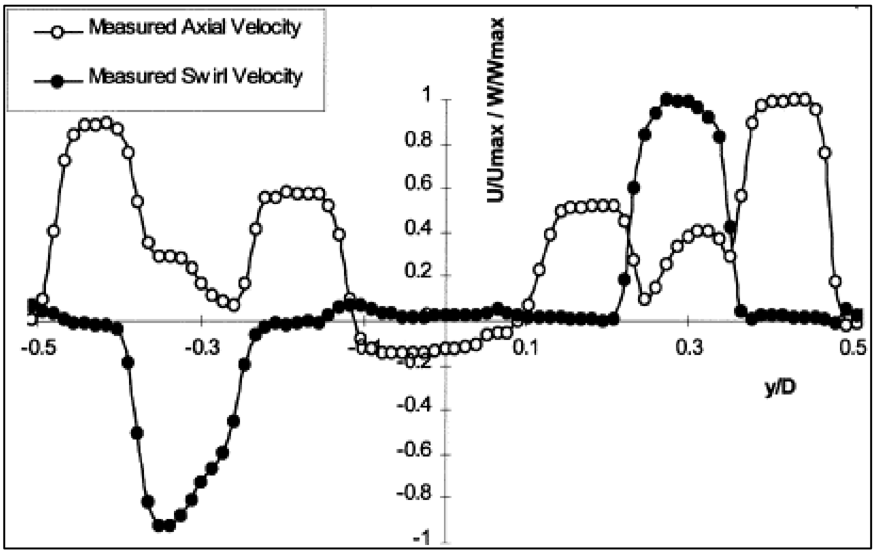

Figure 7.19 Measured axial and tangential velocity profiles at the exit of the single burner (Aroussi et al., 2000)

7.3.4 Turbulent kinetic energy (k)

Swirl flows are characterised by non-isotropic fluctuating components, u′, v′ and w′. The rms fluctuations were measured directly using 3D LDA. The extent of non-isotropic turbulence was examined for 1.6d and 2d pitches of both configurations. Results obtained for the 1.6d pitch of the chequerboard configuration are given in figure 7.20[*]. The figure shows that, at the burner exit, the u′ and w′ fluctuating components of velocity are of similar magnitude, but greater than v′, thus implying that turbulent burner flow is highly anisotropic. Allen (1970) observed the same behaviour when he analysed turbulence characteristics of a single burner with S=0.6. Profiles of turbulence fluctuations taken at axial stages beyond x=0.5d, however, show an increase in isotropic behaviour of the fluctuating components.

---

[*] Results obtained for 1.6d pitch columnar and 2d pitch chequerboard and columnar configurations are given in Appendix D.

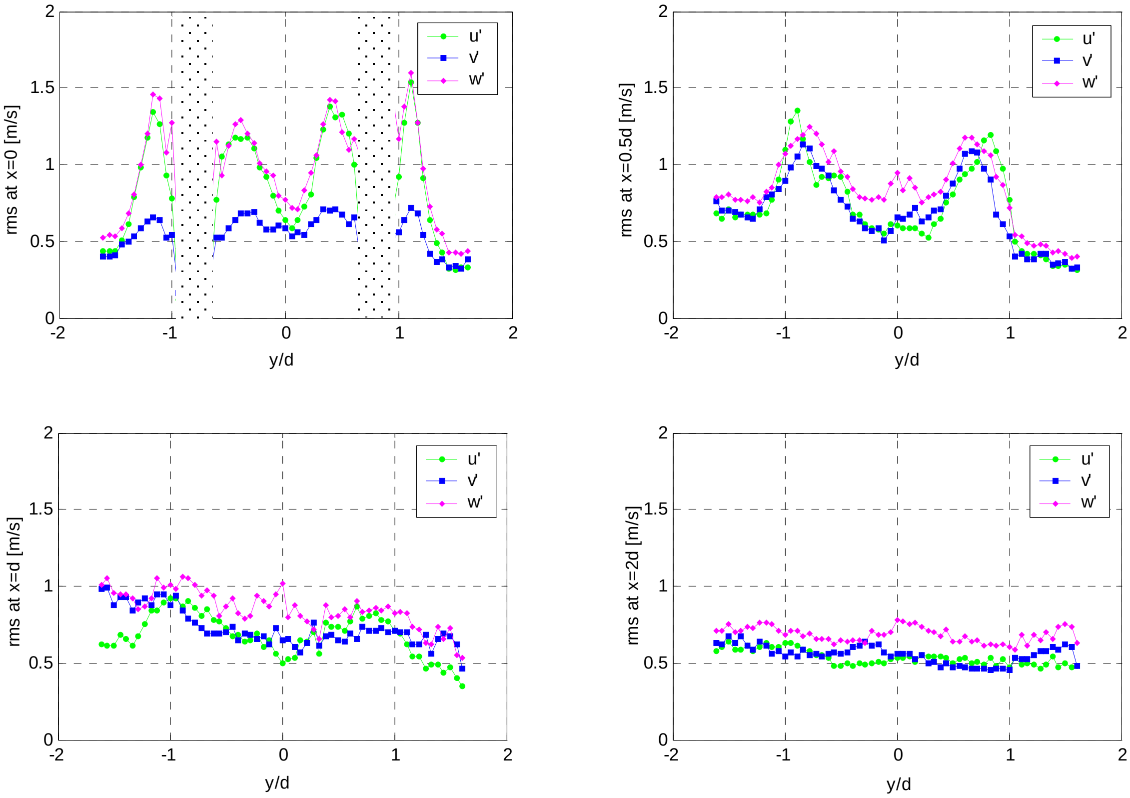

Figure 7.20 RMS fluctuations in three dimensions, u′, v′ and w′, taken for 1.6d pitch of chequered board configuration at x=0, 0.5d, d and 2d distances from the burner panel

Chigier and Dvorak (1975) also examined the extent to which the turbulence is isotropic by comparing rms fluctuating components for flame and cold conditions. They discovered that under cold conditions isotropy was found at x=d (figure 7.21b), over a substantial portion of the cross-section of the jet, with some deviation occurring at the outer edges, where radial components are largest and axial components are smallest. For comparison, figure 7.21a shows the three fluctuating components obtained for 1.6d chequerboard configuration at x=d, indicating that the results of this research are in relative agreement with Chigier and Dvorak’s results.

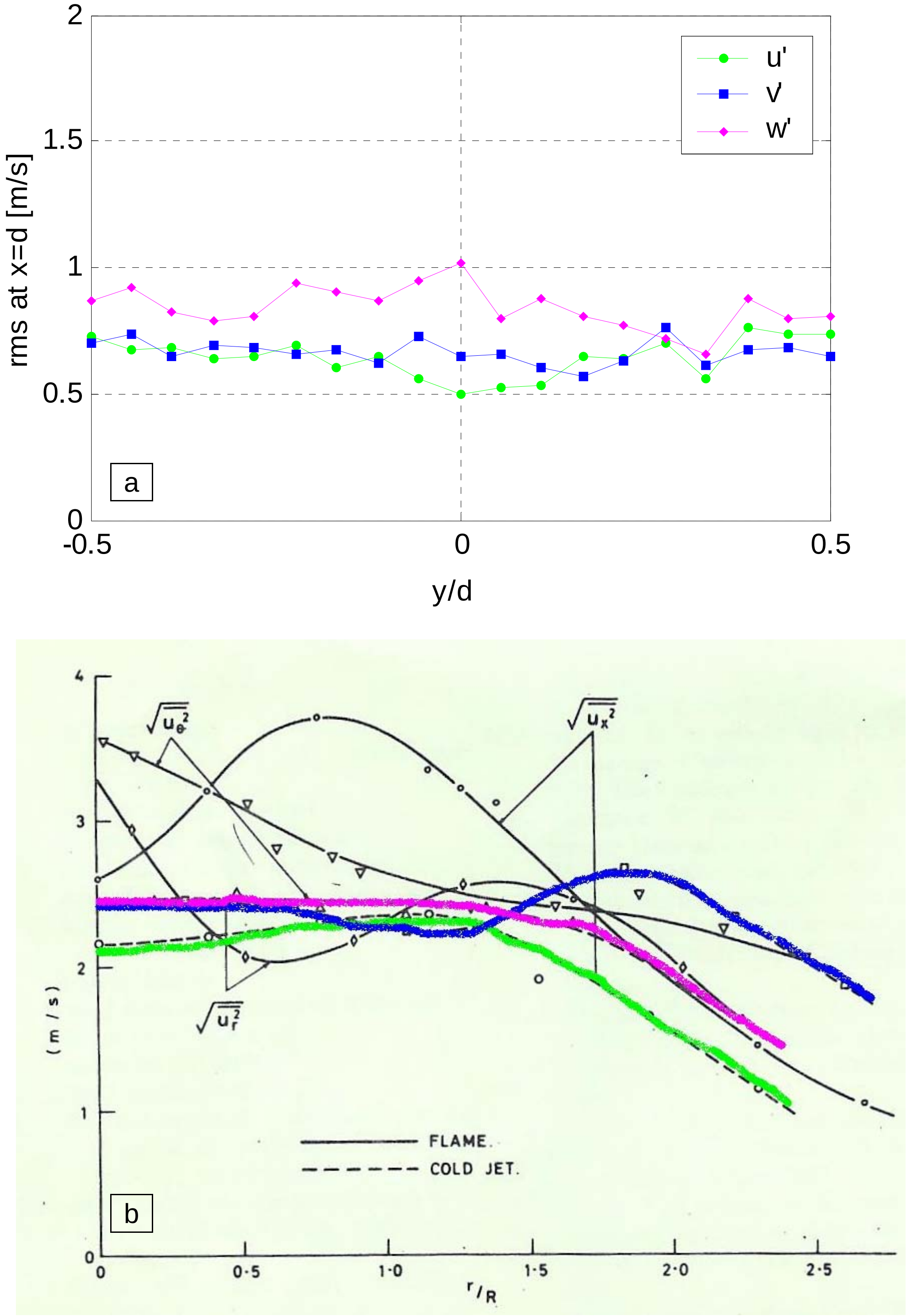

Figure 7.21 RMS fluctuations in three dimensions, u', v' and w', taken at x=d for a) 1.6d pitch of chequered board configuration across the central burner and b) a single burner by Chigier and Dvorak (1975)

Directly measured fluctuating components of the turbulence were used to calculate turbulent kinetic energy. Turbulent kinetic energy per unit mass was calculated using the following formula:

$$k = 0.5(\overline{u'^2} + \overline{v'^2} + \overline{w'^2})$$

where, *u′, v′ and w′* are fluctuating components of axial, radial and swirl velocity respectively.

Profiles of turbulent kinetic energy taken at different axial stages are given in figure 7.22, for 1.6d pitch and figure 7.23, for 2d pitch. Profiles show dissipation of turbulent kinetic energy, as flow moves away from the burner wall. Analysis of the turbulent kinetic energy profiles at x=0.5d shows that the differences between the chequerboard and columnar configurations are more evident at the merging points of central and upper burner jets than the central and lower burners, especially in the case of the 1.6d and pitch. Whilst the levels of turbulence for the two configurations are relatively even across the bottom half of the vertical traverse, they appear much higher for the columnar configuration (and lower for the chequerboard) across the top half of the traverse. It is unclear as to why the levels of turbulence are higher across the top burner in the case of the columnar, and lower in the case of the chequerboard configuration. Kucukgokoglan and Aroussi (2001), came across a similar phenomenon in their experimental study of multi-burner interactions of four burners arranged on a 2x2 array. They found that the decay of the swirl is not symmetrical and invariably one burner dominates and sustains swirl for longer, however, they gave no explanation for such behaviour.

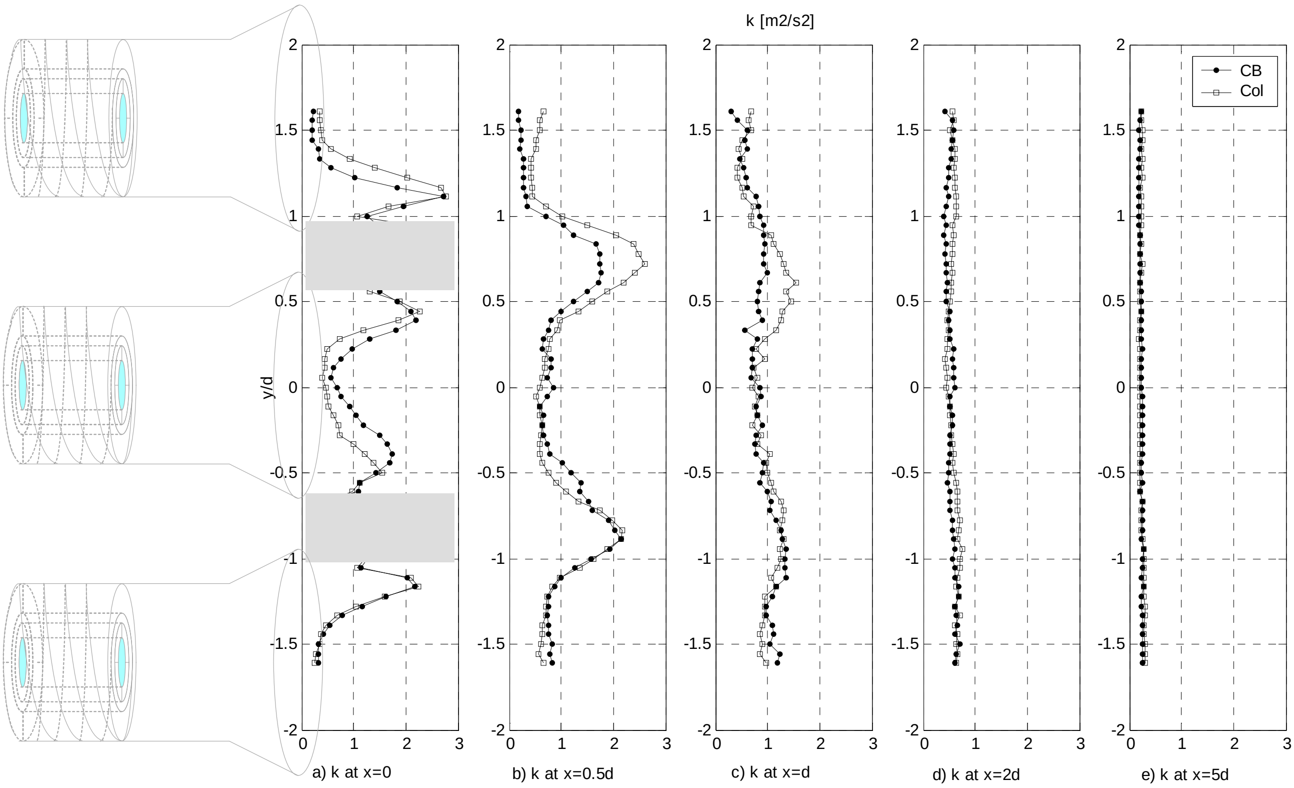

Figure 7.22 Vertical profiles of turbulent kinetic energy, k, taken for 1.6d pitch of chequered board and columnar configurations at x=0, 0.5d, d, 2d and 5d distances from the burner panel

Distribution of the kinetic energy profiles for the 2d pitch (at x=0.5d distance) are relatively evenly matched across the top and bottom half of the traverse, for both configurations (Figure 7.23).

Figures 7.22a and 7.23a show that the highest values of turbulent kinetic energy distributed radially occur at the burner exit. This is in line with Chigier and Dvorak (1975) and Kihm et al. (1990) studies, both of which found the highest values of turbulent kinetic energy at the burner exit (figures 7.24 and 7.25). They conducted studies on a single burner, where they found that levels of turbulent kinetic energy dissipate as flow moves away from the burner exit.

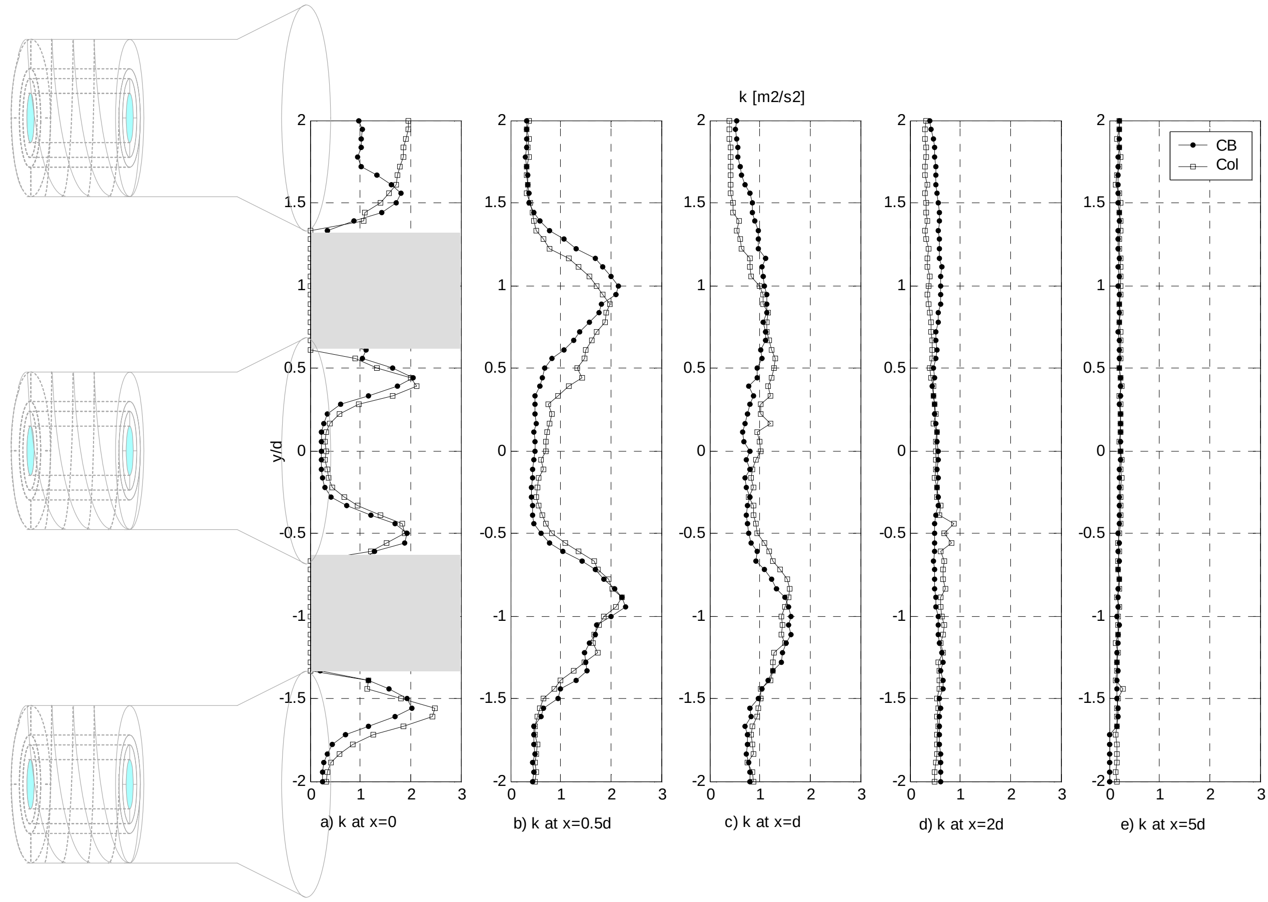

Figure 7.23 Vertical profiles of turbulent kinetic energy, k, taken for 2d pitch of chequered board and columnar configurations at x=0, 0.5d, d, 2d and 5d distances from the burner panel.

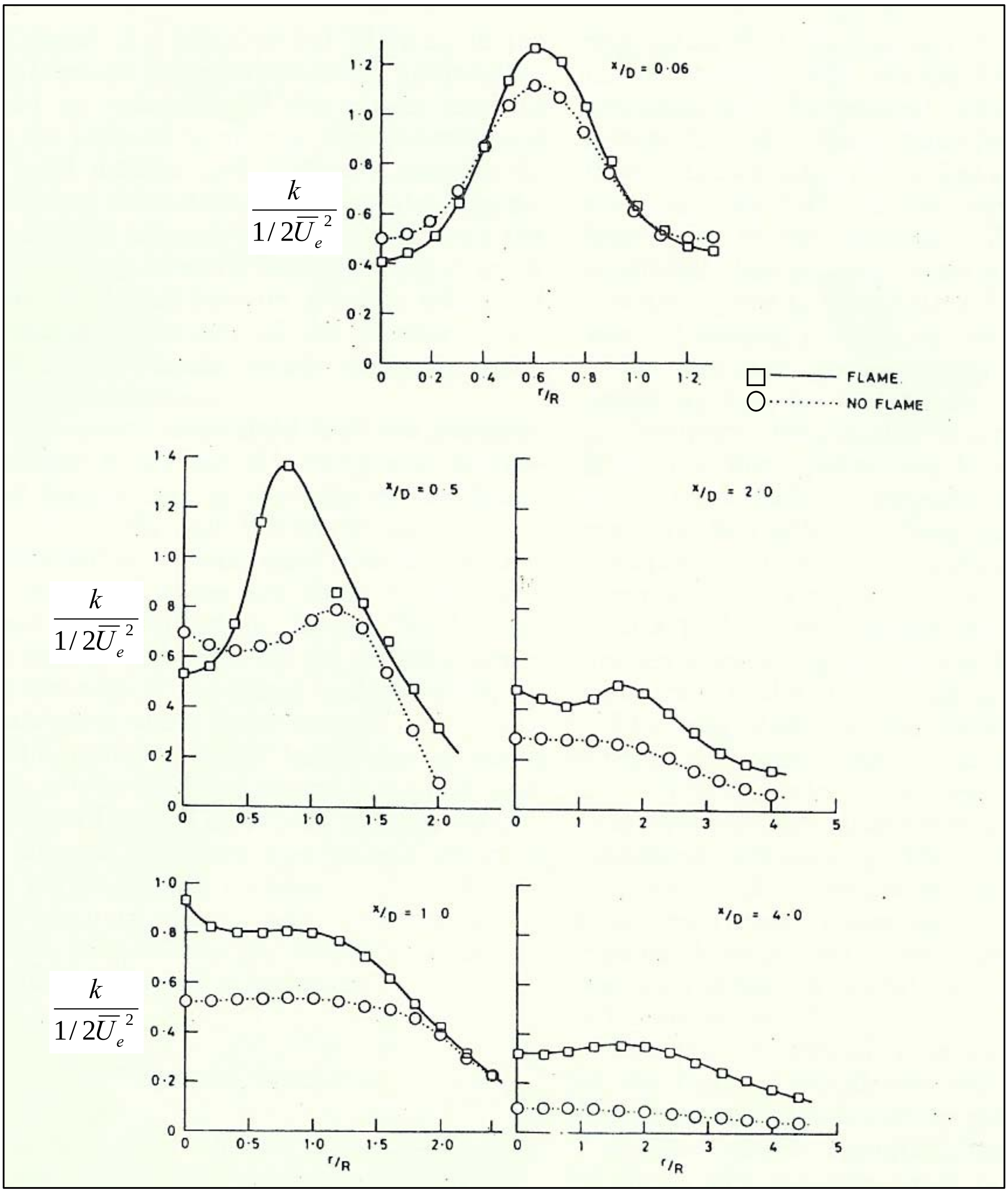

Figure 7.24 Radial profiles of turbulent kinetic energy at various axial stations (Chigier and Dvorak, 1975)

The turbulent kinetic energy profiles for 1.6d and 2d pitches of both configurations along the central burner axis (figure 7.25) show that the area of maximum turbulent kinetic energy occurs approximately at a distance of x=d from the burner exit. This is in disagreement with Chigier and Dvorak's (1975) findings, which indicates that the maximum levels of turbulent kinetic energy occur at x=0.5d. It is likely that this disagreement is due to the effect of burner mixing, which is absent from Chigier and Dvorak's (1975) experiments, since they used a single burner set-up. The shape of Chigier and Dvorak's profile is similar to profiles obtained in this research.

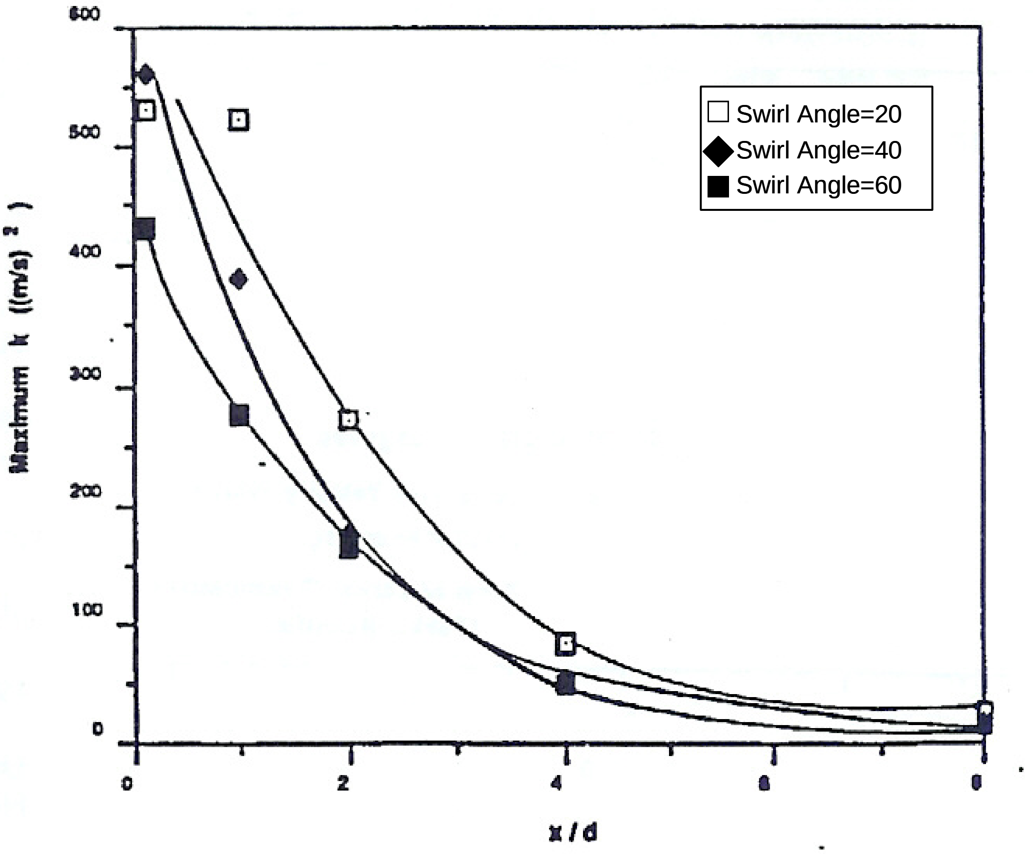

Figure 7.25 Decay of kinetic energy along x/d (Kihm et al., 1990)

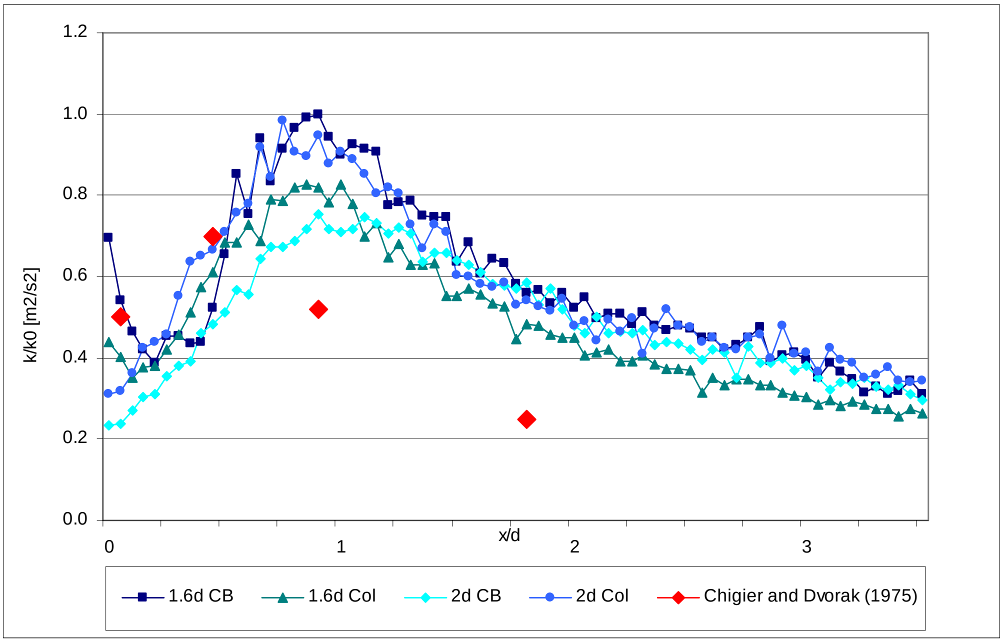

Figure 7.26 Horizontal profiles of turbulent kinetic energy, k, taken for 1.6d and 2d pitches of chequered board and columnar configurations along x-axis plotted against Chigier and Dvorak' (1975) results for a single burner

7.3.5 Reynolds stresses

The Reynolds shear stress arises from the correlation of two components of the velocity fluctuation at the same point (Tritton, 1977). Historically, due to the lack of accurate measurement technology, it was difficult to obtain accurate turbulence measurements, in comparison to the relative ease of measuring mean velocities (Lilley and Chigier, 1970).

Laser measurement technology available for this research enabled direct measurement of Reynolds stresses. Figures 7.27 and 7.28 show Reynolds stresses (u'v', u'w' and v'w'), taken for 1.6d and 2d pitches, respectively, of both configurations at the burner exit. This position was chosen so that the results can be compared with previous research.

Other positions along the x-axis (x=0.5d, d and 2d) have also been plotted and are presented in Appendix D.

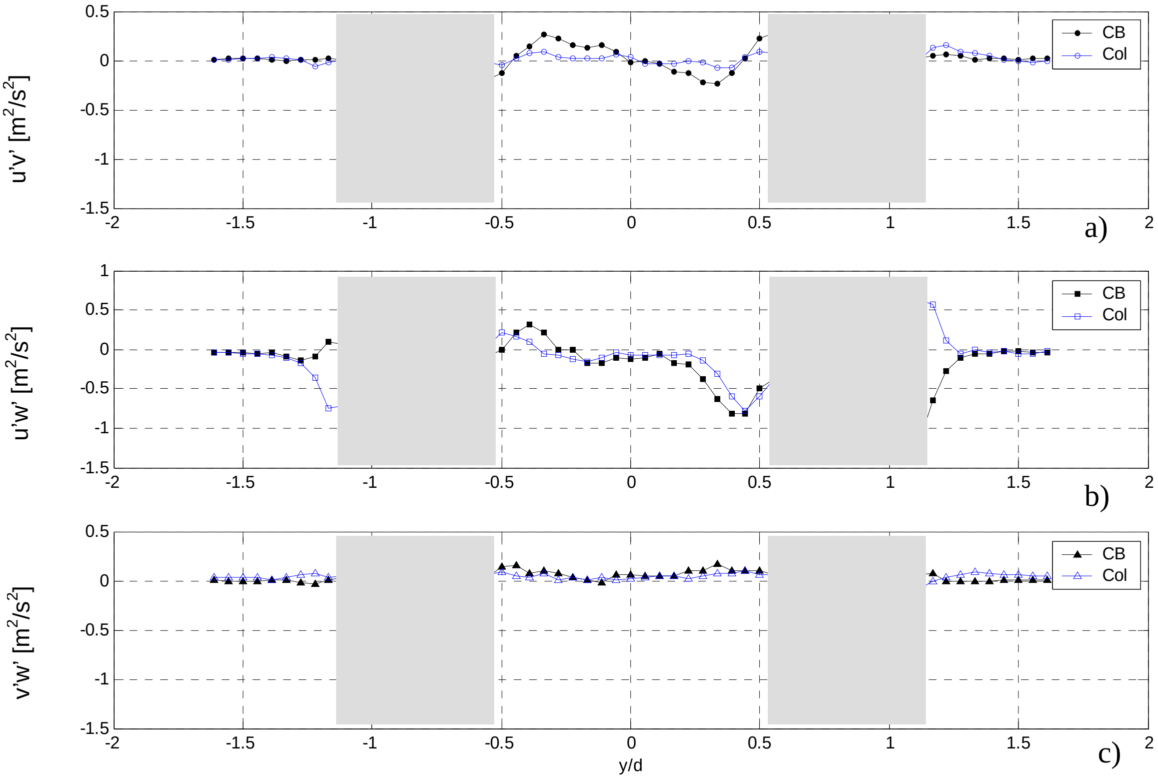

Figure 7.27 Reynolds stresses, u'v', u'w' and v'w', taken for 1.6d pitch of chequerboard and columnar configurations at the burner exit, x=0

Figures 7.27a and 7.28a show radial distributions of the axial Reynolds stress term, u'v'. This is the turbulent shear stress component that would be generated even if there was no swirl (Kihm et al, 1990). The turbulent shear stress profiles have both positive and negative values associated with the mean positive and negative gradients of the mean velocity profiles. Distribution of axial Reynolds stress term, u'v', can be directly related to axial (*u*) and radial (*v*) velocity profiles presented in figures 7.6, 7.8 and 7.15. Therefore, in the recirculation zone across the central burner where the axial velocity gradient is negative and the radial velocity gradient is positive, the axial shear stress is negative (i.e. if u'<0 and v'>0 then u'v'<0). The axial shear stress in positive in the region where the axial velocity gradient is negative, and the radial velocity gradient is negative (i.e. if u'<0 and v'<0 then u'v'>0).

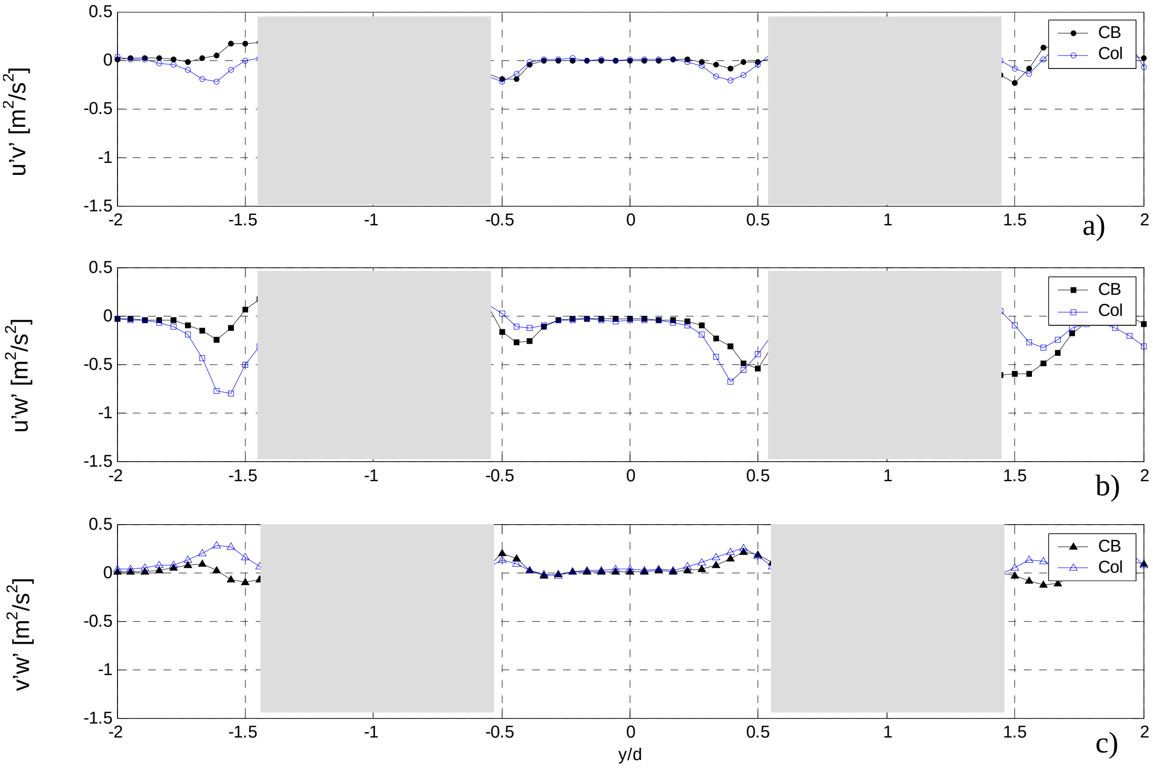

Figure 7.28 Reynolds stresses, u'v', u'w' and v'w', taken for 2d pitch of chequerboard and columnar configurations at the burner exit, x=0

At the burner exit, the radial distribution of tangential shear stress, u'w', (figures 7.27b and 7.28b) shows much higher peak values than for the axial shear stresses, illustrating the importance of the role the tangential shear plays in the swirling flow. This applies to both 1.6d and 2d pitches.

Axial and tangential stress profiles obtained by Kihm et al. (1990) are shown in figure 7.29. Similar to the findings of this research, presented above, they also found that axial shear stress profiles have both positive and negative peaks and that the tangential stresses are more significant in the shear flowfield, relative to the axial shear stresses.

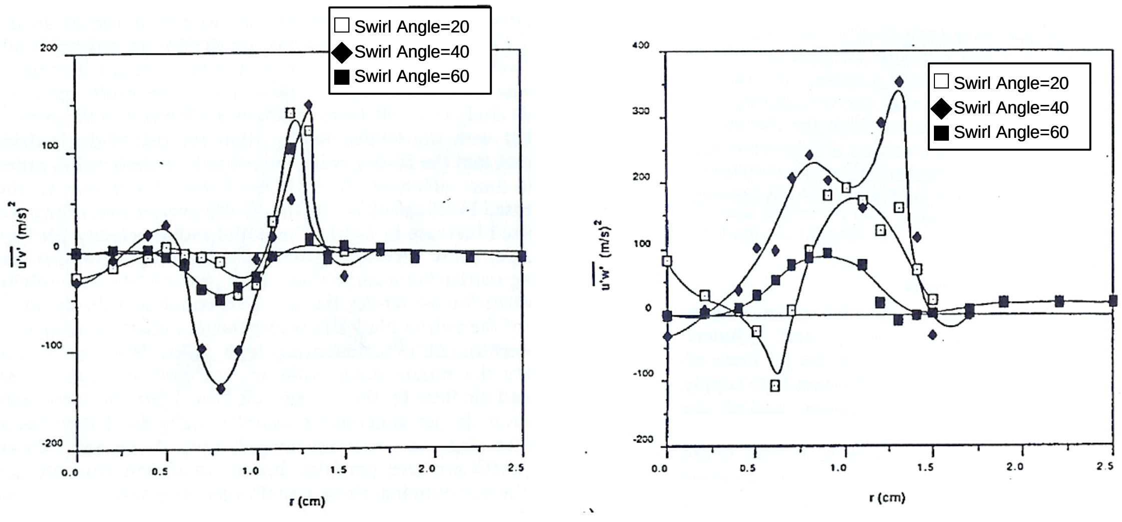

Figure 7.29 Axial and tangential Reynolds stresses at x/d=0.1 (Kihm et al, 1990)

Figure 7.30 shows that the maxima of tangential shear decay faster than those of axial shear. The same behaviour for the decay of the axial and tangential shear maxima was observed by Kihm et al (1990) (figure 7.31).

Figures 7.27c and 7.28c show profiles of the Reynolds shear stresses, correlating the radial and swirl fluctuating components, v'w'. The figure shows that that the v'w' stress component is the weakest of the three shear stress components. However, this shear stress terms is still significant, especially at the burner exit, where the mean radial velocity component has the highest magnitude.

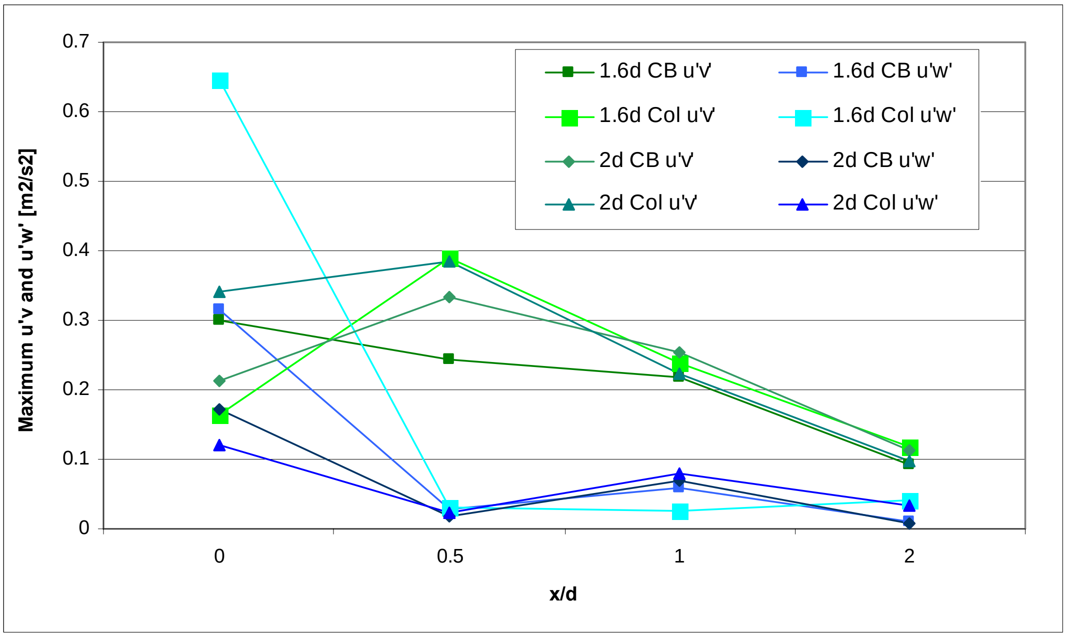

Figure 7.30 Decay of Reynolds stresses, u′v′ and u′w′ at four stations along the x-axis

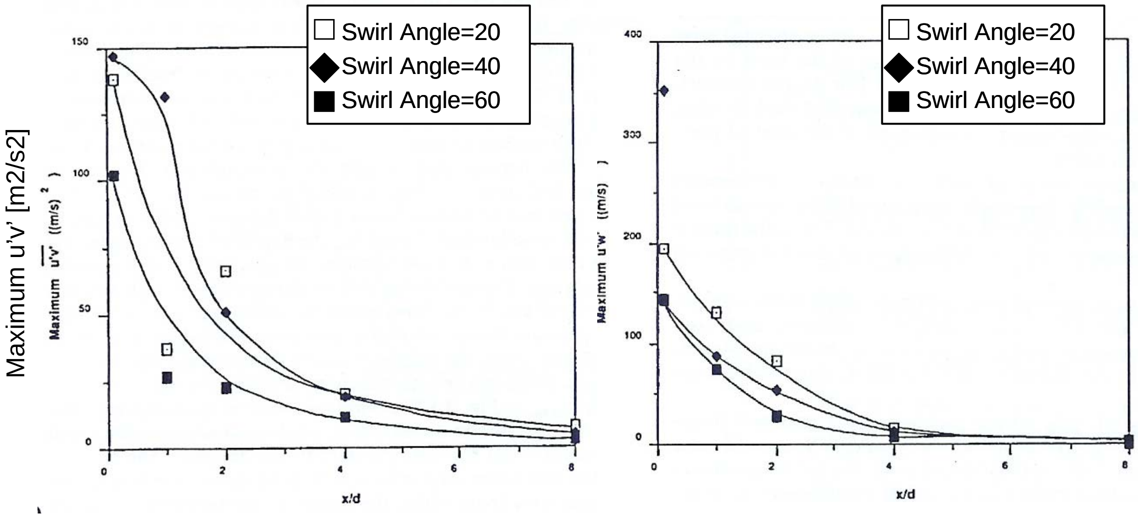

Figure 7.31 Decay of Reynolds stresses, u′v′ and u′w′ at various stations along the x-axis (Kihm et al., 1990)

Figure 7.7 showed that the strongest recirculation occurs close to the mouth of the burner, for both 1.6d and 2d pitches and both configurations. Plotting axial and tangential shear stress components along the central burner line (figure 7.32a-b) shows that stresses are relatively low for 0<x/d<0.5, and then suddenly increase in intensity. This indicates that the stresses are influenced by the recirculation zone and that the stress magnitudes increased closer the exit of the recirculation zone.

Similar finding has been observed by Al-Abdeli and Masri, 2003, who carried out 2-D LDA measurements on a single burner. Figure 7.33 shows radial profiles of axial and tangential shear stresses, at different axial stations. Ali-Abdeli and Masri concluded that both these stresses show that they are higher outside the recirculation zone and this is attributed to the significant velocity gradients occurring near the centreline.

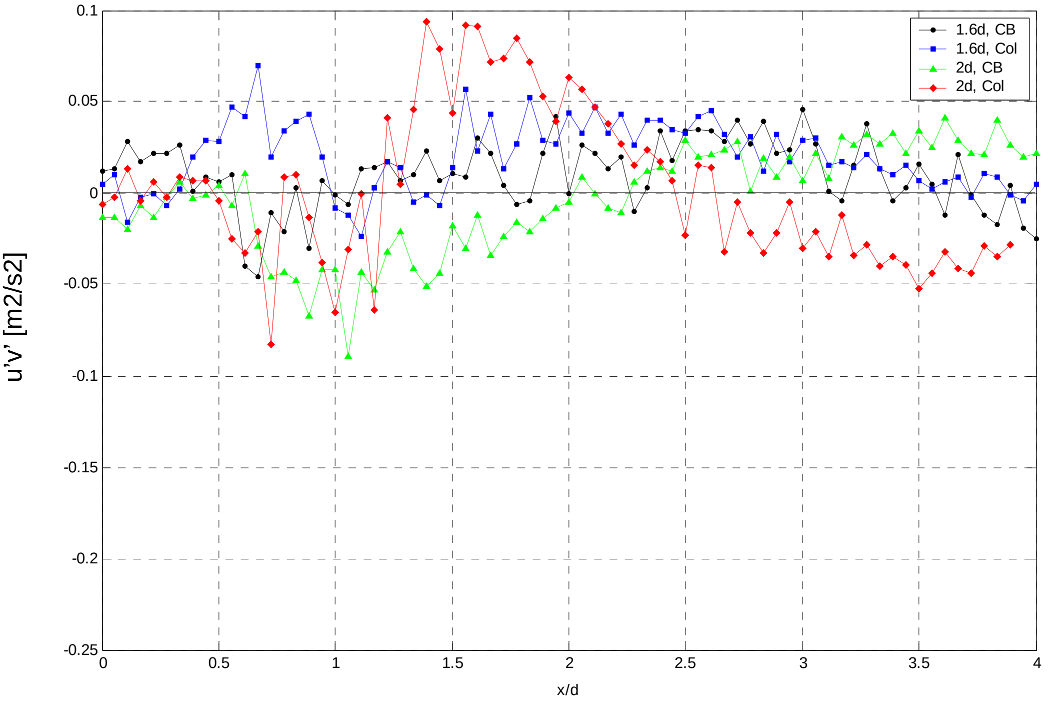

a)

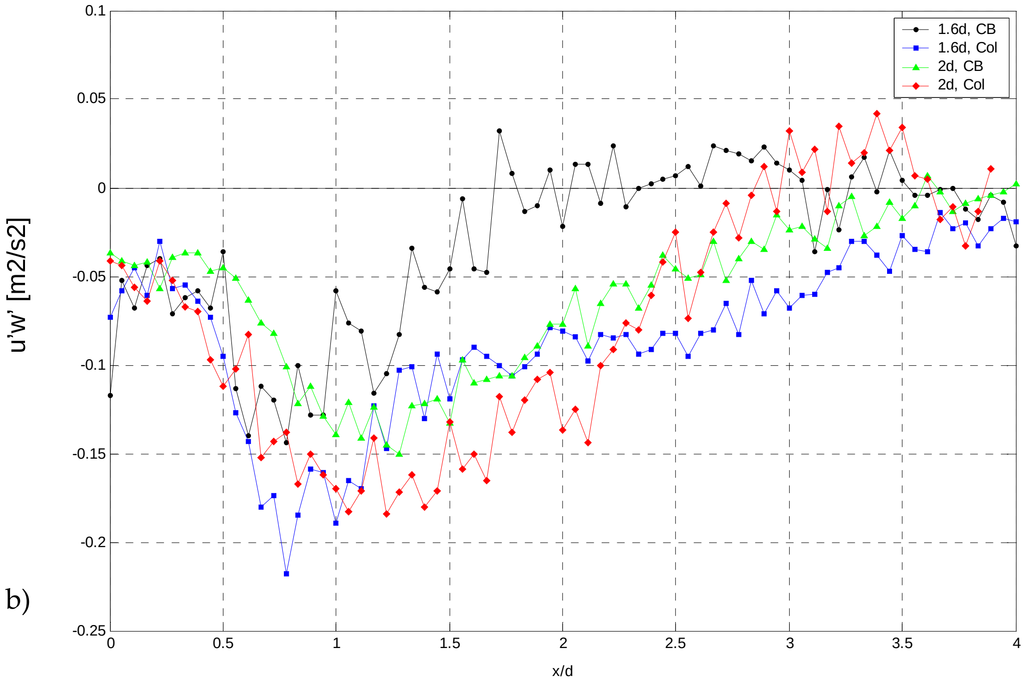

Figure 7.32 Axial (a) and tangential (b) Reynolds stresses along the central burner line taken for 1.6d and 2d pitches of both chequerboard and columnar configurations

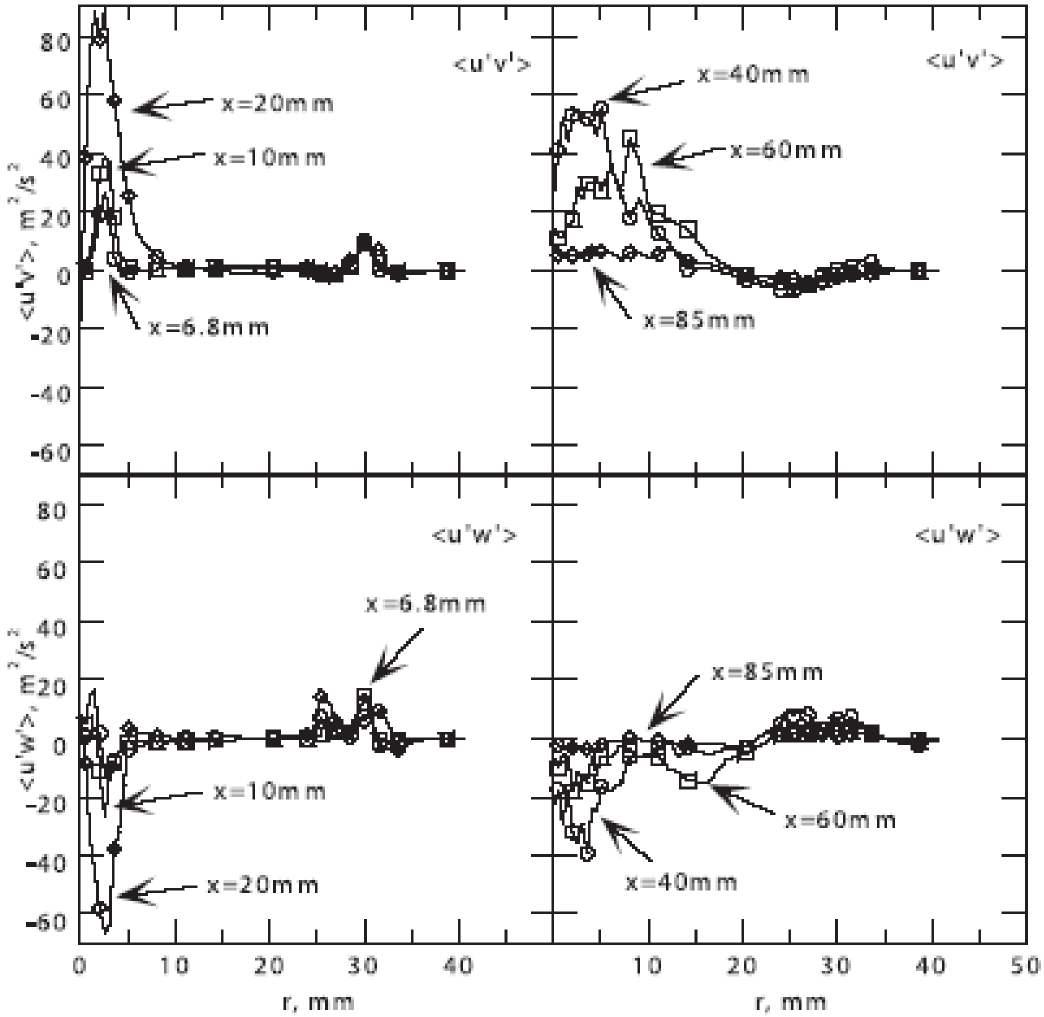

Figure 7.33 Radial plots of shear stresses in swirling flame (Al-Abdeli and Masr, 2003)

7.4 Conclusions

1. Flow visualization analysis showed that the burner jet interaction is directly related to the pitch size. For 1.6d pitch, interaction between adjacent burner flows occurred almost immediately upon leaving the burner exit.

2. The analysis of axial velocity profiles obtained using 3-D LDA showed that a decrease in pitch from 2d to 1.6d causes the width of the recirculation zone, measured at 0.5d distance from the burner exit plane, to decrease by 20% for the chequerboard configuration and 7% for the columnar configuration. It was found that a decrease in pitch from 2d to 1.6d causes the extent of the recirculation, measured along the central burner line, to decrease by 45% for the chequerboard configuration and 26% for the columnar configuration.

It was found that the effect of burner configuration is much more evident in the case of the 1.6d pitch than 2d pitch. For 1.6d pitch, both the width and the extent of recirculation are higher in the columnar configuration case by 10% and 25% respectively. The opposite trend is observed for 2d pitch, where both the width and the extent are lower for the columnar configuration, but only by 4% and 1% percent respectively. The effect of configuration on the wider, 2d pitch, is insignificant.

3. The analysis of the radial velocity profiles showed peak values occurring at the edges of the burner quarl, at the burner exit. Downstream of x=0 axial position, radial velocity profiles became insignificant in both shape and magnitude.

4. Swirl velocity profiles decayed faster for the 2d pitch than for the 1.6d pitch, as the flow moved away from the burner exit. It was found that swirl velocities, measured at the burner exit, were higher for the chequerboard configuration than for the columnar, for both 1.6d and 2d pitches.

5. The analysis of fluctuating components, u′, v′ and w′ showed that the burner flow is highly anisotropic at the burner exit. Profiles of turbulence fluctuations taken at axial stages beyond x=0.5d, however, show an increase in isotropic behaviour of fluctuating components.

6. The analysis of the turbulent kinetic energy profiles showed that differences between the chequerboard and columnar configurations were more evident across the central and upper burner than the lower burner, for both 1.6d and 2d pitches. The turbulent kinetic energy magnitudes peaked at the burner exit, while the profiles decayed downstream of x>0.5d.

7. At the burner exit, the radial distribution of tangential shear stress, u'w', showed much higher peak values than the axial shear stresses, illustrating the importance of the role the tangential shear plays in the swirling flow. The maxima of tangential shear decayed faster than those of axial shear. This applied to both 1.6d and 2d pitches. It was found that v'w' stress component is the weakest of the three shear stress components; however, it is still significant, especially at the burner exit, where the mean radial velocity component has the highest magnitude.

8. It was found that that the shear stresses are influenced by the recirculation zone and that the stress magnitudes increased closer the exit of the recirculation zone.

Chapter 8

Numerical modelling results

Numerical modelling results were obtained using three different turbulence models: k-ε, k-ω and Reynolds Stress Model (RSM). Details of the models are described in chapter 6. The velocity profiles generated from these numerical models, as well as turbulent quantities, such as turbulent kinetic energy and Reynolds stresses were analysed and compared with the experimental data in order to identify the numerical model that provides the best match to the experimental data. The numerical results are also discussed with respect to the previously published work.

8.1 Axial (*u*) velocity profiles

8.1.1 Vertical traverse

Figures 8.1, 8.2, 8.3 and 8.4 show the comparison between the experimental and numerical axial velocity data obtained using the k-ε, k-ω and RSM turbulence models for 1.6d and 2d pitches of chequerboard and columnar configurations.

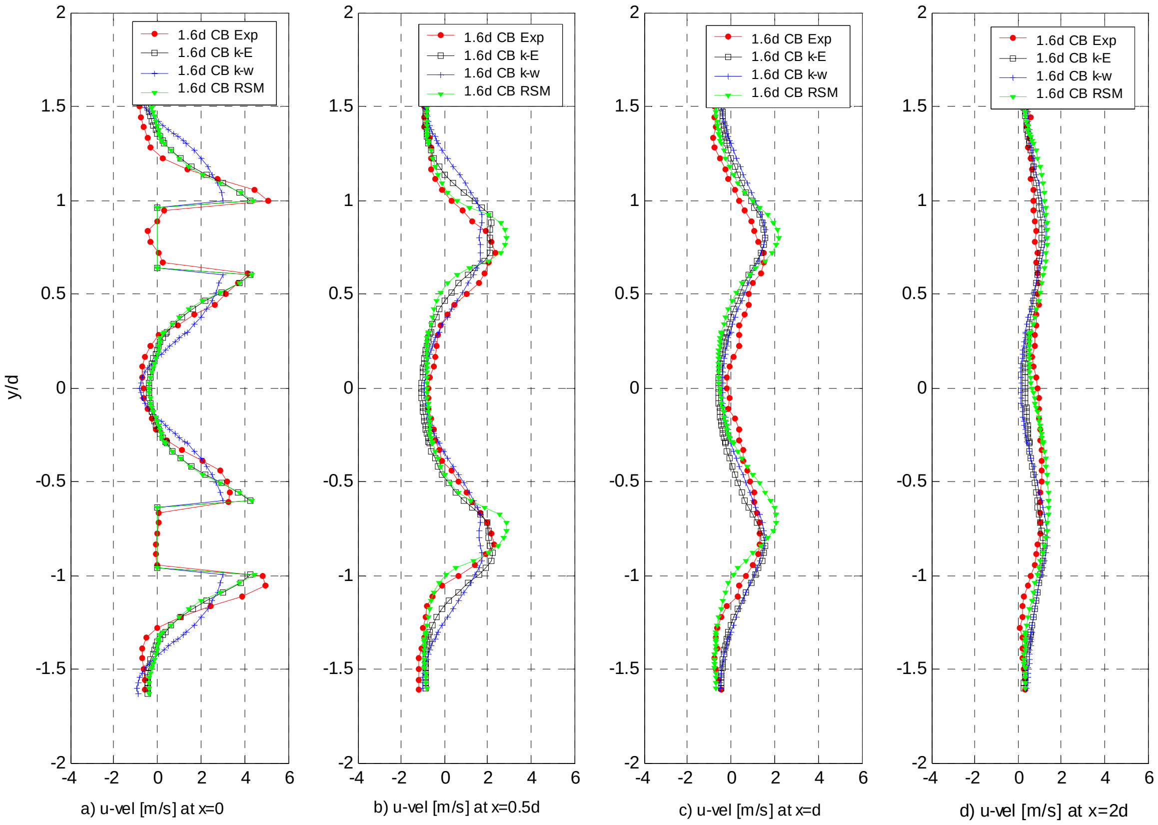

Figure 8.1 Numerical (k-ε, k-w and RSM turbulence models) v experimental comparison of vertical profiles of u velocity in the direction of flow, taken for 1.6d pitch of chequerboard configuration at x=0, 0.5d, d and 2d distances from the burner panel

The vertical velocity profiles in each of the figures are presented at four different positions along the x-axis: 0, 0.5 d, d and 2d distances from the burner exit plane. Since both experimental (chapter 7) and numerical velocity profiles became formless beyond the distance of x=2d, the profiles taken at x=5d have been omitted from comparisons between the experimental and numerical results.

Visual analysis of the four figures gives a clear indication that the k-ω turbulence model gives an inferior fit to the experimental data compared to the k-ε and RSM turbulence models. This is particularly evident at the burner exit for both pitches and configurations. In all four cases, the k-ω turbulence model shows much narrower recirculation zone and smaller peak velocity than measured experimentally. At x=0.5d distance from the burner exit plane, this trend continues, and the k-ω turbulence model still represents the worst fit to the experimental data. However, as the flow moves further away from the burner exit, the match between the experimental data and the k-ω turbulence model improves in all four cases. The consistent underperformance of the k-ω turbulence model could have been caused by either of the two well-known shortcomings of this turbulence model:

Firstly, this model assumes isotropic turbulence (FLUENT 6), which is contrary to the findings presented in the section 7.3.4, chapter 7. The experimental results clearly showed that turbulence is highly anisotropic at the burner exit with isotropy increasing as the flow moves further along the x-axis. This also ties in with improved match between the experimental and numerical results (predicted using the k-ω turbulence model) as the flow moves away from the burner exit, since the model is able to handle prediction of turbulent flows more accurately.

Secondly, Menter (1993) noted a major failing of the basic k-ω model relating to its spurious sensitivity to free-stream conditions. He found that this model is not reliable in flows with detached shear layers.

However, as explained in chapter 3, the k-ε turbulence model also assumes isotropic turbulence (FLUENT 6), but is still able to give relatively good prediction of experimental data, as shown in figures 8.1-8.4. This could be explained by Cazalbou et al. (1994) finding that the k-ε turbulence model has a desirable property of the propagating front solution found near the edge of free-shear flows, which prevents the model's spurious sensitivity to free-stream conditions. It is, therefore, likely that the k-ω turbulence model's spurious sensitivity to free-stream conditions is the main reason for the failure of this model to predict turbulent swirling flow to the same accuracy level as the k-ε turbulence model.

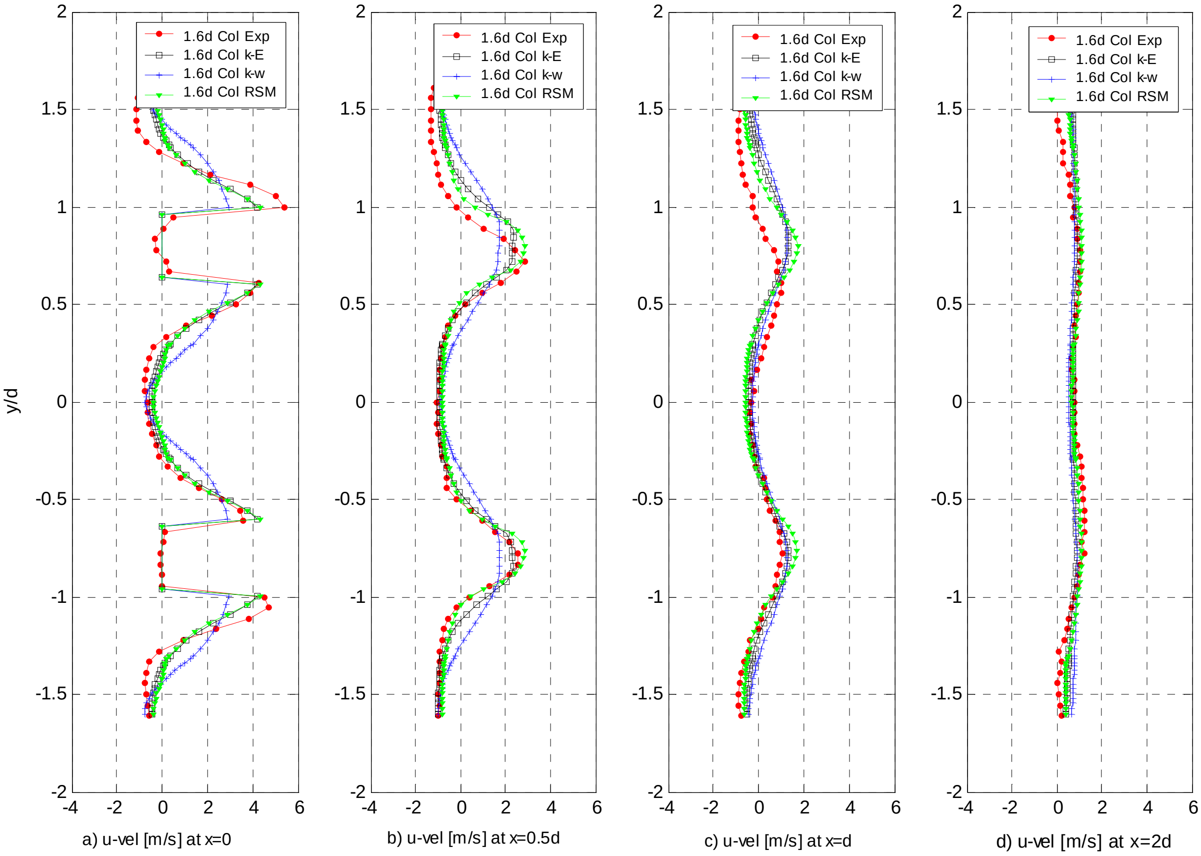

Figure 8.2 Numerical (k-ε, k-w and RSM turbulence models) v experimental comparison of vertical profiles of u velocity in the direction of flow, taken for 1.6d pitch of columnar configuration at x=0, 0.5d, d and 2d distances from the burner panel

Analysis of the remaining two turbulence models, k-ε and RSM, shows that, at the burner exit, there is almost no difference between the two profiles; they virtually overlap each other across the entire vertical traverse (figures 8.1-8.4). The closeness of the match of these two turbulence models to the experimental data appears relatively good in all four cases (i.e. both pitches and both configurations). Whilst the peak velocities seem to be well matched to the experimental data, both the k-ε and RSM turbulence models appear to slightly under-predict the velocities across the recirculation zones.

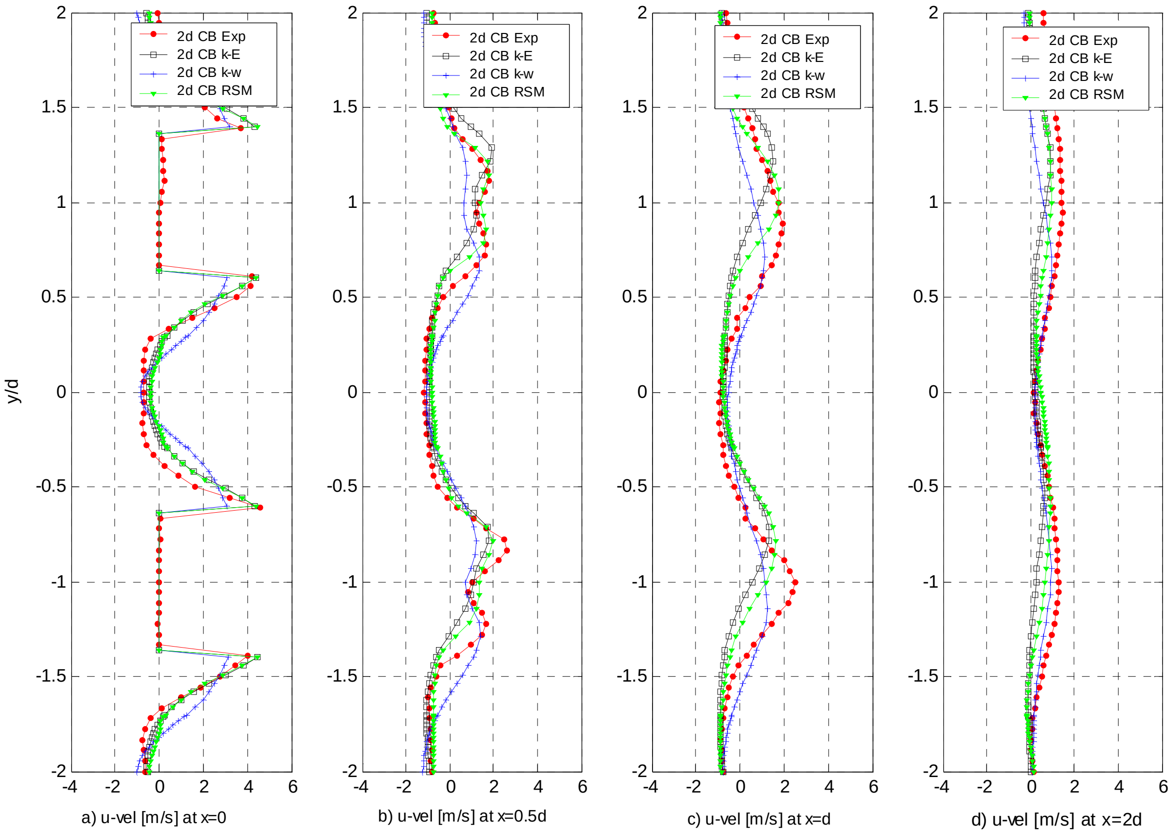

Figure 8.3 Numerical (k-ε, k-w and RSM turbulence models) v experimental comparison of vertical profiles of u velocity in the direction of flow, taken for 2d pitch of chequerboard configuration at x=0, 0.5d, d and 2d distances from the burner panel

A difference between the k-ε and RSM turbulence models compared to the experimental data starts to show as the flow moves away from the burner exit panel. Whilst both models seem relatively accurate in predicting the recirculation areas, the predicted velocity peaks begin to differ from the experimental data from x=0.5d onwards. It appears that, in some cases, a better fit is provided by the k-ε turbulence model and in others by the RSM turbulence model. Overall, however, both models seem to match the experimental data reasonably well, and it is difficult to determine which of the two models provides a better fit just by a visual analysis of the velocity profiles.

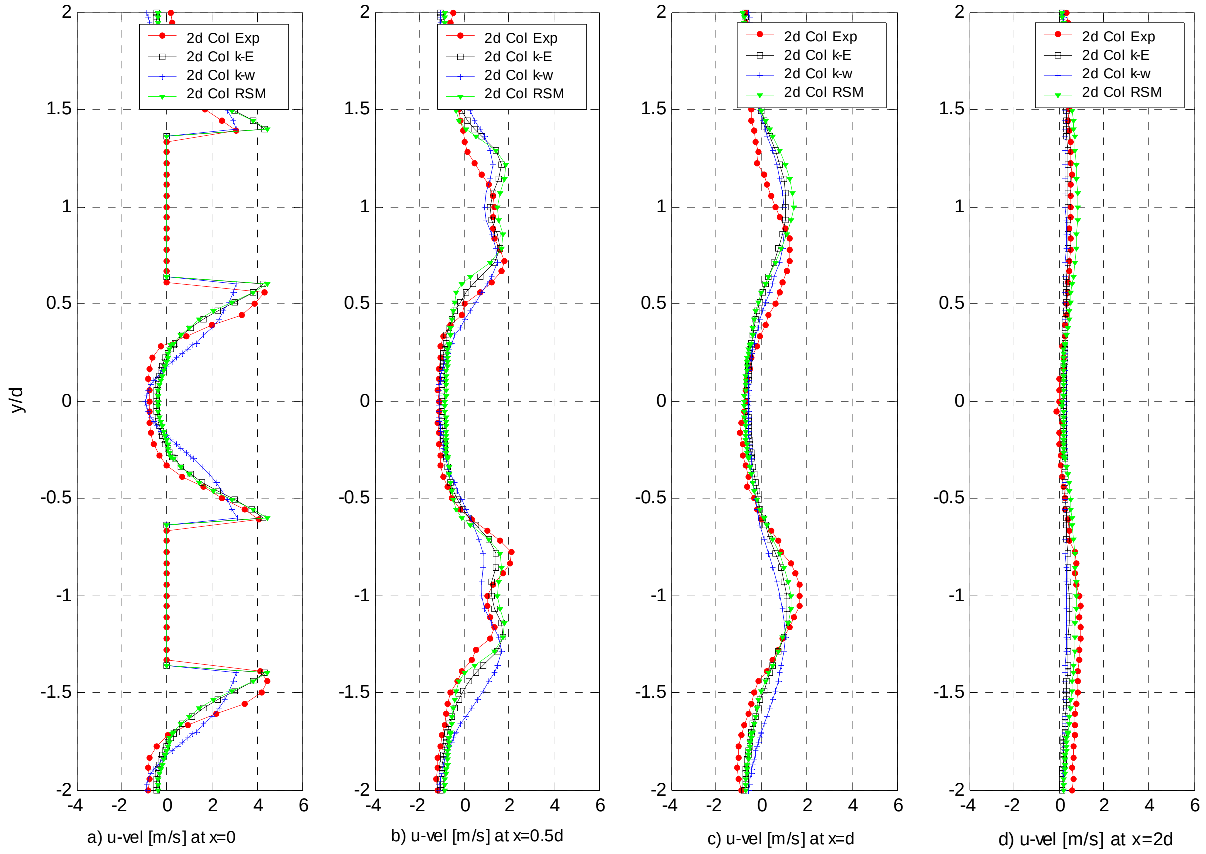

Figure 8.4 Numerical (k-ε, k-w and RSM turbulence models) v experimental comparison of vertical profiles of u velocity in the direction of flow, taken for 2d pitch of columnar configuration at x=0, 0.5d, d and 2d distances from the burner panel

Various other authors, who have previously worked on swirl flow modelling using the k-ε and RSM turbulence models, could not see any consistent advantage in performance of the very complex and computationally expensive RSM model over the simple k-ε turbulence model (Lockwood and Shen, 1994 and Hart et al, 1999).

Tarr and Allen (1997) also evaluated these two turbulence models applied to single burner flow and found that the k-ε model performed as accurately as the RSM, and was therefore adequate for modelling of multiple burner flows. On that basis, both Lockwood and Parodi (1998) and Aroussi (2000) carried out their multi-burner studies using only the k-ε turbulence model.

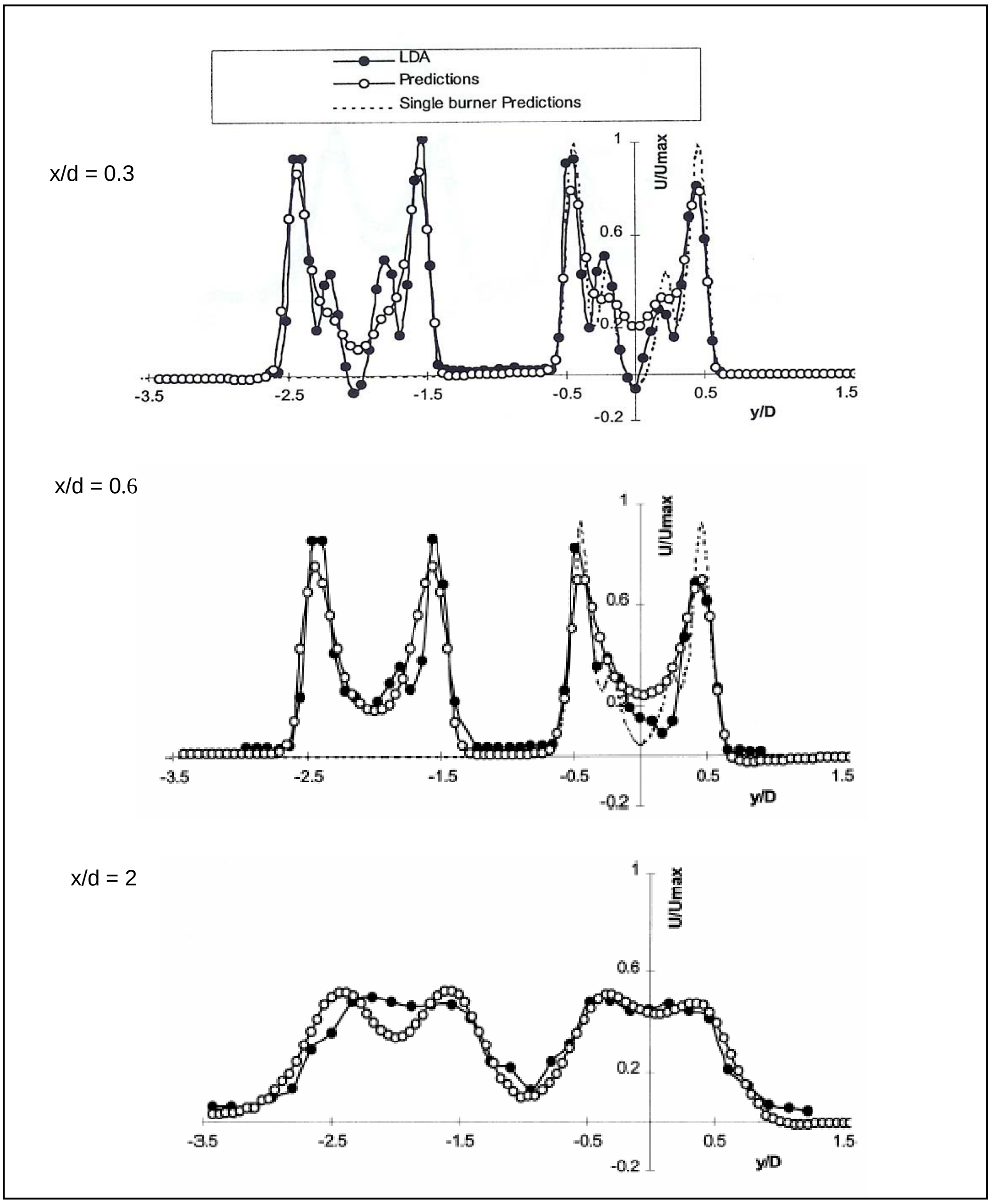

Figure 8.5 Axial velocity profiles at x=0.3d, 0.6d and 2d from the burner exit (Aroussi et al, 2000)

Aroussi et al. (2000) compared the experimental 2D LDA measurements and computational k-ε turbulence model predictions on two burners discharging into the furnace. The burners were arranged on a 3x3 burner panel, with 2d pitch and swirl number of 0.6.

Figure 8.5 shows Aroussi's findings for axial velocity profiles taken at x=0.3d, 0.6d and x=2d distances from the burner exit plane. He concluded that the mixing of multiple swirling jets can be predicted reasonably well using the standard k-ε turbulence model. Aroussi's findings are in line with results of this research presented in figures 8.1-8.4.

It can be seen that the numerical results obtained by Aroussi using the k-ε turbulence model also slightly under-predict experimental velocities across the recirculation zones close to the burner exit (at x=0.3d). However, no direct comparison can be made between Aroussi's results and the results of this research due to different number of burners interacting (Aroussi employed only two burners from the 3x3 grid), different burner design (used burners with triple registers) and higher swirl number (S=0.6). The results can, therefore, be compared only on a qualitative basis.

German and Mahmud (2004) compared the isothermal experimental and numerical axial velocity profiles obtained for a single burner flow (figure 8.6). They used the k-ε and RSM models for the numerical predictions. Their results show that the RSM model accurately predicted the experimentally measured recirculation zone, capturing he subcritical nature of the strongly swirling flow, whilst the k-ε turbulence model failed to do the same.

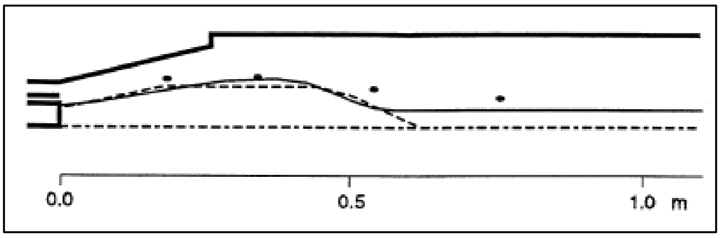

Figure 8.6 Comparisons of measured and predicted IRZ boundaries for isothermal flow (Δ, experimental; - - - , k-ε model; – , RS model) (German and Mahmud, 2004)

8.1.2 Horizontal traverse

Further comparisons of the k-ε, k-ω and RSM turbulence models have been carried out on horizontal axial velocity profiles, and are presented in Figures 8.7 and 8.8.

The k-ω turbulence model was found to consistently provide the most inferior match to the experimental data in all cases, and is therefore not discussed further.

Figure 8.7 shows the experimental and numerical data obtained for the 1.6d pitch of chequerboard and columnar configurations. In the case of the 1.6d pitch of the chequerboard configuration, the extent of the recirculation zone, as well as the velocity decay along the central burner axis, are most closely predicted by the numerical simulation employing the RSM turbulence model. On the other hand, in the case of the columnar configuration, both k-ε and RSM turbulence models provided a close match to the experimentally measured extent of the recirculation zone and the profile of the decaying axial velocity along the central burner axis.

Figure 8.8 shows the horizontal axial velocity profiles for the 2d pitch of both chequerboard and columnar configurations. The analysis showed that the k-ε turbulence model gave the closest match to the experimental data in the case of the 2d pitch of the chequerboard configuration, contrary to the findings for the 1.6d pitch, which showed the RSM model as a better fit. In the case of the columnar configuration, both k-ε and RSM turbulence models provided a close match to the experimental velocity profiles, as was the case for the 1.6d pitch.

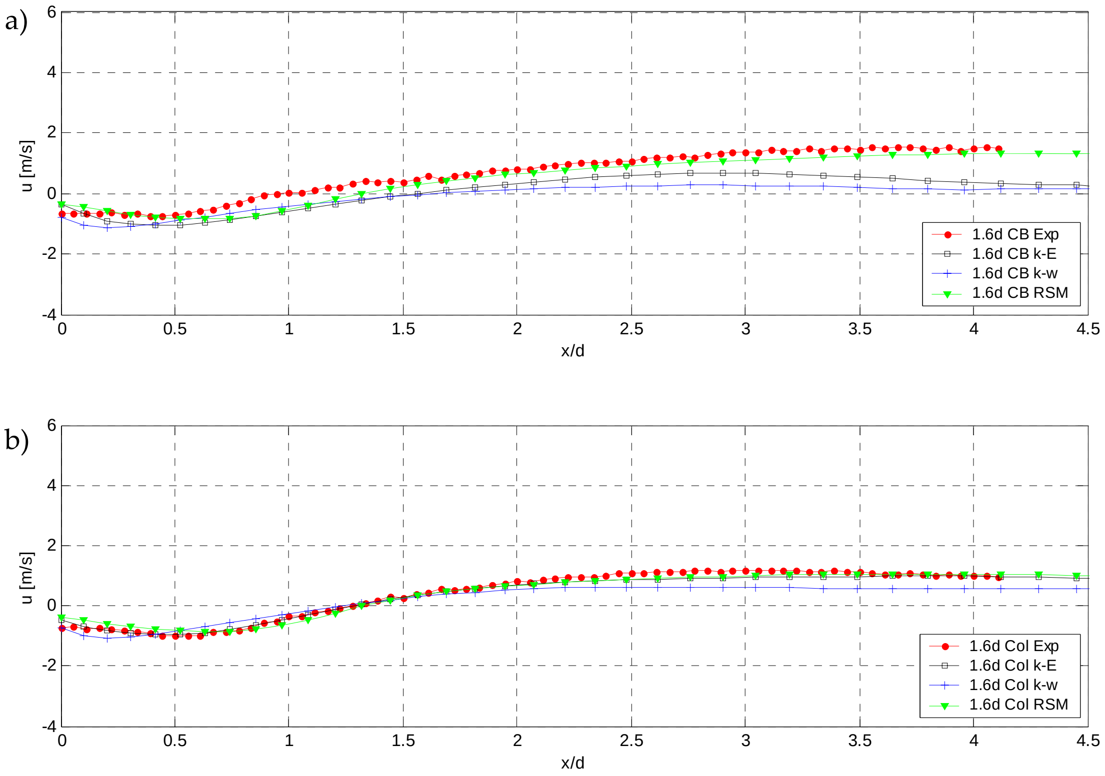

Figure 8.7 Numerical (k-ε, k-w and RSM turbulence models) v experimental comparison of horizontal profiles of u velocity along the x=axis, taken for 1.6d pitch of a) chequerboard and b) columnar configurations

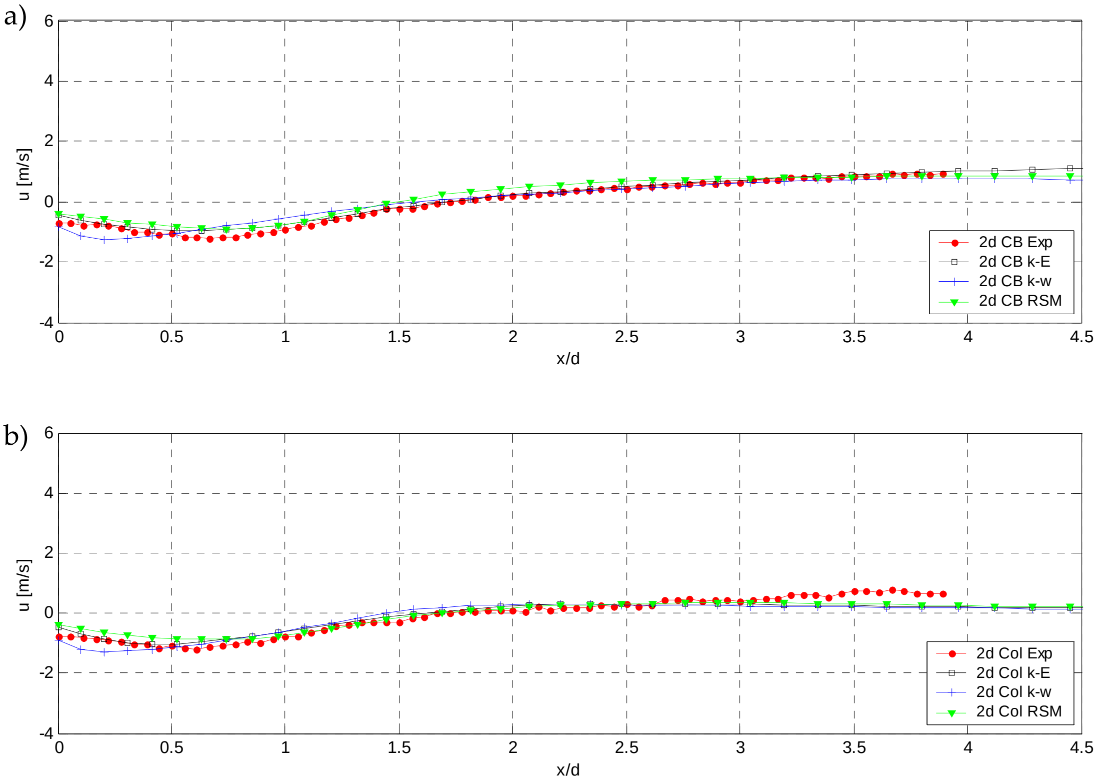

Figure 8.8 Numerical (k-ε, k-w and RSM turbulence models) v experimental comparison of horizontal profiles of u velocity along the x=axis, taken for 1.6d pitch of a) chequerboard and b) columnar configurations

Lai and Nasr (1998) carried out a study on two parallel plane jets for aerospace industry. Their experiments were performed on a two-dimensional flow discharged through two nozzles with 4.25d pitch and zero swirl. They have taken velocity measurement using 2D LDA and compared them to computational results obtained using three turbulence models: k-ε, RNG k-ε and RSM. Figure 8.9 shows comparisons of Lai and Nasr's numerical and experimental results for the axial velocity along the x-axis.

They found that the shape of the numerical results was quite different from that of the experimental measurements, especially in the merging and combined regions, *mp* and *cp*† respectively (figure 8.9). The differences between the results obtained from the three models were greater in the converging region than in the region downstream of the merging point. Furthermore, the decay of the centre-line velocity in the combined region was rather slow for all three turbulence models when compared with experimental results.

Contrary to the findings of Lai and Nasr, my results showed that the decay of the centre-line velocity was rather well predicted by both the k-ε and RSM turbulence models in all cases. The case of the 1.6d pitch of chequerboard configuration (figure 8.7a) is the only case where the RSM showed an advantage compared to the k-ε turbulence model, especially in the downstream flow (x/d>1.5). As was shown in section 7.3.3, this case generates the highest swirl velocities due to its tight-pitched burners and combined swirling burner flows – a type of complex flow which is well accounted for in the RSM's transport equations.

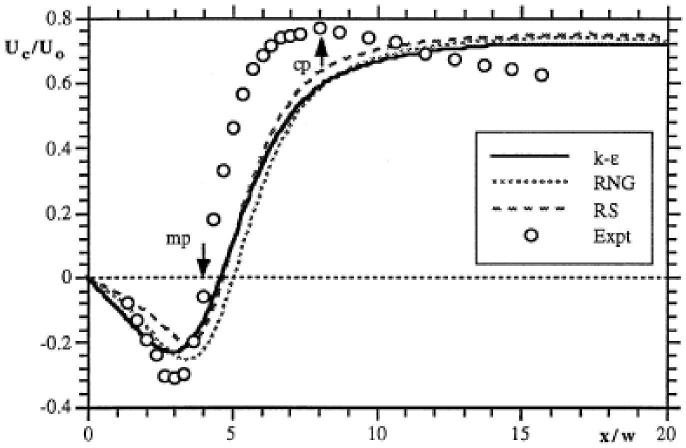

Figure 8.9 Numerical (k-ε, RNG and RS turbulence models) v experimental comparison of mean streamwise velocity distribution along the x axis (Lai and Nasr, 1998)

The visual analysis of the horizontal axial profiles supports the conclusions of the analysis of the vertical velocity profiles: the k-ω turbulence model provides the worst match to the experimental data, whilst it cannot be definitively concluded whether it is

---

† Points where jets begin to merge and combine together to resemble single jet flow are referred to as merging and combined points respectively (Lai and Nasr, 1998).

the k-ε or RSM turbulence model that gives the best prediction of the experimental data.

8.2 Vertical (v) velocity profiles

The analysis of the vertical velocity component, experimental *v*, presented in chapter 7, section 7.3.2, showed that this velocity component becomes insignificant as soon as the flow moves away from the burner exit.

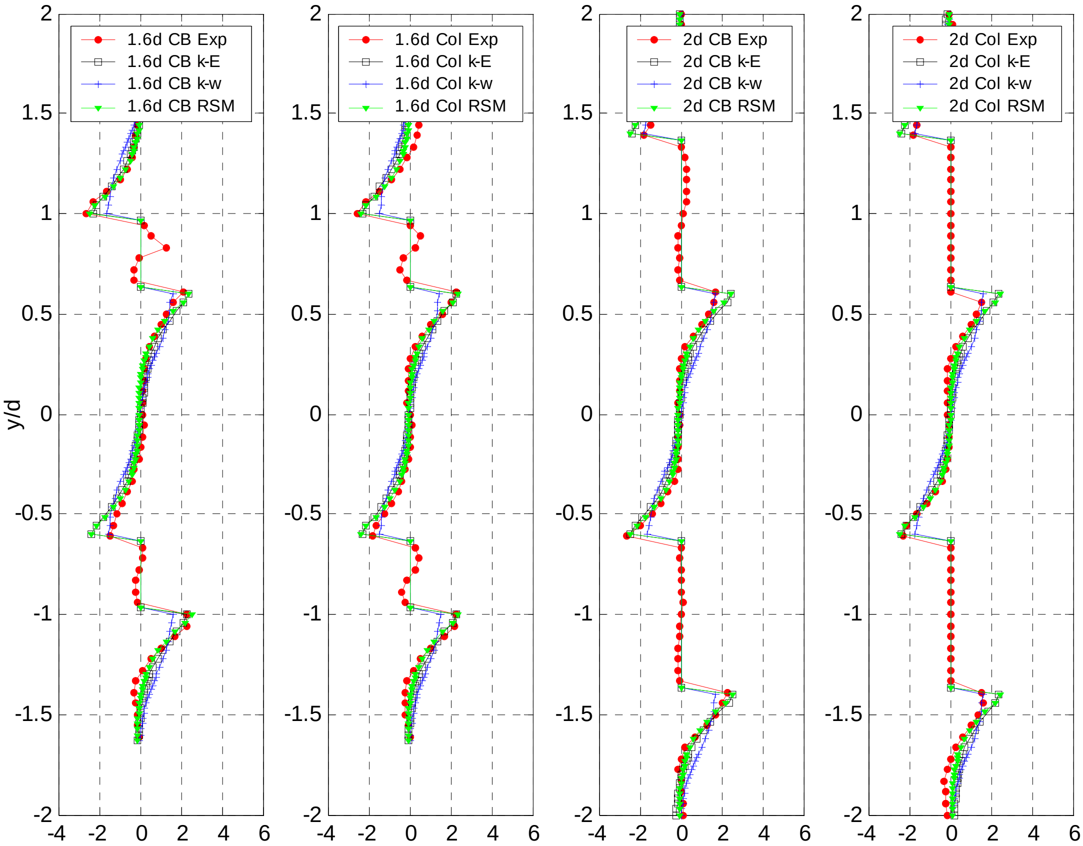

a) v-vel [m/s] at x=0 b) v-vel [m/s] at x=0 c) v-vel [m/s] at x=0 d) v-vel [m/s] at x=0

Figure 8.10 Numerical (k-ε, k-w and RSM turbulence models) v experimental comparisons of vertical profiles of v velocity at the burner exit, taken for a) 1.6d pitch, chequerboard, b) 1.6d pitch, columnar, c) 2d pitch, chequerboard and d) 2d pitch, columnar configurations

The profiles of the vertical velocity component obtained experimentally, as well as the numerical results obtained using the k-ε, k-ω and RSM turbulence models have been taken at x=0, 0.5d, d and 2d distances from the burner exit. However, the analysis has been carried out only for the profiles taken at the burner exit, since this is the only instance where the vertical velocity component has any significance (figure 8.10). For completeness, the rest of the profiles are presented in Appendix E (figures E.1, E.2, E.3 and E.4).

Whilst all three turbulence models provided a very good overall match to the experimental data, the k-ω turbulence model prediction was, again, the worst of the three, with slightly under-predicted peak velocities in all four cases (i.e. for both pitches and both configurations).

8.3 Swirl (w) velocity profiles

Figures 8.11-8.14 show swirl velocity profiles taken along the vertical traverse for the following cases: 1.6d pitch chequerboard configuration, 1.6d pitch columnar configuration, 2d pitch chequerboard configuration and 2d pitch columnar configuration respectively.

The visual analysis of the swirl velocity profiles at the burner exit (x=0) shows that the k-ω turbulence model again provides the worst match to the experimental data (figures 8.11a-8.14a). It appears, however, that the swirl velocity profiles obtained using the k-ε and RSM turbulence models are very similar, and both are generally in a very good agreement with the experimental data.

The analysis of the data downstream of the burner exit shows that the predicted data by all three turbulence models provided a better match to the experimental data in case of the 1.6d and 2d pitches of columnar configuration (figures 8.12 and 8.14 respectively) than in case of the 1.6d and 2d pitches of the chequerboard configuration (figures 8.11 and 8.13 respectively). This is in line with the comparisons of axial velocities taken along the horizontal traverse (section 8.1.2).

As described in chapter 7, section 7.3.3, adjacent jets discharging from a chequerboard configuration tend to combine at the burner exit, resulting in lower shear stresses and higher swirl velocities. The numerical simulations of this flow behaviour have all over-predicted the velocity peaks occurring at merging points between adjacent jets downstream of the burner exit (figures 8.11 and 8.13). The over-prediction is most evident in the case of the k-ω turbulence model, especially for the wider, 2d pitch (figure 8.13). The RSM model, on the other hand, shows the closest match to the experimental data, thus clearly displaying advantages of a turbulence model that accounts for the effect of swirl by solving six partial differential equations, one for the transport of each of the six independent Reynolds stresses.

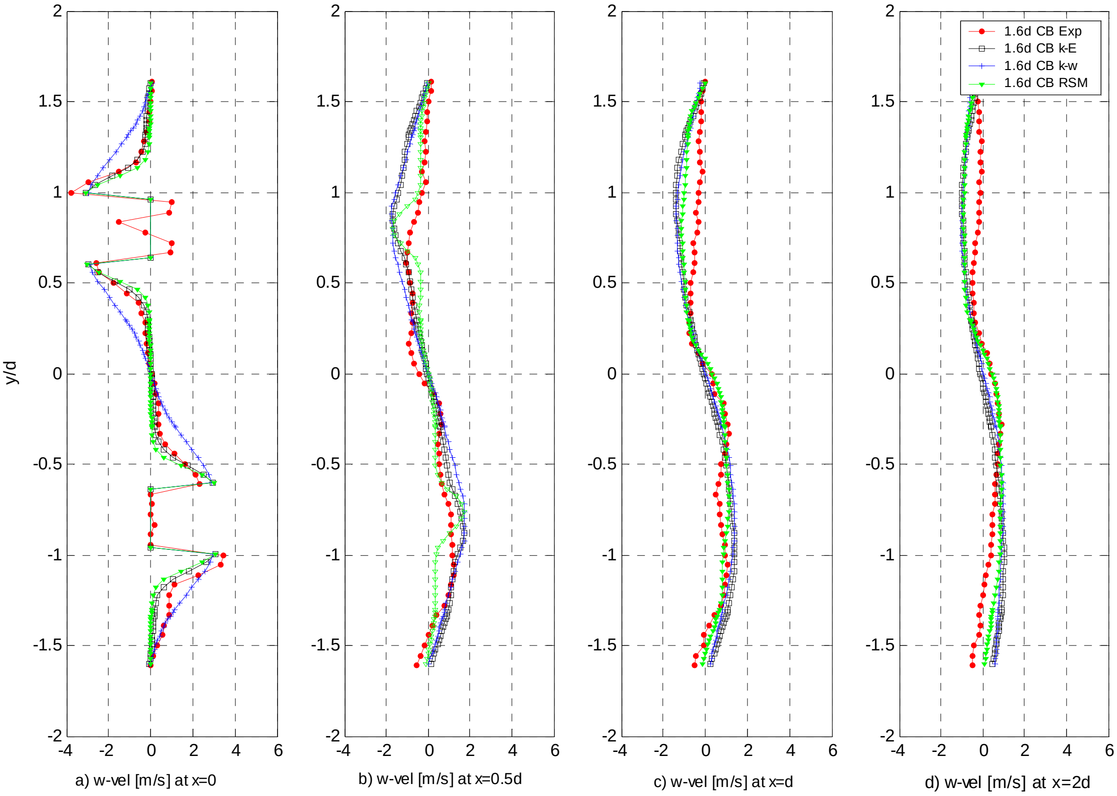

a) w-vel [m/s] at x=0

b) w-vel [m/s] at x=0.5d

c) w-vel [m/s] at x=d

d) w-vel [m/s] at x=2d

Figure 8.11 Numerical (k-ε, k-w and RSM turbulence models) v experimental comparison of vertical profiles of w velocity, taken for 1.6d pitch of chequerboard configuration at x=0, 0.5d, d and 2d distances from the burner panel

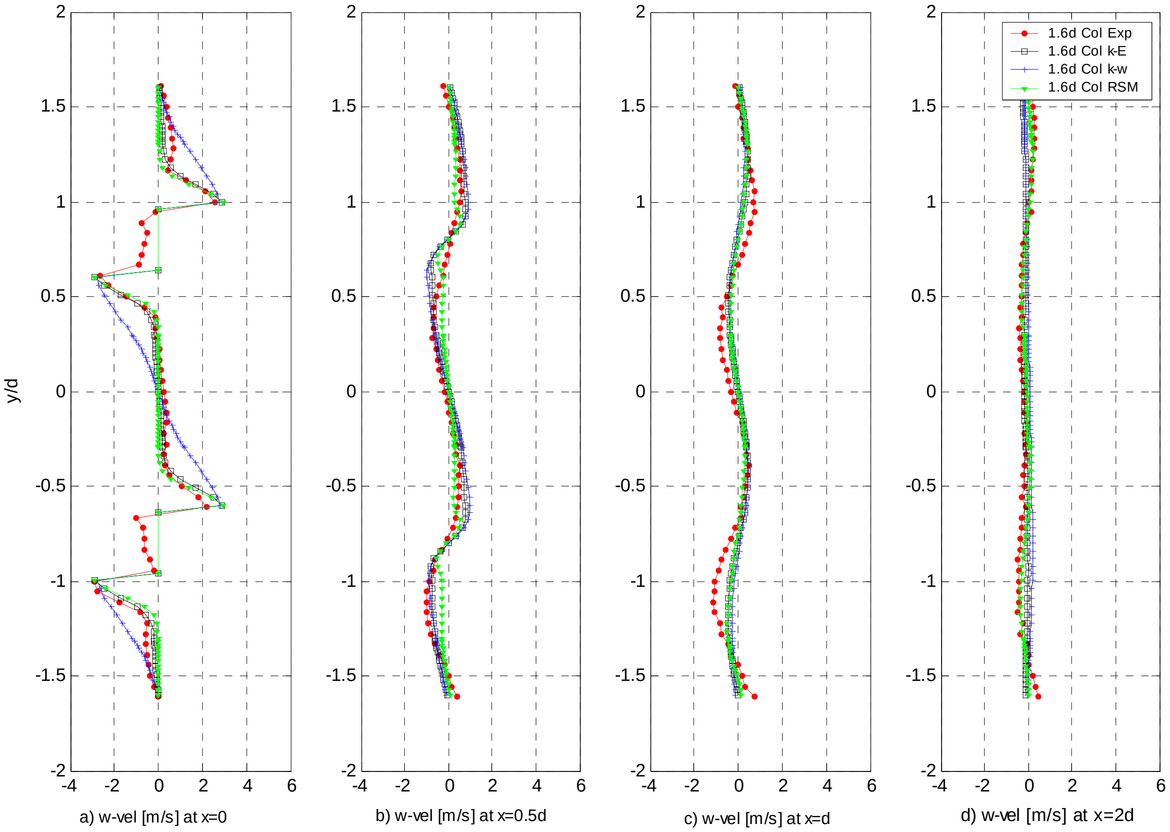

Figure 8.12 Numerical (k-ε, k-w and RSM turbulence models) v experimental comparison of vertical profiles of w velocity, taken for 1.6d pitch of columnar configuration at x=0, 0.5d, d and 2d distances from the burner panel

Figures 8.12 and 8.14 show that the predicted swirl velocity profiles by all three turbulence models for the columnar configuration are generally in a very good agreement with the experimental data. The numerical predictions by all three turbulence models are so close to the experimental data that, in fact, it is very difficult to determine which one of the models provides the best match just by using a visual analysis of the data.

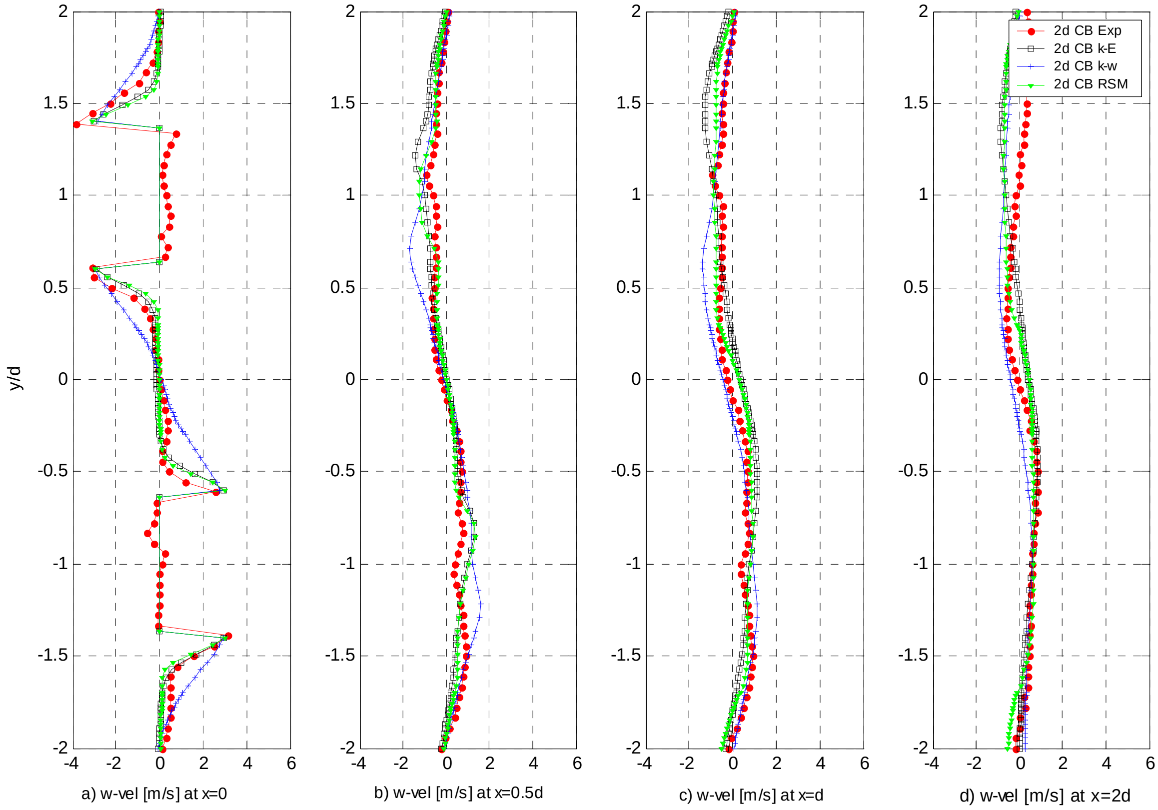

Figure 8.13 Numerical (k-ε, k-w and RSM turbulence models) v experimental comparison of vertical profiles of w velocity, taken for 2d pitch of chequerboard configuration at x=0, 0.5d, d and 2d distances from the burner panel

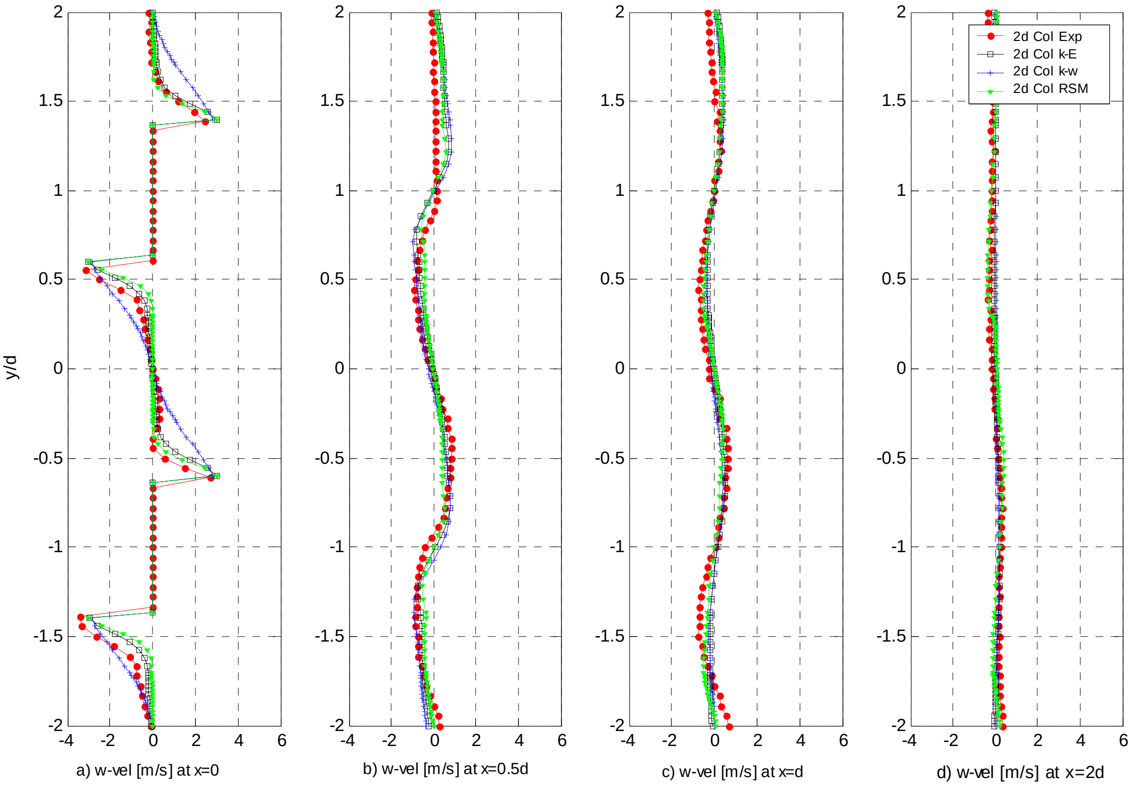

a) w-vel [m/s] at x=0 b) w-vel [m/s] at x=0.5d c) w-vel [m/s] at x=d d) w-vel [m/s] at x=2d

Figure 8.14 Numerical (k-ε, k-w and RSM turbulence models) v experimental comparison of vertical profiles of w velocity, taken for 2d pitch of columnar configuration at x=0, 0.5d, d and 2d distances from the burner panel

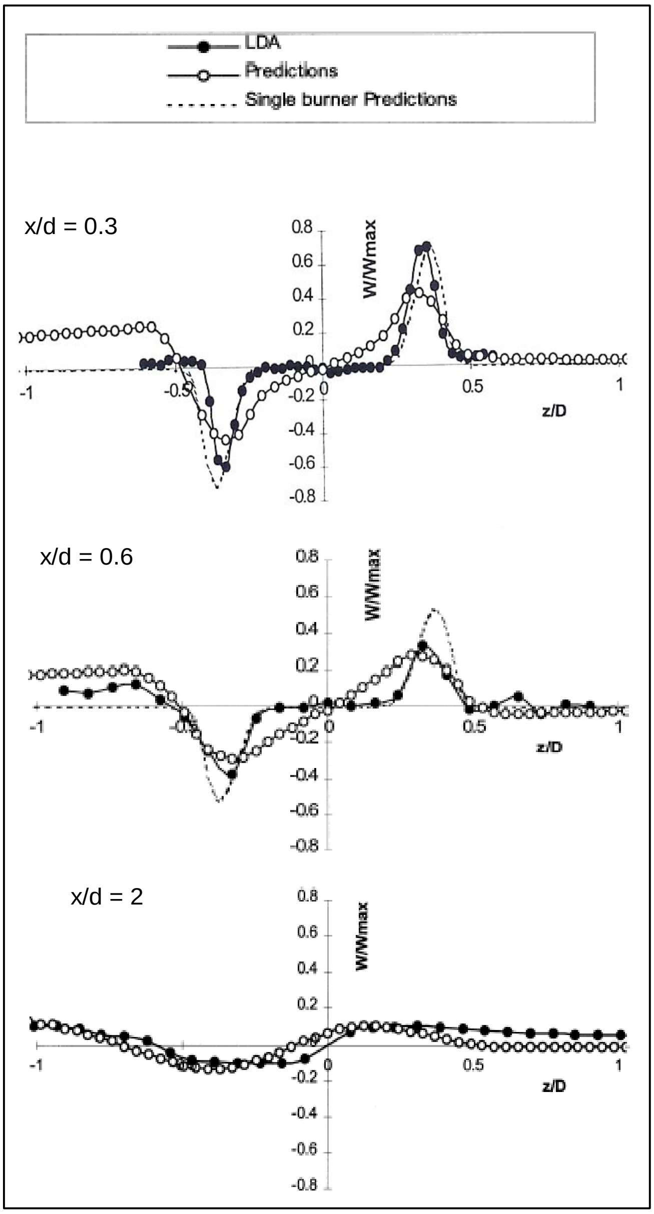

Figure 8.15 Axial velocity profiles at x=0.3d, 0.6d and 2d from the burner exit (Aroussi et al, 2000)

Figure 8.15 shows comparisons of measured (using LDA) and predicted (using the k-ε turbulence model) swirl velocities measured on two burners discharging into the furnace, as part of the Aroussi et al (2000) study described in section 8.1.1. The LDA results, plotted for one of the two burners, were also compared to the single burner results. The authors found that, whilst the rapid decay of swirl has been well predicted by the numerical results, in the near-burner region (x/d=0.3), the shape of the swirl velocity profile, as well as the peak swirl velocities were not predicted correctly.

The results of Aroussi et al (2000) research work, whilst not directly comparable to the results of this PhD research, are useful in a sense of gaining insights in the performance of the relevant numerical turbulence stress models in relation to the experimental data. However, this still does not help achieve conclusions as to performance of the turbulence models applied to the particular burner and furnace geometry used here.

The analysis of the Figures 8.11-8.14 which contain the results of this research shows that the k-ω turbulence model gives inferior performance compared to the k-ε and RSM. Nevertheless, it does not show a clear advantage of the RS turbulence model over the k-ε and vice versa. It is, therefore, necessary to employ a further, statistical analysis, which will be able to clarify which of the two turbulence models provides a closer fit to the experimental data.

8.4 Statistical analysis of experimental and numerical velocity profiles

The results of visual analyses of velocity profiles presented in section 8.1-8.3 showed that the visual analysis alone is not sufficient in determining which numerical model gives the best prediction of experimental data. Therefore, axial and swirl velocity profiles have also been examined using statistical methods in order to quantify discrepancies between experimental and numerical velocity profiles and find which numerical model can be used with confidence to predict the behaviour of multi-burner jets. Given the low significance of radial velocity profiles described in section 8.2, they have been omitted from the statistical analysis.

8.4.1 Mathematical background

This section gives an overview of the well-known statistical methods which have been used to analyse the axial and swirl velocity profiles.

8.4.1.1 Sum of squared errors, SSE

The sum of squared errors statistical method is used to analyse the closeness of the fit between the numerical and experimental data. A value closer to zero indicates that the model has a smaller random error component, and that the fit will be more useful for prediction.

The sum of squared errors is defined using the following formula:

$$SSE = \sum_{t=1}^{n} (y_t - \hat{y}_t)^2$$

where, y is the response value, $\hat{y}$ is the predicted response value and n is the number of observations.

8.4.1.2 Root Mean Square Error, RMSE

This statistic is also known as the fit standard error and the standard error of the regression. It is an estimate of the standard deviation of the random component in the data, and is defined as

$$RMSE = \sqrt{MSE}$$

where, MSE is the mean square error or the residual mean square

$$MSE = \frac{SSE}{n}$$

Just as with SSE, an MSE value closer to 0 indicates a fit that is more useful for prediction.

RMSE is probably the most easily interpreted statistic, since it has the same units as the quantity plotted on the vertical axis.

8.4.2 Statistical analysis

RMSEs were calculated for axial and swirl velocities in order to show the fit between the experimental and numerical data obtained for the k-ε, k-ω and RS turbulence models. Each combination of pitch and configuration was examined. The RSMEs, calculated at the x=0.5d distance from the burner exit, for each combination (i.e. 1.6d chequerboard, 1.6d columnar, 2d chequerboard and 2d columnar) are presented in figure 8.16a, for axial velocity, and figure 8.16b, for swirl velocity.

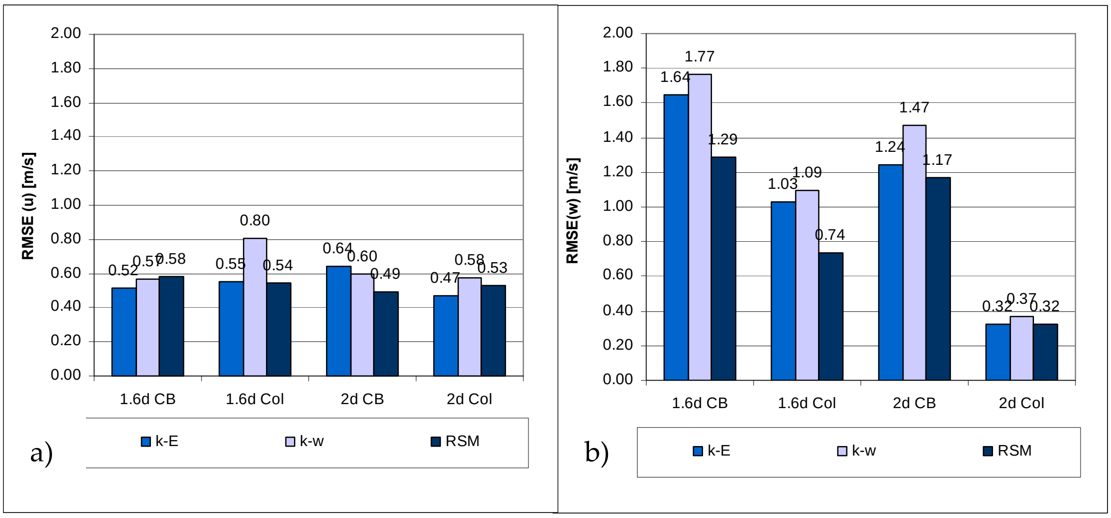

Figure 8.16 Root mean square error (RSME) for 1.6d and 2d pitches of chequerboard and columnar configurations, showing fit between experimental and numerical data (obtained using k-ε, k-w and RSM turbulence models) at x=0.5d for a) axial and b) swirl velocity profiles

From figure 8.16, it can be seen that for the chequerboard configuration (both pitches), RSMEs are lower for the axial velocity profiles than for the swirl velocity profiles, implying that the numerical models are more accurate in predicting axial velocity component, and are less successful in predicting complex, high swirl velocity components. Columnar configuration, 2d pitch swirl velocity profiles seem to have been most accurately predicted by all three turbulence models, showing the smallest RSMEs. The statistical findings confirm the results of the visual analyses where the axial velocities in all cases were reasonably well predicted by numerical models, whilst the swirl velocities were more accurately predicted for the columnar configuration than for the chequerboard.

The statistical analysis for axial velocity profiles (figure 8.16a) shows that the RSME values do not vary greatly between different pitches and configurations. This is, however, not the case for swirl velocity profiles. Figure 8.16b shows that swirl velocities are better predicted for wider-pitch geometry, assuming the configuration is unchanged. Furthermore, it is clear that the swirl velocity profiles obtained for the chequerboard configurations (characterised by the jets which tend to combine) are more difficult predict than those obtained for the columnar configurations (where jets tend to push each other apart).

In terms of selection of the best turbulence model, which provides the closest fit to the experimental data, the statistical analysis confirmed the findings of the visual analysis highlighting the k-ω turbulence model as the least accurate fit to the experimental data, particularly when trying to predict swirl velocities (figure 8.16b).

The comparison between the k-ε and RSM turbulence models reveals that, for prediction of the axial velocity profiles, neither of the models shows clear advantage. The RSME values presented in Figure 8.16a show an even performance between these two models.

The advantage of the RSM turbulence model is more clearly demonstrated in relation to the swirl velocity profiles (figure 8.16b). The RSM model consistently performed better than the k-ε turbulence model, with the exception of the 2d, columnar configuration case, where the two models performed evenly.

A further, 'drill-down' analysis of the RSME values for the swirl velocity profiles revealed interesting patterns in numerical predictions of experimental data. Figures 8.17a-d show RSME values for swirl velocity component taken at four axial stations for 1.6d and 2d pitches of chequerboard and columnar configurations.

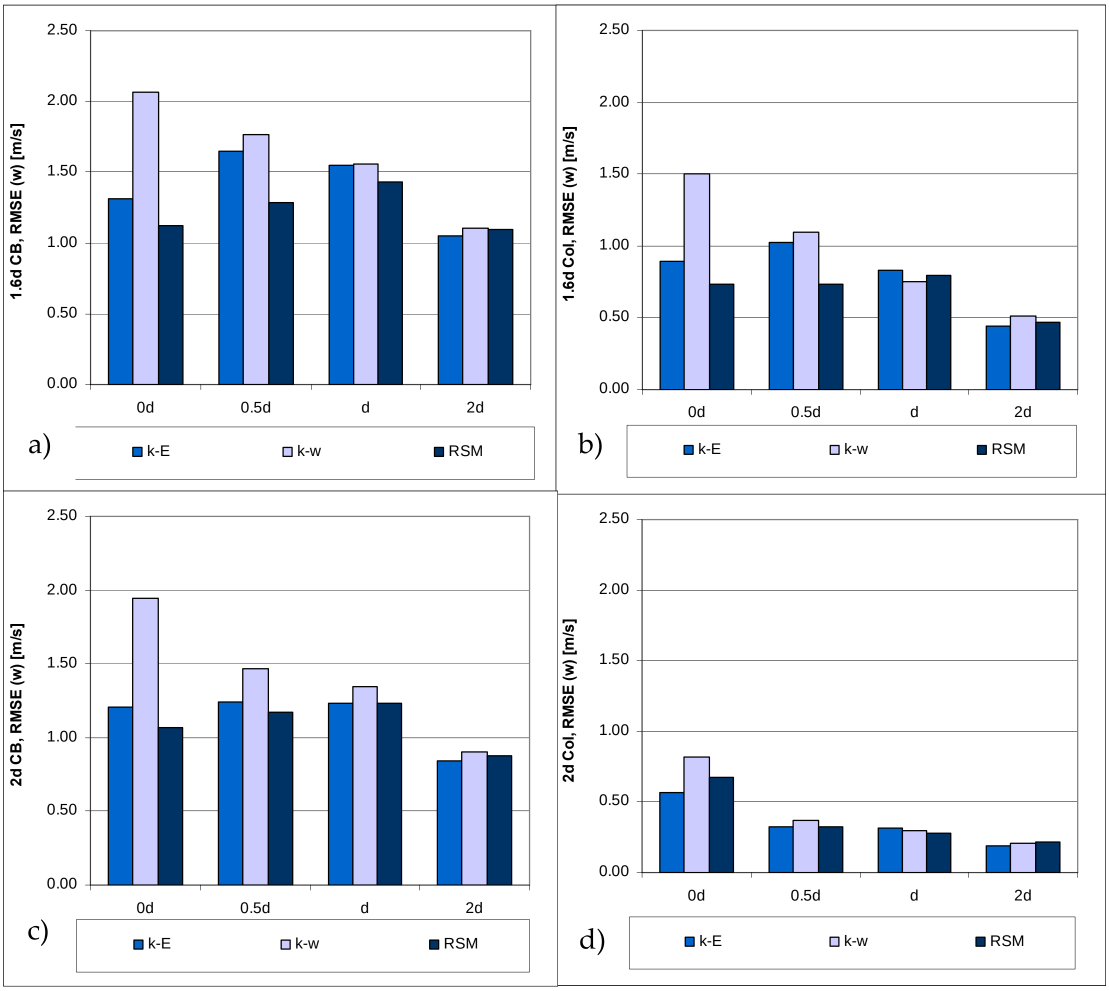

Figure 8.17a-d Root mean square error (RSME) for 1.6d and 2d pitches of chequerboard and columnar configurations, showing fit between experimental and numerical data (obtained using k-ε, k-w and RSM turbulence models) for swirl velocity profiles at x=0, 0.5d, d and 2d

The RSME results, presented in figure 8.17a-d, show that the tighter pitches are more difficult to predict than the wider pitches. Also, keeping the pitch equal, the chequerboard configuration gives less accurate predictions than the columnar configuration.

The results also show that, for the chequerboard configuration, at the axial stations of x=0, 0.5d and x=d, the RSM turbulence model consistently performs better. This region, as shown in Chapter 7, section 7.3.4, is characterised by a highly turbulent, non-isotropic, flow regime, which indicates that the RSM turbulence model can handle this complex regime much better than the k-ε turbulence model, which assumes isotropic flow behaviour.

The advantage of the RSM turbulence model is also evident in the case of the columnar configuration, particularly for the tighter pitch in the area close to the burner exit (figure 8.17b). In the case of the wider pitch of columnar configuration (figure 8.17d), at x=0.5d, d and 2d, there is no clear advantage of any of the three turbulence models, since all three predict the experimental data with reasonable accuracy.

8.5 Turbulent kinetic energy (k) profiles

The statistical analysis of the axial and swirl velocity profiles presented in section 8.4 indicated that the RSM turbulence model gives the most accurate predictions of multiple swirling flows, especially in the area where the flow is characterised by the highly turbulent, non-isotropic behaviour.

In order to investigate if this finding also applies to turbulent quantities, directly measured turbulent quantities were compared to those obtained numerically, using the k-ε and RSM turbulence models. This was done by performing an analysis of turbulent kinetic energy. Experimental values for the turbulent kinetic energy per unit mass were calculated from the directly measured fluctuating components of the turbulence using the following formula:

$$k = 0.5(\overline{u^{'2}} + \overline{v^{'2}} + \overline{w^{'2}})$$

where, *u', v' and w'* are fluctuating components of axial, radial and swirl velocity respectively.

The numerical values for the turbulent kinetic energy profiles were generated as part of the FLUENT results output.

The analysis focused on the performance of the k-ε and RSM turbulence models against the experimentally obtained data. The k-ω turbulence model was not used in the analysis of turbulent kinetic energy profiles, given the overwhelming evidence presented in sections 8.1-8.4, showing the inferior performance of this turbulence model compared to the k-ε and RSM models.

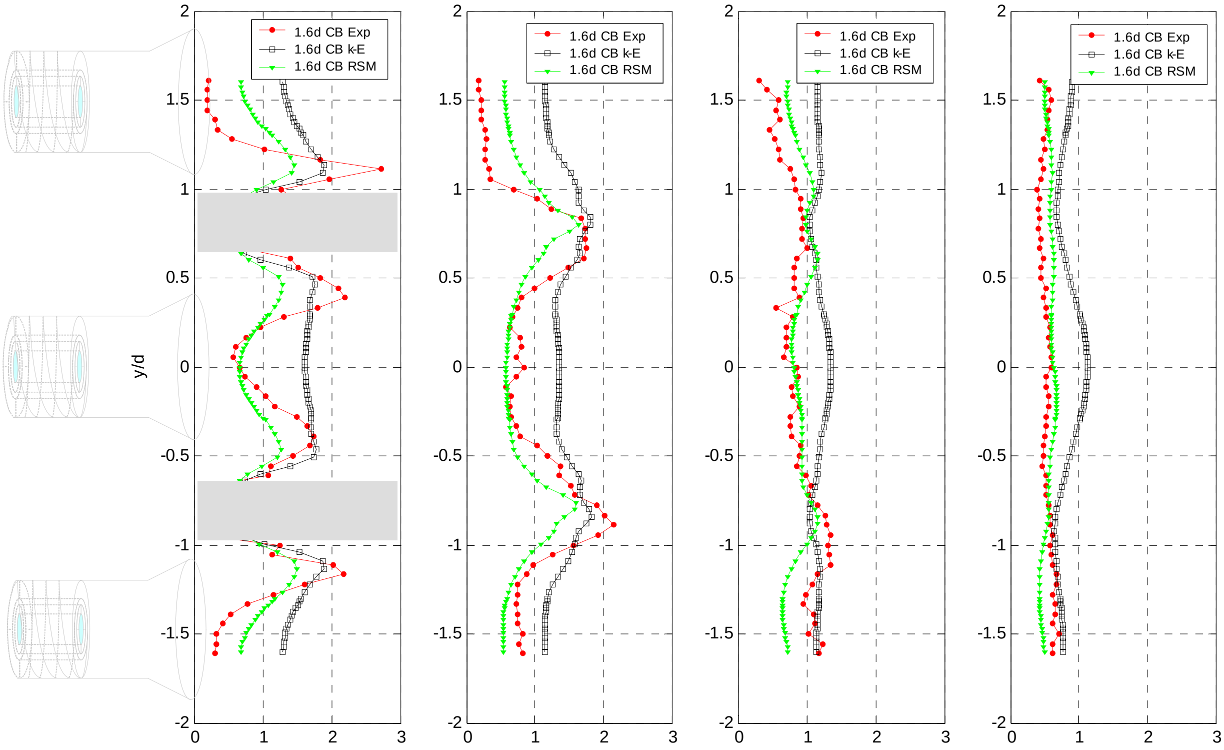

a) k [m2/s2] at x=0 b) k [m2/s2] at x=0.5d c) k [m2/s2] at x=d d) k [m2/s2] at x=2d

Figure 8.19 Numerical (k-ε and RS turbulence models) v experimental comparison of TKE profile, taken for 1.6d pitch of chequerboard configuration at x=0, 0.5d, d and 2d distances from the burner panel

Figures 8.19 to 8.22 show turbulent kinetic energy profiles taken at four different axial stations for 1.6d and 2d pitches of chequerboard and columnar configurations. The region of the wall between the burner quarls shown in grey is for x=0.

Figure 8.19 shows experimental profiles of the turbulent kinetic energy, plotted against the k-ε and RS turbulence models, in the case of the 1.6d pitch of the chequerboard configuration. The measured turbulent kinetic energy is low in the centre of the burner and shows a peak at $y = \pm 0.5d$ for x=0.By x=0.5d, there is a pronounced peak in the mixing region between adjacent burners, which dies away at x=d, and is not visible at x=2d. The RSM model predicts this behaviour relatively well, although lower in magnitude than the measurement. It is a good prediction of the slope and magnitude of the turbulence peaks at x=0.5d. The k-ε model consistently over-estimates the general turbulence and actually predicts the wrong profile at x=d and x=2d.

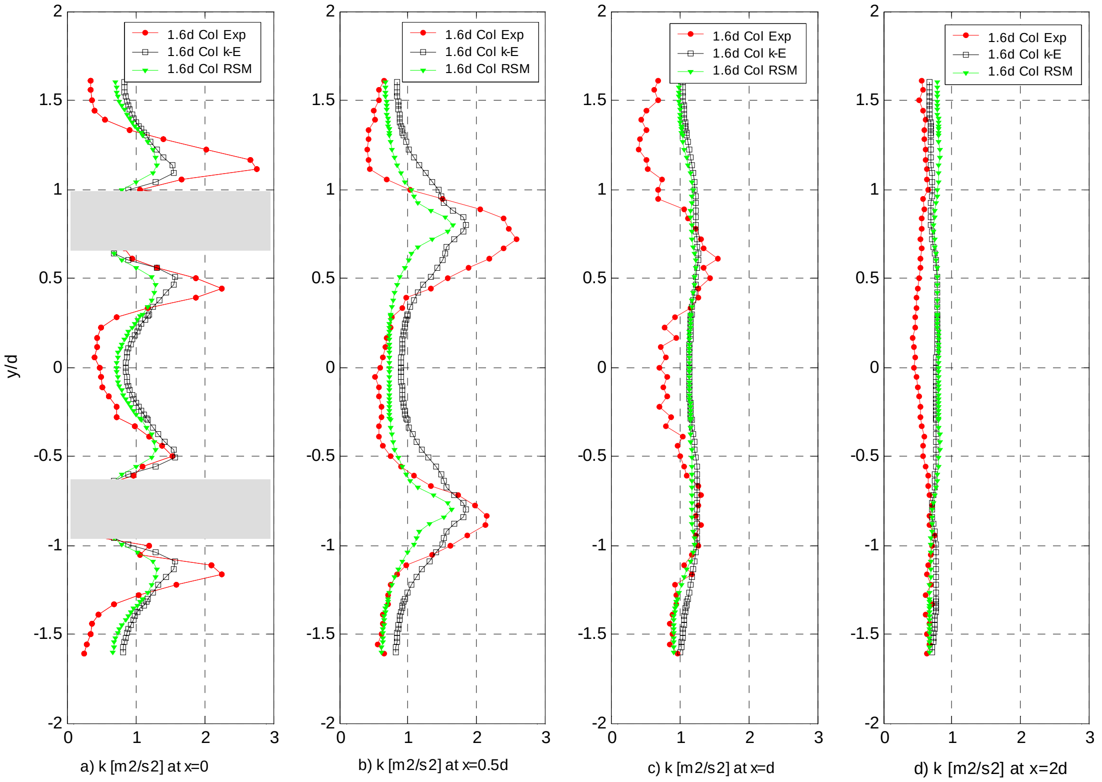

Figure 8.20 Numerical (k-ε and RS turbulence models) v experimental comparison of TKE profile, taken for 1.6d pitch of columnar configuration at x=0, 0.5d, d and 2d distances from the burner panel

In the case of the 1.6d pitch of the columnar configuration shown in Figure 8.20, the RSM turbulence model shows better prediction of experimental turbulent kinetic energy across the recirculation zones than the k-ε turbulence model. The peak values are under-predicted by both models. However, the shape of the turbulent kinetic energy profile obtained using the RSM turbulence model follows the shape of the experimentally obtained profile, whereas the turbulent kinetic energy profile obtained using the k-ε turbulence model diverges from the experimental data by exhibiting a different behaviour in the 'peak' regions.

Figure 8.21 shows the experimental profile of the turbulent kinetic energy, plotted against the k-ε, and RSM turbulence models, in the case of the 2d pitch of the chequerboard configuration. The k-ε and RSM turbulence models only slightly differ in their shapes and magnitudes.

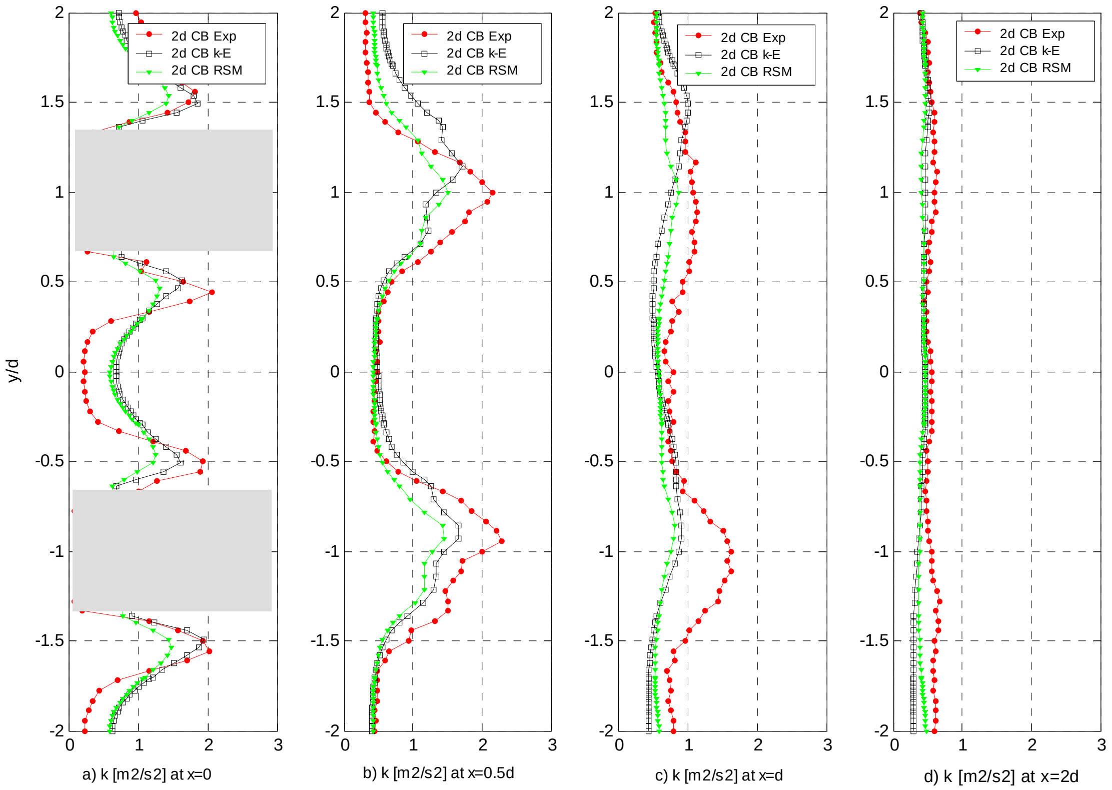

Figure 8.21 Numerical (k-ε and RS turbulence models) v experimental comparison of TKE profile, taken for 2d pitch of chequerboard configuration at x=0, 0.5d, d and 2d distances from the burner panel

Figure 8.21 shows that, at the burner exit, the recirculation zones were under-predicted by both models. The maximum values of the measured turbulent kinetic energy were better predicted by the k-ε turbulence model. However, at x=0.5d, when jets start to merge, the RSM model provided a better prediction of the shape of the profile. Whilst the recirculation zones were reasonably well predicted by both models at this axial station, the opposite was true of the turbulent energy peaks, which were under-estimated. The subsequent turbulent kinetic energy profiles, taken at x=d and 2d, show that both models consistently under-estimate the experimental data.

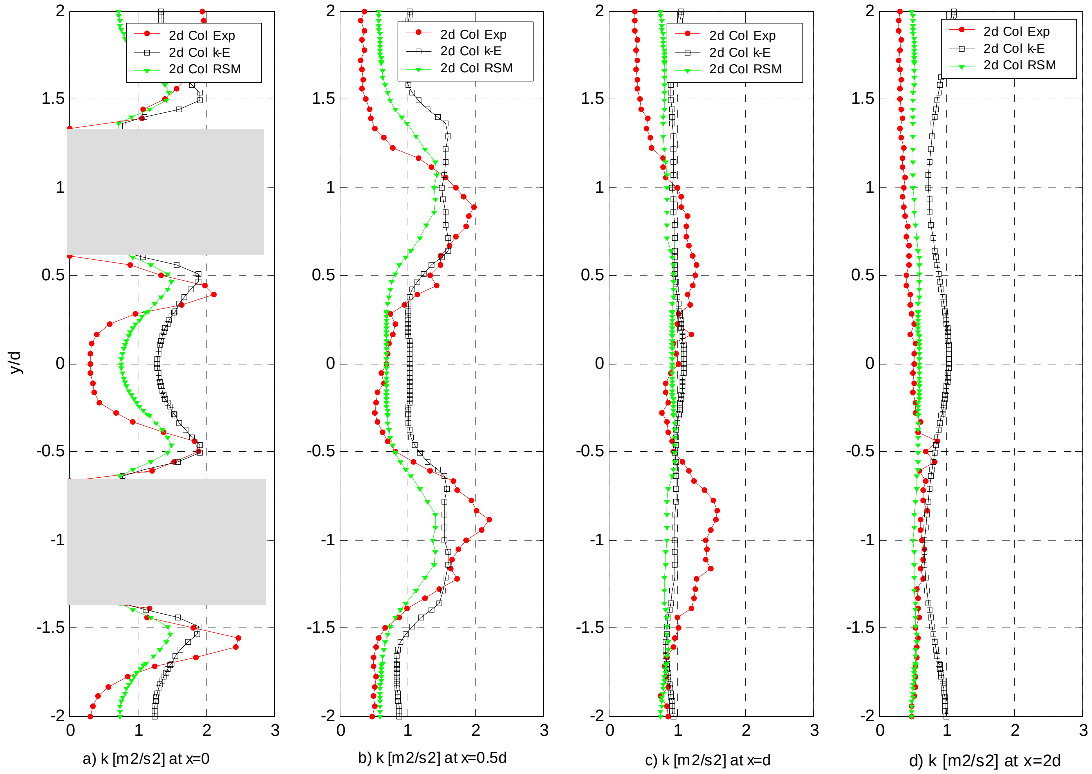

Figure 8.22 Numerical (k-ε and RS turbulence models) v experimental comparison of TKE profile, taken for 2d pitch of columnar configuration at x=0, 0.5d, d and 2d distances from the burner panel

Finally, in the case of the 2d pitch of the columnar configuration (figure 8.22), the RSM turbulence model provided a closer match to the experimental data than the k-ε turbulence model. The closeness of the match between the RSM turbulence model and the experimental data is evident across the recirculation zones, but also in terms of the shape of the profiles. The k-ε turbulence model over-predicted the recirculation zone and also exhibited a different behaviour in terms of the shape of the turbulent kinetic energy profile in the peak regions.

8.5.1 Statistical analysis

The visual analysis of the profiles of the turbulent kinetic energy clearly demonstrates the benefits of using the RSM turbulence model in numerical simulation of isothermal flows in a multi-burner furnace.

To quantify the closeness of the fit between the numerical and experimental profiles of the turbulent kinetic energy, a statistical analysis using the RSME method has been carried out.

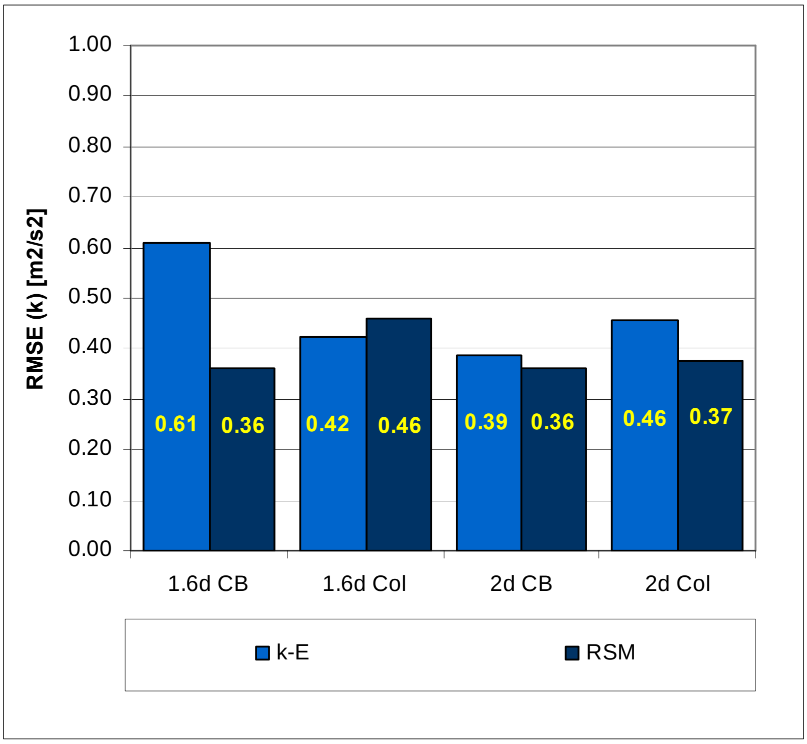

Figure 8.23 Root mean square error (RSME) for 1.6d and 2d pitches of chequerboard and columnar configurations, showing fit between experimental and numerical data (obtained using k-ε and RSM turbulence models) for turbulent kinetic energy profiles at x= 0.5d

The analysis focused on turbulent kinetic energy profiles taken at the x=0.5d axial station. As was shown in Chapter 7, section 7.3.4, in this region, the fluctuating components of turbulence exhibit highly turbulent, non-isotropic flow behaviour, and are therefore extremely difficult to predict using numerical models.

Figure 8.23 shows that, in three out of four cases, the turbulent quantities predicted using the RSM are closer to the experimentally obtained values. The k-ε model performed better only in the case of the 1.6d pitch of columnar configuration. As shown in figure 8.20(b), this is attributed to the k-ε model showing closer match to the experimental data in the peak regions, despite poor performance across the recirculation zones, which were much better predicted by the RSM model.

It can be therefore said, with some of confidence, that the RSM model is a better tool for modelling and prediction of turbulent quantities occurring in multiple swirling flows. Accurate prediction of turbulent quantities could have a major effect on combustion modelling and therefore on the prediction of the NO_x emissions.

8.6 Reynolds stresses

Direct measurements of Reynolds shear stresses obtained using 3D LDA technology have enabled comparison between the experimental and numerical results. Numerical results were obtained using the RS turbulence model. The k-ε and k-ω turbulence models used for numerical modelling in this research did not account for Reynolds stresses, and therefore, could not be compared to the experimental results.

Figures 8.24-8.26 show Reynolds shear stresses (u’v’, u’w’ and v’w’), taken for 1.6d and 2d pitches, of chequerboard and columnar configurations, at x=0.5d axial distance from the burner exit. This position was chosen because it represents a region where turbulent quantities exhibit highly non-isotropic behaviour (section 7.3.4) and where the Reynolds shear stresses are of highest magnitudes (section 7.3.5). For completeness, however, comparisons between the experimental and numerical results for Reynolds shear stress at the burner exit have also been plotted and are presented in Appendix E (figures E.5, E.6 and E.7).

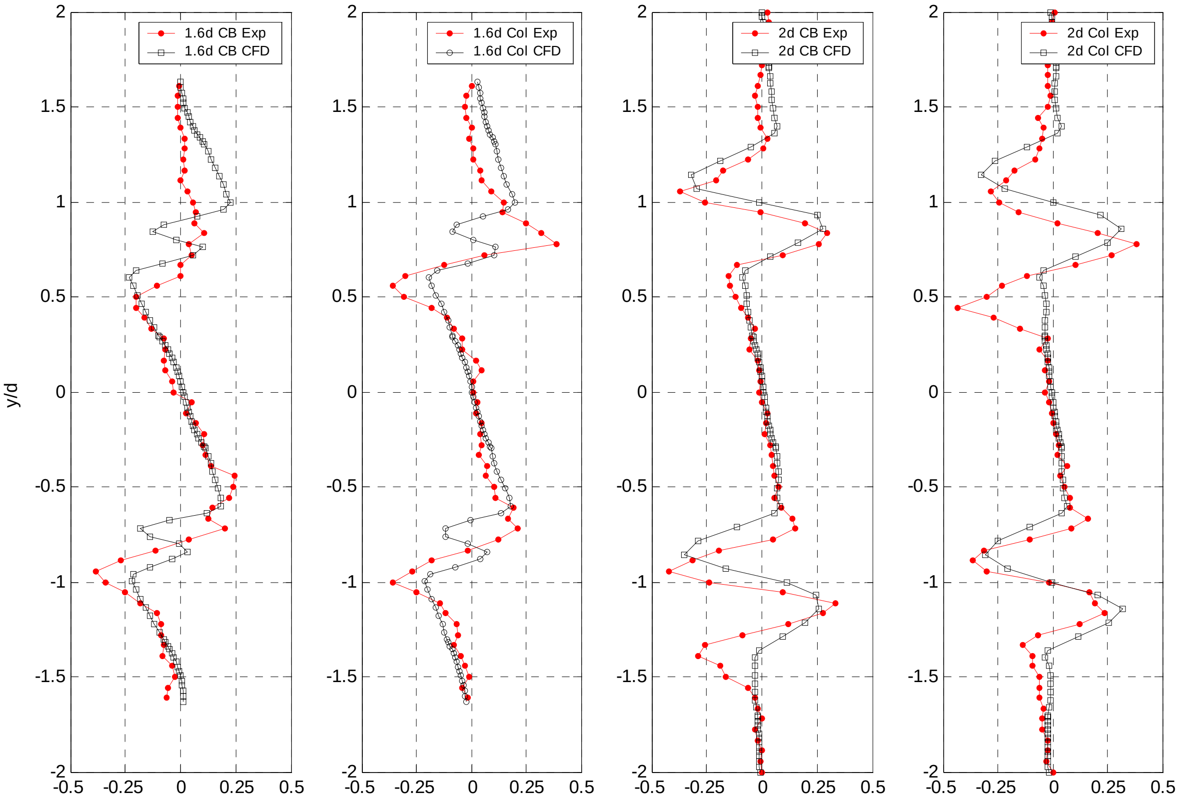

a) UxV at x=0.5d b) UxV at x=0.5d c) UxV at x=0.5d d) UxV at x=0.5d

Figure 8.24 Reynolds shear stress, u′v′, for 1.6d and 2d pitches of chequerboard and columnar configurations, showing the fit between experimental and numerical data (obtained using RSM turbulence model) at x= 0.5d

Figure 8.24 shows comparison between experimental and numerical distribution of turbulent shear stress, *u′v′*. The turbulent shear stress profiles have both positive and negative values associated with the mean positive and negative gradients of the mean velocity profiles. Distribution of the axial Reynolds stress term, u′v′, can be related to profiles of the axial (u′) and radial (v′) fluctuating velocity components presented in figures 7.20, D.3, D.4 and D.5.

The visual analysis shows that the general agreement between the experimental and numerical results for axial Reynolds shear stresses is very good for both pitches and both configurations.

Distribution of the Reynolds shear stress component, u'v', for the 1.6d pitch of chequered board and columnar configuration (figures 8.24a-b) shows discrepancy between the experimental and predicted values in the regions where the axial (u') and radial (v') velocity gradients have the highest magnitudes (figures 7.20 and A7.4). Whilst experimental results for the u'v' shear stress component show single peaks, which reflect the maximum axial velocity gradients, the predicted values for the u'v' shear stress show 'double peaks' in their distribution profiles, which are indicative of partially merged jets.

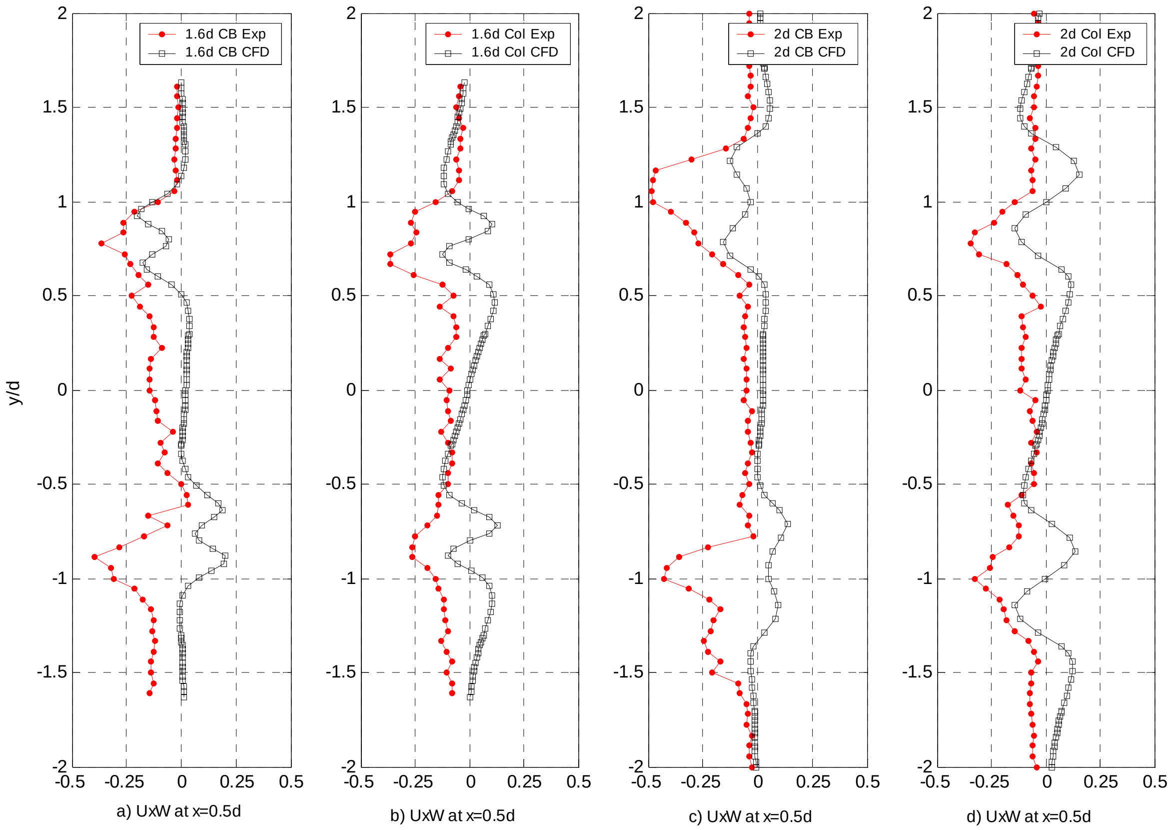

Figure 8.25 Reynolds shear stress, u'w', for 1.6d and 2d pitches of chequerboard and columnar configurations, showing fit between experimental and numerical data (obtained using RSM turbulence model) at x= 0.5d

On the other hand, comparison between experimental and numerical distributions of the axial shear stress component, u'v', for the 2d pitch of chequerboard and columnar configurations, (figures 8.24c-d), shows an excellent agreement between the two sets of results. The 'double peaks' across the maximum velocity gradient regions now appear in both experimental and numerical profiles. These peaks reflect the axial velocity gradient (u') profiles, indicating that, for wider pitch 2d, the jets have only partially merged at the x=0.5d distance from the burner exit (figures D.4 and D.5).

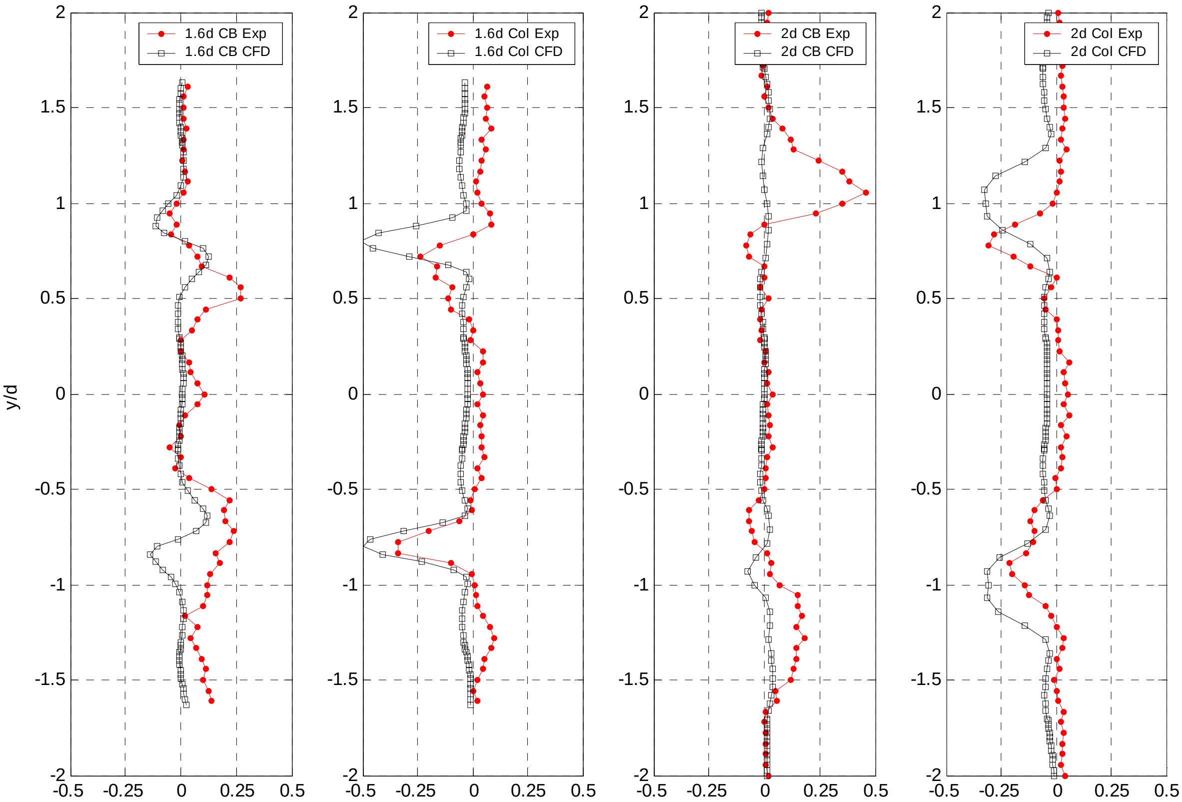

a) VxW at x=0.5d b) VxW at x=0.5d c) VxW at x=0.5d d) VxW at x=0.5d

Figure 8.26 Reynolds shear stress, v'w', for 1.6d and 2d pitches of chequerboard and columnar configurations, showing fit between experimental and numerical data (obtained using RSM turbulence model) at x= 0.5d

Figure 8.25 shows comparison between experimental and numerical distribution of tangential turbulent shear stress, *u'w'*, for 1.6d and 2d pitches of chequerboard and columnar configurations at x=0.5d distance from the burner exit. The agreement between the experimental and numerical tangential shear stress profiles is not as good as in the case of the axial shear stress, u'v', thus indicating that the swirl component is more difficult to predict.

The numerical tangential shear stress profiles clearly distinguish between the chequerboard and columnar configurations: in the case of chequerboard configuration (figure 8.25a and 8.25c), swirl fluctuating components from two adjacent jets combine, and in the case of columnar configuration (figure 8.25b and 8.25d), swirl fluctuating components act in opposite directions, thus pushing the two adjacent jets apart. Experimental results, however, do not show any great difference between the tangential stress distribution profiles of chequerboard and columnar configurations.

Tangential shear stress profiles taken at the burner exit are shown in Figure A8.6. It appears that, at x=0, there is a slightly better agreement between the experimental and numerical results, especially across the top and middle burners.

Overall, tangential shear stress is weaker than the axial shear stress. This shows the significance of the gradient of the axial velocity component (u'), which seems to play a more important role in production of shear stress than the swirl velocity gradient.

Finally, the third Reynolds shear stress component, *v'w'*, correlating radial and swirl fluctuating components is shown in figure 8.26.

The agreement between the experimental and numerical radial shear stress distribution profiles appears relatively good, especially in the case of columnar configuration (figure 8.26b and 8.26d). This is the weakest of the three Reynolds shear stress components, reflecting the lack of influence of the radial fluctuating component (v') on swirling flows.

Comparison between the experimental and numerical distributions of Reynolds shear stresses, u'v', u'w' and v'w', showed that the Reynolds stress components are generally well predicted using the RS turbulence models.

8.7 Conclusions

1. Visual analysis of vertical axial velocity profiles obtained for 1.6d and 2d pitches of chequerboard and columnar configurations showed that the k-ω turbulence model gives an inferior fit to the experimental data compared to the k-ε and RSM turbulence models. This is especially evident at x=0 (burner exit) and x=0.5d distance from the burner exit.

2. Analysis of vertical axial velocity profiles obtained using the k-ε and RS turbulence models shows that, at the burner exit, there is almost no difference between the two profiles. Both the k-ε and RSM turbulence models showed good agreement with peak velocities obtained experimentally. However, both models slightly under-predict the velocities across the recirculation zones. Overall, both models matched the experimental data reasonably well.

3. Analysis of horizontal axial velocity profiles showed that the decay of the centre-line velocity was well predicted by both the k-ε and RS turbulence models in all but one case - the 1.6d, chequerboard configuration. In this case, the differences between the numerical results were most evident, and neither of the two models predicted the decay accurately. The k-ω turbulence model provided the worst match to the experimental data.

4. Analysis of vertical profiles of radial velocity (v) at the burner exit showed that, whilst all three turbulence models provided a very good overall match to the experimental data, the k-ω turbulence model prediction was, again, the worst of the three, with slightly under-predicted peak velocities in all four cases (i.e. for both pitches and both configurations).

5. Analysis of vertical swirl velocity profiles shows that the k-ω turbulence model gives inferior performance compared to the k-ε and RSM model. There is no significant difference between the RS turbulence model over the k-ε and vice versa. The analysis of the data downstream of the burner exit shows that the predicted data by all three turbulence models provided a much better match to the experimental data in case of

the 1.6d and 2d pitches of columnar configuration than in case of the 1.6d and 2d pitches of the chequerboard configuration.

6. Statistical analysis showed that, at x=0.5d distance, RSMEs are lower for the axial velocity profiles than for the swirl velocity profiles, indicating that the numerical models are more accurate in predicting axial velocity component, and are less successful in predicting complex, swirl velocities. An exception was observed in the case of the wide pitch (2d), columnar case, where all three turbulence models provided a close fit to the experimental swirl velocity profiles.

7. Statistical analysis for axial velocity profiles showed that, at x=0.5d distance, the RSME values do not vary greatly between different pitches and configurations. This was not observed for swirl velocity profiles. It was found that swirl velocities are better predicted for wider-pitch geometry. The analysis showed that swirl velocity profiles obtained for the chequerboard configurations are more difficult predict than those obtained for the columnar configurations.

8. Results of the statistical analysis confirmed the findings of the visual analysis highlighting the k-ω turbulence model as the least accurate fit to the experimental data.

9. Statistical comparison between the k-ε and RS turbulence models revealed that, for prediction of the axial velocity profiles, neither of the models showed clear advantage. The advantage of the RS turbulence model was more clearly demonstrated in relation to the swirl velocity profiles, with the RS model consistently performing better than the k-ε turbulence model, with the exception of the 2d, columnar configuration case, where the two models performed evenly.

10. Visual analysis of the turbulent kinetic energy profiles showed that the RS turbulence model provided a closer match to the experimental data than the k-ε turbulence model. This was especially evident in the case of the 1.6d pitch of chequerboard configuration.

11. Visual analysis showed that the general agreement between the experimental and numerical results for axial Reynolds shear stresses is very good for both pitches and

both configurations. The agreement between the experimental and numerical tangential Reynolds shear stress (u’w’) profiles was not as good as in the case of the axial shear stress (u’v’), thus indicating that the swirl component is more difficult to predict. Overall, tangential shear stress was found to be weaker than the axial shear stress. This shows the significance of the gradient of the axial velocity component (u’), which seems to play a more important role in production of shear stress than the swirl velocity gradient. The radial Reynolds shear stress was found to be the weakest of the three Reynolds shear stress components, reflecting the lack of influence of the radial fluctuating component (v’) on swirling flows.

Chapter 9

Conclusions

The current practice of predicting likely exit NOx levels from multi-burner furnaces on the basis of single burner test rig data has been proven inadequate. This is due to effect of burner interactions that occur in multi-burner furnaces. Therefore, to further improve current NOx reduction technologies and gain an improved understanding of the impact of burner interactions, the research of isothermal turbulent flows in interacting low NOx burners in coal-fired furnaces was undertaken.

The aim of this research was to, firstly, experimentally investigate isothermal flow interactions in multi-burner arrays for different swirl directions and burner pitches, and secondly, to carry out numerical modelling in order to determine turbulence models which give the best agreement to experimental data. Experimental investigations were carried out using flow visualisation for qualitative and 3D laser Doppler anemometry for quantitative measurements. Numerical modelling was performed using the

computational fluid dynamics software, Fluent, to compare performance between k-ε, k- ω and RSM turbulence models.
Conclusions of the experimental and numerical investigations are detailed below.

9.1 Conclusions of experimental analysis

1. Flow visualization analysis showed that the burner jet interaction is directly related to the pitch size. For 1.6d pitch, interaction between adjacent burner flows occurred almost immediately upon leaving the burner exit.

2. The analysis of axial velocity profiles obtained using 3-D LDA showed that a decrease in pitch from 2d to 1.6d causes the width of the recirculation zone, measured at 0.5d distance from the burner exit plane, to decrease by 20% for the chequerboard configuration and 7% for the columnar configuration. It was found that a decrease in pitch from 2d to 1.6d causes the extent of the recirculation, measured along the central burner line, to decrease by 45% for the chequerboard configuration and 26% for the columnar configuration.

It was found that the effect of burner configuration is much more evident in the case of the 1.6d pitch than 2d pitch. For 1.6d pitch, both the width and the extent of recirculation are higher in the columnar configuration case by 10% and 25% respectively. The opposite trend is observed for 2d pitch, where both the width and the extent are lower for the columnar configuration, but only by 4% and 1% percent respectively.

3. The analysis of the radial velocity profiles showed peak values occurring at the edges of the burner quarl, at the burner exit. Downstream of x=0 axial position, radial velocity profiles became insignificant in both shape and magnitude.

4. Swirl velocity profiles decayed faster for the 2d pitch than for the 1.6d pitch, as the flow moved away from the burner exit. It was found that swirl velocities, measured at the burner exit, were higher for the chequerboard configuration than for the columnar, for both 1.6d and 2d pitches.

5. The analysis of fluctuating components, u′, v′ and w′ showed that the burner flow is highly anisotropic at the burner exit. Profiles of turbulence fluctuations taken at axial stages beyond x=0.5d, however, show an increase in isotropic behaviour of fluctuating components.

6. The analysis of the turbulent kinetic energy profiles showed that differences between the chequerboard and columnar configurations were more evident across the central and upper burner than the lower burner, for both 1.6d and 2d pitches. The turbulent kinetic energy magnitudes peaked at the burner exit, while the profiles decayed downstream of x>0.5d.

7. At the burner exit, the radial distribution of tangential shear stress, u′w′, showed much higher peak values than the axial shear stresses, illustrating the importance of the role the tangential shear plays in the swirling flow. The maxima of tangential shear decayed faster than those of axial shear. This applied to both 1.6d and 2d pitches. It was found that v′w′ stress component is the weakest of the three shear stress components; however, it is still significant, especially at the burner exit, where the mean radial velocity component has the highest magnitude.

8. It was found that that the shear stresses are influenced by the recirculation zone and that the stress magnitudes increased closer the exit of the recirculation zone.

9.2 Conclusions of numerical analysis

1. Visual analysis of vertical axial velocity profiles obtained for 1.6d and 2d pitches of chequerboard and columnar configurations showed that the k-ω turbulence model gives an inferior fit to the experimental data compared to the k-ε and RSM turbulence models. This is especially evident at x=0 (burner exit) and x=0.5d distance from the burner exit.

2. Analysis of vertical axial velocity profiles obtained using the k-ε and RS turbulence models shows that, at the burner exit, there is almost no difference between the two

profiles. Both the k-ε and RSM turbulence models showed good agreement with peak velocities obtained experimentally. However, both models slightly under-predict the velocities across the recirculation zones. Overall, both models matched the experimental data reasonably well.

3. Analysis of horizontal axial velocity profiles showed that the decay of the centre-line velocity was well predicted by both the k-ε and RS turbulence models in all but one case - the 1.6d, chequerboard configuration. In this case, the differences between the numerical results were most evident, and neither of the two models predicted the decay accurately. The k-ω turbulence model provided the worst match to the experimental data.

4. Analysis of vertical profiles of radial velocity (v) at the burner exit showed that, whilst all three turbulence models provided a very good overall match to the experimental data, the k-ω turbulence model prediction was, again, the worst of the three, with slightly under-predicted peak velocities in all four cases (i.e. for both pitches and both configurations).

5. Analysis of vertical swirl velocity profiles shows that the k-ω turbulence model gives inferior performance compared to the k-ε and RSM model. There is no significant difference between the RS turbulence model over the k-ε and vice versa. The analysis of the data downstream of the burner exit shows that the predicted data by all three turbulence models provided a much better match to the experimental data in case of the 1.6d and 2d pitches of columnar configuration than in case of the 1.6d and 2d pitches of the chequerboard configuration.

6. Statistical analysis showed that, at x=0.5d distance, RSMEs are lower for the axial velocity profiles than for the swirl velocity profiles, indicating that the numerical models are more accurate in predicting axial velocity component, and are less successful in predicting complex, swirl velocities. An exception was observed in the case of the wide pitch (2d), columnar case, where all three turbulence models provided a close fit to the experimental swirl velocity profiles.

7. Statistical analysis for axial velocity profiles showed that, at x=0.5d distance, the RSME values do not vary greatly between different pitches and configurations. This was not observed for swirl velocity profiles. It was found that swirl velocities are better predicted for wider-pitch geometry. The analysis showed that swirl velocity profiles obtained for the chequerboard configurations are more difficult predict than those obtained for the columnar configurations.

8. Results of the statistical analysis confirmed the findings of the visual analysis highlighting the k-ω turbulence model as the least accurate fit to the experimental data.

9. Statistical comparison between the k-ε and RSM turbulence models revealed that, for prediction of the axial velocity profiles, neither of the models showed clear advantage. The advantage of the RSM turbulence model was more clearly demonstrated in relation to the swirl velocity profiles, with the RSM model consistently performing better than the k-ε turbulence model, with the exception of the 2d, columnar configuration case, where the two models performed evenly.

10. Visual analysis of the turbulent kinetic energy profiles showed that the RS turbulence model provided a closer match to the experimental data than the k-ε turbulence model. This was especially evident in the case of the 1.6d pitch of chequerboard configuration.

11. Visual analysis showed that the general agreement between the experimental and numerical results for axial Reynolds shear stresses is very good for both pitches and both configurations. The agreement between the experimental and numerical tangential Reynolds shear stress (u′w′) profiles was not as good as in the case of the axial shear stress (u′v′), thus indicating that the swirl component is more difficult to predict. Overall, tangential shear stress was found to be weaker than the axial shear stress. This shows the significance of the gradient of the axial velocity component (u′), which seems to play a more important role in production of shear stress than the swirl velocity gradient. The radial Reynolds shear stress was found to be the weakest of the three Reynolds shear stress components, reflecting the lack of influence of the radial fluctuating component (v′) on swirling flows.

9.3 Recommendations for future work

The findings that arose from this project relating to the experimental and numerical analysis of the turbulent quantities represent a major advance to the previously published work. It has been found that swirl flows in multi-burner furnaces can be most accurately predicted using the RSM turbulence model. Implementation of this turbulence model in combustion modelling could help more accurate prediction of NOx levels in multi burner furnaces.

It is, therefore, essential that the combustion modelling is carried out in order to determine the sensitivity of the combustion models to the underlying turbulence models. Further, the effects of using the experimentally obtained Reynolds stress components as input data in the RSM turbulence model should be studied.

Particle Image Velocimetry (PIV) has not been done as part of this project. Performing PIV could help create a better understanding of the flow behaviour in a multi-burner furnace.

Finally, Large Eddy Simulation (LES) could be carried out investigate the effect of multi-burner interactions on large, energy-containing eddies.

9.3 Publications arising from the project

My PhD research was awarded the Lord Ezra Award for the outstanding achievement in combustion engineering, at the House of Lords in November 2003.

The project was selected for presentation as one of the top 100 UK engineering projects as part of the Set for Britain competition at the House of Commons in December 2003.

A paper presenting the findings of my research was published in Fuel 82 (2003). A copy of the paper is attached in the Appendix F.

References

Abbas T., Costen P., Hassan M.A. and Lockwood F.C. "The effect of the near burner aerodynamics on pollution stability and combustion in a PF-fired furnace", Combustion Science and Technology, 93, 73-90, 1993

Abbas T., Costa M., et al. "NOx formation and reduction-mechanisms in pulverised coal flames", Fuel, 73, Iss. 9, 1423-1436, 1994

Abramovich, G. N., "The theory of turbulent jets", The MIT Press, Cambridge, Massachusetts, 1963

Ahmed, S.A, "Three component velocity measurements of an isothermal confined swirling flow", Proceedings Institution of Mechanical Engineers, Vol. 211, Part G, IMechE, 1997

Ahlstedt, H., "A comparison of three turbulence models for axysymmetric isothermal swirling flows in the near burner zone", Fourth International Symposium on Process Simulation – Computational Fluid Dynamics Coupled with Chemical Kinetics, Combustion and Thermodynamics, 505-530, 1997

Al-Abdeli Y.M. and Masri A.R., "Stability characteristics and flowfields of turbulent non-premixed swirling flames", Combustion Theory and Modelling, 7, 731-766, 2003

Al-Abdeli Y.M. and Masri A.R., "Precession and recirculation in turbulent swirling isothermal jets", Combustion Science and Technology, Volume 176, Number 5-6, Pages: 645 – 665, May–June 2004

Allen, G. "Combustion development of an industrial scale burner with particular reference to coal blends and co-firing coal with natural gas and sawdust", Atmospheric Combustion of Pulverised Coal and Coal Based Blends for Power Generation", EU Joule II Final Report for Project No JOU2-CT93-0380, 1996

Allen, R.A. "Aerodynamics and interactions of a single and multiple jets with swirl", PhD Thesis, Department of Chemical Engineering & Fuel Technology, Sheffield University, GB, 1970

Aroussi A., Pickering S.J. and Tarr S. "Momentum interchange in a burner bank", Fuel, 79, 1439-1448, 2000

Baker R. J, Bourke, P. J. and Whitelaw J. H., "Measurements of instantaneous velocity in laminar and turbulent diffusion flames using an optical anemometer", Journal of the Institute of Fuel, p.388-395, December 1973

Baker* R. J, Hutchinson P. and Whitelaw J. H., Proceedings European Symposium on Combustion, p.583, Academic Press, 1973

Baker R. J, Hutchinson P., Khalil E. E. and Whitelaw J. H. "Measurements of three velocity components in a model furnace with and without combustion", 15th Symposium on Combustion, The Combustion Institute, Pittsburgh, 1974

Bakker, André, Applied Computational Fluid Dynamics, Fluent Lecture Notes, 2005

Becker, H. A. and Brown, A. P. G., "Velocity Fluctuations in Turbulent Jets and Flames", Twelfth Symposium (International) on Combustion, p.1059, The Combustion Institute, 1969

Beer, J. M. and Chigier, N. A., "Combustion aerodynamics", Applied Science Publishers, London, 1972

Birkhoff, G. and Zarantonello, E. H., "Jets, wakes and cavities", Academic Press Inc, New York, 1957

Bolletini, U., Breussin, F.N. and Weber, R., “A study on scaling of natural gas burners”, IFRF Combustion Journal, Article number 200006, ISSN 1562-479, 2000

Breussin, F., Pigari, F. and Weber, R., “Predicting of the near-burner-zone flow field and chemistry of swirl-stabilised low-NOx flames of pulverised coal using the RNG-k-ε, RSM and k-ε turbulence models”, Twenty-Sixth Symposium on Combustion, The Combustion Institute, 211-217, 1996

Cazalbou, J. B., Spalart, P. R. and Bradshaw, P., “On the behaviour of two-equation models at the edge of turbulent region”, Phys. Fluids, 6, 1797-1804, 1994

Chigier, N. A. and Apak, G. “Interaction of multiple turbulent diffusion flames”, Combustion Science and Technology, 10, 219-231, 1975

Chigier, N. A. and Beér, J. M. “Velocity and static pressure distributions in swirling air jets issuing from annular and divergent nozzles”, Journal of Basic Engineering, 4, 788, 1964 [Paper].

Chigier, N. A. and Chervinsky, A. “Experimental investigation of swirling vortex motion in jets”, Journal of Applied Mech., 34, 443-451, 1967

Chigier, N. A. and Dvorak K. " Laser anemometer measurements in flames with swirl", 15th Symposium on Combustion, The Combustion Institute, Pittsburgh, 1974

Chigier, N. A and Gilbert, J. L. Journal of Inst. Fuel, 41, 105, 1968

Cvoro, V. C. and Easson, W. J., “Optimisation Of Furnace Design For In-Furnace NOx Reduction: The Effect Of Burner Array Configuration On Multiple Burner Jet Interactions”, International Conference on Clean Coal Technologies (CCT), Sardinia, Italy, 2002

Duggins, R. K., “A comparison of turbulence models for swirling flows”, Second International Conference on Fluid Mechanics, 73-77, 1993

Duncan A, Easson WJ and Cvoro V, 2002, Optimisation of Furnace Design for In-Furnace NOx Reduction, Report No. E/01/076, Project 78567/D001, DTI Cleaner Coal R&D Programme, 2001

Durão, D. F. G, Heitor, M. V. and Moreira, A. L. N., "Flow measurements in a model burner – part 1", Journal of Fluids Engineering, 113, 668-674, 1991

Durão, D. F. G, Heitor, M. V. and Moreira, A. L. N., "Flow measurements in a model burner – part 2", Journal of Fluids Engineering, 115, 309-316, 1993

Durbin, P. A. and Patterson Reif, B. A., Statistical theory and modeling for turbulent flows, John Wiley and Sons, 2001

Durrani, T. S. and Greated, C. A., Laser systems in flow measurements, Plenum Press, New York, 1977

Durst, F., Melling, A. and J.H. Whitelaw, "Principles and practice of laser Doppler anemometry", Academic Press, London, 1976

Easson, W.J. "Measurement of the flow field around flame stabilisers in an isothermal low NOx burner", Atmospheric Combustion of Pulverised Coal and Coal Based Blends for Power Generation", EU Joule II Final Report for Project No JOU2-CT93-0380, 1996

FLUENT 6 User's Guide, Fluent Europe Ltd

German, A. E. and Mahmud, T., "Modelling of non-premixed swirl burner flows using a Reynolds-stress turbulence closure", Fuel, 84, 583-594, 2005

Goldstein, S., "Modern developments in fluid dynamics", Dover Publications Inc, New York, 1965

Gray, C., Greated, C.A., McCluskey, D.R. and Easson, W.J., "An Analysis of the Scanning Beam PIV Illumination System", J. Phys. Measurement Science and Technology 2, 717-724, 1991

Gunther, R. and Simon, H., "Turbulence Intensity, Structural Density Functions and Eulerian Scales of Emission in Turbulent Diffusion Flames", Twelfth Symposium (International) on Combustion, p.1069, The Combustion Institute, 1969

Gupta, A. K., Lilley, D. G. and Syred, N., Swirl Flows, Abacus Press, 1984

Gupta, A. K. and Lilley, D. G., "Flowfield modelling and diagnostics, Abacus Press, 1985

Gutmark, E. J., Li, G. and Grinstein, F. F., "Characterisation of multi-swirling flow", Fifth International Symposium on Engineering Turbulence Modelling and Measurements, 873-884, 2002

Hart, J., Naser, J., Witt, P. and Mittoni, L, "Numerical modelling of isothermal burner jets", Second International Conference on CFD in the Mineral and Process Industries, 135-140, CSIRO, Melbourne, Australia, 1999

Heitor, V. and Moreira, A. L. N., "On the analysis of turbulent transport processes in multi-jet burners", Experiments in Fluids, 13, 179 – 189, 1992

Hwang, C. C., Genxing, Z., Massoudi, M. and Ekmann, J. M., "A comparison of the linear and nonlinear k-ε turbulence models in combustors", Journal of Fluids Engineering, 115, 93-102, 1993

IEA, CIAB, "The Future of Coal – Mining Costs and Productivity" by R. Humphris, Future of coal, 1999

IEA, CIAB, Investment in the coal industry, Coal Industry Advisory Board, 2003

IEA, CIAB, Reducing greenhouse gas emissions - the potential of coal, 2005

IEA–Clean Coal, http://www.iea-coal.org.uk/content/default.asp?PageId=97

IEA*, Working Group on Fossil Fuels, Control and minimisation of coal-fired power plant emissions, 2003

Kihm, K.D., Chigier, N. and Sun, F., "Laser Doppler Velocimetry Investigation of Swirler Flowfields", Journal of Propulsion and Power, 6, 346-374, 1990

Kucukgokoglan, S. and Aroussi, A., "Investigation of interaction of swirling burner flows in a model furnace", Sixth Asian Symposium on Visualisation, Paper 013, Pusan, 2001

Kucukgokoglan, S., Aroussi, A., Pickering, S. J. and Menacer, M., "Prediction of interactions between burners in multi-burner systems", Second International Symosium on Multi-Phase Flow and Transport Phenomena, 589-593, 2001

Lai, J. C. S. and Nasr, A., "Two parallel plane jets: comparison of the performance of three turbulence models", Proc. Inst. Mech. Eng., Vol. 212, Part G, 1998

Laurence, J. C. and Benninghoff, J. M., "Turbulence measurements in multiple interfering air jets", NACA, TN. 4029, 1957

Lilley, D. G. and Chigier, N. A., "Nonisotropic turbulent stress distribution in swirling flows from mean value distributions", Journal of Heat and Mass Transfer, 14, 573-585, 1971

Liu, W. M., Ruprecht, A. and Gode, E., "Comparison of different models of turbulence for confined turbulent swirling flows", Fourth International Symposium on Experimental and Computational Aerothermodynamics on Internal Flows, 2, 68-77, 1999

Lockwood F.C. and Parodi S.A. " Burner-burner interaction", Final Technical Report, Performance Prediction in Advanced Coal Boilers, Contract No JOF3-CT95-005, Project Area 1-Project 110, The Imperial College of Science, Technology and Medicine, London, 1998

Lockwood F.C. and Shen, B., "Performance predictions of pulverised-coal flames of power station furnace and cement kiln types", Twenty-Fifth Symposium on Combustion, The Combustion Institute, 503-509, 1994

Massey, B. S., "Mechanics of fluids", Van Nostrand Reinhold (UK) Co. Ltd., 1968

McCluskey, D, An optical investigation of air-particle flows, Thesis (Ph.D), University of Edinburgh, 1992

Menter, F. R., Zonal two-equation k-ω turbulence models for aerodynamic flows, AIAA-93-2906, 1993

Merkzkirch, W., Flow Visualisation, Academic Press, New York and London, 1974

Nasr, A. and Lai, J. C. S., "Two parallel plane jets: mean flow and effects of acoustic excitation", Experiments in Fluids, 22, 251-260, 1997

Pai, S., "Fluid dynamics of jets", Ph.D., Van Nostrand Company (Canada), 1954

Prandtl, L. (Tietjens, O.G), "Fundamentals of hydro- and aerodynamics", Dover publications Inc., New York, 1934

Orsino, S. and Weber, R., "Scaling of low-NOx flames of natural gas", IFRF Combustion Journal, Article Number 200005, ISSN 1562-479X, 2000

Riahi, A., Salcudean, M. and Hill, P. G., "Computer simulation of turbulent swirling flows", International Journal for Numerical Methods in Engineering, 29, 533-557, 1990

Rouse, H., “Advanced mechanics of fluids”, John Wiley and Sons Inc., New York, 1959

Sampath, S. and Ganesan, V., “Measurement of velocity and kinetic energy of turbulence in swirling flows and their numerical prediction”, International Journal for Numerical Methods in Fluids, 6, 229-240, 1986

Schneider, C., Dreizler, A. and Janicka J., “Fluid dynamical analysis of atmospheric reacting and isothermal swirling flows”, Flow, Turbulence and Combustion, 74, 103-127, 2005

Sharif, M. A. R. and Wong, Y. K. E., “Evaluation of the performance of three turbulence closure models in the prediction of confined swirling flows”, Computers and Fluids, 24, 81-100, 1995

Sloan, D. G., Smith, P. J. and Smoot, L. D.,”Modelling of swirl in turbulent flow systems”, Prog. Energy Combust. Sci., 12, 163-250, 1986

Smart J.P. “Some simple considerations on the turbulent mixing process in relation to flame-scaling”, Journal of the Institute of Energy, 71, pp 152-155, 1998

Syred, N., Chigier, N.A., and Beer, J.M., Thirteenth Symposium on Combustion, p 617, The Combustion Institute, 1971

Szasz, R. Z., Fuchs, L. and Caraeni, D. A., “Study of mixing in swirling turbulent jets”, IUTAM Symposium on Turbulent Mixing and Combustion, Fluid Mechanics and its Applications, 70, 221-233, 2002

Tarr S.J. and Allen G. “Flame Interactions”, Final Technical Report, Performance Prediction in Advanced Coal Boilers, Contract No JOF3-CT95-005, Project Area 1-Project 109, Derby, 1997

Tritton, D. J., “Physical fluid dynamics”, Van Nostrand Reinhold (UK) Co. Ltd., 1977

Truelove, J. S., T. F. Wall, Dixon, T. F., and Stewart I. McC., "Flow, mixing and combustion within the quarl of a swirled, pulverised-coal burner", Nineteenth Symposium (International) on Combustion, p.1181, The Combustion Institute, 1982

United States Environmental Protection Agency, Control of mercury emissions from coal-fired electric utility boilers, www.epa.gov, EPA-600/R-01-109, 2002

Vranos, A, Faucher, J.E. and Curtis, W.E., "Turbulent Mass Transport and Rates of Reaction in a Confined Hydrogen-Air Diffusion Flame", Twelfth Symposium (International) on Combustion, p.1051, The Combustion Institute, 1969

Weber, R. and Breussin, F., "Scaling properties of swirling pulverised coal flames: from 180 kW to 50 MW thermal input", International Flame Research Foundation, Twenty-Seventh Symposium (International) on Combustion, The Combustion Institute, p. 2957-2964, 1998

Williams, G.C., Hottel, H.C. and Gurnitz, R.N., "A Study of Premixed Turbulent Flames by Scattered Light", Twelfth Symposium (International) on Combustion, p.1081, The Combustion Institute, 1969

Yang, S. L., Siow, Y. K. Peschke, B. D. and Tacina R. R., "Numerical study of non-reacting gas turbine combustor swirl flow using Reynolds stress model", Journal of Engineering for Gas Turbines and Power – Transactions of ASME, 125, 804-811, 2003

Yeh, L. K. and Lin, C. A, "Turbulence modelling of strongly swirling flows", First International Conference on Computational Fluid Dynamics, 779-780, 2001

Appendix A

A.1 Equations of motion of a viscous compressible fluid

By the second law of motion that the total force acting on a fluid mass enclosed in an arbitrary volume V fixed in space is equal to the rate of change of linear momentum, we obtain the equations of motion of a viscous compressible fluid as follows:

$$\rho \frac{Du_i}{Dt} = \rho\left(\frac{\partial u_i}{\partial t} + u_j \frac{\partial u_i}{\partial x_j}\right) = -\rho X_i + \frac{\partial \tau_{ij}}{\partial x_j} \tag{A.1}$$

where,

X_i represents the i^{th} component of the body force per unit mass and
$\frac{\partial \tau_{ij}}{\partial x_j}$ represents within V due to internal stresses.

The summary convention is used in (A.1), for example, $\frac{\partial u_i}{\partial x_i} = \frac{\partial u_1}{\partial x_1} + \frac{\partial u_2}{\partial x_2} + \frac{\partial u_3}{\partial x_3}$ where

ui are the velocity components along the xi axis (i=1, 2, or 3).

According to the Navier-Stokes assumption that the stress τ_{ij} is proportional to the strain, in the theory of the mechanics of a viscous fluid, the following equations apply:

$$\begin{aligned} \tau_{ij} &= \tau_{ij}' - p\delta_{ij} \\ \tau_{ij}' &= \mu\left(\frac{\partial u_i}{\partial x_j} + \frac{\partial u_j}{\partial x_i}\right) + \mu_1\left(\frac{\partial u_k}{\partial x_k}\right)\delta_{ij} \end{aligned} \tag{A.2}$$

where μ and μ1 are the coefficients of viscosity and are in general functions of p, ϱ and T. δij=0, i ≠ j; δij=1, i = j. i, j, k = 1, 2, or 3.

Another assumption, usually made is:

$$3\mu_1 + 2\mu = 0 \qquad \text{(A.3)}$$

which means that there is no dissipation of energy in a spherically symmetrical expansion or contraction, implying only one coefficient of viscosity.

Substitution of (A.2) and (A.3) into (A.1) gives the Navier-Stokes equations of motion for a compressible fluid (Pai, 1954).

A.2 Reynolds equations of motion of turbulent flow

The Reynolds equations for incompressible fluids are:

$$\begin{aligned}
\rho\frac{D\overline{u}}{Dt}+\frac{\partial\rho\overline{u'^2}}{\partial x}+\frac{\partial\rho\overline{u'v'}}{\partial y}+\frac{\partial\rho\overline{u'w'}}{\partial z}&=-\frac{\partial\overline{p}}{\partial x}+\mu\nabla^2\overline{u}\\
\rho\frac{D\overline{v}}{Dt}+\frac{\partial\rho\overline{u'v'}}{\partial x}+\frac{\partial\rho\overline{v'^2}}{\partial y}+\frac{\partial\rho\overline{v'w'}}{\partial z}&=-\frac{\partial\overline{p}}{\partial y}+\mu\nabla^2\overline{v}\\
\rho\frac{D\overline{w}}{Dt}+\frac{\partial\rho\overline{u'w'}}{\partial x}+\frac{\partial\rho\overline{v'w'}}{\partial y}+\frac{\partial\rho\overline{w'^2}}{\partial z}&=-\frac{\partial\overline{p}}{\partial z}+\mu\nabla^2\overline{w}
\end{aligned} \qquad \text{(A.4)}$$

Appendix B

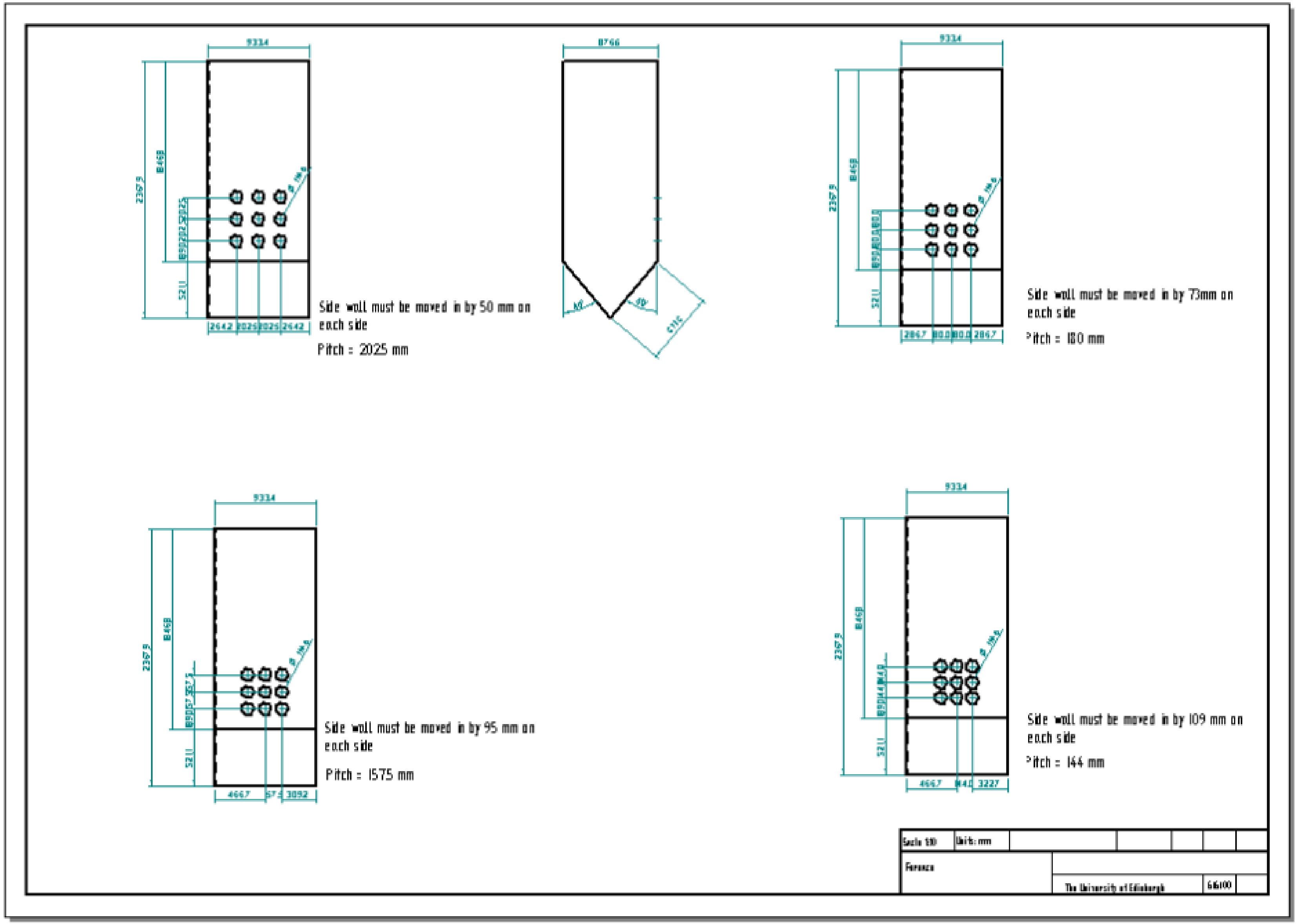

Figure B.1 *Furnace front panels with four different pitching arrangements*

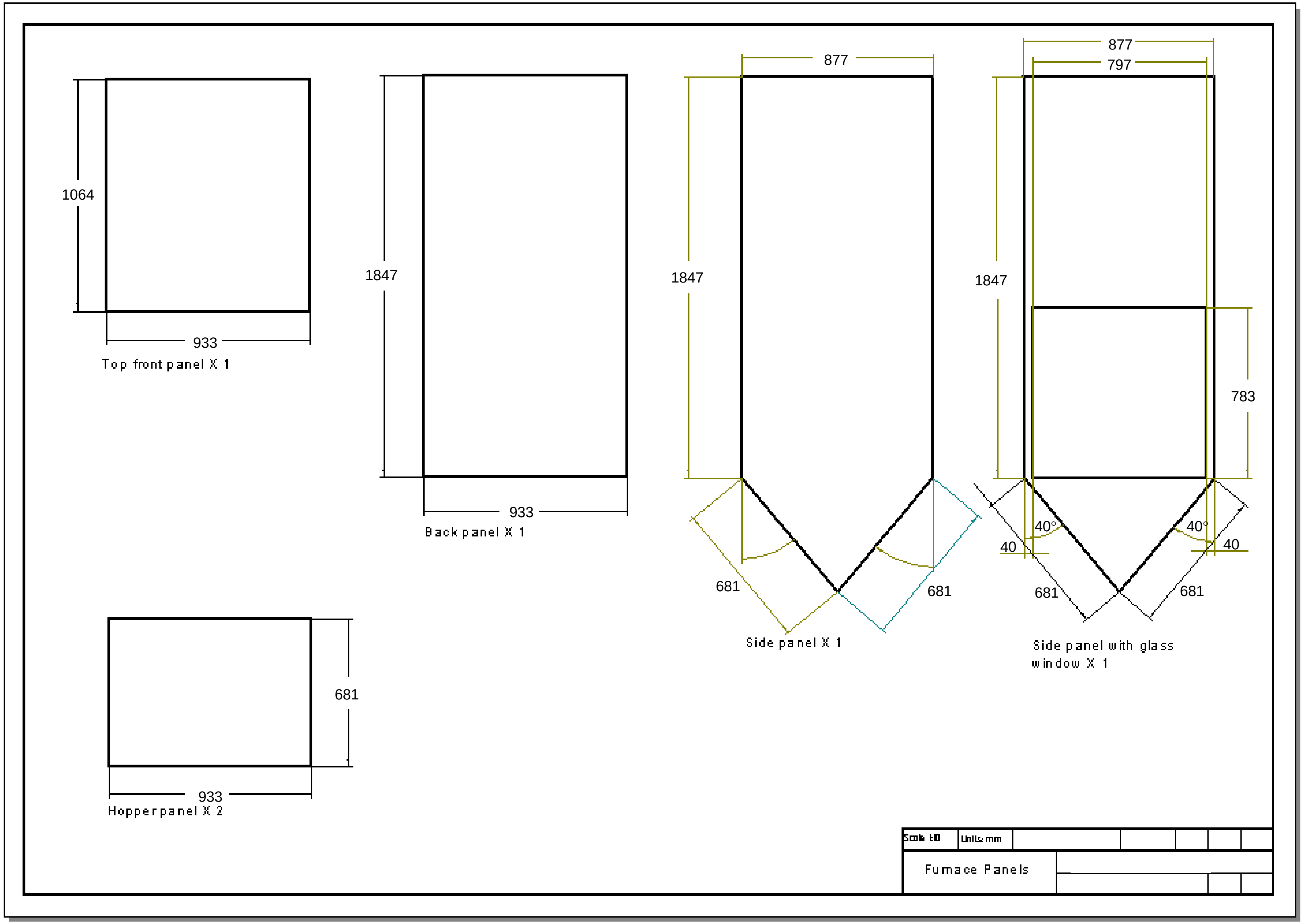

Figure B.2 *Furnace assembly*

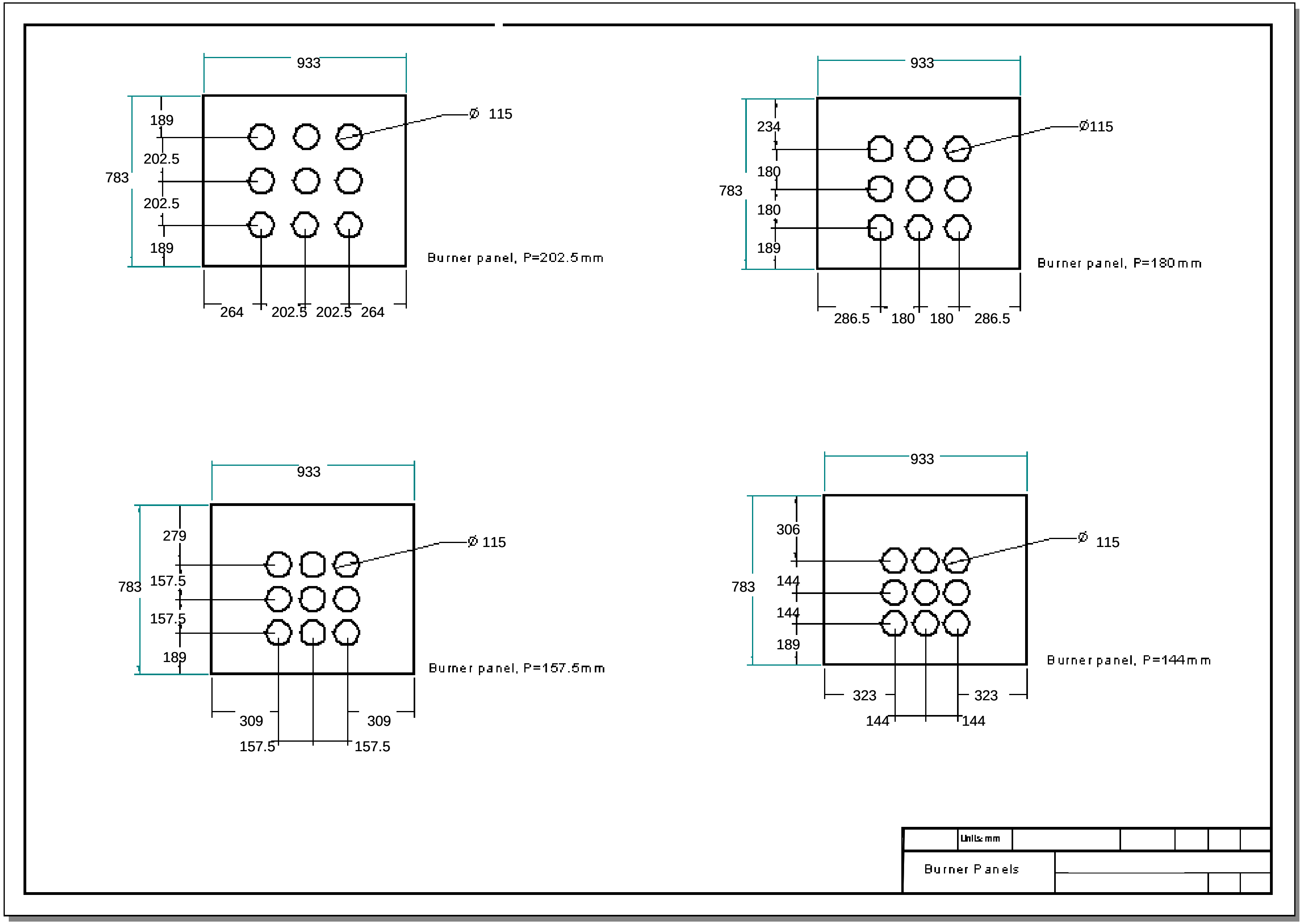

Figure B.3 *Burner panels with four different pitching arrangements*

Appendix C

C.1 Equations for the k-ε turbulence model

Fluent lecture notes (Bakker, 2005) have been used as a reference to describe the governing equations of turbulence models.

C.1.1 Boussinesq hypothesis

Many turbulence models are based upon the Boussinesq hypothesis. It was experimentally observed that turbulence decays unless there is shear in isothermal incompressible flows. Turbulence was found to increase as the mean rate of deformation increases. In 1877, Boussinesq proposed that the Reynolds stresses could be linked to the mean rate of deformation.

Using the suffix notation where i, j, and k denote the x-, y-, and z-directions respectively, viscous stresses are given by:

$$\tau_{ij} = \mu\, e_{ij} = \mu\left(\frac{\partial u_i}{\partial x_j} + \frac{\partial u_j}{\partial x_i}\right) \tag{C.1}$$

Similarly, linking Reynolds stresses to the mean rate of deformation gives:

$$\tau_{ij} = -\rho\overline{u_i' u_j'} = \mu_t\left(\frac{\partial U_i}{\partial x_j} + \frac{\partial U_j}{\partial x_i}\right) \tag{C.2}$$

A new quantity appears - the turbulent viscosity μ_t. The turbulent viscosity is also known as eddy viscosity, and unit is the same as that of the molecular viscosity: Pa.s.

We can also define a kinematic turbulent viscosity: $\nu_t = \mu_t / \varrho$. Its unit is m^2/s. The turbulent viscosity, whilst it is not homogeneous (it varies in space), it is assumed to be isotropic (it is the same in all directions). This assumption is valid for many flows, but not for all (e.g. flows with strong separation or swirl).

C.1.2 Equations for the k-ε turbulence model

The k-ε model focuses on the mechanisms that affect the turbulent kinetic energy (per unit mass), k. The instantaneous kinetic energy k(t) of a turbulent flow is the sum of mean kinetic energy K and turbulent kinetic energy, k:

$$\begin{aligned} K &= \tfrac{1}{2}\left(U^2 + V^2 + W^2\right) \\ k &= \tfrac{1}{2}\left(\overline{u'^2} + \overline{v'^2} + \overline{w'^2}\right) \\ k(t) &= K + k \end{aligned} \tag{C.3}$$

ε is the dissipation rate of k. If k and ε are known, the turbulent viscosity can be modelled as:

$$\nu_t \;\propto\; \vartheta \ell \;\propto\; k^{1/2} \frac{k^{3/2}}{\varepsilon} \;=\; \frac{k^2}{\varepsilon} \tag{C.4}$$

where, $\nu_t(m^2/s) \;\propto\; \vartheta(m/s)\,\ell(m)$ is the kinematic turbulent viscosity expressed as the product of a velocity scale and a length scale, on dimensional grounds.

C.1.2.1 Equations for mean flow kinetic energy, K

The equation for the mean kinetic energy is as follows:

$$\underset{(I)}{\frac{\partial(\rho K)}{\partial t}} + \underset{(II)}{div(\rho K\mathbf{U})} \;=\; div\left(\underset{(III)}{-P\mathbf{U}} + \underset{(IV)}{2\mu\mathbf{U}E_{ij}} - \underset{(V)}{\rho\mathbf{U}\overline{u_i'u_j'}}\right) - \underset{(VI)}{2\mu E_{ij}.E_{ij}} - \underset{(VII)}{(-\rho\overline{u_i'u_j'}.E_{ij})} \tag{C.5}$$

where, E_{ij} is the mean rate of deformation tensor.

Equation (C.5) can be read as:

(I) the rate of change of K, plus
(II) transport of K by convection, equals
(III) transport of K by pressure, plus
(IV) transport of K by viscous stresses, plus
(V) transport of K by Reynolds stresses, minus
(VI) rate of dissipation of K, minus
(VII) turbulence production.

C.1.2.2 Equations for turbulent kinetic energy, k

The equation for the turbulent kinetic energy k is as follows:

$$\underset{(I)}{\frac{\partial(\rho k)}{\partial t}} + \underset{(II)}{div(\rho k\mathbf{U})} = div\left(-\underset{(III)}{\overline{p'\mathbf{u}'}} + \underset{(IV)}{2\mu\overline{\mathbf{u}'e_{ij}'}} - \underset{(V)}{\rho\tfrac{1}{2}\overline{u_i'.u_i'u_j'}}\right) - \underset{(VI)}{2\mu\overline{e_{ij}'.e_{ij}'}} + \underset{(VII)}{(-\rho\overline{u_i'u_j'}.E_{ij})} \qquad \text{(C.6)}$$

where, e_{ij}' is fluctuating component of rate of deformation tensor.

Equation (C.6) can be read as:

(I) the rate of change of k, plus
(II) transport of k by convection, equals
(III) transport of k by pressure, plus
(IV) transport of k by viscous stresses, plus
(V) transport of k by Reynolds stresses, minus
(VI) rate of dissipation of k, plus
(VII) turbulence production.

C.1.2.3 Model equation for turbulent kinetic energy, k

The equation for k contains additional turbulent fluctuation terms, which are unknown. Again, using the Boussinesq assumption, these fluctuation terms can be linked to the mean flow.

The following (simplified) model equation for k is commonly used:

$$\underset{(I)}{\frac{\partial(\rho k)}{\partial t}} + \underset{(II)}{div(\rho k\mathbf{U})} = \underset{(III)}{div\left[\frac{\mu_t}{\sigma_k} grad\ k\right]} + \underset{(IV)}{2\mu_t E_{ij}.E_{ij}} - \underset{(V)}{\rho\varepsilon} \tag{C.7}$$

where,

(I)	is the rate of increase
(II)	is convective transport
(III)	is diffusive transport
(IV)	is the rate of production
(V)	is the rate of destruction.

The Prandtl number, σ_k, connects the diffusivity of k to the eddy viscosity. Typically, a value of 1 is used.

C.1.2.4 Turbulent dissipation and dissipation rate, ε

Whilst the equations for K and k look quite similar, the k equation mainly contains primed quantities, indicating that changes in k are mainly governed by turbulent interactions. Furthermore, term (VII) appears equal in both equations, but it is actually negative in the K equation (destruction) and positive in the k equation (energy transfers from the mean flow to the turbulence).

The viscous dissipation term (VI) in the k equation $-2\mu\overline{e_{ij}'.e_{ij}'}$ describes the dissipation of k because of the work done by the smallest eddies against the viscous stresses.

The rate of dissipation per unit mass, ε, can then be defined as:

$$\varepsilon = 2\nu\overline{e_{ij}'.e_{ij}'} \tag{C.8}$$

Since the analytical equation for ε is extremely complex, containing many unknown higher order terms, this equation can not be solved, and simplified model equations need to be derived.

A model equation for ε is derived by multiplying the k equation by (ε/k) and introducing model constants.

The following (simplified) model equation for ε is commonly used:

$$\underset{(I)}{\frac{\partial(\rho\varepsilon)}{\partial t}} + \underset{(II)}{div(\rho\varepsilon\mathbf{U})} = \underset{(III)}{div\left[\frac{\mu_t}{\sigma_\varepsilon} grad\ \varepsilon\right]} + \underset{(IV)}{C_{1\varepsilon}\frac{\varepsilon}{k}2\mu_t E_{ij}.E_{ij}} - \underset{(V)}{C_{2\varepsilon}\rho\frac{\varepsilon^2}{k}} \qquad \text{(C.9)}$$

where,

(I) is the rate of increase

(II) is convective transport

(III) is diffusive transport

(IV) is the rate of production

(V) is the rate of destruction.

The Prandtl number, σ_ε, connects the diffusivity of ε to the eddy viscosity. Typically, a value of 1.3 is used. Typical values of 1.44 and 1.92 for the model constants, C1ε and C2ε, are used.

C.1.2.5 Calculating the Reynolds stresses from k and ε

The turbulent viscosity is calculated from:

$$\mu_t = C_\mu \frac{k^2}{\varepsilon} \qquad C_\mu = 0.09 \qquad \text{(C.10)}$$

The Reynolds stresses are then calculated as follows:

$$-\rho\overline{u_i' u_j'} = \mu_t\left(\frac{\partial U_i}{\partial x_j} + \frac{\partial U_j}{\partial x_i}\right) - \frac{2}{3}\rho k\delta_{ij} = 2\mu_t E_{ij} - \frac{2}{3}\rho k\delta_{ij}$$

$$\delta_{ij} = 1 \quad if\ i = j \quad and \quad \delta_{ij} = 0 \quad if\ i \neq j \qquad \text{(C.11)}$$

The $(2/3)\rho k\delta_{ij}$ term ensures that the normal stresses sum to k. The shortfall of the k-ε model leads is that it leads to all normal stresses being equal, which is usually inaccurate.

C.2 Equations for the Reynolds stress (RSM) turbulence model

RSM closes the Reynolds-Averaged Navier-Stokes equations by solving additional transport equations for the six independent Reynolds stresses. Transport equations, derived by Reynolds, average the product of the momentum equations with a fluctuating property. Closure modelling also requires one equation for turbulent dissipation, with isotropic eddy viscosity assumption is avoided. Resulting equations contain terms that need to be modelled.

C.2.1 Reynolds stress transport equation

This equation describes six partial differential equations, one for the transport of each of the six independent Reynolds stresses. The exact equation for the transport of the Reynolds stress R_{ij}:

$$\underset{(I)}{\frac{DR_{ij}}{Dt}} = \underset{(II)}{P_{ij}} + \underset{(III)}{D_{ij}} - \underset{(IV)}{\varepsilon_{ij}} + \underset{(V)}{\Pi_{ij}} + \underset{(VI)}{\Omega_{ij}} \tag{C.12}$$

where,

(I) is the rate of change of $R_{ij} = \overline{u_i' u_j'}$ plus transport of R_{ij} by convection

(II) is the rate of production P_{ij}; this term is retained in its exact form

(III) is transport by diffusion D_{ij}; this term is modelled using a gradient diffusion assumption

(IV) is the rate of dissipation ε_{ij}; this term is related to ε as calculated from the standard ε equation, although more advanced ε models are also available

(V) is transport due to turbulent pressure-strain interactions π_{ij}; this term includes pressure fluctuations due to eddies interacting with each other, and due to interactions between eddies and regions of the flow with a different mean velocity. The overall effect is to make the normal stresses more isotropic and to decrease shear stresses. It does not change the total turbulent kinetic energy. This is a difficult term to model, and various models are available. The Launder model is most commonly used. Improved, non-equilibrium models are also available.

(VI) is transport due to rotation Ω_{ij}; this term is retained in its exact form.

C.2.1.1 Production equation

Exact:
$$P_{ij} = -\left(R_{im}\frac{\partial U_j}{\partial x_m} + R_{jm}\frac{\partial U_i}{\partial x_m} \right) \quad \text{(C.13)}$$

C.2.1.2 Diffusive transport equation

Exact:
$$D_{ij} = \frac{\partial J_{ijk}}{\partial x_k} \quad \text{(C.14)}$$

where,
$$J_{ijk} = \overline{u_i' u_j' u_k'} + \overline{p'(\delta_{jk} u_i' + \delta_{ik} u_j')} \quad \text{(C.15)}$$

Model:
$$D_{ij} = \frac{\partial}{\partial x_m}\left(\frac{\nu_t}{\sigma_k}\frac{\partial R_{ij}}{\partial x_m} \right) = div\left(\frac{\nu_t}{\sigma_k} grad(R_{ij}) \right) \quad \text{(C.16)}$$

where, ν_t is the turbulent kinematic viscosity calculated in the standard way.

C.2.1.3 Dissipation equation

Exact:
$$\varepsilon_{ij} = 2\mu \overline{\frac{\partial u_i'}{\partial x_k}\frac{\partial u_j'}{\partial x_k}} \quad \text{(C.17)}$$

Model:
$$\varepsilon_{ij} = \tfrac{2}{3}\varepsilon\delta_{ij} \quad \text{(C.18)}$$

C.2.1.4 Pressure strain equation

Exact:
$$\Pi_{ij} = -\overline{p'\left(\frac{\partial u_i'}{\partial x_j} + \frac{\partial u_j'}{\partial x_i} \right)} \quad \text{(C.19)}$$

Model:
$$\Pi_{ij} = -C_1 \frac{\varepsilon}{k}(R_{ij} - \tfrac{2}{3}k\delta_{ij}) - C_2(P_{ij} - \tfrac{2}{3}P\delta_{ij}) \qquad \text{(C.20)}$$

where, P is pressure.

C.2.1.5 Rotational equation

Exact:
$$\Omega_{ij} = -2\omega_k (R_{jm}e_{ikm} + R_{im}e_{jkm}) \qquad \text{(C.21)}$$

where,

e_{ijk} is -1, 0, or 1, depending on the indices and

ω_k is the rotation vector.

C.3 CFD model mesh refinement

The primary goal of solution-adaptive grid refinement is to efficiently reduce the numerical error in the digital solution (FLUENT 6).

A test case selected for the grid refinement sensitivity study was the 1.6d pitch, chequerboard configuration, with k-ε turbulence model. Gradient of velocity magnitudes were adapted in two steps. The first refinement threshold was set at 0.01, and the second at 0.005. Cells with gradients above the value set as the refinement threshold were then marked for refinement. Figures C3.1 and C3.2 show the velocity distribution in the CFD test case model taken at x=0.5d, after the first and second stage refinement respectively.

Figure C3.3 shows profiles of axial velocity for the test case obtained using the k-ε turbulence model. The figure compares the two-stage gradient refinement profile to the initial profile of axial velocity, with no gradient refinement. The figure shows that there was no significant change in measurement when the refined mesh was used.

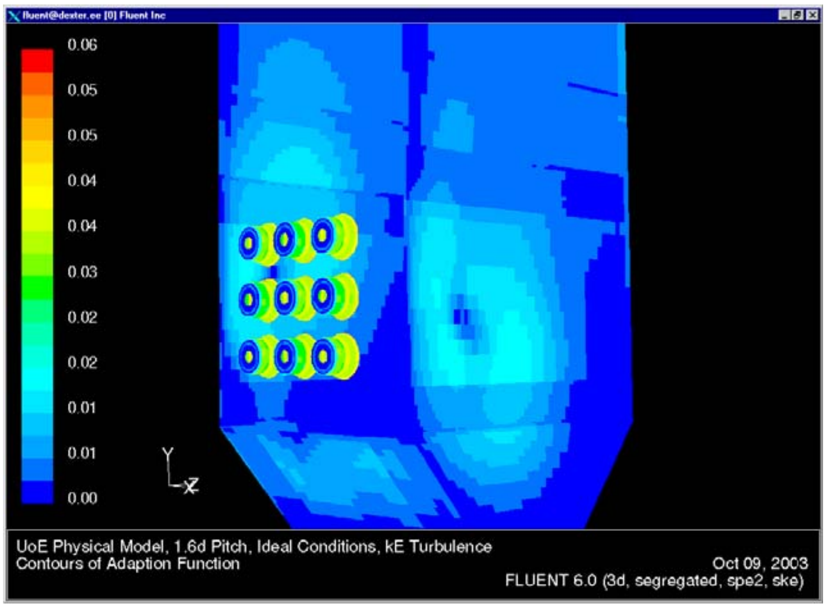

UoE Physical Model, 1.6d Pitch, Ideal Conditions, kE Turbulence
Contours of Adaption Function
Oct 09, 2003
FLUENT 6.0 (3d, segregated, spe2, ske)

Figure C3.1 *Gradient refinement threshold of 0.01*

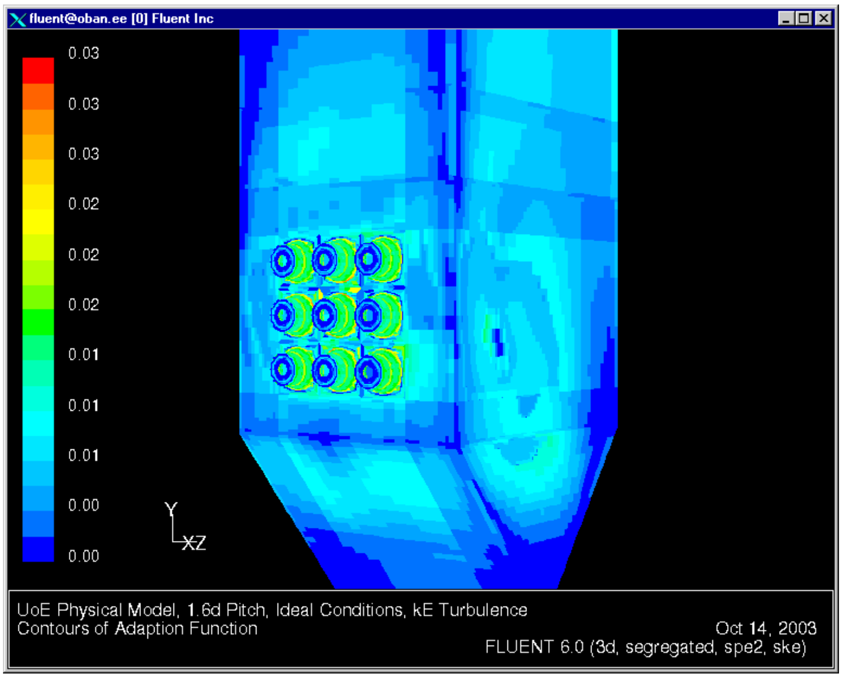

UoE Physical Model, 1.6d Pitch, Ideal Conditions, kE Turbulence
Contours of Adaption Function
Oct 14, 2003
FLUENT 6.0 (3d, segregated, spe2, ske)

Figure C3.2 *Gradient refinement threshold of 0.005*

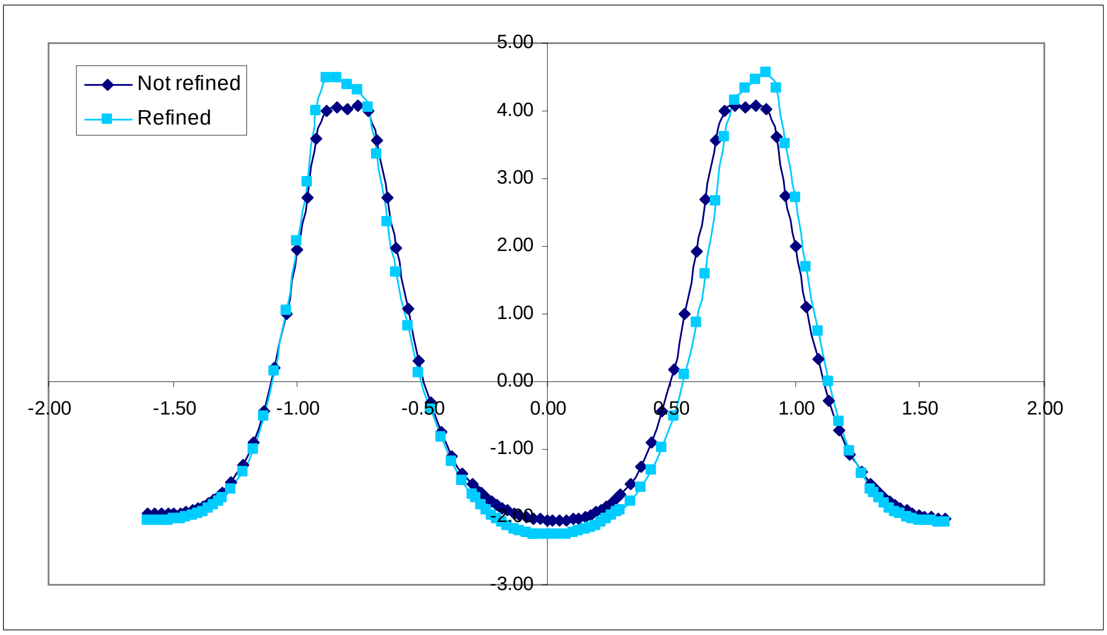

Figure C3.3 *'Refined 'and 'unrefined' vertical profiles of axial velocity taken for 1.6d pitch of chequerboard configuration at x=0.5d, simulated using the k-ε turbulence model*

Appendix D

D.1 Radial (*v*) velocity profiles

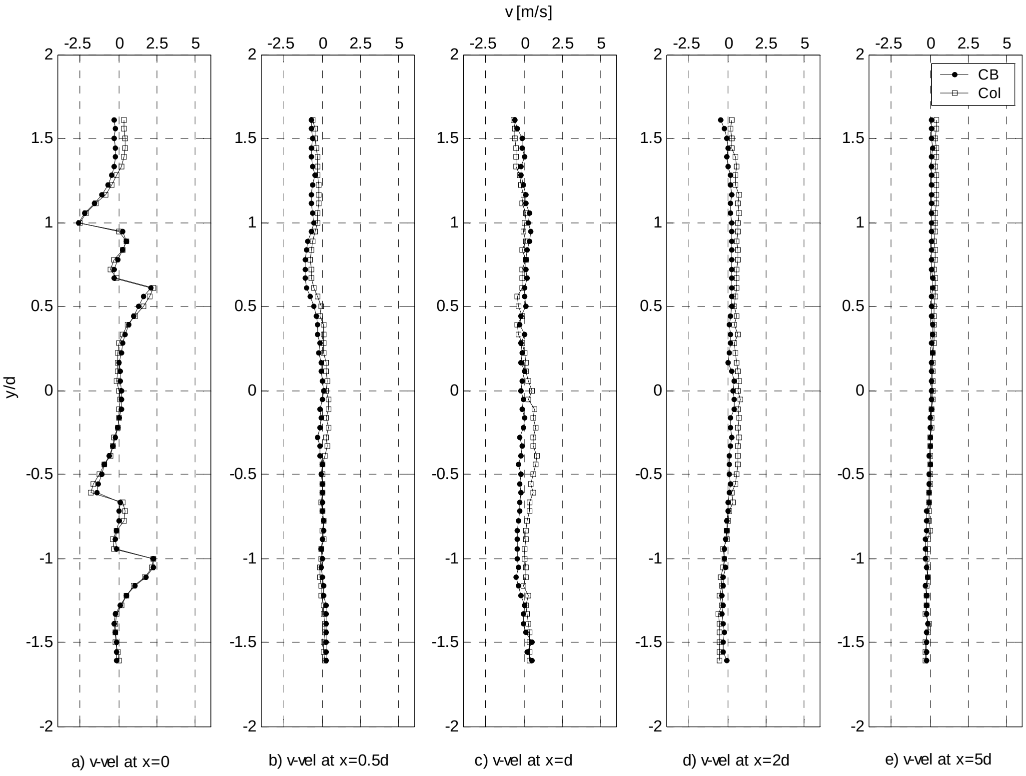

a) v-vel at x=0 b) v-vel at x=0.5d c) v-vel at x=d d) v-vel at x=2d e) v-vel at x=5d

Figure D.1 *Vertical profiles of v velocity, taken for 1.6d pitch of chequered board and columnar configurations at x=0d, 0.5d, d, 2d and 5d distances from the burner panel.*

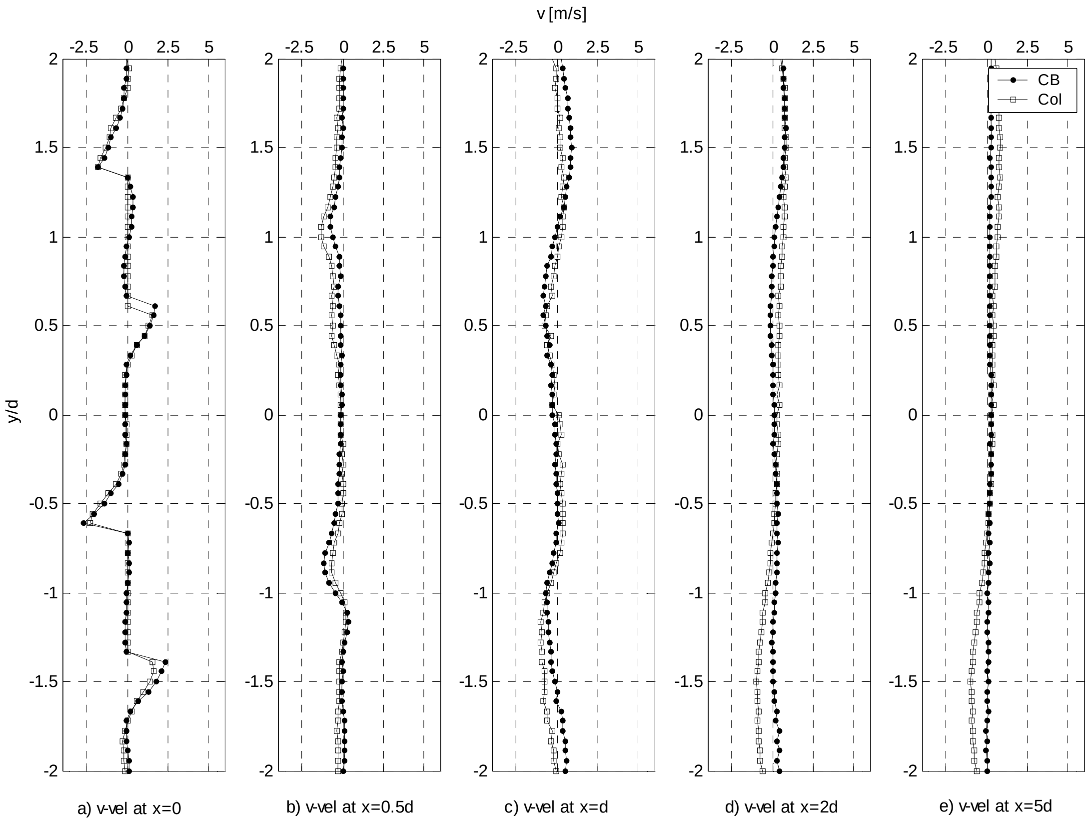

Figure D.2 *Vertical profiles of v velocity, taken for 2d pitch of chequered board and columnar configurations at x=0d, 0.5d, d, 2d and 5d distances from the burner panel.*

D.2 Turbulent kinetic energy, k

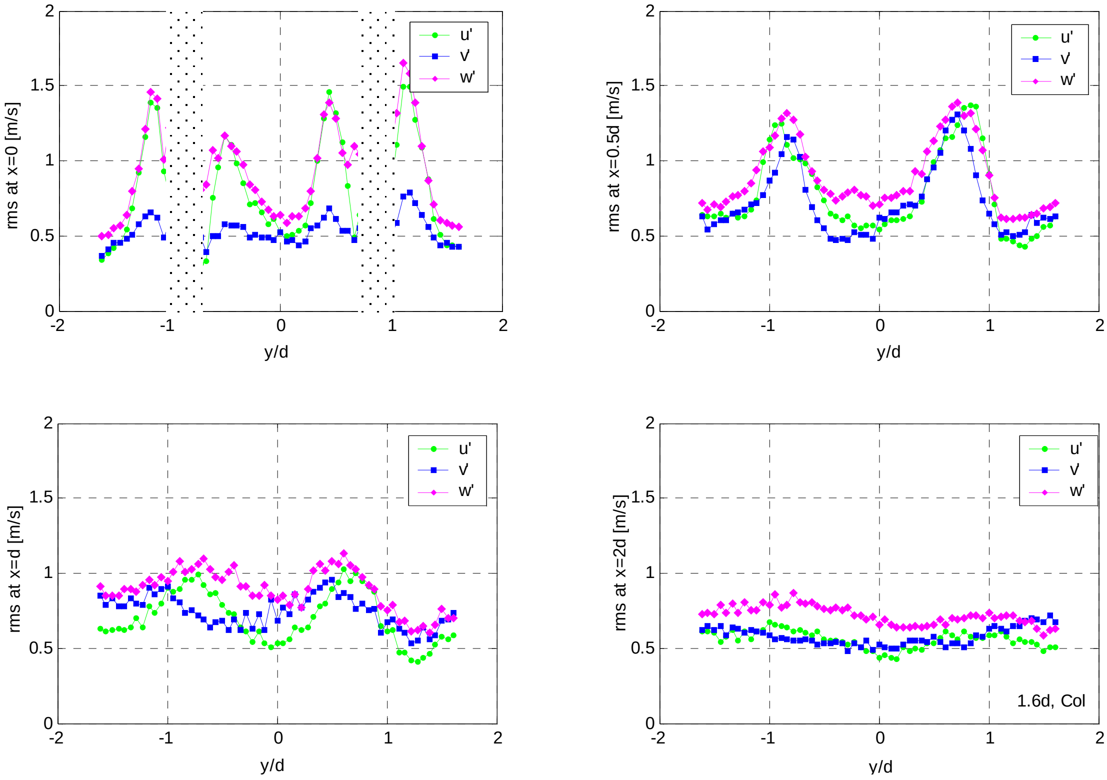

Figure D.3 *RMS fluctuations in three dimensions, u′, v′ and w′, taken for 1.6d pitch of columnar configuration at x=0, 0.5d, d and 2d distances from the burner panel*

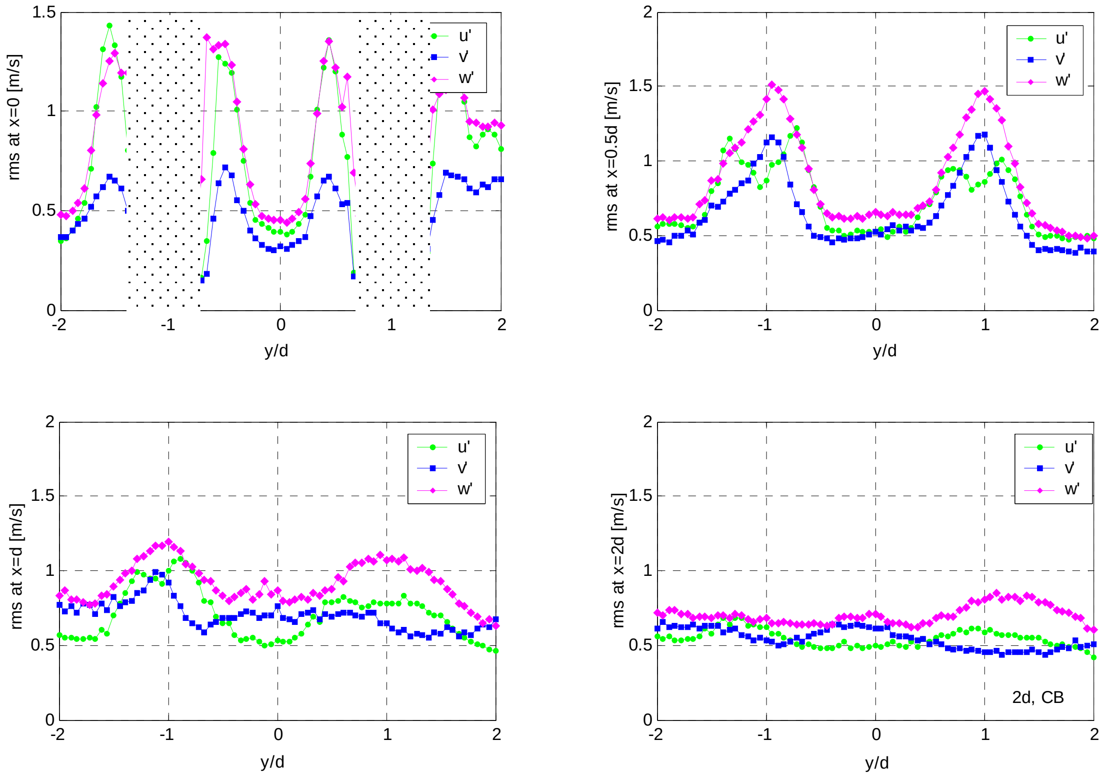

Figure D.4 *RMS fluctuations in three dimensions, u′, v′ and w′, taken for 2d pitch of chequerboard configuration at x=0, 0.5d, d and 2d distances from the burner panel*

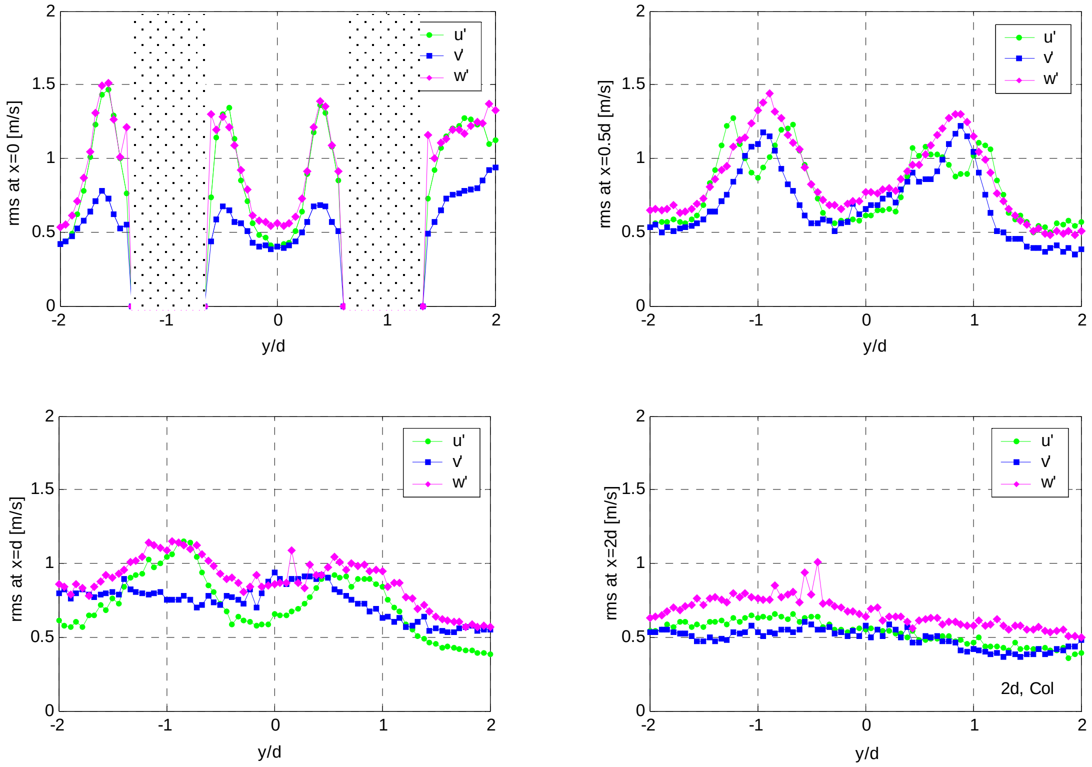

Figure D.5 *RMS fluctuations in three dimensions, u', v' and w', taken for 2d pitch of columnar configuration at x=0, 0.5d, d and 2d distances from the burner panel*

D.3 Reynolds stresses

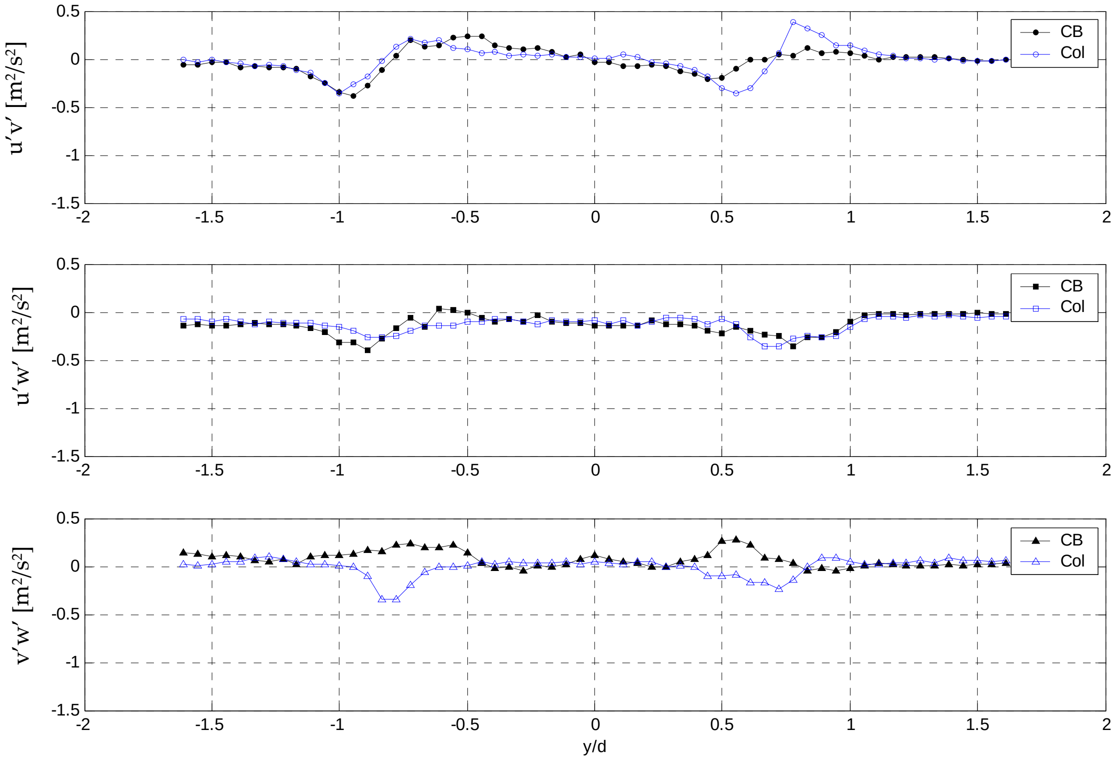

Figure D.6 *Reynolds stresses, u'v', u'w' and v'w', taken for 1.6d pitch of chequerboard and columnar configurations at x=0.5d*

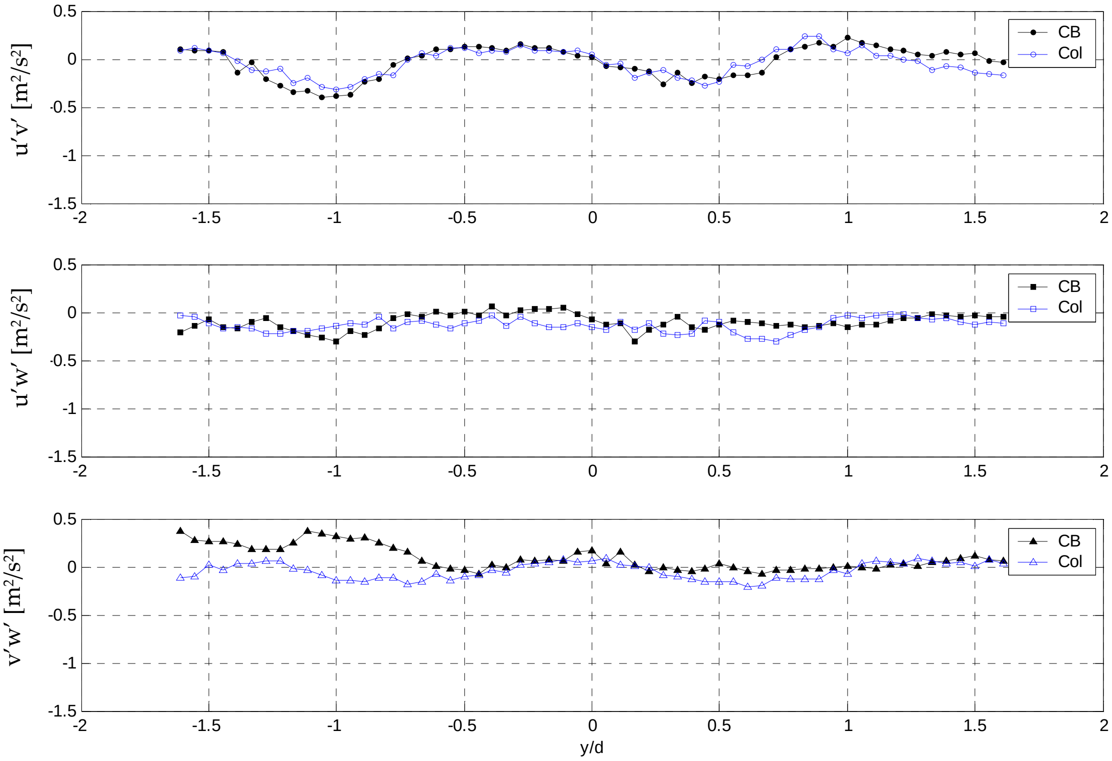

Figure D.7 *Reynolds stresses, u'v', u'w' and v'w', taken for 1.6d pitch of chequerboard and columnar configurations at x=d*

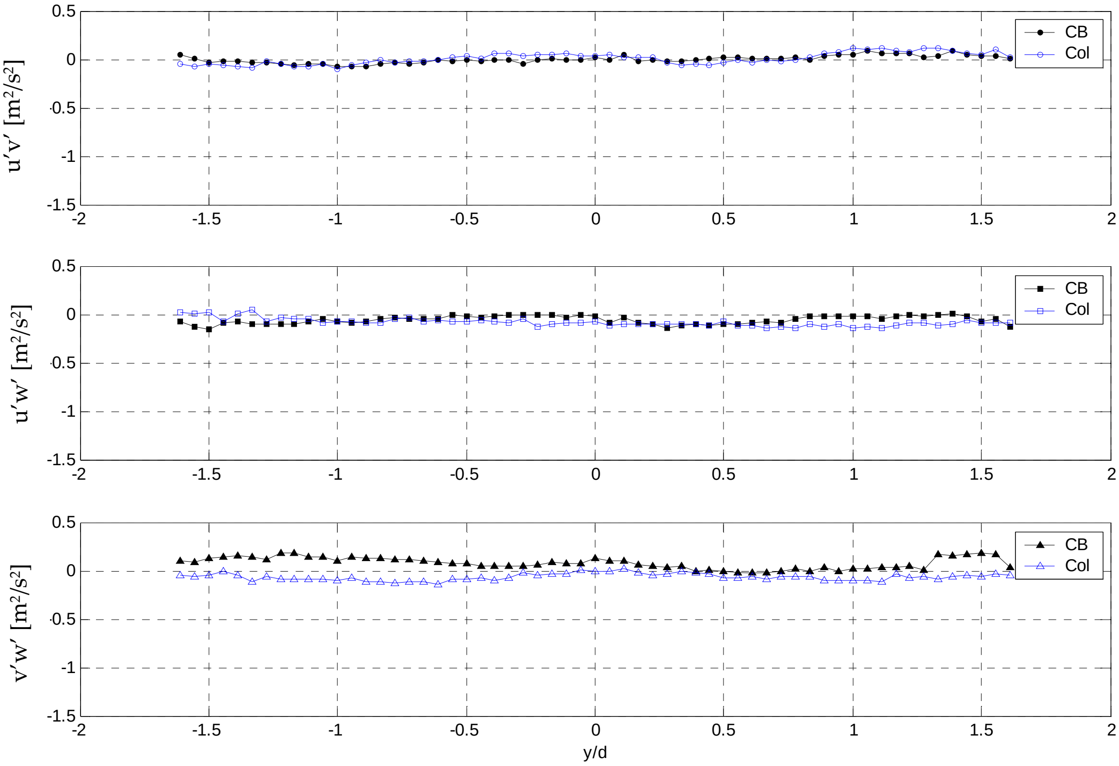

Figure D.8 *Reynolds stresses, u′v′, u′w′ and v′w′, taken for 1.6d pitch of chequerboard and columnar configurations at x=2d*

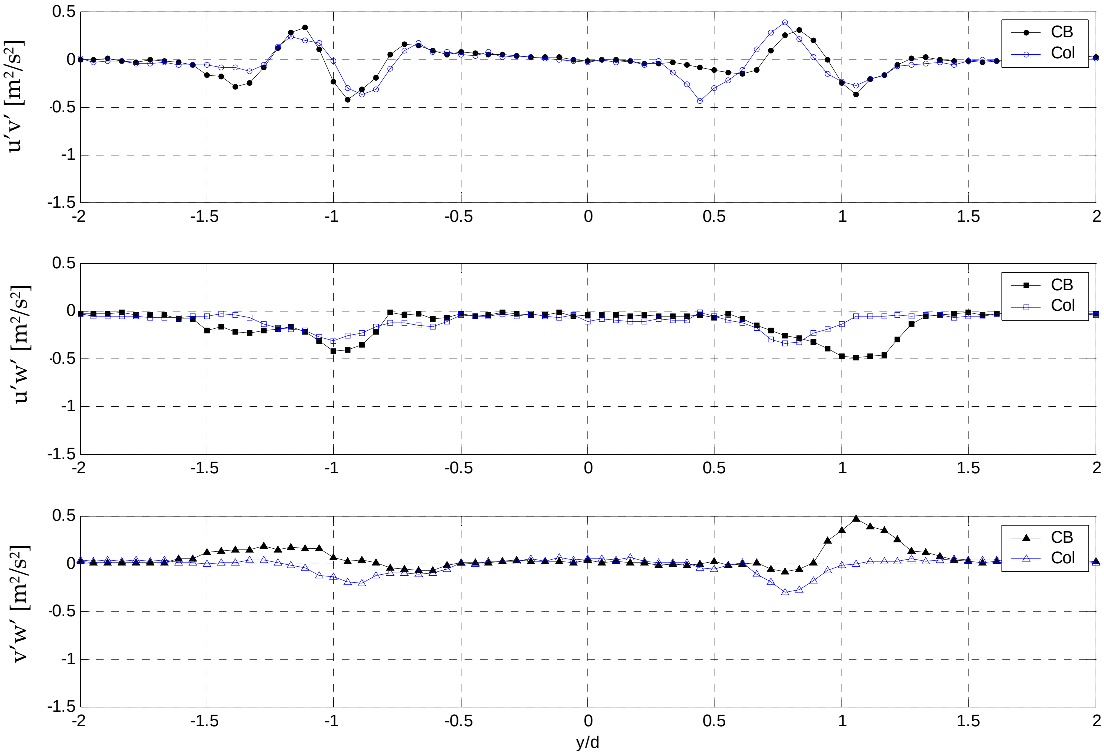

Figure D.9 *Reynolds stresses, u′v′, u′w′ and v′w′, taken for 2d pitch of chequerboard and columnar configurations at x=0.5d*

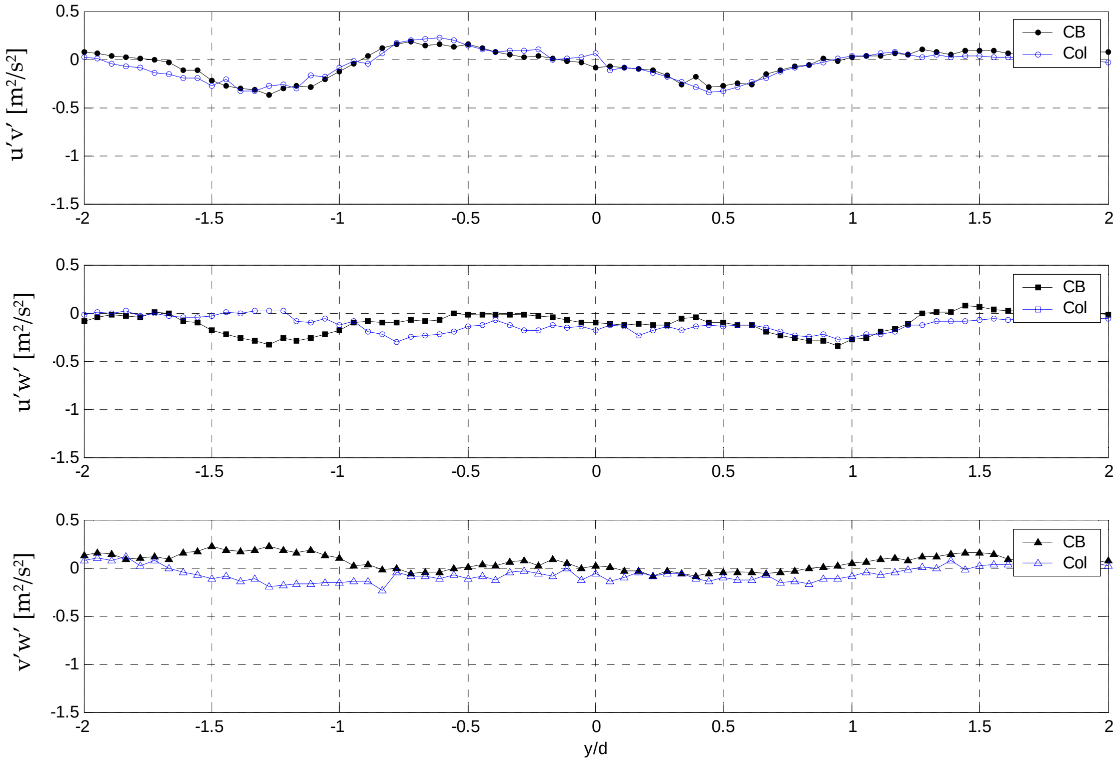

Figure D.10 *Reynolds stresses, u'v', u'w' and v'w', taken for 2d pitch of chequerboard and columnar configurations at x=d*

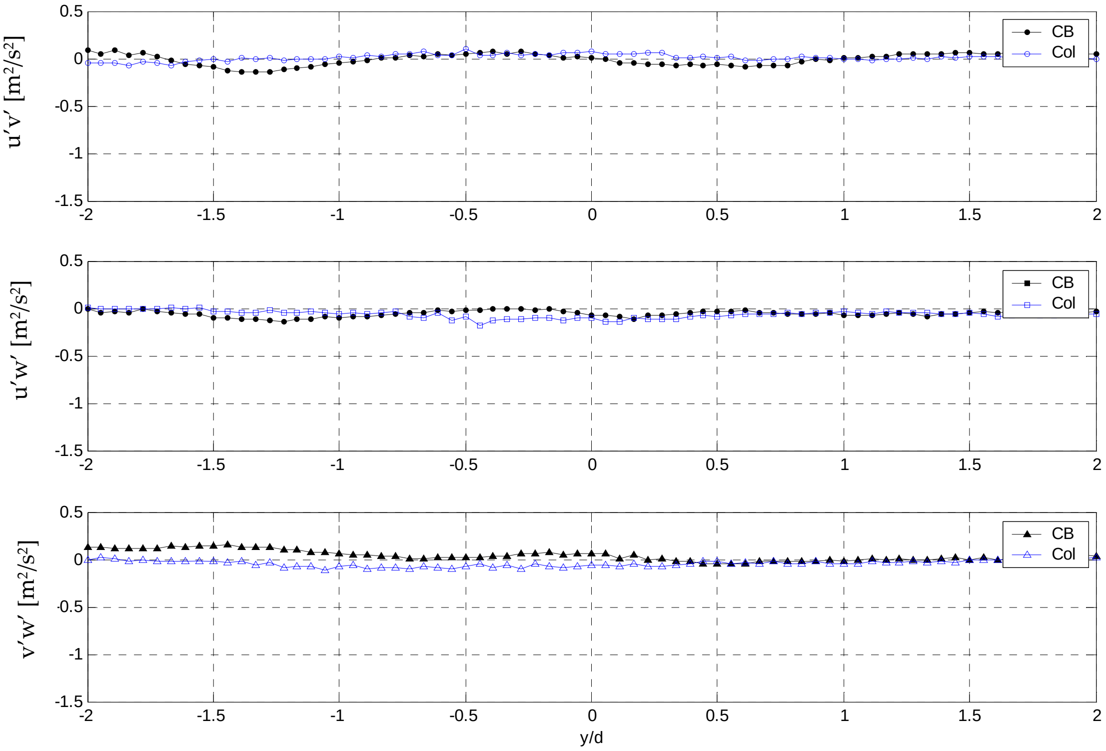

Figure D.11 *Reynolds stresses, u′v′, u′w′ and v′w′, taken for 2d pitch of chequerboard and columnar configurations at x=2d*

Appendix E

E.1 Radial (*v*) velocity profiles

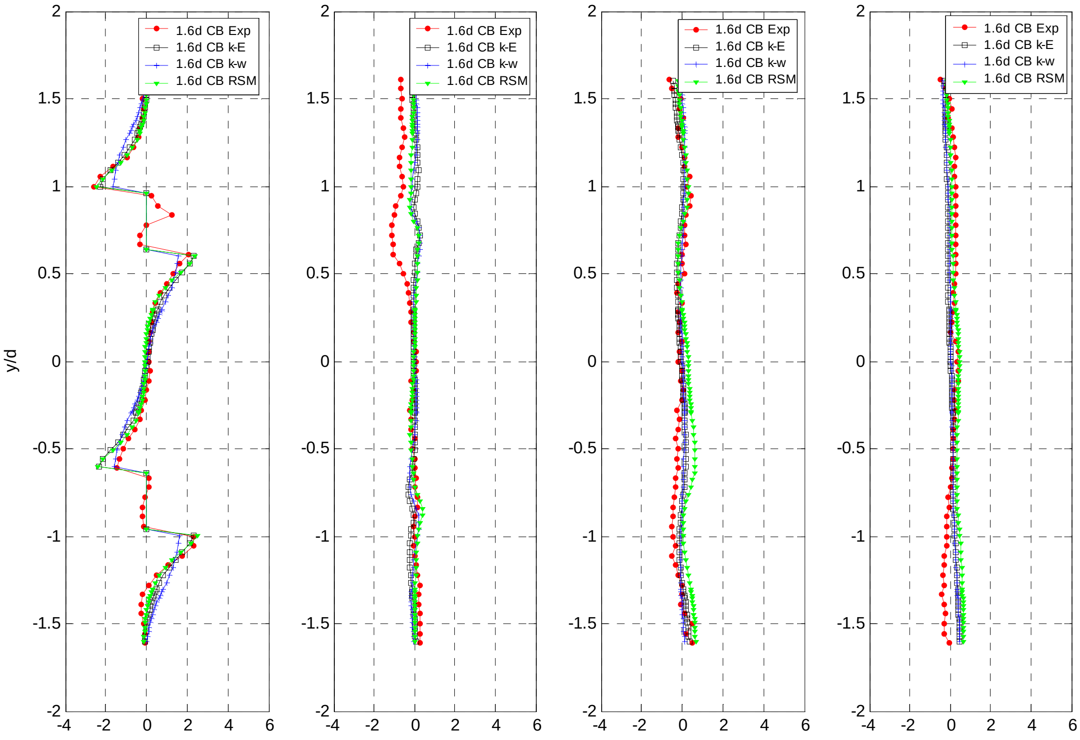

a) v-vel [m/s] at x=0 b) v-vel [m/s] at x=0.5d c) v-vel [m/s] at x=d d) u-vel [m/s] at x=2d

Figure E.1 *Numerical (k-ε, k-w and RSM turbulence models) v experimental comparisons of vertical profiles of v velocity at x=0, 0.5d, d and 2d, taken for 1.6d pitch of chequerboard configuration*

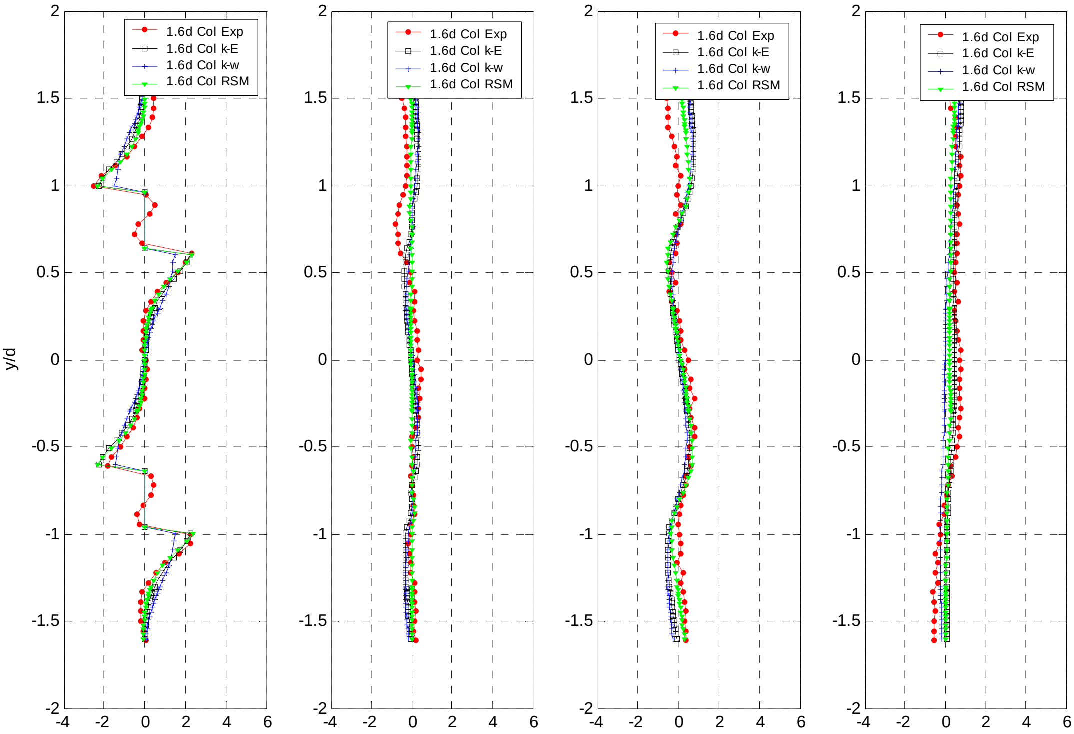

a) v-vel [m/s] at x=0 b) v-vel [m/s] at x=0.5d c) v-vel [m/s] at x=d d) v-vel [m/s] at x=2d

Figure E.2 *Numerical (k-ε, k-w and RSM turbulence models) v experimental comparisons of vertical profiles of v velocity at x=0, 0.5d, d and 2d, taken 1.6d pitch of columnar configuration*

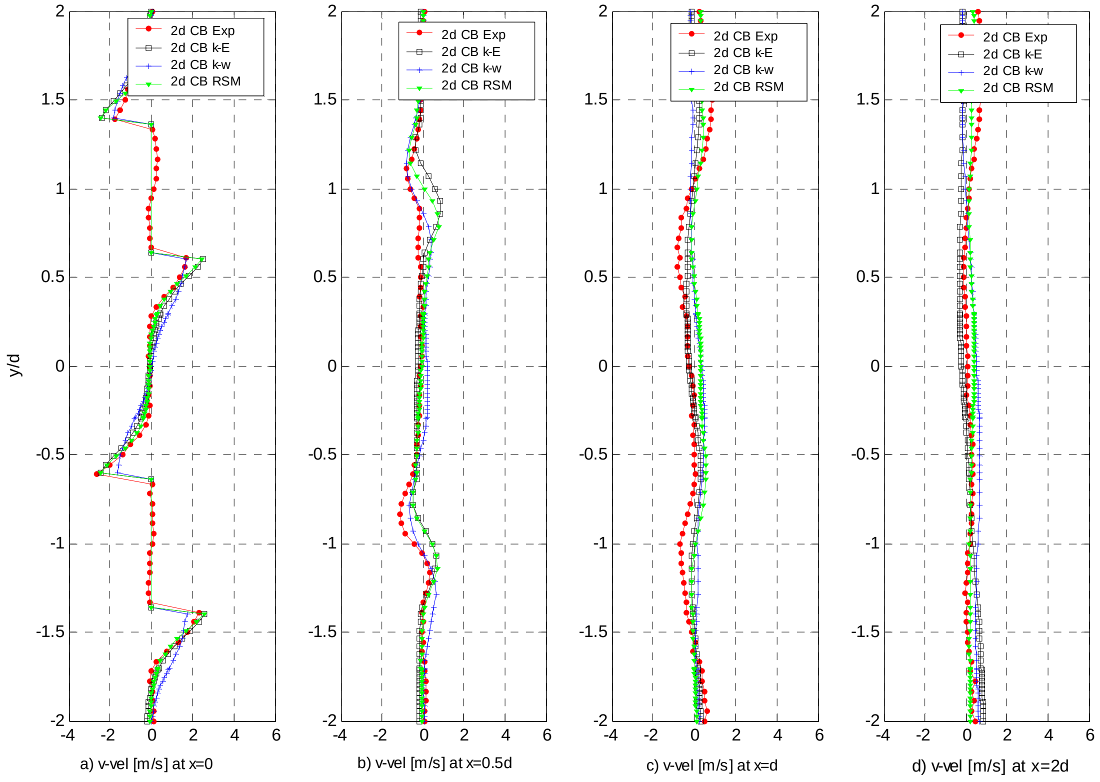

Figure E.3 *Numerical (k-ε, k-w and RSM turbulence models) v experimental comparisons of vertical profiles of v velocity at x=0, 0.5d, d and 2d, taken for 2d pitch of chequerboard configuration*

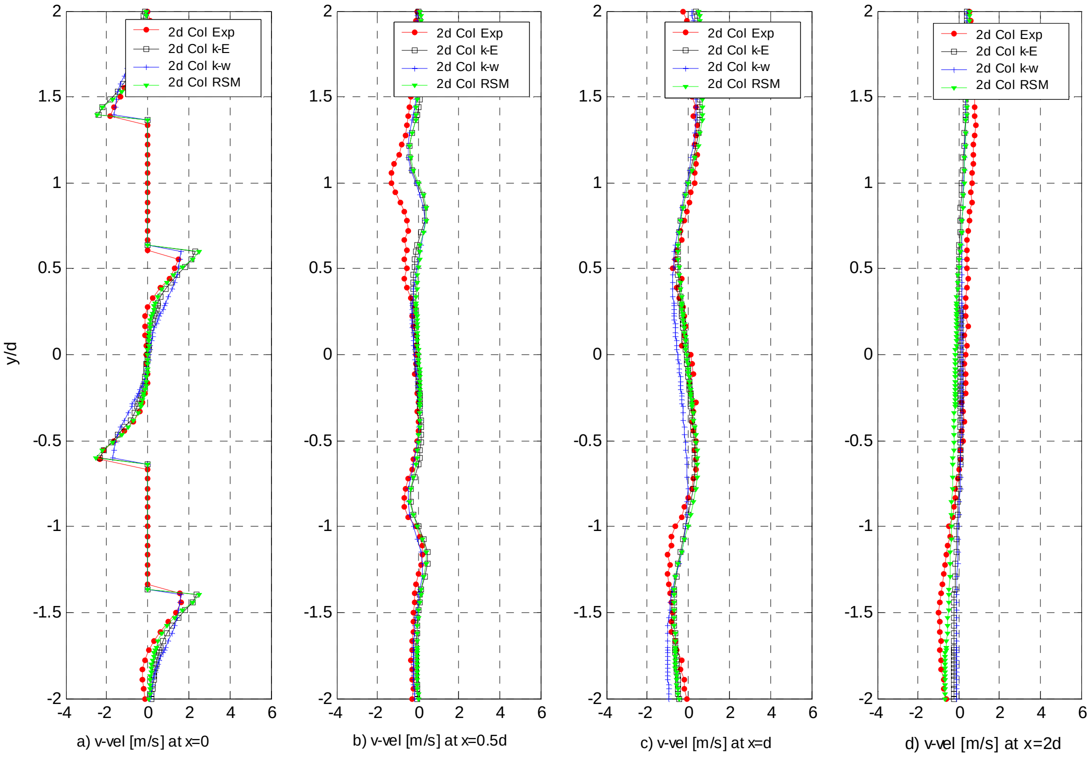

Figure E.4 *Numerical (k-ε, k-w and RSM turbulence models) v experimental comparisons of vertical profiles of v velocity at x=0, 0.5d, d and 2d, taken for 2d pitch of columnar configuration*

E.2 Reynolds stresses

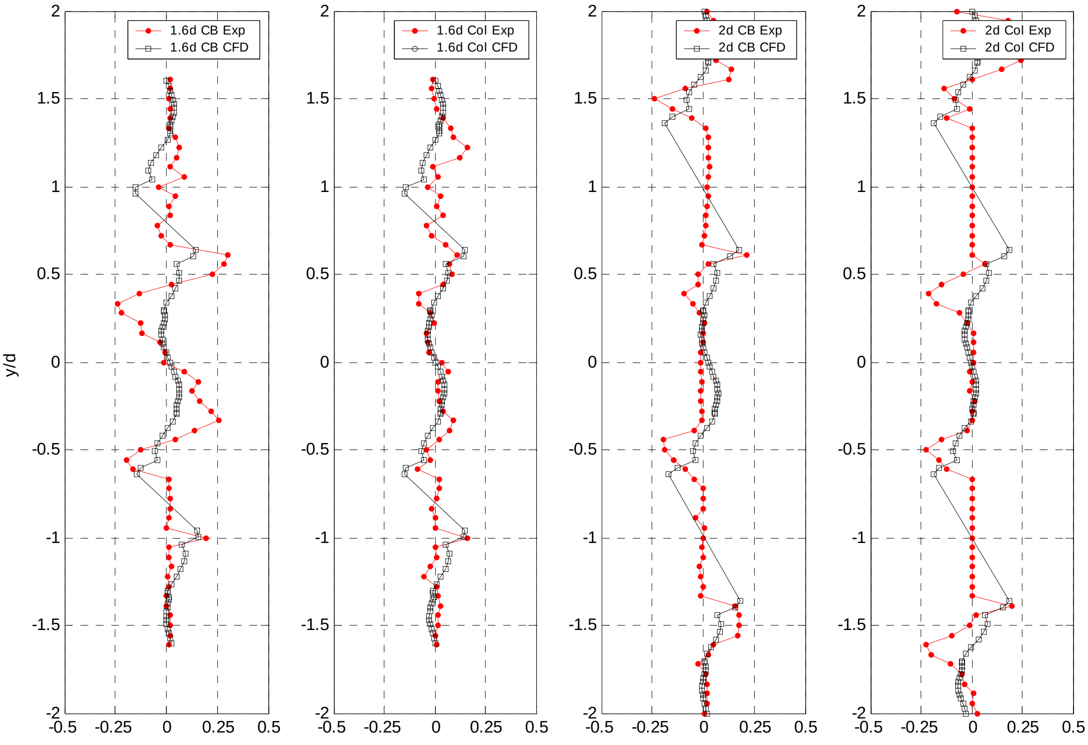

a) UxV at x=0 b) UxV at x=0 c) UxV at x=0 d) UxV at x=0

Figure E.5 *Reynolds shear stress, u'v, for 1.6d and 2d pitches of chequerboard and columnar configurations, showing fit between experimental and numerical data (obtained using RSM turbulence model) at x= 0*

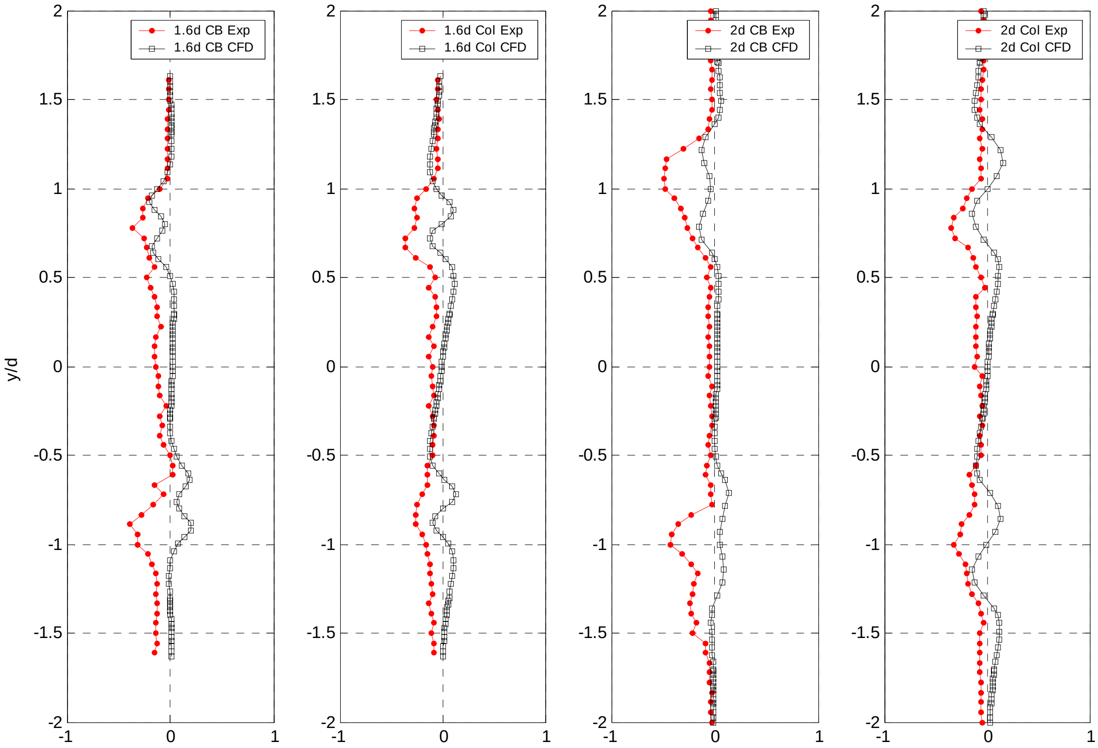

a) UxW at x=0 b) UxW at x=0 c) UxW at x=0 d) UxW at x=0

Figure E.6 *Reynolds shear stress, u'w', for 1.6d and 2d pitches of chequerboard and columnar configurations, showing fit between experimental and numerical data (obtained using RSM turbulence model) at x= 0*

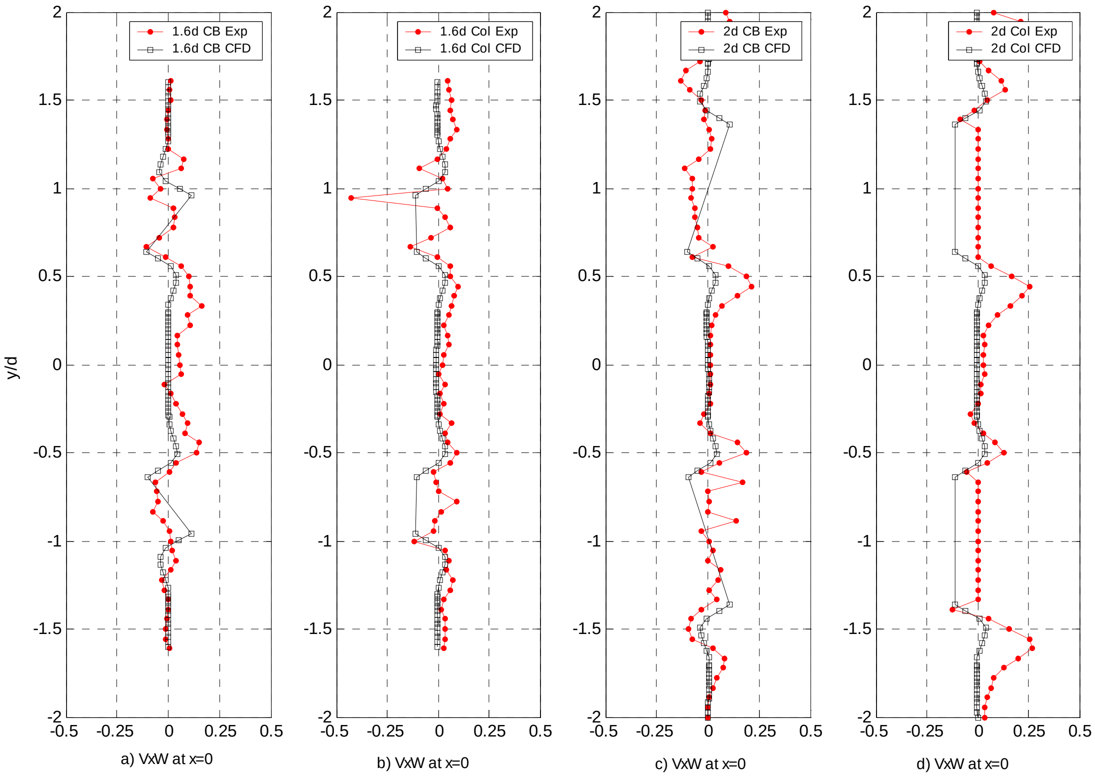

Figure E.7 *Reynolds shear stress, v'w', for 1.6d and 2d pitches of chequerboard and columnar configurations, showing fit between experimental and numerical data (obtained using RSM turbulence model) at x= 0*

Appendix F